PREDICTIVE MODELING, SIMULATION, AND OPTIMIZATION OF LASER PROCESSING TECHNIQUES: UV NANOSECOND-PULSED LASER MICRO-MACHINING OF POLYMERS AND SELECTIVE LASER MELTING OF POWDER METALS

By

LUIS ERNESTO CRIALES ESCOBAR

A dissertation submitted to the

Graduate School-New Brunswick

Rutgers, The State University of New Jersey

In partial fulfillment of the requirements

For the degree of

Doctor of Philosophy

Graduate Program in Industrial and Systems Engineering

Written under the direction of

Tuğrul Özel

And approved by

____

____

____

____

____

New Brunswick, New Jersey

May 2016

ABSTRACT OF THE DISSERTATION

Predictive Modeling, Simulation, and Optimization of Laser Processing Techniques: UV Nanosecond-pulsed Laser Micro-machining of Polymers and Selective Laser Melting of Powder Metals

by LUIS ERNESTO CRIALES ESCOBAR

Dissertation Director:

Assoc. Prof. Tuğrul Özel

One of the most frequently evolving areas of research is the utilization of lasers for micro-manufacturing and additive manufacturing purposes. The use of laser beam as a tool for manufacturing arises from the need for flexible and rapid manufacturing at a low-to-mid cost. Laser micro-machining provides an advantage over mechanical micro-machining due to the faster production times of large batch sizes and the high costs associated with specific tools. Laser based additive manufacturing enables processing of powder metals for direct and rapid fabrication of products. Therefore, laser processing can be viewed as a fast, flexible, and cost-effective approach compared to traditional manufacturing processes.

Two types of laser processing techniques are studied: laser ablation of polymers for micro-channel fabrication and selective laser melting of metal powders. Initially, a feasibility study for laser-based micro-channel fabrication of poly(dimethylsiloxane) (PDMS) via experimentation is presented. In particular, the effectiveness of utilizing a nanosecond-pulsed laser as the energy source for laser ablation is studied. The results are analyzed statistically and a relationship between process parameters and micro-channel dimensions is established. Additionally, a process model is introduced for predicting channel depth. Model outputs are compared and analyzed to experimental results. The second part of this research focuses on a physics-based FEM approach for predicting the temperature profile and melt pool geometry in selective laser melting (SLM) of metal powders. Temperature profiles are calculated for a moving laser heat source to understand the temperature rise due to heating during SLM. Based on the predicted temperature distributions, melt pool geometry, i.e. the locations at which melting of the powder material occurs, is determined. Simulation results are compared against data obtained from experimental Inconel 625 test coupons fabricated at the National Institute for Standards & Technology via response surface methodology techniques. The main goal of this research is to develop a comprehensive predictive model with which the effect of powder material properties and laser process parameters on the built quality and integrity of SLM-produced parts can be better understood. By optimizing process parameters, SLM as an additive manufacturing technique is not only possible, but also practical and reproducible.

ACKNOWLEDGMENTS

"*Far and away the best prize that life has to offer is the chance to work hard at work worth doing."* –Theodore Roosevelt

The development and completion of this dissertation would not have been possible without the support of many individuals and institutions. First, I would like to give thanks to my adviser, Dr. Tuğrul Özel, for his enthusiastic guidance throughout the past four years. It has truly been a pleasure to work with Prof. Özel. I would like to thank Dr. Susan Albin, Dr. Alkan Donmez, Dr. Yogesh Jaluria, and Dr. Myong-Kee Jeong for accepting my invitation to be part of my dissertation committee and providing valuable feedback along the way. Additionally, I would like to give special thanks to Dr. Shawn Moylan and Dr. Brandon Lane, from the National Institute of Standards and Technology.

I give thanks to the Lord for giving me the opportunity to write this dissertation and giving me the chance to grow as a person. I am very grateful to my parents and my sister, who have supported me at every turn from a thousand leagues away. Their unrivaled optimism is the catalyst that pushes me forward when I need it the most.

Last and most definitely not least, I would like to dedicate this work to my wife Jessica Lauren. Through all the ups and downs, you have been the one constant in my life. As a chapter in our life comes to an end, I cannot wait to see how our next adventure unfolds. This is for you.

TABLE OF CONTENTS

LIST OF FIGURES

LIST OF TABLES

Chapter 1 INTRODUCTION

1.1 Laser Processing of Materials

One of the most frequently evolving areas of research is the utilization of lasers for processing materials for manufacturing products in the form of material removal e.g. laser micro-machining, or in the form of powder material fusion for additive manufacturing e.g. selective laser melting. The use of laser as a tool for the development of micro-scale devices arises from the need for flexible and rapid manufacturing at a low-to-mid cost. Laser processing techniques also benefit from not requiring access to clean-room facilities. Furthermore, they do not require additional elements such as masks (lithographic processes) or molds (hot embossing processes). Minor modifications to the design would require a completely new mask (in the case of lithography) or mold (for hot embossing), so flexibility of the process is a huge, distinct advantage when it comes to utilizing laser micro-manufacturing. Laser processing provides an advantage over micro-milling due to faster manufacturing times of large batch sizes and high costs associated with specific tools, as is the case for micro-milling. Therefore, laser micro-machining can be viewed as a fast, flexible, cost-effective approach to classical micro-manufacturing processes. The flexibility of laser processing can be best seen in the wide array of geometries that can be attained through this manufacturing technique.

Laser processing techniques can be classified into two categories: laser ablation processes and laser-based additive manufacturing processes. Laser ablation is defined as the process of removing material from a surface by irradiating it with a high-energy laser beam. Laser ablation itself is the result of complex photochemical processes that are highly sensitive to the conditions in which the process is executed. Laser-based additive manufacturing (AM) covers a wide range of direct and rapid response fabrication methods that are typically performed in layer-by-layer building format. The laser is used as a high energy source to partially or fully melt powder material, which solidifies giving form to a 3-D structure. For both manufacturing techniques, the outcome of the process itself depends on the material properties, the laser characteristics and the processing parameters.

1.2 Laser Types

Lasers can be classified in many different ways. One method of laser classification is by wavelength of the light emitted. Based on wavelength, lasers can be broadly classified into three categories: ultraviolet (UV) with a wavelength of 10-380 nm, visible light with a wavelength of 380-700 nm, and near-infrared (NIR) with a wavelength of 700-1100 nm lasers. A different way of classifying lasers is by emission type. Lasers that emit light uninterruptedly are referred to as continuous wave (CW) lasers, while lasers that emit light periodically are classified as pulsed lasers. Pulsed lasers can be further classified based on pulse frequency. For instance, lasers whose pulse frequency is in the nanosecond range are referred to as “short” lasers. “Ultra-short” lasers are those whose pulse frequency is in pico- or femtosecond range. The type of laser to be utilized will vary based on the application and the manufacturing technique.

1.3 Materials for Laser-based Processing

Difficult-to-process materials are among the most commonly utilized during laser micro-manufacturing. All solid materials (metals, ceramics, and polymers) can be manufactured using a laser, given the appropriate choice of laser and process parameters. The studies in this document focus on laser ablation of polymers for micro-fluidic medical devices and laser-based additive manufacturing of powder metals. In particular, powder material properties defer from those of the bulk material, especially when the material is subject to heating and cooling. Therefore, material properties must be studied in depth to grasp a full understanding of laser processing.

1.3.1 Polymers

Polymers are the material of choice for applications where cost-effectiveness is the principal requirement. They are known for having favorable thermal and chemical resistances, molding temperature, and other surface derivation properties. Furthermore, many polymers are also classified as biocompatible materials; they can be used in medical applications without risk of a negative reaction from a patient. Transparent polymers are polymers whose degree of cristallinity approaches zero or one. They are generally the result of a polymer with an amorphous molecular chain, which provides them with an ample range of mechanical properties and phase behavior. Polymers are easily obtained at a low cost for a wide variety of options, allowing them to be the ideal material for mass production of disposable devices on a cost-effective basis.

Polyurethane based polymers are known as the most biocompatible polymers, therefore they are often used in the production of artificial heart valves, blood vessels, and skin tissue. Polysiloxane is used in breast implants, artificial tendons, skin tissue, blood vessels, and heart valves (Stieglitz et al., 2000). Polyamide is utilized in retina implants, while polyethylene is used in disposable tubes, boxes, and syringes, and polyamide is the main material in the production of catheter tubes (Chu, 1990). Polyetheretherketone (PEEK) scaffolding is used to stimulate bone growth due to its unique geometry and composition. In particular, recent research has focused on using Polymethylmethacrylate

(PMMA) as the main material for microchannel generation. PMMA has been a popular choice for medical devices applications based on its biocompatibility, low cost, thermal stability and mechanical properties. Polydimethylsiloxane (PDMS) is the most widely used silicon based polymer, another transparent polymer with promising applications in the biomedical devices field, since it is also biocompatible. PDMS micro-channels are generally manufactured using soft lithography or hot embossing. Little research has been performed on nanosecond laser processing of PDMS micro-channels, although some articles can be found on micro-channel generation using ultra-short pulsed lasers (Huang and Guo, 2009).

1.3.2 Metals

Metals are often preferred in manufacturing applications due to their strength. Laser ablation of metals is a challenging task due to the high vaporization point and high reflectivity of most metals. Although very challenging, laser ablation of metals is still possible with the use of short and ultra-short pulsed lasers with the appropriate choice of laser parameters. On the other hand, powder metals are ideally suited for laser-based additive manufacturing processes.

Ti-6Al-4V is a titanium-based two-phase alloy which is very popular in manufacturing applications due to its corrosion resistance, high specific and mechanical strength, super-plasticity, low-weight, and biocompatibility, among many other properties. Its biocompatibility makes it a prime candidate for medical devices and implant applications and it is also widely used in aeronautical, aerospace, and automotive applications due to its high strength-to-weight ratio and high temperature strength properties.

316L Stainless Steel (316L SS) is an austenitic stainless steel that possesses excellent toughness and weldability characteristics. Grade 316L is the low carbon version of Grade 316 SS, which makes it easier to machine. 316L also has higher corrosion resistance than similar stainless steel grades. 316L SS is widely utilized in marine applications, pharmaceutical applications, and medical implants such as pins, screws, and total hip and knee replacements.

Inconel 625 (IN 625) is a nickel-based (nickel-chromium) alloy often used in various applications including naval and aircraft structures, gas turbines, and jet engines due to its high strength at elevated temperatures, superb fatigue properties, excellent corrosion resistance, and good weldability characteristics. The chemical composition of Ti-6Al-4V, 316L Stainless Steel, and Inconel 625 is given in Table 1.1.

Table 1.1. Chemical composition of some metal alloys.

Ti-6Al-4V Alloy

Element	Al	V	O	H	N	C	Fe	Si	Ti
wt%	6.0	4.0	0.15	0.02	0.04	0.04	0.025	0.02	Balance

316L Stainless Steel

Element	C	Mn	Si	Cr	S	P	Mo	Ni	Fe
wt%	0.03	2.0	0.75	17	0.03	0.045	2.00	12.0	Balance

Inconel 625 Alloy

Element	Cr	Fe	Mo	C	Mn	Si	Al	Ti	Ni
wt%	20	5.0	8.00	0.1	0.5	0.5	0.4	0.4	Balance

1.4 Laser-based Micro-Channel Fabrication for Micro-fluidics Applications

Micro-fluidics comprises the set of analytical systems that are able to manipulate, process, and control small quantities of fluids. These devices use components such as micro-channels, electrodes, columns, and reactors that handle volumes in the order of nanoliters and picoliters. Applications of micro-fluidics devices include lab-on-a-chip devices, DNA analysis, drug delivery devices, nerve regeneration, microfluidic chip devices, and many others. The basic components of many micro-fluidic systems are the micro-channels in which fluid flows. In these channels, separation or mixing of liquids takes place within the micro-fluidics system. Therefore, achieving lower cost in directly fabricating micro-channels for micro-fluidics may lead to a wider utilization of this technology.

Complex micro-channel systems of good quality can be developed through laser processing. This complexity is required due to the need to integrate individual elements of different characteristics (fluids, biological/chemical, electrical, etc.) into a single device to increase the functionality of the device. Therefore, research into micro-channel generation using laser processing is of vital importance for the development of micro-scale devices. The vast majority of the latest research performed on laser processing of micro-channels on polymeric materials has focused on the use of "ultra-short" (pico or femtosecond) pulsed lasers (Gómez et al., 2005, Suriano et al., 2011, Day and Gu, 2005). This is due to their higher cooling rates and lower Heat-Affected Zone (HAZ) regions, which are a direct result of the higher peak power produced relative to pulsed nanosecond or continuous wave lasers. A higher cooling rate is ideal because it generates lower peripheral thermal damage (due to the lower HAZ) and creates less debris (e.g. burrs) during the channel creation process. Although the results have been very promising, ultra-short or fast lasers are very expensive, unstable at times, and therefore not suitable for mass production operations. On the other hand, nanosecond lasers are considered more stable, can provide a cheaper alternative to pico or femtosecond pulsed lasers, and are more suitable for production operations. The vast majority of research has focused on the use of UV pico or femtosecond pulsed lasers (Roberts et al., 1997, Waddell et al., 2002) in microfluidics processing, while only recently have IR or NIR lasers been used for laser micro-micromachining (Krüger et al., 2005, Wolynski et al., 2011, Teixidor et al., 2012, Teixidor et al., 2013) with promising results. However, laser wavelength and pulse frequency are not the only parameters which affect the quality of the process, while there is a need to better understand the laser energy intensity levels for ablation of transparent polymers.

The size and shape of the intended part can be controlled by changing certain process parameters during the micro-manufacturing operation. Among the process parameters that determine the resulting geometry, the most important are laser fluence and scanning speed, although laser power, Q-switch delay, pulse frequency, scanning rate and focused beam distance from the surface are all relevant as well. The number of passes and the processing sequences are also important factors to take into account in laser ablation, since one of the objectives is to obtain process repeatability; in other words, to be able to replicate the process and obtain consistent part geometry in successive experiments. In such cases, the main objective is to obtain process parameters that account for the highest material removal rate and high-quality, consistent geometries. Furthermore, the fact that most of the research has been conducted for pico and femtosecond pulsed UV lasers, while the more cost-efficient nanosecond pulsed laser processing has not been fully explored (for both UV and IR lasers), presents a very attractive opportunity to do very important research work. The development of more accurate theoretical mathematical models for thermal simulations would be very beneficial, since it would allow for a better understanding of the process and would simplify the process of obtaining the best laser process parameters. In order to achieve such a model, the properties of the laser utilized must be fully understood and characterized. To illustrate this point, one of the disadvantages of laser processing in transparent polymers has to do mainly with peripheral thermal damage and the debris generated during the manufacturing process.

1.5 Laser-based Additive Manufacturing of Metal Powders

Parts and components that usually show some degree of geometric customization such as orthodontic and orthopedic implants for medical applications are ideal candidates for processing using additive manufacturing techniques (Bertol et al., 2010). Additive manufacturing is also suitable for repairing or replacing aging parts and components for aerospace and marine application. However, lack of process robustness and fabricated product reliability constitute the major roadblock to certification as accepted production processes, thereby preventing wide implementation of AM technologies in critical industries. In many industries, especially in those where retaining mechanical properties is also a must as part of design requirements, large variations in fabricated part properties and structural integrity prevents AM metal technologies from replacing other traditional manufacturing processes. Additive manufacturing encompasses a wide array of specific techniques, which can be separated into two groups: powder bed fusion processes and blown powder jet-based deposition processes. Powder bed fusion processes will be one of the central themes of this dissertation.

1.5.1 Selective Laser Melting (SLM)

Selective laser melting (SLM) is a laser-based powder bed fusion additive manufacturing process that allows the creation of three-dimensional parts by selectively melting metallic powders and their subsequent solidification. In SLM, the powder material is completely melted and solidified. A traditional SLM set-up typically requires a high power laser source (Figure 1.1). Some of the key advantages of SLM over other manufacturing techniques include: (i) high flexibility in manufacturing complex shapes, (ii) quick process setup avoiding the need for tooling, and (iii) high suitability for product customization and use of multi-materials. These advantages allow for quick transition between manufacturing products of different geometries within the same station.

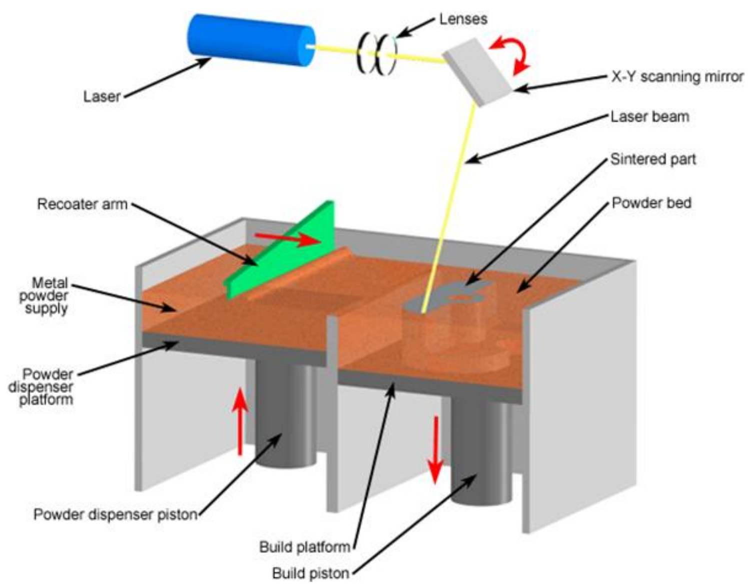

Figure 1.1. A selective laser melting system (DMLS by EOS GmbH).

The most attractive feature of SLM is the ability to use this process to produce highly complex geometries and structures that would normally not even be feasible using conventional production techniques. However, SLM has a major disadvantage: the laser heating process is known for its rapid heating times and unstable cooling times, which result in the formation of pores and voids in the microstructure, which often lead to reduced material density and loss of dimensional accuracy and process repeatability.

In selective laser melting, laser parameters, process parameters, and material properties must be studied jointly to obtain a better understanding of the laser processing of powder metals. Laser parameters consist of those characteristics which are unique to the laser equipment: maximum power, wavelength, beam spot diameter, and laser beam energy distribution. Usually, these parameters cannot be modified. Selective laser melting involves a set of processing parameters: laser power (P), laser spot size (d), scanning path direction or strategy, scanning velocity (v_s), stripe width (w), hatch distance (h), and layer thickness (s) as shown in Figure 1.2. Typically, laser spot size is considered fixed (e.g. d=100 μm), but laser power, scanning rate, hatch distance, and layer thickness can be modified to increase or decrease the *energy intensity* ($E=P/v_s \times h \times s$) for controlling the melting of the powder material. As a result, the hatch overlap factor (d/h) can be determined, which along with energy intensity, affects the resultant melt pool geometry, heat affected area, quality of fusion, cooling rate, formation of solidification microstructure, etc.

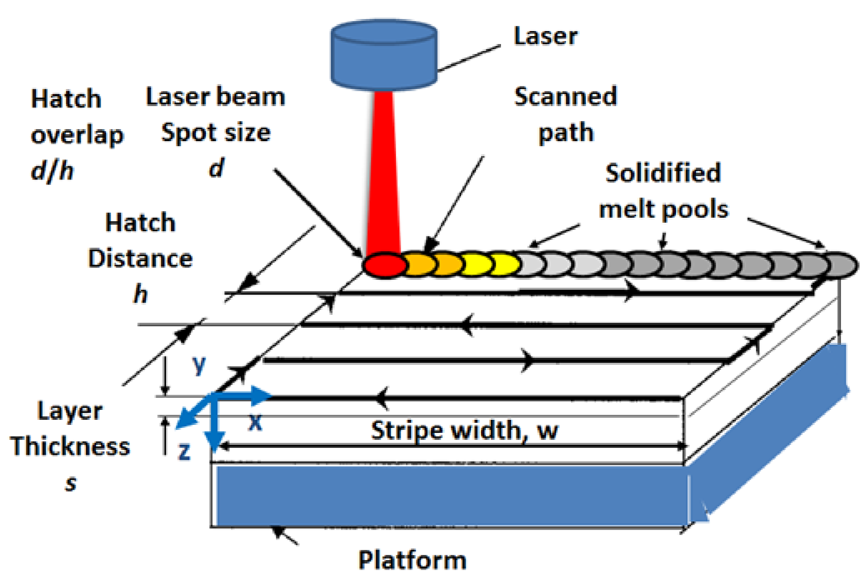

Figure 1.2. SLM process variables.

1.5.2 Selective Laser Sintering (SLS)

Selective laser sintering is another additive manufacturing technique similar in nature to SLM. As the name indicates, in SLS the material is not fully melted, but rather it is sintered requiring post-processing to obtain a fully dense part. Sintering is the process by which a solid mass of material is created by compression via heating or pressure mechanisms, without reaching the melting point. In this way, the resulting part has a completely different microstructure and density/porosity when compared to a part that was processed using SLM.

Many researchers have attempted to model the SLS process. Among them, Kolossov (Kolossov et al., 2004) developed a thermal model of SLS utilizing finite element analysis. Their model incorporated the non-linear behavior of thermal conductivity and specific heat, due to the change in temperature and phase. However, they did not take into consideration changes in density and the creation of residual stress in their model. Patil & Yadava (Patil and Yadava, 2007) analyzed the effect of laser processing parameters such as laser power, beam diameter, laser on-time, laser off-time, and hatch spacing in the temperature distribution of a single powder layer under SLS, using a finite element approach. Yin (Yin et al., 2012) developed a simulation of the temperature distribution for Laser Micro-Sintering (LMS) that analyzed the effect of process parameters on temperature distribution and the geometry of the melt pool. An accurate temperature distribution is necessary to predict the dimensions and characteristics of the melt pool.

1.5.3 Electron-Beam Melting (EBM)

Electron beam melting is another type of additive manufacturing technique for metal powders, in which the laser energy source is replaced by an electron beam. In EBM, full melting of the powder material is achieved, making the process more similar in nature to SLM than the SLS process. Gong (Gong et al., 2013) developed an FEM-based transient thermal model for powder-based electron beam additive manufacturing of Ti-6Al-4V. A moving conical volumetric heat source is employed to model beam penetration into the material. Mathematical expressions for the cross-sectional area and the length-to-depth ratio of the melt pool are derived.

1.6 Modeling and Simulation of Laser-based Processing Techniques

One of the key challenges of laser processing is to be able to accurately determine the laser/material interaction that leads to the finished part's properties. This relationship can be explicitly described by means of a physics-based thermal model. A well-developed model can be used to relate the inputs (laser processing parameters, material properties) to the outputs (resulting part geometry, material properties). At the center of such a model is the evolution of the material temperature. This is a heat transfer problem which can be described by using partial differential equations that must be solved to obtain the temperature history. Such equations can be evaluated through numerical means, such as the finite difference method or the finite element method.

1.6.1 Modeling of Laser Ablation of Polymers for Micro-Channel Fabrication

In order to understand the thermally activated ablation mechanism, a prediction of temperature rise in the workpiece must be performed accurately for given laser processing parameters. Experimenting and modeling laser based thermal processing and ablation of materials has been of great interest for researchers (Miotello and Kelly, 1995, Chichkov et al., 1996, Jeong et al., 1998, Gower and Rizvi, 2000, Gusarov and Smurov, 2003) with modeling work done by Park (Park et al., 1996), Ki & Mazumder (Ki and

Mazumder, 2005), Chichkov (Chichkov et al., 1996), Momma (Momma et al., 1997), and Ramanathan and Molian (Ramanathan and Molian, 2002), among others. The temperature distribution can be obtained by solving the heat equation. Based on the assumptions made, the solution to the heat equation can be found analytically or numerically. The model implemented in this study uses a finite-difference method (FDM) approach to calculate temperature rise. The thermal model and subsequent analysis for laser processing of micro-channels can be complemented with a mathematical model to predict the resulting micro-channel geometry profile. This channel profile model can be derived off the model presented by Yuan and Das (Yuan and Das, 2007) and it is based on solving the energy balance equation.

1.6.2 Modeling of Selective Laser Melting of Metals Powder

Recent efforts in predictive modeling for SLM-based additive manufacturing of metal powders have been directed into understanding the relationship between material and process parameters, in particular the effect of heating and quick cooling times in the resulting micro-structure (Yin et al., 2012, Sun et al., 2013, Yadroitsev et al., 2013, Amato et al., 2012, Wang et al., 2012, Jia and Gu, 2014). Therefore, temperature distribution plays a significant role in the resulting properties of the parts manufactured through selective laser melting. Accurately describing the temperature distribution during and after the process is vital to obtaining high-quality samples. The temperature distribution for SLM can be calculated by solving the heat transfer problem using either an analytical solution approach or a numerical solution approach. Furthermore, a numerical solution can be obtained two-fold: with a finite element analysis (FEA) approach, and by means of applying the finite difference method (FDM). Rosenthal

(Rosenthal, 1946) was the first author to address the problem of the physics of a moving heat source and developed an analytical solution. Eagar & Tsai (Eagar and Tsai, 1983) attempted to find an analytical expression for the geometry of the melt pool produced by a traveling, Gaussian-distributed heat source. They were the pioneering authors to introduce a 2-D heat source. Goldak (Goldak et al., 1985) were the first to introduce a 3D heat source, by using a double ellipsoidal moving heat source to calculate the temperature field utilizing finite element modeling. Gusarov (Gusarov et al., 2003) developed a model to calculate the thermal conductivity of a powder bed based on the molecular structure of the powder. Gusarov (Gusarov et al., 2007) continued his investigations into SLM by developing an FE model to analyze the effect of scanning velocity in the SLM process, concluding that an interval of scanning velocities exists in which the re-melted tracks due to scanning are uniform. Van Elsen (Van Elsen et al., 2007) provided both analytical and FDM numerical solutions to the heat conduction equation for a localized moving heat source. Roberts (Roberts et al., 2009) developed a 3-D finite element model for predicting the transient temperature field for multiple layers of parts, using a death and rebirth technique. Aggarangsi (Aggarangsi et al., 2003) studied the melt pool size for laser-based deposition near a free edge utilizing an FEM approach. Aggarangsi used Rosenthal’s solution, described in the previous section, to validate their results. Pinkerton & Li (Pinkerton and Li, 2004) modeled the geometry of a moving laser melt pool utilizing energy and mass balance equations along with a one-dimensional heat conduction approach, thereby ignoring convective and radiation losses from the melt pool. However, all thermo-physical properties are assumed to be temperature independent. A different approach was employed by Tang and Landers (Tang and

Landers, 2010), who developed an empirical process model to calculate melt pool geometry. Jahn (Jahn et al., 2012) developed an FEM model based on heat conduction, a free melt surface, a moving phase boundary, and the implementation of the Navier-Stokes equations to obtain melt pool geometry in solid-liquid-solid phase transition problems. Vásquez (Vásquez et al., 2012) developed a 3D quasi-stationary finite element model to analyze multi-physics laser-material interaction. Conservation of energy, conservation of mass, and conservation of momentum are considered. This model also takes into account vapor trapped by plasma, which is re-solidified at high laser power levels. Zeng (Zeng et al., 2013) addressed some of the limitations of implementing a numerical methods approach in laser additive manufacturing models, such as mesh size by developing a dynamic mesh method. An enthalpy approach was used to account for the effect of latent heat of fusion and latent heat of vaporization in the change of phase. As pertains to the microstructural analysis of SLM produced parts, Thijs (Thijs et al., 2010) studied the effects of SLM process parameters on the microstructure of Ti-6Al-4V. α, α' (acicular martensite) and β phases were observed along with the intermetallic Ti3Al that appeared as dark bands around melt pools. Song (Song et al., 2012) performed a study on SLM process parameter selection using temperature distributions obtained from FEA with solid elements, as well as experiments. Simonelli (Simonelli et al., 2012) reported that the β phase was not observed in SLM processing of Ti-6Al-4V due to fast cooling rates. Sun (Sun et al., 2013) provided a good approach for selecting SLM process parameters for Ti-6Al-4V in order to maximize relative density based on Taguchi methods and ANOVA results. Dai (Dai and Gu, 2014) investigated the densification process and temperature distribution of WC/Cu composite powder during SLM process using a Finite Volume

Method (FVM). Yadroitsev (Yadroitsev et al., 2013) investigated the effects of SLM process on the microstructure of Ti-6Al-4V by taking direct measurements of the surface temperature distribution using a CCD camera. The size of the molten pool was also measured. α' and β phases are observed. SLM processed parts were then heat treated to observe the changes in their microstructures and a detailed analysis was provided. The α' phase was found to be not as hard as in ferrous alloys due to high dislocation density and fine lamellar structure. Amato (Amato et al., 2012) and Wang (Wang et al., 2012) fabricated Inconel 718 alloy parts using SLM process, analyzing the microstructure and mechanical behavior. Jia and Gu (Jia and Gu, 2014) also analyzed the densification, microstructure and properties of SLM-manufactured IN 718 parts, establishing a relationship between process parameters and microstructural and mechanical properties.

1.7 Process Parameter Optimization for SLM of Metal Powders

The relationship between explanatory variables, e.g. laser parameters and material properties, and response variables, e.g. part density/porosity and melt pool geometry, can be established using response surface methodology (RSM). By utilizing properly designed physical and simulation experiments applying Design of Experiments methodology, an optimal response is determined via a second-degree polynomial model. Key objectives, such as relative density compared to the bulk material, processing rate, and energy consumption are identified and can be optimized via multi-objective optimization algorithms such as Multi-Objective Genetic Algorithms (MOGA) and Multi-Objective Particle Swarm Optimization (MOPSO).

1.8 Motivation

Laser-based processing of materials is a rapidly growing area of research. Although many efforts have been directed at analyzing the effect of process parameters and material properties in the resulting part geometry and microstructure, no conclusive efforts have been presented. The common method for optimization of process parameters is through trial and error via experimentation, which can be very time-consuming, costly, and inefficient. Predictive modeling and simulation techniques can often be used as an alternative to experiments when the effect of input parameters on resulting part quality needs to be analyzed. An experimentally validated model can be utilized for process parameter optimization purposes.

In this dissertation, two types of laser processing techniques were studied: laser ablation of PDMS for micro-channel fabrication and selective laser melting of metal powders, specifically IN 625. Traditional experimentation was executed to validate and corroborate the results obtained through physics-based simulations. Then, through a dual theoretical-experimental approach, the relationship between process parameters and resulting part quality will be established via effects modeling. The final result will be a predictive model which can be utilized to determine the optimal conditions for laser-based processing of materials.

1.9 Objectives

The following are the objectives of this research:

Objective 1: To investigate the feasibility of micro-machining PDMS polymer using nanosecond laser pulses at an UV wavelength of 355 nm and determine the quality of the micro-channels fabricated using nanosecond pulsed laser as the energy source.

Objective 2: To establish a relationship between process inputs (fluence or laser power, pulse overlap or scanning velocity) and outputs (channel width, channel depth) for PDMS micro-channel fabrication with a nanosecond pulsed laser.

Objective 3: To develop a FE physics-based thermal model for selective laser melting of metal powders. The model can be used to obtain temperature profiles throughout the process which would be critical for determining the resulting melt pool geometry.

Objective 4: To establish the relationships between inputs (laser power, scanning velocity, and hatch distance) and outputs (part density, melt pool geometry) for SLM of IN 625 powder from experimental results.

Objective 5: To experimentally validate and calibrate the FE model for SLM of IN 625 using temperature data acquired during fabrication of test coupons.

Objective 6: To optimize process parameters in SLM of IN 625 for maximum relative density, maximum processing rate, and minimum energy consumption.

1.10 Organization of the Dissertation

This dissertation is divided into 8 chapters, organized as follows:

In Chapter 2, the results of a feasibility study for laser-based micro-channel fabrication of PDMS via experimentation are presented. In particular, the effectiveness of utilizing a nanosecond-pulsed laser as the energy source for laser ablation is studied. The results are analyzed statistically using ANOVA and a relationship between process parameters and micro-channel dimensions is established. Additionally, a simple 1D Finite Difference Method model is introduced as a tool for predicting channel depth. Model outputs are compared and analyzed to experimental results.

In Chapter 3, a physics-based finite element (FE) model for Selective Laser Melting of metal powders is presented. The results are limited to single-track modeling, processed in a single layer of material. The model is developed by solving the heat convection-diffusion equation using a finite element formulation. A comparison between the results obtained with this model and published work available in the literature is presented. Initially, three metal powders are considered: Ti-6Al-4V, 316L Stainless Steel, and Inconel 625. A sensitivity analysis study is also presented, detailing the effect of varying process parameters in melt pool geometry, peak temperature, and time above melting temperature. This sensitivity analysis is important because there are instances where process parameters cannot be fully defined or measured, e.g. laser spot size.

In Chapter 4, the SLM model is expanded to multi-hatch simulations. Results are presented for processing of Inconel 625 powder under a set of process parameters suggested by the National Institute of Standards & Technology (NIST) in conjunction with the manufacturers of the SLM machine. An experimental design based on the Box-Behnken design of experiments approach is presented for manufacturing of IN 625 test coupons.

In Chapter 5, analysis of experimental data from SLM-built test coupons with Inconel 625 powder is presented. Parts were fabricated at the facilities of the National Institute of Standards & Technology (NIST) following the experimental design outlined in the previous chapter. The density of the test coupons was measured experimentally and compared to that of solid IN 625. Results of this analysis are used to establish the relationship between process parameters and resulting part density, by means of response surface methodology (RSM) techniques. Electro-polished surfaces of the fabricated parts were analyzed using Optical Microscopy to determine melt pool geometry.

In Chapter 6, validation of the physics-based finite element model is conducted. Temperature predictions are validated using melt pool measurements obtained in the previous chapter, as well as thermal data captured during the fabrication of the test coupons. Temperature data captured during the experiments is not sufficient to do a complete validation of the temperature field, due to limitations on the temperature range that can be captured by the thermal camera and difficulties estimating the emissivity of the powder material. However, confidence intervals for measured temperatures are defined and compared to simulation results. With the validated model, a set of simulation experiments is utilized to determine peak temperature and time above melting temperature for multiple combinations of process parameters.

In Chapter 7, multi-objective optimization of process parameters for SLM of Inconel 625 is presented. Two optimization problem sets are considered. In the first set, key objectives are maximization of relative density of additively fabricated test coupons, maximization of processing rate of powder material and minimization of energy consumption per unit volume of powder. The second optimization set considers maximization of relative density of additively fabricated test coupons, minimization of peak temperature during the process, and minimization of time above the melting temperature for specific locations of the powder bed.

In Chapter 8, main contributions and conclusions of this research are presented and future research considerations are outlined.

Chapter 2 NANOSECOND-PULSED LASER-BASED MICRO-CHANNEL FABRICATION OF PDMS AT 355 NM UV WAVELENGTH

2.1 Introduction

Pulsed laser processing has many applications in micro-manufacturing such as fabricating stents and micro-fluidics devices for medical applications, components for microelectromechanical systems (MEMS) and optical elements in photonics applications. Some of the advantages of laser processing include its high precision and its ability to focus high energies on a small area. By virtue of being a contact-free process, it avoids the possibility of contamination due to tool contact-based wear, coolant, or lubricant fluids. This is particularly important when manufacturing components for medical devices that require rigorous process accreditation. Pulsed laser systems have the capability to process many different materials, depending on the laser light characteristics such as wavelength, pulse length and fluence. Many applications for laser processing of polymers have been demonstrated in literature. For these applications, different types of laser systems have been used. Calixto & Padilla (Calixto and Padilla, 1996) used a He-Ne laser at 633 nm wavelength and a CO_2 laser at 1060 nm wavelength on polymer films to fabricate diffractive optical elements, whereas Hong et al. (Hong et al., 2010) and Yuan & Das (Yuan and Das, 2007) used a CO_2 laser for microfluidic channels in polymethylmethacrylate (PMMA). Pugmire et al. (Pugmire et al., 2002)and Waddell et al. (Waddell et al., 2002) used a nanosecond pulsed KrF excimer laser at UV wavelength of 248 nm for machining micro-channels in different polymers such as polyethyleneterephthalate-glycol (PETG), polycarbonate (PC), polyvinylchloride (PVC), and PMMA. Chen et al. (Chen et al., 2003) used a Xe-Cl excimer laser at 308 nm wavelength and a frequency quadrupled Nd:YAG laser at UV wavelength of 266 nm for micromachining of polymer D-lactic acid (PDLA) and polyvinyl alcohol (PVA) biodegradable polymers. Picosecond and femtosecond pulsed lasers have been used for the processing (e.g. micro-machining) of transparent polymers providing very high peak intensities, due to ultra-short pulse duration and high peak intensities with little or no thermal damage to the workpiece. Although nanosecond laser interaction with transparent polymers produces mainly photo-thermal ablation and may cause some peripheral thermal damage and associated debris or crazing, this type of lasers remain much more affordable, reliable and commonly available for micro-manufacturing in industry. Nd:YAG lasers are widely used at the fundamental near infrared (NIR) wavelength (1064 nm) and have the potential to process transparent polymers more adequately when using the harmonics of the fundamental wavelength to generate laser irradiation at the UV wavelengths (e.g. 355 nm and 266 nm wavelengths as third and fourth harmonics of the 1064 nm wavelength). Therefore, it is important to investigate different effects of nanosecond laser processing transparent polymers at the UV wavelengths (e.g. 355 nm or 266 nm). The previous work done by the other researchers including the work by Teixidor et al. (Teixidor et al., 2013) explored mainly laser micromachining of PDMS at NIR wavelength of 1064 nm. However, the UV wavelength light obtained in nanosecond pulsed laser provides additional opportunities to promote photo-chemical ablation and reduces the thermal damage caused by photo-thermal ablation. This is the main premise of further investigating the physical laser irradiation of transparent PDMS polymers with proposed process models in nanosecond pulsed laser micromachining at the UV wavelength (< 400 nm).

Among the different applications that can take advantage of pulsed laser processing, the fabrication of micro-fluidic devices is of particular interest. Micro-fluidics is defined as the use of analytical systems that are able to manipulate, process, and control small quantities of fluids. These devices use components such as microchannels, electrodes, columns, and reactors that handle volumes in the order of nanoliters and picoliters. Its applications include: lab-on-a-chip devices, DNA analysis, drug delivery devices, nerve regeneration, microfluidic chip devices, and many others. The basic components of many microfluidic systems are the micro-channels in which fluid flows. In these channels, separation or mixing of liquids takes place within the micro-fluidics system. Therefore, achieving lower cost in directly fabricating micro-channels for micro-fluidics may provide a wider utilization of this technology. Hence, this work aims to study the feasibility and viability of nanosecond pulsed laser processing in the fabrication of robust quality micro-channels, as well as the effect of UV laser irradiation parameters on the width and depth of micro-channels fabricated with PDMS.

2.2 Techniques for PDMS Micro-channel Fabrication

Manufacturing of micro-channels in PDMS has been an important focus of micro-fluidics research. PDMS offers significant advantages over other materials, such as optical transparency, bio and chemical compatibility, low cost, superior bonding, and low water permeability. Single-level PDMS micro-channels, also referred to as two-dimensional micro-channels, can be manufactured using a variety of methods and techniques, among which molding/casting, photolithography, and soft lithography have been widely studied. These single-level channels (30-100 μm in depth) can then be stacked together to create complex three-dimensional micro-channel structures, via physical clamping or spin coating. Three-dimensional micro-channel structures are preferred because they can contain suspended cantilevers and buried or blind channels. More recent techniques aimed at generating complex multi-level microchannels without using a layer-by-layer approach have been developed as well (Yun and Yoon, 2008, Wu et al., 2002, Hofmann et al., 2001, Jo et al., 2000).

As mentioned previously, there are several ways in which to produce PDMS micro-channels for micro-fluidics applications. Most advanced manufacturing techniques follow the general principles of molding: micro-channels are generating by creating a structured pattern master with the desired shape, pouring PDMS onto the master, and utilizing thermal curing to obtain the desired part. Advanced manufacturing techniques, such as photolithography and soft lithography differ on how the structured master pattern is created and how or what kind of thermal curing is applied.

2.2.1 Photolithography

In photolithography, a photomask is placed on a photoresist and exposed to UV light to create a mold. The photomask consists of an opaque plate with transparencies that allow light to pass through in a specified pattern onto the photoresist. The photoresist is then processed with a solvent that etches specific areas of the photoresist, based on its qualities. The photoresist is a light-sensitive material that can be either positive or negative. A positive resist is a photoresist in which the section that is exposed to light by the photomask becomes soluble. Therefore, the portion of the photoresist that was exposed will be removed by the solvent via etching. On the other hand, a negative resist is a photoresist in which the section that is exposed to light by the photomask becomes insoluble and the unexposed section is etched instead. In both scenarios, the final product is referred to as the master pattern, where the desired micro-channel structure and geometry appear as reliefs. For PDMS micro-channel fabrication, an epoxy-based photoresist (SU 8) on a silicon wafer is commonly utilized. Liquid PDMS is pressed against the mold via pouring or spin-coating, and cured in an oven. This process, called replica molding, generates a negative replica of the master pattern. The PDMS mold is peeled from the master pattern and is ready for use.

The main disadvantages of photolithography for the creation of micro-channels consist of i) the need for a flat substrate for the generation of the mold, ii) the lack of effectiveness at creating non-flat surfaces, iii) the need for extremely clean conditions, and iv) the lack of geometrical flexibility of the process: the produced mold can only be used to generate one specific micro-channel pattern. The disadvantage is that the micro-channel geometry is 2.5D, corresponding to the protruded 3D geometry of the 2D pattern of the mask. The process is not capable of producing micro-channels with a varying 3D geometry.

2.2.2 Soft Lithography

Soft lithography is a suite of non-photolithographic methods for replicating a pattern, and differs from photolithography in that it uses soft, elastomeric elements in pattern formation (Xia and Whitesides, 1998). In general, the process can be separated into two components. The first part of the soft lithography process deals with the production of the elastomeric elements, while the second part consists of the use of these elements to create specific geometries (patterns), which are defined by the elastomeric element’s relief structure (Rogers and Nuzzo, 2005). In soft lithography, an elastomer like PDMS can be used to create the master. Soft lithography techniques can be divided into three major categories based on how the specific geometries are created using the mold: i) printing techniques, ii) replica molding techniques, and iii) embossing (Gates et al., 2004).

Printing techniques are named as such because they involve material transfer from the mold onto the substrate. Specific soft lithography printing techniques include micro-contact printing (μCP) and nano-transfer printing (nTP). Replica molding techniques have been described in the photolithography section earlier and can be further divided into three subfields: micro-transfer molding, micro-molding in capillaries and UV-molding. In most cases, excess material is removed via an etching process (He et al., 2010), (Vlachopoulou et al., 2013). Finally, embossing consists of creating a pattern on a flat surface by applying a mold to said surface using pressure (Russo et al., 2002), (Goral et al., 2010).

One of the main advantages of using PDMS, or a similar material, has to do primarily with scale; feature dimension is reduced from the micrometer scale in photolithography to the nanometer scale in soft lithography. Additionally, soft lithography techniques do not require access to a clean room.

2.3 Experimental Design and Set-up for Laser Micro-Machining

2.3.1 Experimental Set-up

The experimental set up used in this work comprises of a vibration-free board, a Nd:YAG pulsed laser system with a third harmonic generating unit providing a UV wavelength of 355 nm, and an optical beam delivery system that includes a beam expander, a mirror, and a focal objective lens, and a positioning stage to manipulate the PDMS workpiece together with a computer numerical controlled (CNC) table along the three Cartesian coordinates of X, Y, and Z. This experimental set up available at the Manufacturing & Automation Research Laboratory at Rutgers University is presented in Figure 2.1.

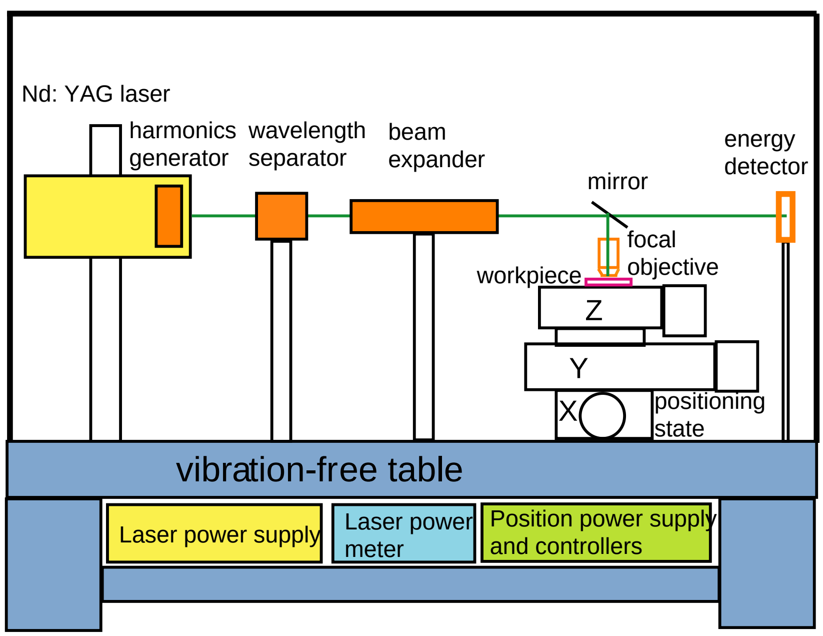

Figure 2.1. The experimental set-up for the laser micromachining of micro-fluidic channels.

The laser source used is a nanosecond Q-switched high energy solid-state Nd:YAG laser (Continuum Surelite I-10) with a fundamental wavelength λ=1064 nm, average power P=4.85W at a pulse frequency f=10 Hz, pulse duration τ=5 ns and an unfocused laser beam diameter of $\approx$ 6mm. Harmonic generating units were used to obtain first a 532 nm wavelength (second harmonic) and then a UV wavelength of 355 nm (third harmonic). A high magnification focal objective (15×) used for this experiment provides a spot size diameter (*d*) of 0.075 mm at this UV wavelength. From the previous experimental work by Teixidor (Teixidor et al., 2013), in which the laser power was measured with changing Q-switch delay time, it was found that a Q-switch delay of 180 μs provides the highest and most stable laser average power for this system. Thus, this particular delay time was used for the experiment. The system has a central computer control, which determines the movement of the X, Y, and Z stages for translation of the workpiece under the focused laser spot. The pulse energy at the exit port was measured by using an EPM1000 Joule meter (Coherent Molectron Detector, Inc.) with a Coherent EnergyMax sensor J-50MB-YAG.

2.3.2 Definition of fluence and pulse overlapping: factor selection

Two main process parameters were investigated: fluence and pulse overlapping (PO) factor. The fluence is denoted with Φ [J/cm^2] is calculated using the expression given by **Equation 2.1**:

$$\Phi = \frac{E}{A} = \frac{4E}{\pi d^2} \tag{2.1}$$

where E is pulse energy [mJ] and A is spot area [cm^2]. The fluence is affected by the flash lamp drive voltage [kV], Q-switch delay time [μs], spot size diameter [μm], and the Z-level of the focusing objective [μm] which provides depth of focus. In these experiments the spot size diameter, d=75 μm, is held constant throughout. Therefore, the fluence was determined solely as a function of the pulse energy, which was adjusted by setting the drive voltage of the laser to the desired quantity. The concept of pulse overlapping factor, denoted with O_f [%], is defined as the percentage amount of overlap between the diameters of two consecutive pulses, as illustrated in Figure 2.2.

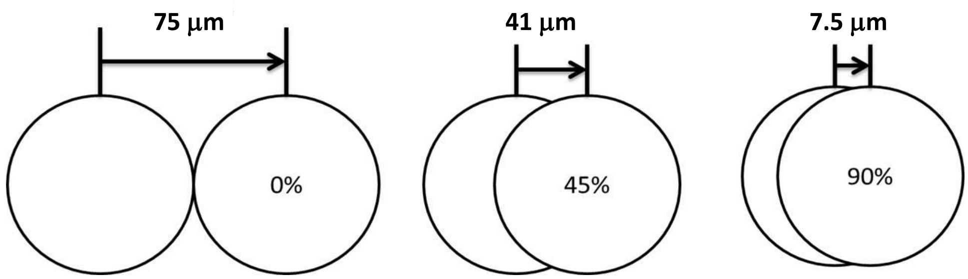

Figure 2.2. Schematic illustration of the concept of overlapping with a 75 µm spot size.

Pulse overlapping factor (O_f) is a function of the scanning rate (S_r), defined as number of pulse per unit length, and the spot size diameter (d). It is calculated as given in Equation 2.2:

$$O_f = 100 * \left(1 - \frac{1}{d * S_r}\right) \tag{2.2}$$

The scanning rate is related to the scanning speed or velocity (v_s) and the pulse frequency (f) by:

$$S_r = \frac{f}{v_s} \tag{2.3}$$

Therefore, the pulse overlapping can be written as:

$$O_f = 100 * \left(1 - \frac{v_s}{d * f}\right) \tag{2.4}$$

As mentioned previously, a constant spot size diameter (d=75 µm) is used. By keeping the pulse frequency constant at f=10 Hz, the overlapping is varied by modifying only the laser scanning speed or velocity (or scanning rate).

2.3.3 Selection of factor levels for PDMS microchannel fabrication

Most of the process variables affect the fluence and/or the pulse overlapping as outlined in the previous section. For this reason, the work in this section focuses on the effects of these two process parameters on the micro-channel quality and process viability. From a previous work done by Teixidor et al. (Teixidor et al., 2013) the best results with micro-channel geometry and finish were found by locating the beam focal point 50 μm above the surface. Therefore, this particular value for focal point location (z-level) was used in the experimental procedure. Simultaneously, a screening experiment was performed in order to approximate an appropriate range of factors for fluence and pulse overlapping. By keeping the spot size diameter constant, fluence is uniquely determined by the laser pulse energy, which in turn is controlled by modifying the laser drive voltage. Screening experiments were conducted to identify high, medium, and low values for the drive voltage that would result in corresponding high, medium, and low pulse energy (and therefore, fluence) values. These settings will be used for PDMS laser micro-machining experiments, as seen in **Table 2.1**.

Table 2.1. Measured pulse energy based on the drive voltage (for PDMS).

Drive Voltage, V_d [kV]	**Pulse Energy, E [mJ]**
1.00	35
1.05	51
1.10	73

A similar screening procedure was conducted to determine acceptable ranges for pulse overlapping by applying the medium energy setting. For little pulse overlapping (O_f<85%), consecutive pulses are not close enough to each other, which cause the channels to have a very rough edge. As the pulse overlapping increases, the channels depict a smoother edge, obtaining the most acceptable result with O_f =95% pulse overlapping. For values higher than this threshold, e.g. 98%, excessive burning of the material occurs. Therefore, three different values for scanning rate were selected which correspond to pulse overlapping values between O_f =85 and 95%. A low, medium, and high scanning rate corresponding to O_f =85, 90, and 95% pulse overlapping were chosen for PDMS. In conclusion, only the drive voltage and the scanning rate are modified between experiments, while the remaining process parameters were fixed i.e. spot size diameter d=75 μm, a pulse frequency of f=10 Hz, a Q-switch delay time of τ=180 μs, and UV wavelength of λ=355 nm. A full-factorial experimental design consisting of 2 factors and 3 levels for micro-machining of micro-channels was constructed. An array of $3^2 = 9$ channels was machined by using the process parameter values given in Table 2.2 for PDMS.

Table 2.2. Process parameters for laser micro-machining of PDMS (Criales et al., 2015b)

Channel	**Fluence, Φ [J/cm^2]**	**Pulse Overlapping, O_f [%]**	**Laser Power**	**Scanning Speed**
1	792	85	Low	High
2	1154	85	Mid	High
3	1652	85	High	High
4	792	90	Low	Mid
5	1154	90	Mid	Mid
6	1652	90	High	Mid
7	792	95	Low	Low
8	1154	95	Mid	Low
9	1652	95	High	Low

After the micro-machining experiments, the depth and width of all of the micro-channels were measured using a Gamma Scientific Inc. 700-10 measuring microscope with a 40x magnification and a numerical aperture of 0.30. The channel cross-sectional images were taken with a Celestron LCD/Digital camera, mounted on the microscope. Image processing software (Image Pro Insight 8.0) was used to obtain the channel profile. The device was calibrated using a reference scale with 1 μm marks. In order to access and measure the cross-section of the micro-channels, the samples were sliced using a sharp razor blade for PDMS. The cross-sectional cuts were made 1.5 mm from the edge of the channel, and every 3 mm between cuts for a total of 5 cuts. Then, a cross-sectional image was taken and processed to determine the width and depth measurements at different locations for each channel.

2.4 Experimental Results

Several micro-channels were fabricated with laser micro-machining process by following the experimental plan discussed in the previous section. Different width measurements were taken. Five measurements were taken along the channel length in order to obtain a mean value of microchannel width; one at 1.5 mm from the edge of the channel, then every 3 mm, with the last one at 1.5 mm from the end of the channel. The depth of each micro-channel (ablation depth) was also measured by taking a measurement at these same locations. These results are summarized in Table 2.3.

Table 2.3. Results of measurements in fabricated micro-channels

Fluence, Φ [J/cm^2]	**Scanning Rate, S_r [pulses/mm]**	**Overlapping, O_f [%]**	**W_{avg} [μm]**	**D_{avg} [μm]**	***St. Dev. Width* [μm]**	***St. Dev. Depth* [μm]**
792	89	85	85	9	1.4	4.6
1154	89	85	126	20	1.4	2.5
1652	89	85	137	30	2.3	4.0
792	133	90	93	26	1.4	2.8
1154	133	90	119	33	2.8	3.3
1652	133	90	120	44	2.1	4.5
792	267	95	102	33	1.1	3.1
1154	267	95	106	47	3.4	2.9
1652	267	95	96	59	3.3	2.1

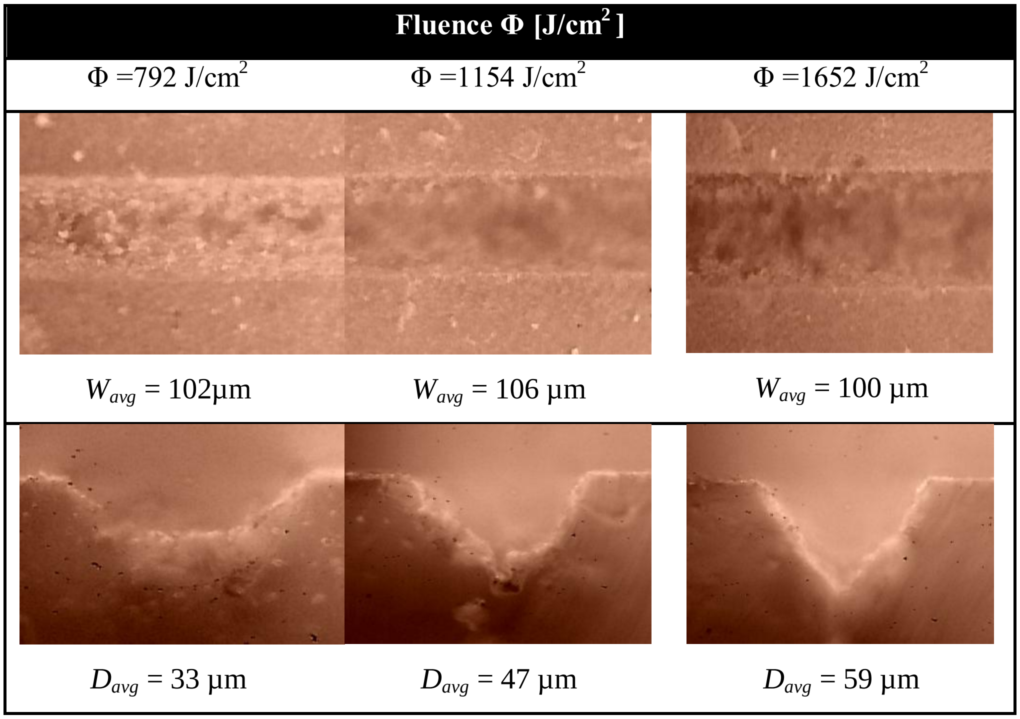

Figure 2.3. Microchannel views for PDMS experiments (O_f= 95%) (Criales et al., 2015b)

Figure 2.3 shows some of the PDMS micro-channels obtained by laser micro-machining at 355 nm. The effects of the drive voltage adjusted fluence and the scanning rate on the micro-channel width and depth are presented in Figure 2.4.

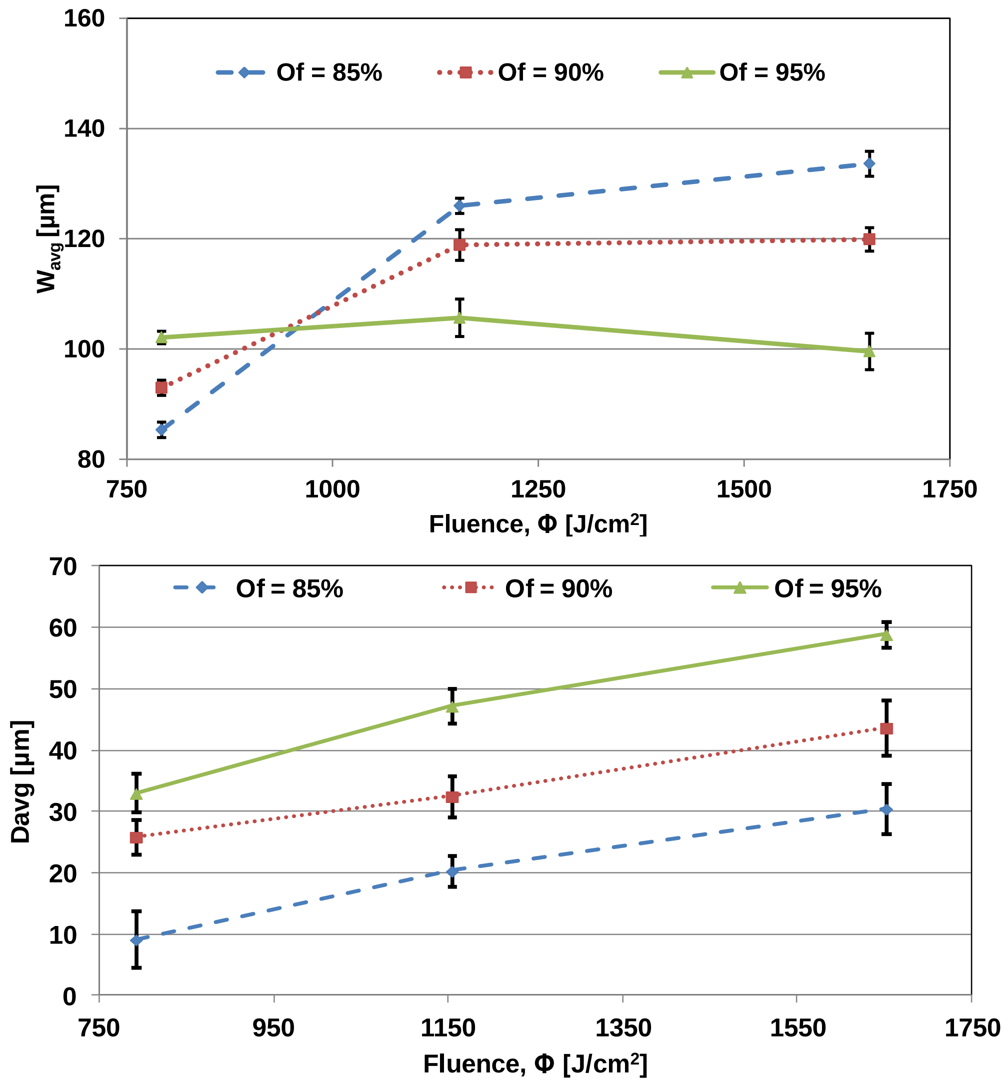

Figure 2.4. Effect of process parameters on micro-channel width and depth. (Criales et al., 2015b)

Increasing fluence tends to result in increased micro-channel width and depth. Only for the case in which the highest scanning rate is utilized is non-increasing width observed, and for this case the channel width remains constant. Increasing scanning rate increases micro-channel width for the lowest fluence value (792 J/cm^2), while it decreases micro-channel width for larger fluence values (1154 and 1652 J/cm^2). Both parameters have an effect on the quality of the micro-channel and on the material removal rate (MRR), as seen in **Figure 2.5**. Both parameters have an effect on the quality of the micro-channel.

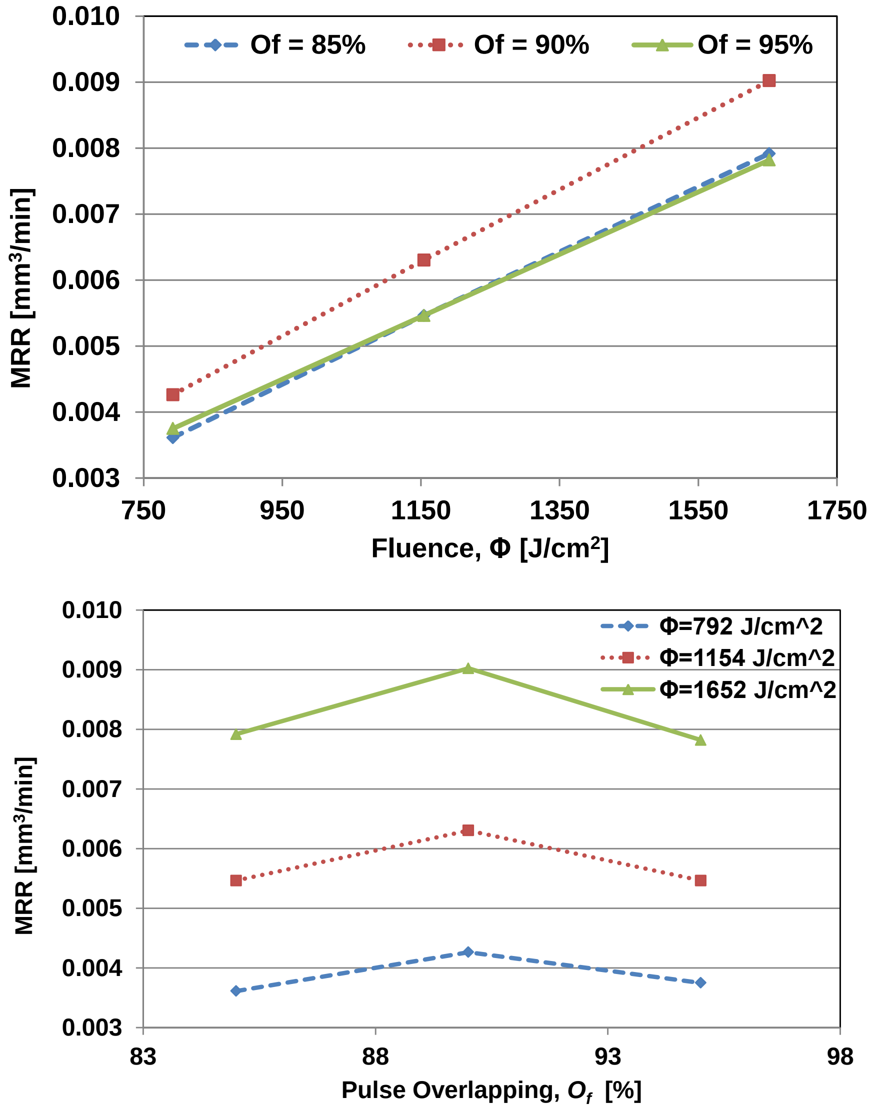

Figure 2.5. Effect of fluence and pulse overlapping on material removal rate. (Criales et al., 2015b)

2.5 Analysis of Variance

The ANOVA analysis was performed using Matlab. The *anovan* function was used for multiway (n-way) analysis of variance (ANOVA), which tests the effects of multiple factors on the mean of the depth and width dimensions measured for micro-machining PDMS micro-channels. It should be noted that scanning rate (S_r) and overlapping factor (O_f) are related to each other and not fully independent factors; therefore scanning rate was excluded from ANOVA. The p-values for null hypotheses on the two main effects (fluence and overlapping factor) and their two-factor interaction were computed. Tables 2.4 and 2.5 give the ANOVA table for means of depth and width measurements of PDMS micro-channels, respectively. The tables also give the number of degrees of freedom corresponding to each type of variation. It can be seen that the fluence has the strongest effect on controlling the width dimensions of micro-channels (see F values), whereas overlapping has the strongest effect on controlling the depth dimensions of the micro-channels in both PMMA and PDMS. The two-factor interactions of overlapping factor (O_f) and fluence (Φ) also affect the micro-machining process, as shown by the significantly small *p*-values.

Table 2.4. The ANOVA table for depth measurements of PDMS micro-channels

Source	*SS*	*DF*	*MS*	*F*	*p-value*
O_f	1156.3	2	578.16	113.86	2.71e-16
Φ	5641.2	2	2820.62	555.48	8.74e-28
$O_f * \Phi$	3522.9	4	880.72	173.45	5.42e-23
Error	182.8	36	5.08		
Total	10503.2	44			

Table 2.5. The ANOVA table for width measurements of PDMS micro-channels

Source	*SS*	*DF*	*MS*	*F*	*p-value*
O_f	5178.98	2	2589.49	215.39	0
Φ	3542.71	2	1771.36	147.34	0
$O_f * \Phi$	107.82	4	26.96	2.24	0.0837
Error	432.8	36	12.02		
Total	9262.31	44			

Next, a mathematical model for calculating the channel depth profile using the physics of the laser ablation process will be discussed.

2.6 Channel Profile Model

In laser irradiation of PDMS polymer, there are two active mechanisms which may lead to ablation; photochemical and photothermal mechanisms. In a photochemical mechanism, chemical bonds in a polymer are broken by the photon energy of the laser irradiation. Due to relatively high energy of the polymer bonds in PDMS, polymer bond energy cannot be chemically broken using a laser irradiation of λ=355 nm wavelength that corresponds to about 1.16 eV photon energy. Therefore, the active mechanism in laser ablation at λ=355 nm wavelength is photothermal ablation. For this reason, a mathematical modeling of channel depth profile was also developed. A mathematical modeling approach similar to the one utilized by Yuan and Das (Yuan and Das, 2007) was pursued, as described below.

For each element, the energy balance equation can be described as follows: the laser input energy is equal to the sum of the energy that conducts into the surface element and the energy that goes into decomposition:

$$E_{laser}dxdz = E_{conduction}dA + E_{decomposition}dxdz \tag{2.5}$$

The laser energy density is given by:

$$E_{laser} = \frac{\alpha P}{\sqrt{\pi} r v_s} e^{-x^2/R^2} \tag{2.6}$$

Where a is the absorptance of PDMS at the Nd:YAG laser third harmonic wavelength of λ=355 nm, P is the average laser power, r is the laser beam radius at the focal waist, and v_s is the laser scanning speed. The absorptance is given for λ=355 nm Nd:YAG laser as α=4.8x10^{-4} for PDMS.

The decomposition energy is given by:

$$E_{decomposition}dxdz = \rho L D(x)\, dx\, dz \tag{2.7}$$

where ρ is the density of PDMS, L is the latent heat of decomposition from PDMS to DMs, and $D(x)$ is the depth of the channel at location x. The energy conducted into the surface is given by:

$$E_{conduction}dA = \left[\int_{-\infty}^{\infty} \rho c_p (T_v - T_0) \tan\theta dz\right] dxdz = \rho c_p (T_v - T_0) D(x) dxdz \tag{2.8}$$

where c_p is the specific heat, T_0 is the room temperature and T_v is the decomposition temperature. From Equations 2.6-2.8, Equation 2.5 becomes:

$$\frac{\alpha P}{\sqrt{\pi} R v_s} e^{-x^2/r^2} dxdy = \rho L D(x) dxdz + \rho c_p (T_v - T_0) D(x) dxdz \tag{2.9}$$

Therefore, the channel depth $D(x)$ can be expressed as:

$$D(x) = D(0) e^{-x^2/r^2} \tag{2.10}$$

where $D(0)$ is the depth in the middle of the channel (when x=0) and can be solved as

$$D(0) = \frac{\alpha P}{\sqrt{\pi} r v_s \rho [L + c_p (T_v - T_0)]} \tag{2.11}$$

Table 2.6. Properties for micro-channel modeling (Criales et al., 2015b)

PDMS Modeling Parameter	Value
Density, ρ [kg/m^3]	967
Latent heat of fusion, L [J/kg]	350000
Decomposition temperature, T_v [K]	2400
Focal beam waist size, R [μm]	37.5
Specific heat, c_p [J/kgK]	1461
Absorptance, α [1/cm]	4.8 x 10^{-4}

The material properties and process parameters used in the channel profile model are summarized in Table 2.6. The depth profile model was computed in Matlab. Figures 2.6-2.8 show the experimental channel profiles, irradiated at 355 nm, and the superimposed modeling results for different combinations of fluence and overlapping. Comparison of predicted and actual depth profile is also found acceptable indicating the validity of this process model.

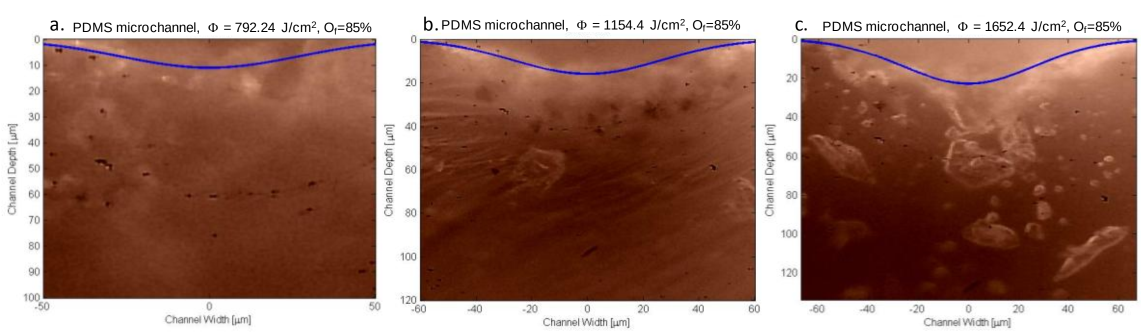

Figure 2.6. Comparison of experimental and predicted micro-channel profiles (λ=355 nm UV wavelength) with 85% pulse overlapping (SR = 89 pulses/mm): a) Φ = 792.24 J/cm^2, b) Φ = 1154.40 J/cm^2, c) Φ = 1652.38 J/cm^2. (Criales et al., 2015b)

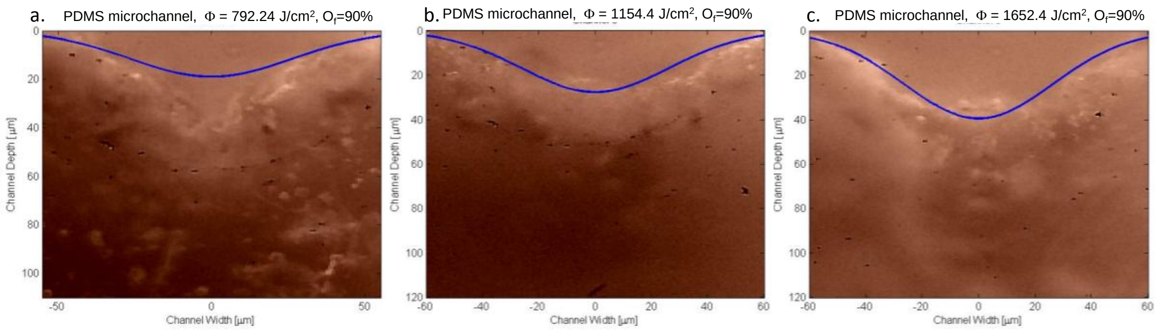

Figure 2.7. Comparison of experimental and predicted micro-channel profiles (λ=355 nm UV wavelength) with 90% pulse overlapping (SR = 133 pulses/mm): a) Φ = 792.24 J/cm^2, b) Φ = 1154.40 J/cm^2, c) Φ = 1652.38 J/cm^2. (Criales et al., 2015b)

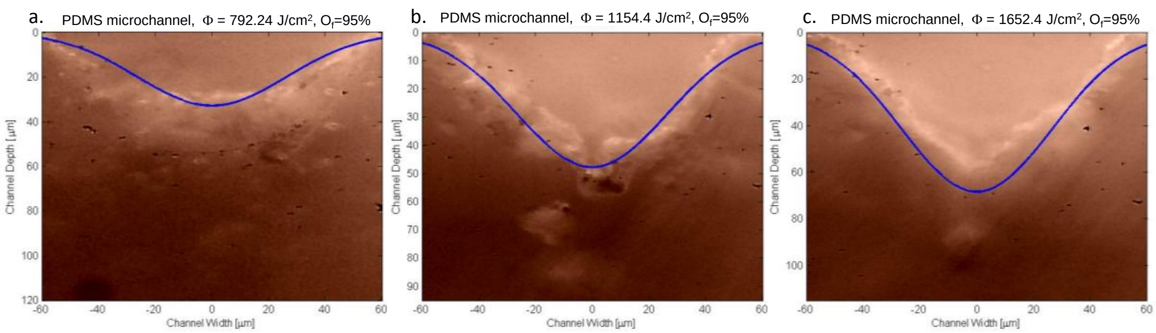

Figure 2.8. Comparison of experimental and predicted micro-channel profiles (λ=355 nm UV wavelength) with 95% pulse overlapping (SR = 267 pulses/mm): a) Φ = 792.24 J/cm^2, b) Φ = 1154.40 J/cm^2, c) Φ = 1652.38 J/cm^2. (Criales et al., 2015b)

2.7 Thermal Modeling

To obtain a temperature profile in the depth direction, a thermal model was developed based on a solution to the heat equation. Without loss of generality, it was assumed that x is the direction corresponding to the constant speed of a moving source, y is the direction perpendicular to x on the polymer surface, and z is the depth into the polymer. The general convection-diffusion equation is given by:

$$\frac{\partial \rho u}{\partial t} + \frac{\partial \rho h V}{\partial x} = k\left(\frac{\partial^2 T}{\partial x^2} + \frac{\partial^2 T}{\partial y^2} + \frac{\partial^2 T}{\partial z^2}\right) + q \tag{2.12}$$

where u is the internal energy [J], h is the enthalpy [J], ρ is the density [g/cm^3], k is the thermal conductivity [W/cm K], q is the heat source [W/cm^3], T is the material temperature [K], and V is the velocity of the material in fluid phase [cm/s].

Since the PDMS is ablated, it was expected that little to no material to be present in fluid phase so that the convection term drops out resulting in the well-known heat conduction equation. Material properties are a function of temperature, which yields:

$$\rho(T)C(T)\frac{\partial T}{\partial t} = k(T)\left(\frac{\partial^2 T}{\partial x^2} + \frac{\partial^2 T}{\partial y^2} + \frac{\partial^2 T}{\partial z^2}\right) + q \qquad (2.13)$$

Since the objective is to determine the depth at which ablation occurs, only the temperature profile in the z-direction (depth) is considered. Heat conduction in the x- and y-directions is not considered due to the limitations that arise from attempting to solve 2D and 3D equations numerically. Therefore, it is assumed that conduction occurs principally in the z-direction:

$$\rho(T)C(T)\frac{\partial T}{\partial t} = k(T)\frac{\partial^2 T}{\partial z^2} + q \qquad (2.14)$$

The laser intensity decays as it penetrates the material. This phenomenon can be modeled according to Beer-Lambert's law as follows:

$$I(z,t) = I(0,t)e^{-\alpha z} \qquad (2.15)$$

where $I(0,t)$ is the intensity at the surface [W/cm^2] and α is the absorption coefficient [1/cm]. The heat source $S(z,t)$ is calculated by taking the negative of the derivative of the intensity with respect to the z-direction while considering the effect of the material's reflectivity to laser irradiation. It is assumed that a percentage of the laser energy, given by R, is reflected by the material. R is an optical property of the material and will change according to the laser wavelength. For PDMS at UV wavelengths, R is assumed to be 0.4:

$$q = S(z,t) = \begin{cases} (1-R)I(0,t)\alpha e^{-\alpha z}, & t \le t_p \\ 0, & o.w. \end{cases} \quad (2.16)$$

To solve the heat equation numerically, we introduce the Crank-Nicolson scheme of the Finite Difference Method, which gives an unconditionally stable, yet very numerically intensive solution for temperature as a function of time along the depth of the polymer. This approach is based on central difference in space and the trapezoidal rule in time, which provides second-order convergence in time. When considering this 1-D case, the Crank-Nicolson scheme becomes a combination of the forward Euler method at time t=n and the backward Euler method at time t=$n+1$. One key aspect of employing this approach is that for this particular type of differential equation, the Crank-Nicolson method is unconditionally stable. Therefore, very small time and space steps can be considered. For time dependent derivatives, we utilize the forward derivative, so that the derivate of temperature at depth (z) with respect to time, at t= i, is given by:

$$\frac{\partial T_z^i}{\partial t} \approx \frac{T_z^{i+1} - T_z^i}{\Delta t} \quad (2.17)$$

For the second derivative of temperature with respect to the spatial dimension, z, the Crank-Nicolson discretization is given by:

$$\frac{\partial^2 T_z^i}{\partial z^2} \approx \frac{T_{z-1}^i - 2T_z^i + T_{z+1}^i}{(\Delta z)^2} + \frac{T_{z-1}^{i+1} - 2T_z^{i+1} + T_{z+1}^{i+1}}{(\Delta z)^2} \quad (2.18)$$

Replacing Equations 2.17 and 2.18 in the simplified heat equation, Equation 2.14, results in a finite difference formulation of the temperature profile:

$$\rho(T)C(T)\left(\frac{T_z^{i+1} - T_z^i}{\Delta t}\right) = k(T)\left(\frac{T_{z-1}^i - 2T_z^i + T_{z+1}^i + T_{z-1}^{i+1} - 2T_z^{i+1} + T_{z+1}^{i+1}}{(\Delta z)^2}\right) + q \quad (2.18)$$

Solving for $T(z)$ at time $i+1$ gives the implicit equation:

$$T_z^{i+1} = T_z^i + \frac{k\Delta t}{\rho C}\left(\frac{T_{z-1}^i - 2T_z^i + T_{z+1}^i + T_{z-1}^{i+1} - 2T_z^{i+1} + T_{z+1}^{i+1}}{(\Delta z)^2}\right) + \frac{q\Delta t}{\rho C} \quad (2.19)$$

The 1-D heat conduction equation was solved with Matlab, using the Crank-Nicolson scheme presented in Equation 2.19. The parameters given in Table 2.7 were utilized in the numerical analysis.

Table 2.7. Finite difference method simulation parameters. (Criales et al., 2015b)

Parameter	**Value**
Total duration, t_{max} (s)	2
Material thickness, D (mm)	20
Time step, Δt (s)	5×10^{-4}
Space step, Δz (mm)	0.1
Number of time steps	4000
Number of space steps	2000

The choice of simulation parameters, namely the time and space steps, was made based on the achieving proper convergence. The following assumptions were made:

- No heat consumption (or loss) throughout the process.
- Use of peak beam intensity of the Gaussian beam profile.
- Laser absorption coefficient is independent of temperature.

The following initial and boundary conditions are applied to solve the heat equation:

- $T(t = 0,\ z) = 300\ K$ (initial temperature is room temperature).
- $T(t,\ z = D) = 300\ K$ (fixed temperature at the bottom of the sample).

By comparing the predicted temperature against the vaporization temperature of the material, it is possible to calculate the maximum depth at which the material ablates, which corresponds to the depth of the channel. The results are summarized in Table 2.8.

Table 2.8. Thermal model prediction for PDMS micro-channel depth. (Criales et al., 2015b)

Fluence, Φ [J/cm^2]	**Pulse Overlapping, O_f [%]**	**Predicted Channel Depth, D_{sim} [μm]**	**Actual Channel Depth, D_{avg} [μm]**
792	85	15	9
1154	85	24	20
1652	85	35	30
792	90	29	26
1154	90	37	33
1652	90	49	44
792	95	36	33
1154	95	51	47
1652	95	65	59

The temperature model overestimates the channel depth. This is due to the analysis being done in only the *z*-direction. Normally, heat would be conducted in the *x*- and *y*-directions as well. Additionally, the model does not account for material removal. In other words, the thermal model works under the assumption that the material which is heated past the vaporization point can continue conducting heat to the rest of the sample. The combination of these two factors leads to an overestimation of the channel depth because the model causes heat to be conducted further into the material when, in reality, this heat would be dissipated before vaporizing the target depth. Figure 2.9 show the evolution of temperature at the surface of the PDMS sample as a function of time for O_f =85%, 90%, and 95% pulse overlapping. Each figure also contains temperature profiles for the three fluence level settings. It can be seen how enough heat is generated to ablate the material.

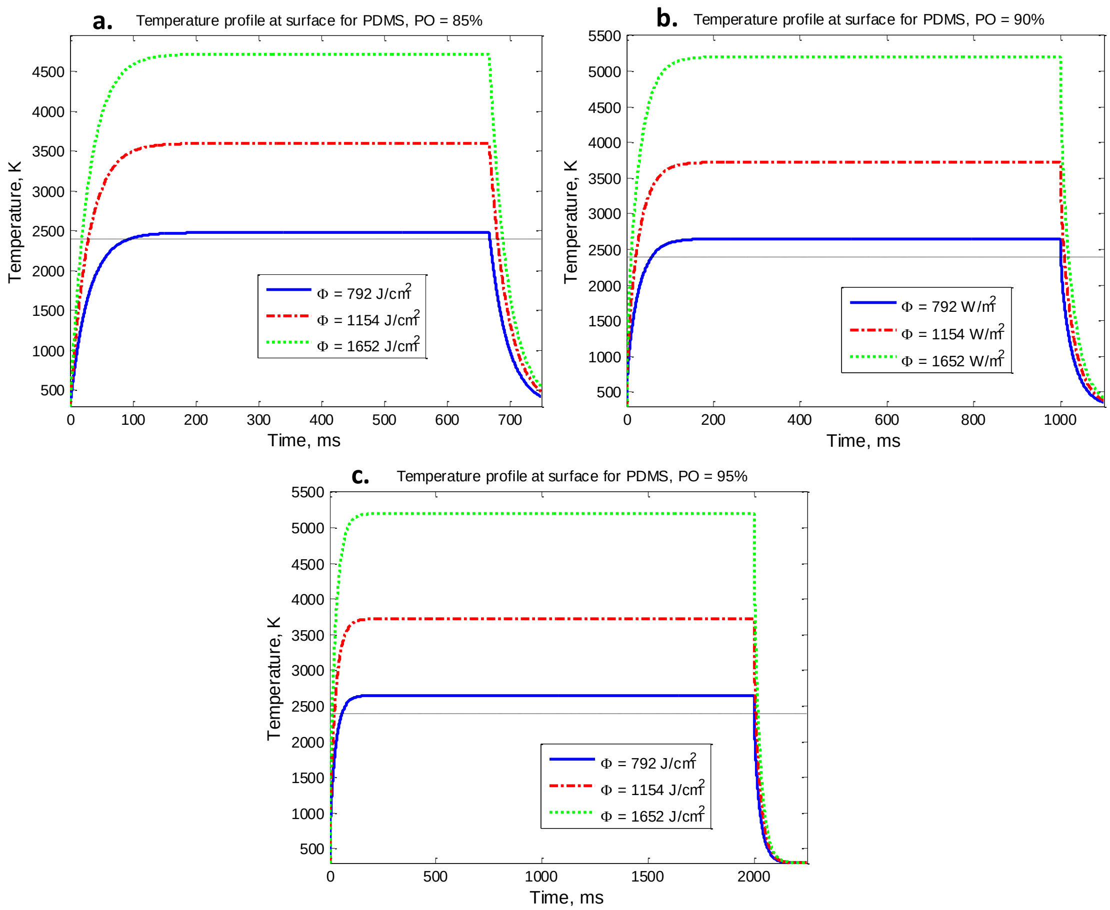

Figure 2.9. Temperature profile at surface of PDMS samples (λ=355 nm UV wavelength) with a) O_f =85% overlapping, b) O_f =90% overlapping, and c) O_f =95% overlapping. (Χριαλεσ ετ αλ., 2015β)

2.8 Comparison of manufacturing techniques for PDMS micro-channels

Beyond determining the feasibility of utilizing UV nanosecond pulsed lasers for PDMS micro-channel fabrication, it is also necessary to compare and contrast the qualities of this process with those of other PDMS micro-channel manufacturing techniques, as detailed in Table 2.9.

Table 2.9. Summary of manufacturing techniques for PDMS micro-channel fabrication.

Manufacturing Process	Quality	Processing Time	Operating Cost	Flexibility
Photolithography (He et al., 2010)	High	High	High	Low
Soft Lithography (Rogers and Nuzzo, 2005)	High	High	High	Low
Pico and femtosecond-pulsed laser (Suriano et al., 2011)	High	Low	High	High
NIR Nanosecond-pulsed laser (Teixidor et al., 2013)	Low	Low	Low	High
UV Nanosecond-pulsed laser (Criales et al., 2015b)	Medium	Low	Low	High

UV nanosecond-pulsed laser manufacturing of PDMS micro-channels stands out as a promising technique due to the low processing time required, the low operating cost (despite a higher initial set-up cost) and its high process flexibility, which allows the user to change or modify micro-channel geometry and layout quickly and efficiently.

2.9 Summary and Conclusions

Nanosecond pulsed laser micro-machining of PDMS polymers has been achieved with an Nd:YAG laser using the third harmonic of the fundamental wavelength to obtain UV (355 nm) laser irradiation. This study reveals the viability of using UV laser irradiation with high energy intensity nanosecond pulses on fabrication of micro-channels in PDMS polymers. Process models for micro-channel profile and temperature into the depth direction have been proposed for effective process planning and optimization. This feasibility study generates the following conclusions:

- Both fluence and beam overlapping factors are significant process parameters to be considered in any micro-channel fabrication based on pulsed laser micro-machining.
- For PDMS channels, higher scanning rates produce deeper channels, while increasing fluence (Φ=792-1652 J/cm^2) also increases the channel depth. However, the effect of increasing fluence is more noticeable in micro-channel depth than that of increasing scanning rate at S_r= 89-267 pulses/mm or O_f=85-95%.
- PDMS channels have a consistent geometry throughout, as shown by the standard deviation of the width and depth measurements taken.
- Insufficient chemical ablation and dominant thermal ablation mechanisms produce some damage to the workpiece and crazing on the surrounding area of the machined path.
- Physical and thermal models for predicting the depth and the profile of laser-ablated channels validated with experimental results are found to be very useful for process planning purposes.

Chapter 3 SINGLE-TRACK MODELING FOR SELECTIVE LASER MELTING OF POWDER METALS

3.1 Introduction

Laser-based powder metal additive manufacturing (or more commonly 3-D printing) technology has been rapidly growing and finding applications in various industries. Of particular interest are medical implants, automotive and aerospace parts, and any other devices with complex geometries and structures. However, the build part quality and process performance in terms of dimensional accuracy, surface roughness, structural integrity, resultant mechanical properties and related processing times has not been at the desired industry-ready levels (Kruth et al., 2007, Levy, 2010) and some challenges have remained to this day. For this reason, predictive process modeling and optimization for improved dimensional quality, product reliability, and overall productivity is of great interest to current on-going research efforts (Amato et al., 2012, Anam et al., 2013, Jia and Gu, 2014, Dai and Gu, 2014, Yadroitsev et al., 2014, Zeng et al., 2013, Yin et al., 2012).

Selective Laser Melting (SLM), is an additive manufacturing (AM) process started in 1995 at the Fraunhofer Institute ILT in Aachen, Germany. The SLM process aims to selectively and directly melt the powder metal in the form of localized melt pools, which once solidified create a fully dense 3-D metal part. Direct Metal Laser Sintering (DMLS), which was developed by EOS Company in Munich, Germany, is also an AM process that selectively sinters or fully melts the metal powder to obtain porous or fully dense 3-D metal parts, as required. Additive manufacturing processes are especially beneficial for high performance metals, such as fully dense titanium alloys, nickel-based super alloys, and tool steel. These materials are difficult for traditional computer numerical control (CNC) machines or rapid prototyping (RP) machines to fabricate. For example, titanium and its alloys have proven to be technically superior and cost-effective materials for a wide variety of aerospace, industrial, marine, medical, and commercial applications. Parts or products cast and/or machined from these high performance metals are very expensive, partly due to the processing difficulties and complexities during machining and casting. There is an urgent need for uniform and defect-free microstructure in laser based powder metal fusion and deposition processes. As these processes are used for the high performance metals described previously, predicting and controlling fusion and deposition quality is critical. This is due to the fact that these metals are most likely the critical components of a structure in applications such as an aircraft wing, body joints and medical implants. Once the entire part is built, it is very impractical to repair a defect somewhere within the part as these parts have high hardness, toughness and strength.

There are outstanding challenges to quality assessment in additive manufacturing. These approaches and their challenges include: i) use of non-destructive evaluation to inspect the deposited parts, which is not adequate due to irregular surface finish of as-deposited parts that often obscures the evaluation results. ii) setting more conservative process requirements to avoid quality issues in part-to-part and machine-to-machine variations that limit repeatability: most of the current AM machines cannot meet these conservative requirements, and lastly iii) predictive modeling of melt pool changes and temperature during additive manufacturing processes, which are mainly affected by variations from one layer to the next due to heat accumulation. The current strategy is to monitor melt pool size as an indication of temperature for process control. However, this strategy consists of controlling process parameters to try to maintain a constant temperature. Its effectiveness can be discounted due to the effect of other process parameters and part geometry. Also, defects such as porosities and cracks may not be fully captured with this approach. Thus, an effective and predictive process modeling and control system is needed that would open up new opportunities for the powder metal fusion or deposition industry through the improvement of process robustness and achieving higher quality and productivity.

Among the various AM processes, Selective Laser Melting is a laser-based powder metal additive manufacturing process that allows the creation of 3-D parts by selectively and directly melting metallic powders and their subsequent solidification. The SLM process uses powder-in-bed procedure and it is quite similar to Selective Laser Sintering, but it uses a much higher energy density which enables full melting of the material (Santos et al., 2006, Mercelis and Kruth, 2006). Similarly, some studies focused on studying the resulting microstructure of components fabricated by SLM (Gu and Shen, 2009). At high laser energy intensities, Direct Metal Laser Sintering (DMLS) can perform the selective laser melting process where selectively and directly metal powder is melted and solidified to form fully dense 3-D metal parts. If the desire is to obtain lower density parts, the DMLS process can be utilized to produce parts with porous structures as well.

When comparing SLM to other traditional manufacturing techniques, the SLM process has some clear advantages: (i) high flexibility in manufacturing of complex geometries, (ii) a process setup that does not require tooling, and (iii) high degree of product customization that allows the use of multi-materials. These advantages are reflected in reduced transition times between manufacturing products of different characteristics at the same location. The most attractive feature of SLM is that it allows the user to manufacture highly complex geometries and structures that could not be manufactured using conventional production techniques. The laser heating process characteristic of SLM is known for its rapid heating times and unstable cooling times, as well as the extended time above melting temperature for key locations, which results in the formation of pores and voids in the microstructure and often lead to reduced material density, mechanical or fatigue properties and loss of process repeatability (Vandenbroucke and Kruth, 2007). The large variation that leads to decreased process repeatability is the biggest obstacle preventing the widespread of used of SLM as a common industrial practice.

Laser parameters, process parameters, and material properties must be studied jointly to obtain a better understanding of laser processing of powder metals. Laser parameters consist of those characteristics which are unique to the laser equipment: maximum power, wavelength, beam spot diameter, and laser beam energy distribution. Usually, these parameters cannot be modified easily. For example, the EOS-M270 DMLS machine features a maximum Yb:fiber laser power of P_{max}=200W, laser wavelength in the NIR range (λ=1060 nm), and spot size diameter of d=100 μm. There are also processing parameters which affect the quality of SLM produced parts: laser power (P), laser wavelength (λ), laser spot size (d), scanning path direction or strategy, scanning speed (v_s), stripe width (w), stripe overlap, hatch distance (h), and layer thickness (s), which are shown in Figure 3.1. Laser power, scanning speed, hatch distance, and layer thickness can be modified to increase or decrease the *energy intensity* ($E=P/v_s \times h \times s$) applied to the powder material. Similarly, the hatch overlap factor (d/h) is defined, the variation of which leads to changes in the resultant melt pool geometry, heat affected area, cooling rate, formation of solidification microstructure, and solidified stripe integrity in each layer.

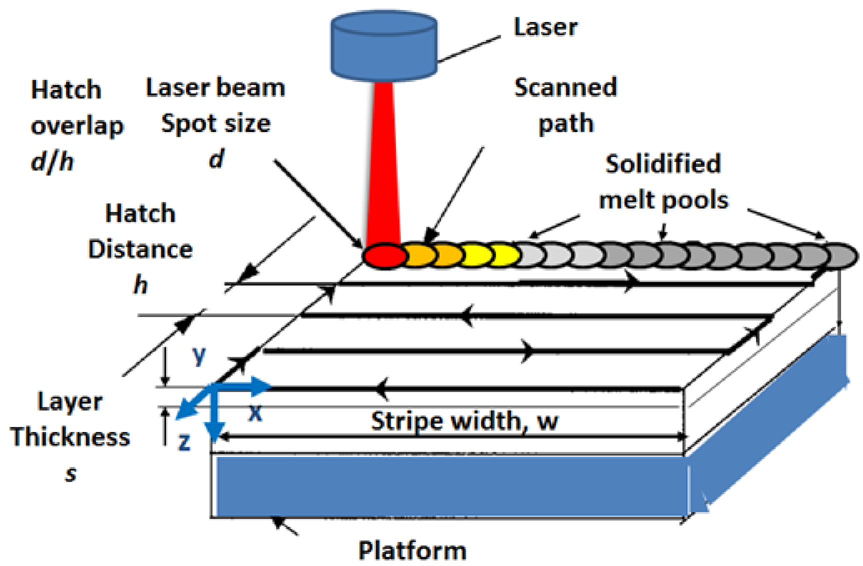

Figure 3.1. SLM process variables.

The SLM equipment used in experimental work also determines the kind of metal powder alloy that can be used. This is due to the SLM equipment manufacturer's restriction on the type of powder (d_{powder}, average powder particle diameter) that can be used as well as the inert gas environment available in equipment configuration, employed to reduce the effects of metallic oxidation. Therefore, material properties such as particle diameter and powder material density will changed depending on the machine's manufacturer. Table 3.1 summarizes some of the known metal powder properties and SLM processing parameters as presented by researchers in the literature.

Table 3.1. SLM parameters used for various metal powder materials

Reference	**Alloy**	**Powder size, d_{powder} [μm]**	**Laser power, P [W]**	**Laser wavelength λ [nm]**	**Laser spot size, *d* [μm]**	**Scan speed, v_s [m/s]**	**Hatch distance, *h* [μm]**	**Layer thickness, *s* [μm]**
(Anam et al., 2013)	IN 625	37	200-120	1060	100	0.7-1.1	100	20-40
(Yadroitsev et al., 2010)	IN 625	20	50	1075	70	0.13	60-140	20-60
(Gusarov et al., 2007)	316L SS	20	30	1060	60	0.12, 0.16, 0.24	Single track	50
(Hussein et al., 2013)	316L SS	N/A	100	N/A	150	0.10, 0.20, 0.30	75	1000
(Roberts et al., 2009)	Ti64	30	120	1060	100	0.22	Single track	30
(Fischer et al., 2004)	Pure Ti	30	3	1060	100	0.001	Single track	N/A
(Song et al., 2012)	Ti64	30	110	1064-1100	34	0.2-0.6	N/A	50
(Dai and Gu, 2014)	WC/Cu	Cu: 15 WC: 0.6	600-900	N/A CO_2 laser	600	0.04, 0.03	N/A	250

In this chapter, the 2-D heat transfer problem corresponding to laser melting of powder metal during single-track processing is solved using an in-house developed Finite Element Method-based program, written in MATLAB. The 2-D problem is partially extended to 3-D via two 2-D solutions, in order to investigate the temperature profile laterally on the surface of the powder bed and vertically into the depth of the powder bed. Two important conclusions are drawn from the resulting temperature field throughout the duration of the process: a) a history of the melt pool geometry, and b) the time spent above the melting temperature for each location of the powder bed. Most researchers who have attempted to optimize process parameters for SLM use predicted melt pool geometry as the key output. Little to no attention has been paid by previous researchers to utilizing the time at temperature as a key factor in resulting dimensional quality. Furthermore, thorough analysis of melting and solidification times could be applied to predict microstructure composition, and therefore, mechanical properties. In summary, time at temperature seems like a more viable candidate for process optimization. The second advantage presented is model flexibility. The research presented in literature uses readily available 3-D FEM based thermal analysis packages, which are used to obtain temperature distributions in an effort to predict melt pool geometry. However, commercial software packages are limited in expansion and implementation.

The proposed model will be utilized to properly describe how material and process parameters relate to density and melt pool geometry of SLM-produced parts, as shown in Chapter 6. The aim of the current chapter is to present the predictive modeling framework, through the development of thermal and melt pool modeling, for SLM of a single track of metal powder. Three materials are considered in this chapter: Ti-6Al-4V titanium alloy, AISI 316L stainless steel, and Inconel 625 nickel alloy. A sensitivity study into the effect of process parameters during SLM of a single track of IN 625 is presented as well.

3.2 Thermal Modeling

3.2.1 Formulation of Heat Transfer Problem

The initial task is to establish thermal models that can be used to calculate the temperature distribution during selective laser melting and solidification of metal powder. Obtaining an accurate temperature distribution is vital in order to appropriately describe the effects of fast heating and cooling times in the resulting part microstructure, and therefore, the dimensional quality and structural integrity of the manufactured part. The temperature distribution for this process can be calculated using a numerical solution approach, by means of solving the heat equation. Previous work by this research group included the development of a 1-D temperature profile model (Criales and Özel, 2014), which utilizes an FDM-based Crank-Nicolson scheme to solve the heat conduction equation in the z-direction (depth).

The heat transfer problem is solved using the 3-D heat convection-diffusion equation given in Equation 3.1.

$$\frac{\partial \rho u}{\partial t} + \frac{\partial \rho h \vec{V}}{\partial x} = k\left(\frac{\partial^2 T}{\partial x^2} + \frac{\partial^2 T}{\partial y^2} + \frac{\partial^2 T}{\partial z^2}\right) + q \qquad (3.1)$$

where u is the internal energy, h is the enthalpy, ρ is the density, T is the material temperature, k is the thermal conductivity, $\vec{V}$ is the average velocity vector of the moving medium, and q is the volumetric heat.

The first term of Equation 3.1 describes the variation in internal energy, which can be rewritten as $du = d\underline{h} = C_p\, dT$, where C_p is the isobaric specific heat. To determine whether natural convection plays a significant role in the heat transfer problem, Grashof's number which approximates the ratio of the buoyancy to viscous force acting on a fluid is calculated. Grashof's number is a function of gravity (g), the coefficient of thermal expansion (β), the difference in temperature between the moving medium (T_∞) and the surface (T_s), the depth of the melt pool (D) and the kinematic viscosity (v).

$$Gr = \frac{g\beta(T_s - T_\infty)D}{v^2} \qquad (3.2)$$

For this particular problem, a very low Grashof's number is obtained, indicating that the effect of natural convection in the moving melt pool is negligible. This is in agreement with Gusarov's assertion that the effect of natural convection is negligible when high scanning velocities, above ~100 mm/s, are utilized in the SLM process (Gusarov et al., 2007). By applying these two concepts to the convection-diffusion equation, Equation 3.3 is obtained.

$$\rho C_p \frac{\partial T}{\partial t} = \frac{\partial}{\partial x}\left(k \frac{\partial T}{\partial x}\right) + \frac{\partial}{\partial y}\left(k \frac{\partial T}{\partial y}\right) + \frac{\partial}{\partial z}\left(k \frac{\partial T}{\partial z}\right) + q \tag{3.3}$$

Solving the 3-D heat transfer equation is computationally costly, and with adequate assumptions, the problem can be simplified to a 2-D problem as explained in the next three sections.

3.2.1.1 2-D XY Heat Transfer Model

In the heat transfer problem described in Equation 3.4, the temperature T is a function of time t and of two space variables x and y which represent the scanning direction (x) and the hatching direction (y), respectively, while the conduction into the depth (z) direction is not considered.

$$\rho C_p \frac{\partial T}{\partial t} = \frac{\partial}{\partial x}\left(k \frac{\partial T}{\partial x}\right) + \frac{\partial}{\partial y}\left(k \frac{\partial T}{\partial y}\right) + q \tag{3.4}$$

The source term q is also independent of the depth direction (z). Solving at z = 0, the temperature field is obtained at the surface of the powder bed. The heat transfer inside the material occurs through conduction, while heat is loss to the environment via convection. The effect of radiation is not a significant source of heat loss and therefore is not taken into consideration in the current model.

3.2.1.2 2-D XY and XZ Heat Transfer Models

The 2-D temperature field can be considered as a cross-section of the full 3-D profile. This is a strong but necessary assumption in order to reduce the 3-D model into 2-D models where the melt pool is the main focus of the model. Equation 3.4 is written in the XY- and XZ-plane as:

$$\rho C_p \frac{\partial T}{\partial t} = \frac{\partial}{\partial x}\left(k \frac{\partial T}{\partial x}\right) + \frac{\partial}{\partial z}\left(k \frac{\partial T}{\partial z}\right) + q \quad (3.5)$$

$$\rho C_p \frac{\partial T}{\partial t} = \frac{\partial}{\partial y}\left(k \frac{\partial T}{\partial y}\right) + \frac{\partial}{\partial z}\left(k \frac{\partial T}{\partial z}\right) + q \quad (3.6)$$

where z represents the direction into the powder bed depth. It is worth noting that the temperature at the intersecting line of the XY- and XZ-planes must be the same in both XY and XZ simulations for the model to be consistent. The same concept applies to the intersecting line of the XY- and YZ-planes used in XY and YZ simulations. This would not be the case under the current assumptions because the three 2-D heat equations are used to solve three fundamentally different problems. We address this issue with the use of Dirichlet boundary conditions as explained in Section 3.2.

3.2.2 Definition of Material Properties

Thermal properties of the solid (bulk) material, i.e. density, specific heat, and thermal conductivity, vary according to temperature. Therefore, material properties are written as:

$$\rho_{bulk} = f_1(T) \quad (3.7)$$

$$C_{bulk} = f_2(T) \quad (3.8)$$

$$k_{bulk} = f_3(T) \quad (3.9)$$

For most metals, it can be assumed that thermal properties vary linearly with temperature. Once the material has melted, the thermal properties are those of the material in liquid form. For example, thermo-physical properties for solid and liquid phases are available for titanium and nickel-based alloys (Boivineau et al., 2006), and 316L stainless steel (Hussein et al., 2013). Similarly, powder density is another key material property for proper temperature analysis of Selective Laser Melting. Powders consist of a large number of very fine particles, whose small size allows them to be compacted or loosened into a wide array of packing densities. One way to model powder density is to consider it as a fraction of the bulk density:

$$\rho_{powder} = (1-\tau)^{\gamma}\rho_{bulk} \qquad (3.10)$$

Additionally, thermal properties such as thermal conductivity of the powder material can also be related to the bulk properties of the material by the porosity of the powder:

$$k_{powder} = (1-\tau)^{\beta}k_{bulk} \qquad (3.11)$$

In these representations, τ is the porosity of the powder material, indicating that at τ=0 the powder is fully dense. ρ_{bulk} is the bulk density of solid material, e.g. for Ti-6Al-4V, ρ_{bulk}= 4.45 g/cm^3 and k_{bulk} is the thermal conductivity of the bulk material, e.g. for Ti-6Al-4V, k_{bulk}= 6.80 W/mK.

By considering values of τ between 0 and 1, the effective density of the metal powder can be expressed. As a result of this approach, powder material porosity becomes a process variable in the SLM of powder metals. Also γ and β are model coefficients specific to the powder material, and must be determined experimentally (Roberts et al., 2009). Therefore, γ and β are generally not known for most powder materials. In this case it is assumed that γ and β are equal to 1, reducing Equations 3.10 and 3.11 to:

$$\rho_{powder} = (1-\tau)\rho_{bulk} \qquad (3.12)$$

$$k_{powder} = (1-\tau)k_{bulk} \qquad (3.13)$$

3.2.3 Latent Heat of Fusion

In order to model the molten region properly, it is important to account for the phase change between solid and liquid in the thermal model. Because these alloys are not pure substances, the phase change does not occur isothermally at a specific temperature but occurs between the solidus and liquidus temperatures (T_s and T_l) with a net change in enthalpy. The equivalent specific heat formulation will be used to model the phase transformation as a nonlinearity in the specific heat as shown in Equation 3.14.

$$C_{eq}(T) = \begin{cases} C_p(T)\ ,\ T \leq T_s \\ C_p(T) + \frac{L_f}{T_l - T_s},\ T_s < T < T_l \\ C_l\ ,\ T \geq T_l \end{cases} \tag{3.14}$$

where $C_p(T)$ is the specific heat of the solid material before it reaches the solidus temperature, C_l is the specific heat of the material in liquid phase, L_f is the latent heat of fusion of the material, T_s is the solidus temperature, and T_l is the liquidus temperature.

This formulation allows the reduction of a two region problem with a discontinuous jump to a single region problem, and has been used by various authors such as Van Elsen and Song (Van Elsen et al., 2007, Song et al., 2012).

3.2.4 Laser Heat Source Model

The laser heat source can be modeled using a Gaussian-like continuous wave laser beam or a uniform beam (flat-top) for which the fundamental wavelength, the maximum power, and the spot diameter are given. Additionally, a focused beam can be considered, resulting in a smaller spot size diameter and higher energy density output. By varying the drive voltage, it is possible to modify and control the energy and average power. For practical modeling purposes, it is assumed that a constant z-level is maintained. Using the

Gaussian distribution for beam intensity, the moving heat source on the surface (XY-plane) can be represented as given in Equation 3.15.

$$q = (1-R)\frac{2P}{\pi w_o^2} e^{-2\left((x-x_o)^2+(y-y_o)^2\right)/w_o^2} \qquad (3.15)$$

Where R is the reflectivity of the material, P is the laser power, w_o is the waist size, and r is the distance from the beam center. The waist size is the distance at which the laser reaches $1/e$ of its peak power and varies based on the experimental setup.

The laser penetration in the depth (z) direction is assumed to be insignificant, meaning that the laser energy is absorbed solely on the surface. In the case of the XZ simulation, the y-coordinate is fixed, causing the heat source distribution to be solely a function of x. The presence of heat conduction in the y direction in the XY case, and the lack of conduction in this direction in the XZ case, results in misleading temperatures in the XZ case. The same issue arises in the YZ case, where the x-coordinate is fixed, resulting in the heat source distribution being a function of y only. Therefore, an alternate approach is required in order to obtain meaningful and comparable results for temperatures in the XY, XZ, and YZ planes. Furthermore, specific planes of interest must be chosen. In the XY case, the region of interest is the surface, where $z = 0$. For the XZ case, the main region of interest is the centerline of the track ($y = 0$). For the YZ case, the regions of interest are the starting and ending point of each track ($x = 0$ and $x = x_{\text{end}}$). When comparing XY- and XZ-planes, or XY- and YZ-planes, the temperature at the intersection of the planes must be the same, as seen in Figure 3.2 for XY-XZ. This can be accomplished by solving the problem in the XY plane, and then using the resulting temperature field as an input to the XZ and YZ simulations in a single-direction coupled approach.

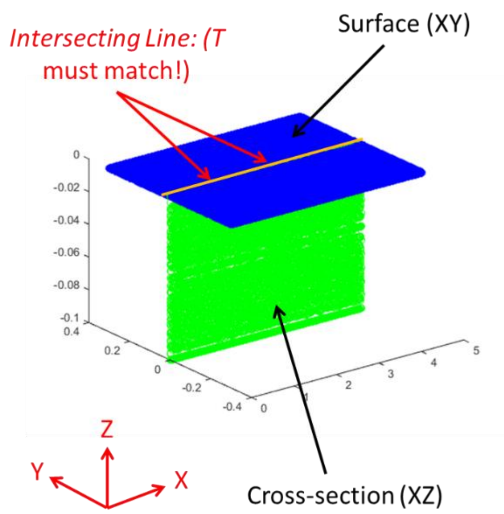

Figure 3.2. XY- and XZ-planes for simulation modeling

3.3 Finite Element Formulation

The following finite element formulation is used to represent the workpiece with a finite element mesh and applying a numerical scheme to solve the heat conduction equation (Criales et al., 2015a). The Finite Element Method (FEM) is a technique used to obtain an approximate solution to a boundary value problem for a partial differential equation by dividing the problem domain into smaller parts, or elements, via weighted residual methods. The Galerkin method is utilized to represent the current continuous problem as a discrete problem with as a mesh of small elements and shape functions, N_i's, assigned to each element of the mesh. The weak Galerkin form, as shown in Equation 3.16, is obtained by multiplying the heat conduction equation for the XY case with a test function $W = W(\mathbf{x})$, and integrating over the domain Ω:

$$\int_{\Omega} W\left[\rho C_p \frac{\partial \tilde{T}}{\partial t} - \frac{\partial}{\partial x}\left(k\frac{\partial \tilde{T}}{\partial x}\right) - \frac{\partial}{\partial y}\left(k\frac{\partial \tilde{T}}{\partial y}\right) - q\right] d\Omega = 0 \qquad (3.16)$$

The finite element formulation for the XZ case is analogous and can be written similarly. In Equation 3.17, the solution $\tilde{T}$ is approximated over the domain as:

$$\tilde{T}(x) = \sum_{a=1}^{n_{nodes}} N_a \tilde{T}_a \tag{3.17}$$

where n_{nodes} is the number of nodes in an element. The Galerkin method restricts the W's to be the same basis functions as the solution:

$$W(x) = \sum_{b=1}^{n_{nodes}} N_b W_b \tag{3.18}$$

where N_b's represent the shape functions of the chosen element evaluated at node b, and W_b's are arbitrary scalars at each node. Substituting Equations 3.17 and 3.18 into Equation 3.16 yields:

$$\int_\Omega \Big[\sum_{b=1}^{n_n} N_b W_b \sum_{a=1}^{n_n} N_a \rho C_p \frac{\partial \tilde{T}_a}{\partial t} - \sum_{b=1}^{n_n} N_b W_b \sum_{a=1}^{n_n} N_a \frac{\partial}{\partial x}\Big(k \frac{\partial \tilde{T}_a}{\partial x}\Big) -$$

$$\sum_{b=1}^{n_n} N_b W_b \sum_{a=1}^{n_n} N_a \frac{\partial}{\partial y}\Big(k \frac{\partial \tilde{T}_a}{\partial y}\Big) - \sum_{b=1}^{n_n} N_b W_b\, q\Big]\, d\Omega = 0 \tag{3.19}$$

Note that all terms have a sum over $N_b W_b$. Since W_b's are arbitrary constants, the $\sum_{b=1}^{n_n} N_b W_b$ can be collected outside

$$\sum_{b=1}^{n_n} W_b \int_\Omega \Big[\sum_{a=1}^{n_n} N_a \rho C_p \frac{\partial \tilde{T}_a}{\partial t} - \sum_{a=1}^{n_n} N_a \frac{\partial}{\partial x}\Big(k \frac{\partial \tilde{T}_a}{\partial x}\Big) - \sum_{a=1}^{n_n} N_a \frac{\partial}{\partial y}\Big(k \frac{\partial \tilde{T}_a}{\partial y}\Big) - q\Big]\, d\Omega =$$

$$\sum_{b=1}^{n_n} W_b R_b = 0 \tag{3.20}$$

where R_b is the residual of the equation in element level. Equation 3.20 can be written in a more compact form, as given in Equation 3.21.

$$\mathbf{C}(T)\dot{\mathbf{T}} + \mathbf{K}(T)\mathbf{T} = \mathbf{q} \tag{3.21}$$

In this formulation, $\mathbf{C}(T)$ is the heat capacity matrix, $\mathbf{K}(T)$ is the heat conduction matrix, $\mathbf{T}$ is the nodal temperature vector, $\dot{\mathbf{T}}$ is the nodal temperature rate vector and $\mathbf{q}$ is the heat source vector. The heat capacity matrix is a function of both material properties (density, heat capacity) and the shape function matrix, $\mathbf{N}$, as shown in Equation 3.22.

$$\mathbf{C}(T) = \int_\Omega \rho C_p \mathbf{N}^T \mathbf{N}\, d\Omega \tag{3.22}$$

Similarly, the heat conduction matrix is a function of thermal conductivity and the shape function matrix:

$$\mathbf{K}(T) = \int_{\Omega} k\mathbf{B}^T\mathbf{B}\, d\Omega \tag{3.23}$$

In Equation 3.23, matrix **B** is obtained by taking the partial derivative of the shape function matrix **N** with respect to the spatial coordinates. Furthermore, the heat vector is given by Equation 3.24.

$$\mathbf{q} = \int_{\Omega} q\mathbf{N}^T\, d\Omega \tag{3.24}$$

The element shape functions for a 2nd order isoparameteric triangle are given by Equation 3.25.

$$\mathbf{N} = [\xi(2\xi - 1)\ \ 4\xi\ \ 4\xi(1\xi - \eta)\ \ \eta(2\eta - 1)\ \ 4\eta(1 - \xi - \eta)\ \ (1 - \xi - \eta)(2(1 - \xi - \eta) - 1)] \tag{3.25}$$

The variables ξ and η in Equation 3.25 are two independent variables used to describe the local coordinates of the nodes in each triangular element. Integration over the problem domain is done via Gaussian quadrature, which calculates the function to be integrated at discrete points and adds them together using a weighting function. Since the heat capacity and heat conduction matrices are functions of temperature, they must be recalculated at every time step of the process as the temperature field evolves. Therefore, an implicit approach must be utilized to obtain the temperature field, as shown in Equation 3.26:

$$\mathbf{C}(T)\left(\frac{\Delta\mathbf{T}}{\Delta \mathrm{t}}\right) + \mathbf{K}(T)\mathbf{T}^{\mathrm{t}+\Delta \mathrm{t}} = \mathbf{q} \tag{3.26}$$

The phase change temperature region is small (between solidus and liquidus temperatures) for the materials in this study, so phase transition occurs very quickly. The time step, Δt, must be chosen small enough so that solution convergence is obtained and the fast heating and cooling times characteristic of SLM can be fully studied. Once a suitable value of Δt has been selected, Equation 3.26 is solved iteratively at each time step using the Newton-Raphson method, to obtain the change in the temperature field shown in Equation 3.27:

$$\Delta \mathbf{T} = (\Delta t \times (\mathbf{C}^{-1}\mathbf{K}) + \mathbf{I})^{-1}(\Delta t \times \mathbf{C}^{-1}(\mathbf{q} - \mathbf{K}\mathbf{T}^{t})) \qquad (3.27)$$

After solving for the change in temperature, the new temperature field is calculated using Equation 3.28:

$$\mathbf{T}^{t+\Delta t} = \mathbf{T}^{t} + \Delta \mathbf{T} \qquad (3.28)$$

The residual vector **R** is calculated using Equation 3.27:

$$\mathbf{R} = (\Delta t \times (\mathbf{C}^{-1}\mathbf{K}) + \mathbf{I}) \times \Delta \mathbf{T} - \Delta t \times \mathbf{C}^{-1}(\mathbf{q} - \mathbf{K}\mathbf{T}^{t})) \qquad (3.29)$$

When the norm of **R** is less than the specified error tolerance, the current iteration is completed and the temperature at the following time step is calculated. If the norm of the vector is greater than the specified error tolerance, a new iteration of the same time step is repeated using the newly obtained temperature field.

3.3.1 Heat Source and Boundary Conditions in XY

Figure 3.3 provides an overview of the problem geometry in XY, XZ, and YZ- planes and related assumptions. In the XY simulation, Neumann boundary conditions are used on all boundaries. The heat flux coefficient is calculated using the procedure outlined in the following section.

3.3.1.1 Boundary Conditions in XY-plane Simulation

Boundary conditions must be selected properly to account for situations where the simulated powder bed workpiece is not sufficiently large. Adiabatic boundary conditions, although simple to implement and with no computational cost, would trap the applied heat by the laser source within the workpiece leading to larger than expected temperatures. This effect can be easily observed by tracking the temperature of the nodes near the boundaries: if the temperature of the boundaries rises significantly above the initial value, then Neumann boundary conditions are required to allow heat to escape the workpiece via conduction. In Sections 5 and 6 of this Chapter, one short track of powder metal is processed and the heat affected zone never reaches the workpiece's boundaries, so the use of adiabatic boundary conditions is acceptable. For the multi-hatch simulation case explored in Chapter 4 and beyond, adiabatic boundary conditions are not acceptable and Neumann boundary conditions must be considered. To implement Neumann boundary conditions, the heat flux coefficient must be determined.

3.3.1.2 Heat Source in XY-plane Simulation

The XY model considers a moving heat source, where the heat is distributed to the elements that fall within the beam area at any time step, based on the relative locations of elements to the beam center as described by Equation 3.15. Therefore, **q** vector is calculated directly from the heat intensity of the laser beam. The heat is applied on these elements internally as a heat source via energy consistent lumping of the laser beam captured by an element's area and the location of each element within the beam. The variation of the power intensity with distance from the center of the Gaussian beam is also accommodated and a continuous wave laser source is utilized. The heat source vector $q(x,y,t)$ moving in the x-direction is realized by calculating the center position of the laser at time step i+1, so that $x_{i+1} = v_s \Delta t + x_i$ where v_s is the scanning speed of the laser beam during the SLM process. The 2-D meshes in the finite element formulation shown in Figure 3.3, Figure 3.4, and Figure 3.5 are comprised of 6292 triangular elements for the XY model, 2192 triangular elements for the XZ model, and 1325 elements for the YZ model respectively.

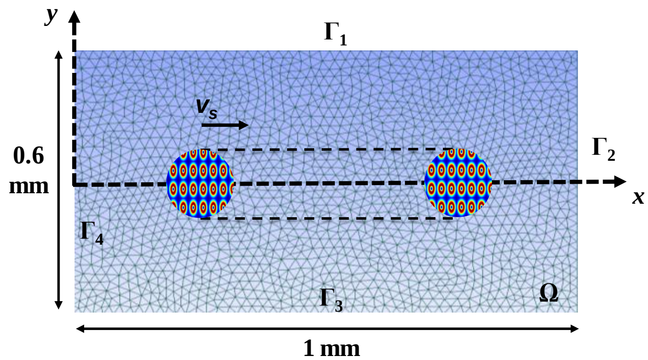

Figure 3.3. Sample powder bed mesh for 2-D FEM simulation of SLM, XY view. Γ_1, Γ_2, Γ_3, and Γ_4 are Neumann boundary conditions.

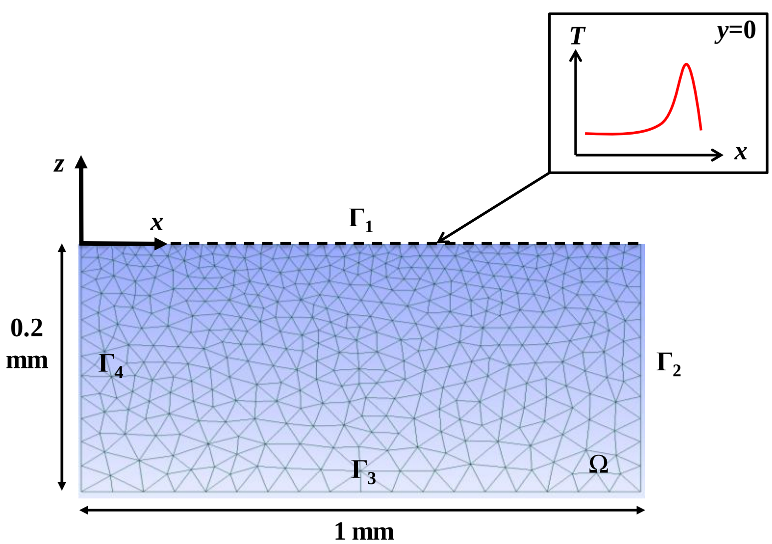

Figure 3.4. Sample powder bed mesh for 2-D FEM simulation of SLM, XZ view. Γ_1 is a fixed temperature boundary obtained from XY (Dirichlet BC). Γ_2, and Γ_4 are Neumann BC. Γ_3 is a fixed temperature boundary equal to the temperature of the plate (Dirichlet BC).

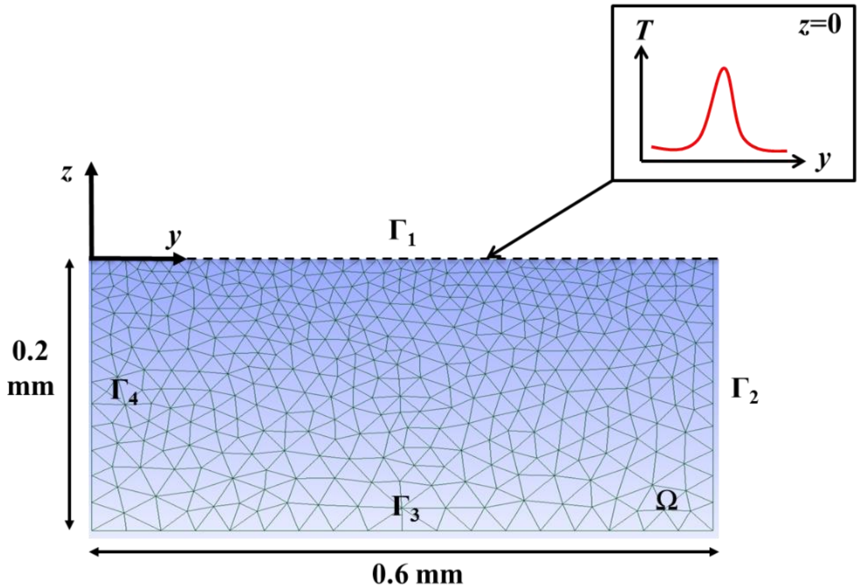

Figure 3.5. Sample powder bed mesh for 2-D FEM simulation of SLM, YZ view. Γ_1 is a fixed temperature boundary obtained from XY (Dirichlet BC). Γ_2, and Γ_4 are Neumann BC. Γ_3 is a fixed temperature boundary equal to the temperature of the plate (Dirichlet BC).

3.3.2 Heat Source and Boundary Conditions in XZ and YZ

In the XZ and YZ simulations, there is no heat source (**q**=0) and a Dirichlet boundary condition is applied in order to model the correspondent effect of laser processing. Without loss of generality, assume that the XZ plane of interest is given by y=0, meaning that the vertical plane through the center of the laser track is considered, and the YZ plane of interest is given by x = 0+ (very close to the beginning of the track). At each time step of the XZ and YZ model simulations, the temperature at the top boundary (z=0), Γ_1, is set equal to the temperature obtained from the XY simulation at the corresponding location (see Equation 3.30).

$$T_{XZ}\,(x, z = 0, t)|_{y=0} = T_{YZ}\,(y, z = 0, t)|_{x=0+} = T_{XY}(x, y = 0, t)|_{z=0} \tag{3.30}$$

This method of adjusting the top boundary during the XZ simulation can only be utilized after a full temperature history at the surface is obtained. Neumann boundary conditions are applied on the side boundaries: Γ_2 and Γ_4 , while Γ_3 is a Dirichlet boundary for both the XZ and YZ cases. The temperature at the bottom of the powder bed ($z = z_{max}$) is set to 353 K. In special cases, the side boundaries and the bottom boundary can be considered to be adiabatic to simplify the process. As explained in Section 3.1.1 of this Chapter, this assumption is only acceptable if the heat-affected zone does not reach the boundary in question. The initial temperature is also given by: $T_{xz}(x, z\ , t = 0) = T_{yz}(y, z\ , t = 0) = 353\ K$.

For each simulation, the scanning direction is the positive x-direction. The problem geometry for the XY, XZ, and YZ cases is shown in Figures 3.3, 3.4 and 3.5, respectively. The meshed powder bed has length 1 mm, width of 0.6 mm and depth of 0.2 mm. The laser source scans a track that is 0.5 mm in length. Powder bed geometry was chosen sufficiently large so that heat from the laser source can dissipate throughout the powder bed without having an effect on the temperature distribution, so, for simplicity, adiabatic boundary conditions can be used in this very specific example for the XY-plane. This approach is also employed by Roberts (Roberts et al., 2009), who considered a 1 x 1 x 0.15 mm rectangular block of powder in their study. Hussein (Hussein et al., 2013) makes special note of a sufficiently thick powder layer so that heat transfer at the bottom is negligible. However, in this simulation the bottom boundary condition in the XZ and YZ models is set as a Dirichlet boundary in which the temperature is set to that of the heated platform. These FE models have been implemented in MATLAB and results are presented in Section 3. Temperature solutions in XY and XZ planes will be utilized in determining the melt pool geometry. Therefore, once a 2-D temperature field is obtained, it is passed as the main input for the melt pool model, as described in the following section.

3.4 Development of Temperature-Based Melt Pool Modeling

The goal of this work is to utilize predicted and validated temperature distributions to determine the regions of solid, liquid + solid, and liquid phases in order to identify melt pool shape and size. During the SLM process, the laser beam melts the material which then extends to the trailing section of the scanning direction (see Figure 3.6). This molten area that follows the laser is referred to as the melt pool, similar to the weld pool observed in welding processes. As the laser beam moves, the melt pool changes in size and shape due to various laser and material properties such as the non-homogeneous laser power output and material porosity. The material outside this melt pool region has melted and re-solidified or is still in powder form. Material can still be in powder form because it has been thermally unaffected or because of incomplete fusion after some heating. By modeling the phase change computationally as described in the thermal modeling section, the molten area is obtained by identifying the locations with temperature higher than the liquidus temperature from the temperature field obtained through the FE simulation.

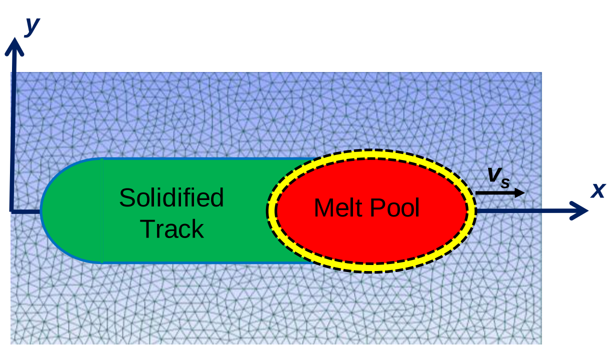

Figure 3.6. Sample melt pool geometry for 2-D FEM simulation of SLM in XY plane.

Melt pool shapes have been measured in various research studies. Verhaeghe (Verhaeghe et al., 2009) has studied SLM of Ti-6Al-4V powder and by solving heat transfer problem via an enthalpy formulation. SLM processing parameters were d_{powder} = 30 μm, s= 30 μm, R= 0.36, v_s= 300 mm/s, P= 20, 40, 60, and 80 W. They have measured melt pool cross-sections at different laser power (see Figure 3.7a). Gusarov (Gusarov et al., 2007) also reported measured melt pool geometry in SLM of 316L SS at different scan speeds (see Figure 3.7b).

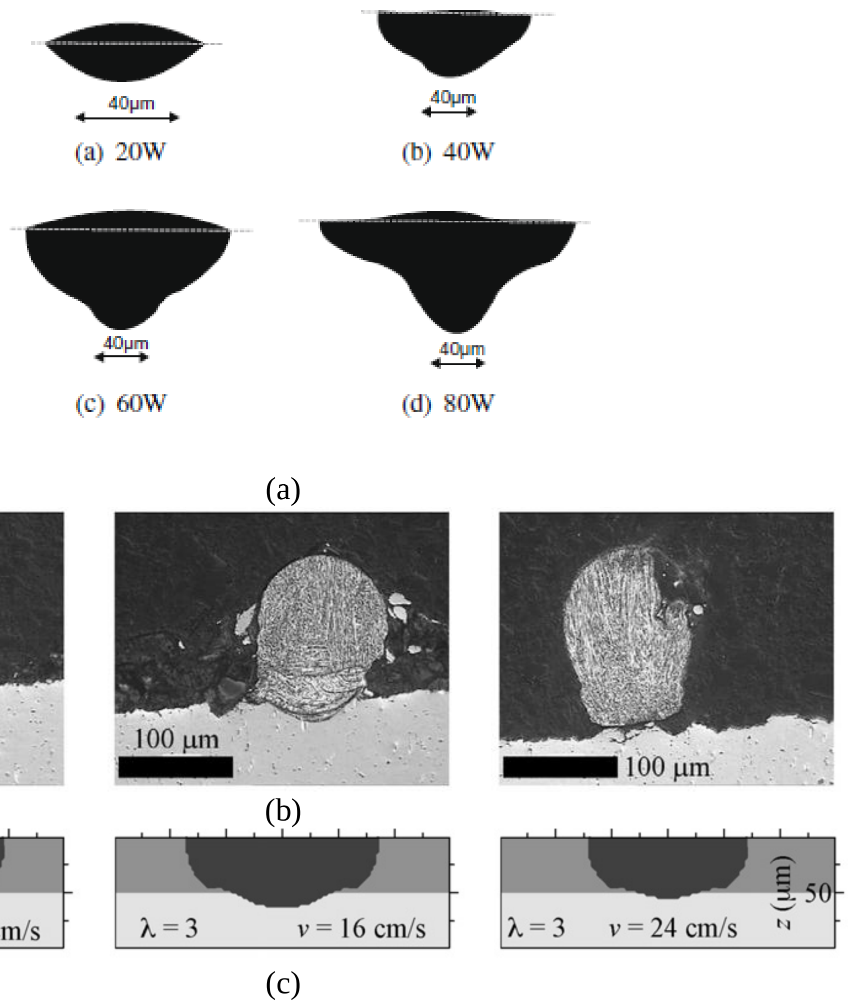

Figure 3.7. (a) Measured melt pool cross-sections in YZ view at different laser power levels (substrate level is indicated by a dashed line) in SLM of Ti64 (Verhaeghe et al., 2009) and (b) measured melt pool XY view and (c) calculated melt pool cross-section (dark zone) in YZ view at different scanning rates in SLM of 316L SS (Gusarov et al., 2007)

3.5 Model Comparison to Previously Published Results

There have been a number of research studies reported about the effects of SLM process parameters on the process performance and outcome. Experiments are often conducted to validate predicted **temperature distribution** (temperature [K]) and **melt pool size** (length, width, and depth [μm]). In this work, model validation was conducted by comparing the proposed model's results to those found in the literature. There is a clear lack of experimental data available for validation, due to the complex nature of temperature recording during SLS/SLM processes (Chivel and Smurov, 2010). In particular, two characteristics make it very challenging to obtain accurate temperature distributions experimentally. The first is the inability to obtain temperature readings at a location other than the surface of the powder bed. The second of these limitations arises from the micro-sized nature of the process: most available infrared cameras have a minimum resolution of 25 μm, which limits their usability to identifying the maximum temperature on the surface. Identification of the melt pool dimensions suffers from some of the same limitations. Due to the lack of experiment-based temperature distributions, we initiated our model validation by comparing our results to those obtained via simulation by Roberts et al. (Roberts et al., 2009) for Ti-6Al-4V titanium-based alloy, and to the results obtained by Hussein et al. (Hussein et al., 2013) for 316L stainless steel.

3.5.1 Model comparison for Ti-6AL-4V titanium alloy

Material, laser, and process parameters employed for this simulation are given in Table 3.2, matching what was reported by Roberts et al. (Roberts et al., 2009). A porosity factor of τ = 0.4 is considered. The material was preheated to 353K. In this case, the temperature distribution presented by Roberts et al. was partially validated by comparing to the preliminary results obtained experimentally by Fischer et al. (Fischer et al., 2004) using an infrared thermal camera to measure the temperature on the surface. The reflectivity of the powder material is not known, so it is assumed based on common values for metals.

Table 3.2. Simulation parameters for SLM of Ti-6Al-4V

Parameter	**Value**	**Reference**
Liquidus Temperature, T_l [K]	1933	Boivineau et al. 2006
Solidus Temperature, T_s [K]	1873	Boivineau et al. 2006
Solid Density, ρ [kg/m^3]	4450	Boivineau et al. 2006
Latent Heat of Fusion, L_f [J/g]	275	Boivineau et al. 2006
Specific Heat, C_p (T) [J/kg K]	$0.611T + 332.26$	Boivineau et al. 2006
Thermal Conductivity, k (T) [W/m K]	$0.015T - 1.334$	Boivineau et al. 2006
Reflectivity, R	0.75	Assumption
Powder Bed Thickness, s [μm]	30	Roberts et al 2009
Laser Power, P [W]	120	Roberts et al 2009
Spot Size Diameter, d [μm]	100	Roberts et al 2009
Scanning Speed, v_s[mm/s]	220	Roberts et al 2009

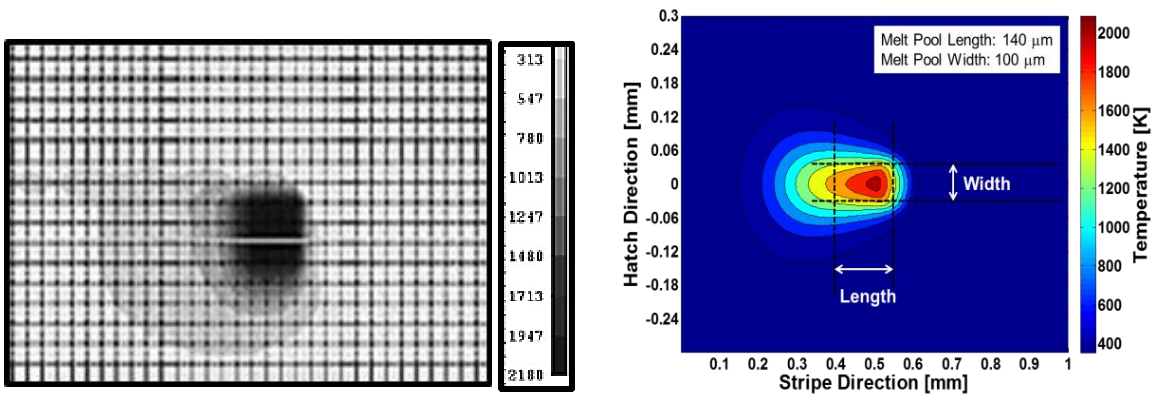

(a) (b)

Figure 3.8. (a) Temperature contour at surface of powder bed in XY view as reported by Roberts et al. (Roberts et al., 2009), (b) Temperature contour and melt pool geometry obtained in XY view using the proposed FE model. (Criales et al., 2015a)

As shown in Figure 3.8, our results are comparable compared to those obtained by Roberts et al. Roberts et al. reported a maximum temperature on the surface of approximately 2000K. The maximum temperature on the powder bed surface obtained in our simulation was 2080K, which seems reasonable when compared to the value obtained by Roberts et al. and considering that we are modeling a 2-D case where conduction into the powder bed (z-direction) is not taken into account. Additionally, we were able to identify the melt pool dimensions at any given time by comparing the temperature distribution obtained previously with the solidus and liquidus temperatures of Ti-6Al-4V, as shown in Figure 3.9. Material that has fully melted and will then solidify is shown in dark red. Material in the solidus + liquidus stage is shown in yellow. Finally, material that is currently below the solidus temperature is shown in blue. The advantage of presenting results in this manner is that the shape of melt pool can be easily observed. It is important to note that material below the solidus temperature may be material that has been melted previously and has re-solidified due to the rapid cooling process characteristic of SLM. By superimposing melt pool data at all moments in time, it is possible to obtain an estimate of manufactured track dimensions by determining what locations have melted and re-solidified. This can be achieved by looking at the maximum temperature reached by a node during the entire simulation. This would create a natural tie-in between selecting process parameters and predicting resulting dimensional quality by looking at temperature distributions.

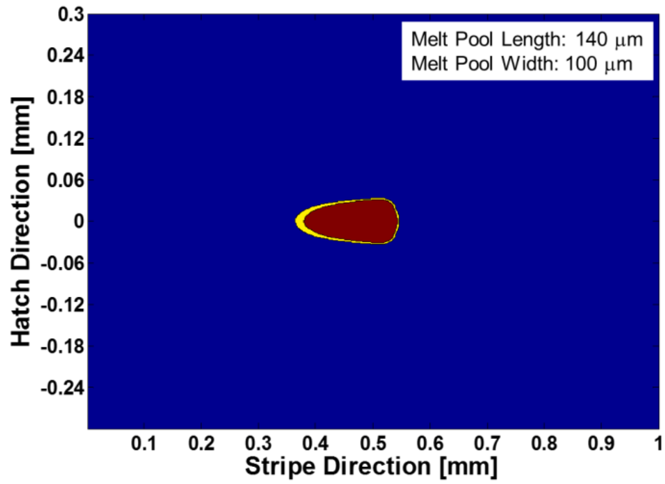

Figure 3.9. 2-D XY melt pool prediction. Blue: $T < T_s$; Yellow: $T_s < T < T_l$; Red: $T > T_l$

Figure 3.10 provides insight into the temperature evolution for a fixed point in the 2-D field. By studying three fixed locations, it is possible to gain an understanding of how the temperature rises above the liquidus temperature (melting of the powder) and later drop below it (solidification). The time above the liquidus temperature, t_m, is critical for microstructure formation. The effect of latent heat of fusion can be seen in the cooling mechanism, as the time between the solidus temperature and liquidus temperature is slightly longer.

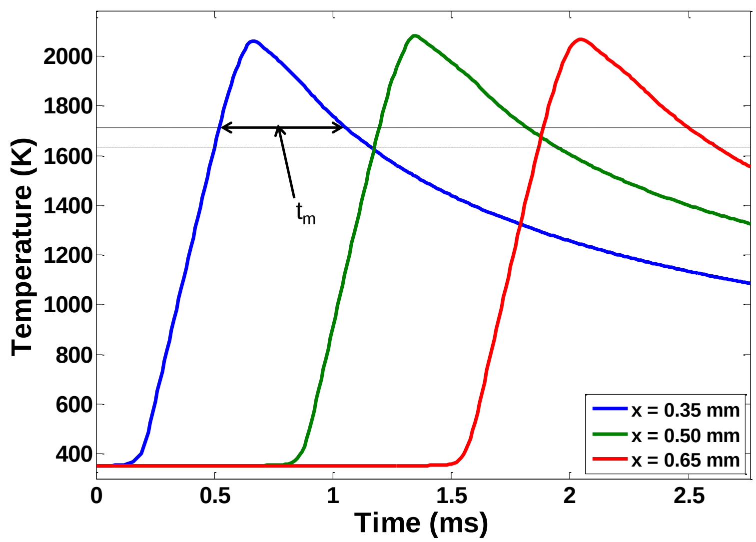

Figure 3.10. Temperature evolution for SLM of Ti64 at surface of powder bed (z= 0), along the track centerline (y= 0), for x= 0.35 mm, x= 0.50 mm, and x= 0.65 mm

3.5.2 Model comparison for 316L stainless steel

Further model validation was performed on SLM of 316L stainless steel for the processing conditions reported by Hussein et al. (Hussein et al., 2013). Powder material, laser, and process parameters used for this simulation are given in Table 3.3. For this material, temperature dependent properties were not available. A porosity factor of τ = 0.4 is considered. The material was preheated at 353K, or 80ºC. Figure 3.11 shows the temperature distribution obtained with the FE model simulation when using the parameters suggested by Hussein et al., as given by Table 3.3. Hussein et al. reported a maximum temperature on the surface of approximately 2600K for the given parameters, while our simulation reached a peak temperature of 2568K. Hussein et al. also provided a melt pool dimensions prediction based on the temperature distribution. Figure 3.12 shows a side-by-side comparison between Hussein et al.'s temperature prediction and the prediction obtained with the proposed model.

Table 3.3. Simulation parameters for SLM of 316L SS

Parameter	Value	Reference
Liquidus Temperature, T_l [K]	1713	MatWeb
Solidus Temperature, T_s [K]	1663	MatWeb
Solid Density, ρ [kg/m^3]	8027	MatWeb
Latent Heat of Fusion, L_f [kJ/kg]	277	Azo Materials
Specific Heat, C_p [J/kg K]	450	MatWeb
Thermal Conductivity, k [W/m K]	14.6	MatWeb
Reflectivity, R	0.7	Hussein et al 2013
Powder Bed Thickness, s [μm]	1000	Hussein et al 2013
Laser Power, P [W]	100	Hussein et al 2013
Spot Size Diameter, d [μm]	150	Hussein et al 2013
Scanning Speed, v_s[mm/s]	200	Hussein et al 2013

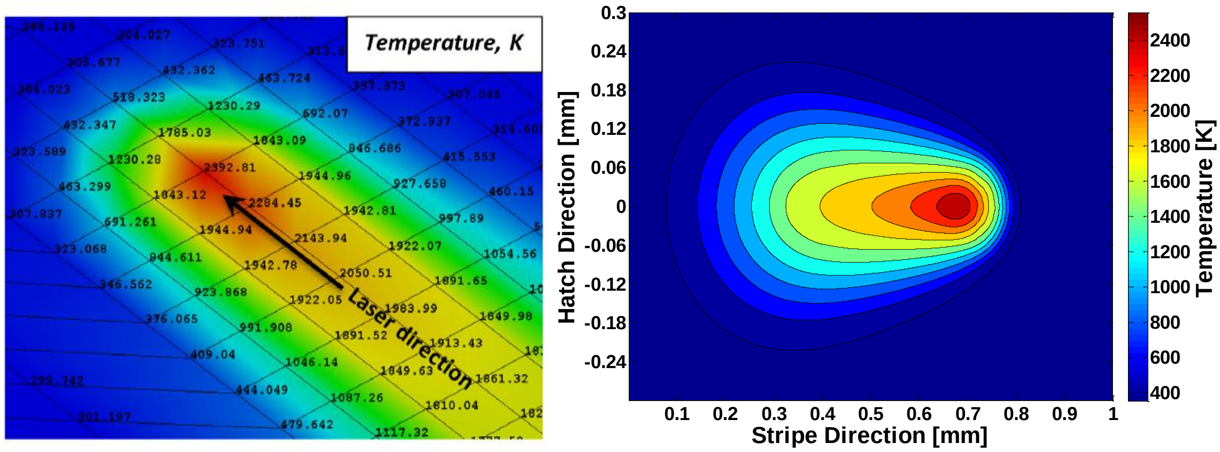

(a) (b)

Figure 3.11: (a) Temperature contour at surface of powder bed in XY view as reported by Hussein et al. (Hussein et al. 2013), (b) Temperature contour obtained using the proposed 2-D XY FE model.

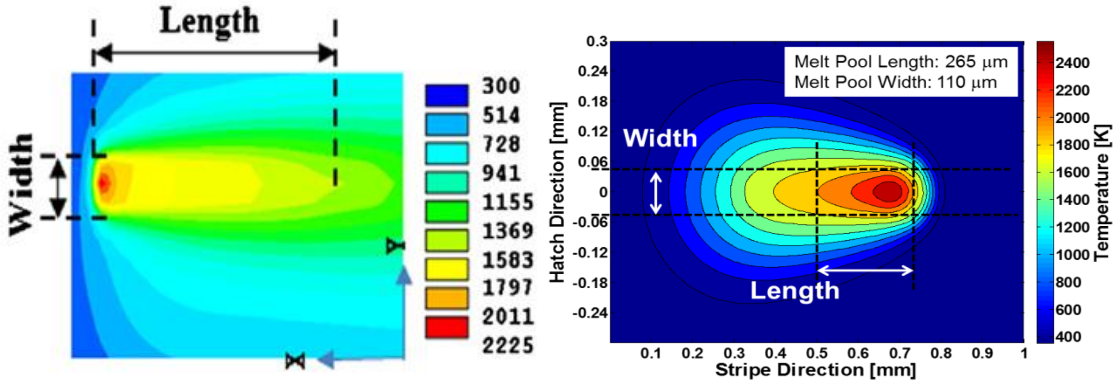

Figure 3.12. (a) Melt pool prediction at surface of powder bed in XY view as reported by Hussein et al. (Hussein et al. 2013), (b) Melt pool prediction obtained using the proposed 2-D XY FE model.

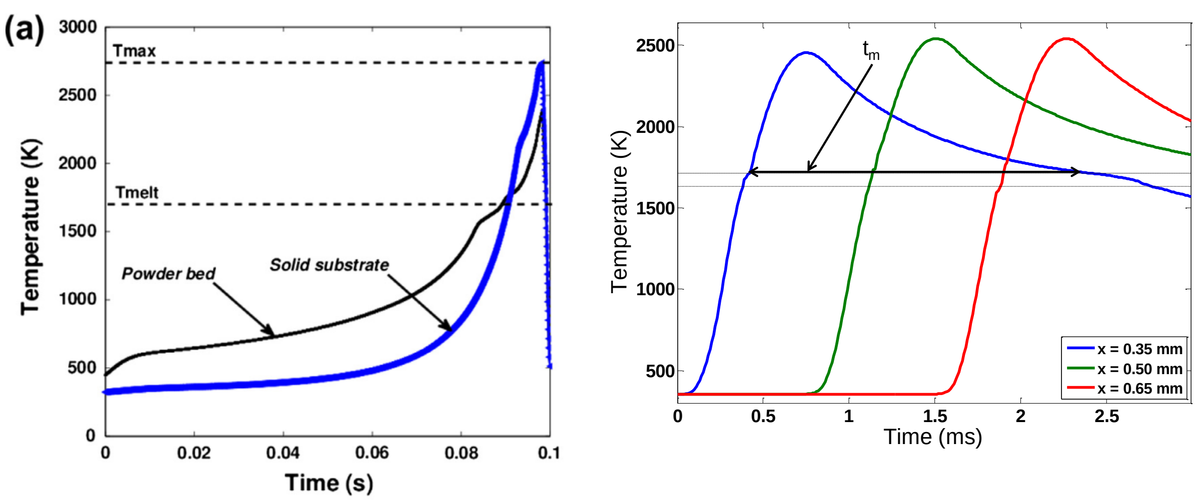

Figure 3.13. Temperature evolution for SLM of SS 316L at surface of powder bed (z= 0), along the track centerline (y= 0): (a) Hussein et al. 2013 and (b) this study for x= 0.35 mm, x= 0.50 mm, and x= 0.65 mm.

Figure 3.13 shows the temperature profile along the track centerline for three specific locations: beginning, middle, and end of the processed track. Notice that the time above the melting temperature, t_m, is very large relative to the overall processing time. This is due to the very high temperatures reached when processing 316L SS under these conditions. This is a good example of the ultimate objective of the model: to identify regions of possible overheating for process optimization.

3.5.3 Model comparison for IN625 nickel-based alloy

Additional model validation has been performed on SLM of Inconel 625 nickel-based alloy powder for the processing conditions reported by Yadroitsev (Yadroitsev et al., 2010). Powder material, laser, and process parameters used for this simulation are given in Table 3.4.

Table 3.4. Simulation parameters for SLM of IN 625 (Yadroitsev et al. 2007)

Parameter	Value	Reference
Liquidus Temperature, T_l [K]	1623	**Special Metals DS**
Solidus Temperature, T_s [K]	1563	**Special Metals DS**
Solid Density, ρ [kg/m^3]	8440	**Special Metals DS**
Latent Heat of Fusion, L_f [kJ/kg]	227	**Special Metals DS**
Specific Heat, C_p (T) [J/kg K]	$0.2437T + 338.98$	**Special Metals DS**
Thermal Conductivity, k (T) [W/m K]	$0.015T + 5.331$	**Special Metals DS**
Reflectivity, R	0.7	**Assumption**
Powder Bed Thickness, s [μm]	50	**Yadroitsev 2010**
Laser Power, P [W]	50	**Yadroitsev 2010**
Spot Size Diameter, d [μm]	70	**Yadroitsev 2010**
Scanning Speed, v_s[mm/s]	130	**Yadroitsev 2010**

Currently, there is no available data in the literature regarding temperature distribution during SLM of IN 625, from either numerical simulations or experimental results. Therefore, we are unable to corroborate our results against previously published work. Figure 3.14 shows the temperature distribution obtained by the FE simulation along with images from re-solidified tracks, as reported by Yadroitsev. Figure 3.15 shows the melt pool dimension for the XY and XZ simulations based on the liquidus temperature of IN 625. The extension of the current thermal model allows for scanning multiple tracks (multi-hatch simulation that will be given in Chapter 4 of this dissertation) and prediction of stripe length and width, which would allow for a better comparison to experimentally-obtained results.

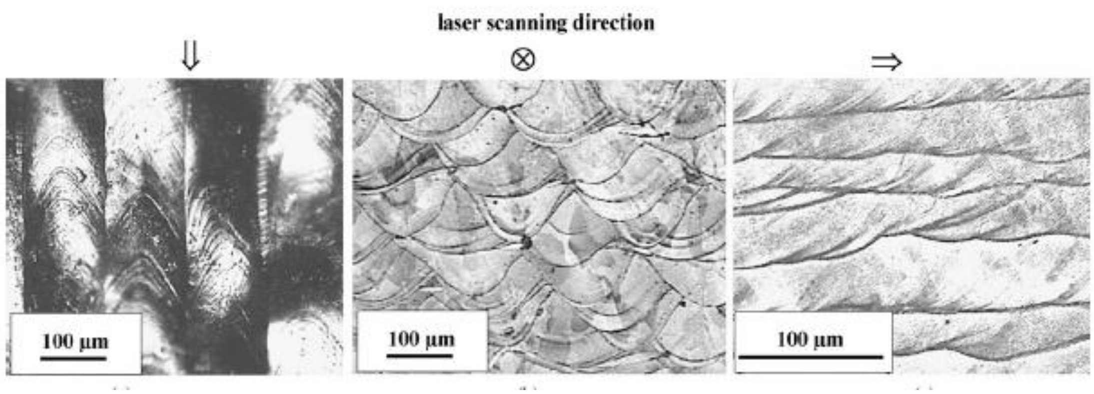

(a) (b) (c)

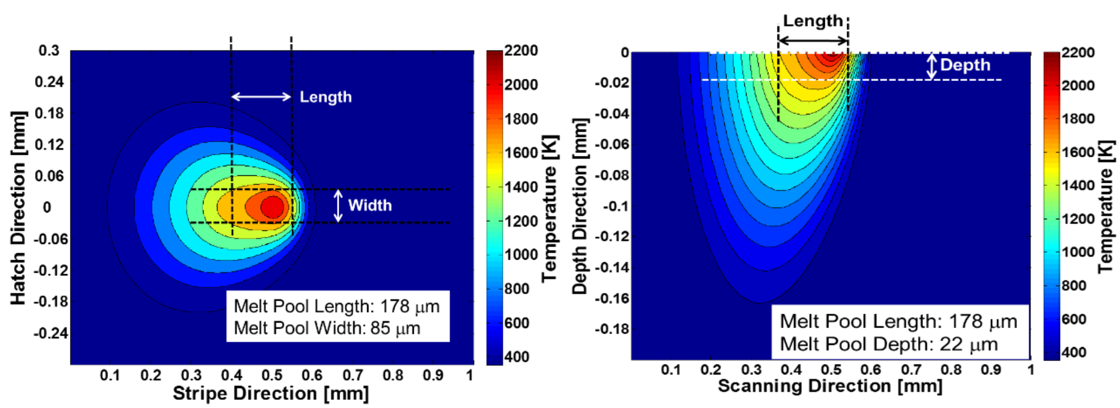

(d) (e)

Figure 3.14. Measured melt pool geometry in SLM of IN 625: (a) on the surface (XY view), (b) cross-section (YZ view) (c) longitudinal section (XZ view) (Yadroitsev et al., 2010), (d) (e) Temperature contour obtained using the proposed FE model in XY and YZ views.

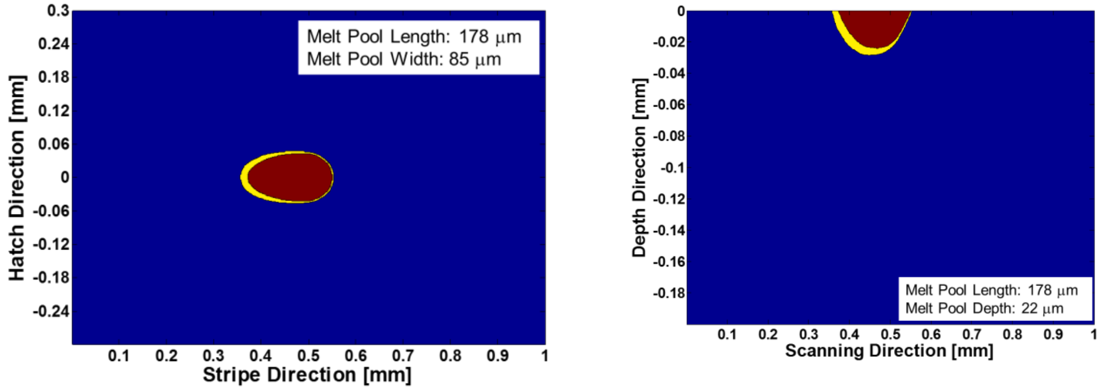

(a) (b)

Figure 3.15. Measured melt pool geometry in SLM of IN 625: (a) on the surface (XY view) (b) longitudinal section (XZ view)

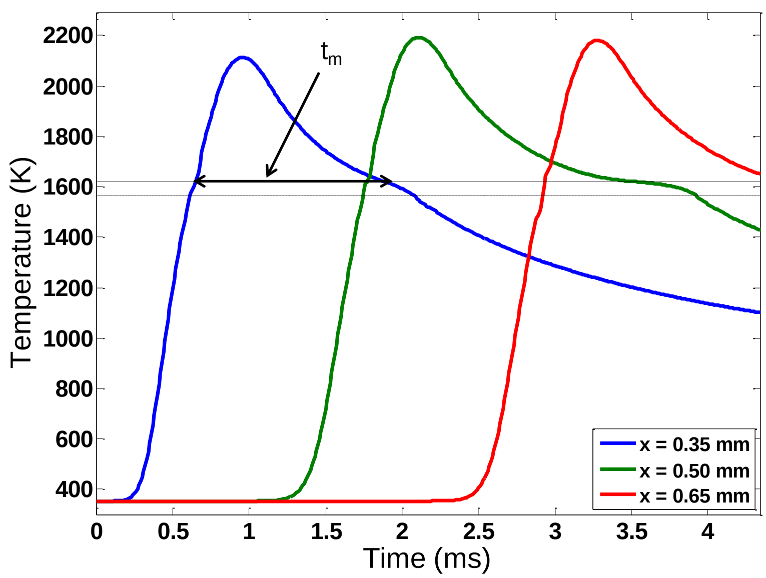

Figure 3.16. Temperature evolution for SLM of IN 625 at surface of powder bed (z = 0), along the track centerline (y=0), for x=0.35 mm, x=0.50 mm, and x=0.65 mm

For comparison purposes, the simulation results are summarized in Table 3.5. The values given for peak temperature and time above melting temperature correspond to a specific location of the powder bed (x=0.35 mm, y=0 mm), or 100 μm from laser center starting point in the scanning direction along the track centerline. By singling out the locations in which the peak temperature is the highest, possible overheating zones can be identified. Similarly, locations in which peak temperature is low are good indicators of areas where incomplete fusion may occur.

Table 3.5. Summary of simulation results at x=0.35 mm (100 μm from laser starting point)

Material	Peak Temp	Time above T_l
Ti-6Al-4V	2062.0K	0.67 ms
316L Stainless Steel	2453.9K	2.41 ms
Inconel 625	2112.5K	1.21 ms

3.6 Sensitivity Analysis

A sensitivity analysis of the Selective Laser Melting (SLM) process was performed to determine how several outputs vary as a result of variation or perturbation of process and material parameters (Criales et al., 2016). For this preliminary study, we considered a single-layer process in which a single hatch (track) of length 0.5 mm is scanned. The parameters taken into consideration are those reported by Yadroitsev (Yadroitsev et al., 2010), which are summarized in Table 3.6.

Figure 3.17 shows the temperature distribution on the surface of the powder bed, as obtained with the FE simulation model. A future extension of our model would allow for scanning multiple tracks and prediction of multi-track length and width, which would allow for a better comparison to experimentally-obtained results.

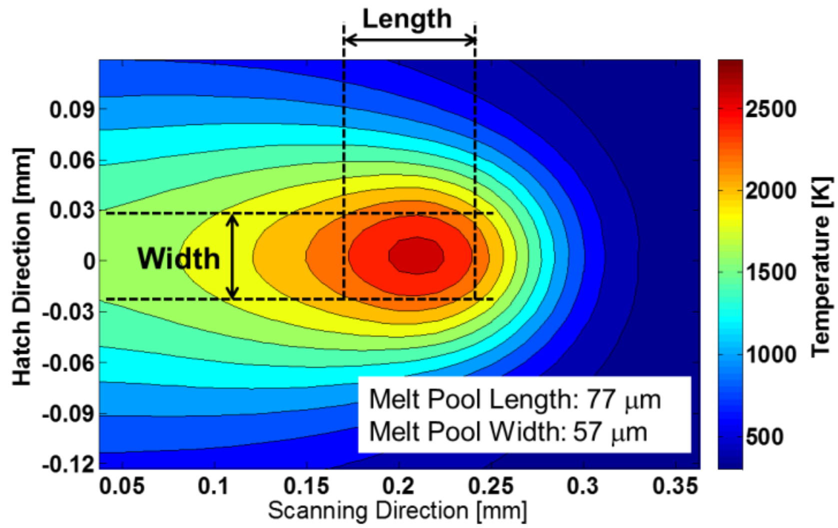

Figure 3.17. Measured melt pool geometry in SLM of IN 625: Temperature contour obtained using the proposed FE model

3.6.1 Sensitivity of FEM model to Material Properties

Since this is a numerically-based solution, the results will also be sensitive to several finite element-related parameters: length and width of the workpiece, number of elements in the mesh, and time step to solve, *dt*. The use of adiabatic boundaries, were heat is not lost, implies that the workpiece has to be large enough so that the heat affected region is not close to the boundaries. Table 3.6 shows the comparison of simulation results for several FE model numerical parameters. The last row, highlighted in green, shows the numerical simulation parameters chosen to perform the sensitivity analysis, based on two criteria: time step and time to execute.

Table 3.6. Simulation results for several FE model numerical parameters. (Criales et al., 2016)

Time Step	Workpiece/Mesh Dimensions				Melt Pool at $t = t_{max}/2$			Time to execute	
dt (μs)	L (mm)	W (mm)	# Elem.	# Vert.	L (mm)	W (mm)	Peak Temp (K)	In Secs	In mins
10	500	300	1556	777	74	46	2787	530	8.8
1	500	300	23896	11947	72	45	2840	5665	94.4
10	1000	600	6206	3102	76	45.6	2170	1144	19.1
10	5000	600	31288	15643	75	45	2170	4901	81.7
10	1000	1000	9992	4995	80	40	2157	1601	26.7
5	1000	600	6206	3102	74	46.8	2178	3734	62.2

The melt pool geometry is obtained by noting the nodes where the temperature is above the liquidus temperature, as shown in Figure 3.18. By executing the physics-based FE model, the temperature distribution along the surface of the powder bed (XY) can be obtained at any specific moment in time (see Figure 3.18).

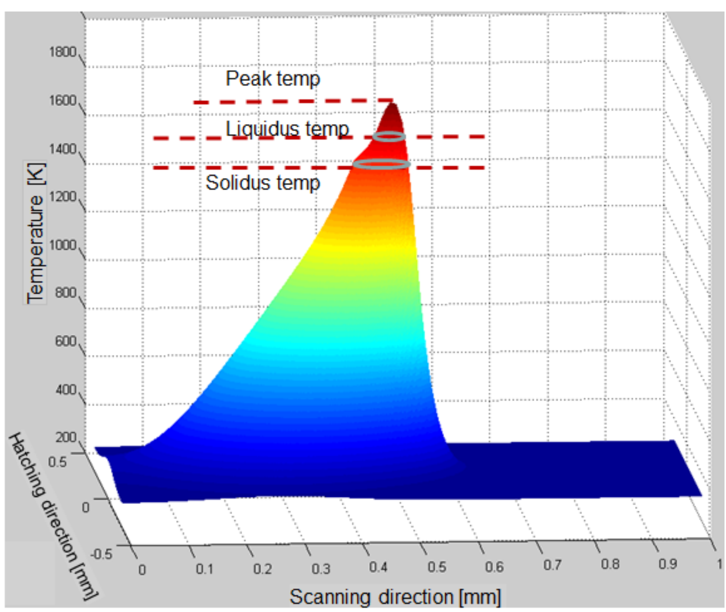

Figure 3.18. Temperature distribution at center of single track. (Criales et al., 2016)

Additionally, the temperature at specific locations along the track can be plotted as a function of time (see Figure 3.19). This allows us to calculate the temperature that the material spends above the liquidus temperature. This time of exposure above the melting temperature is a key variable in microstructure prediction.

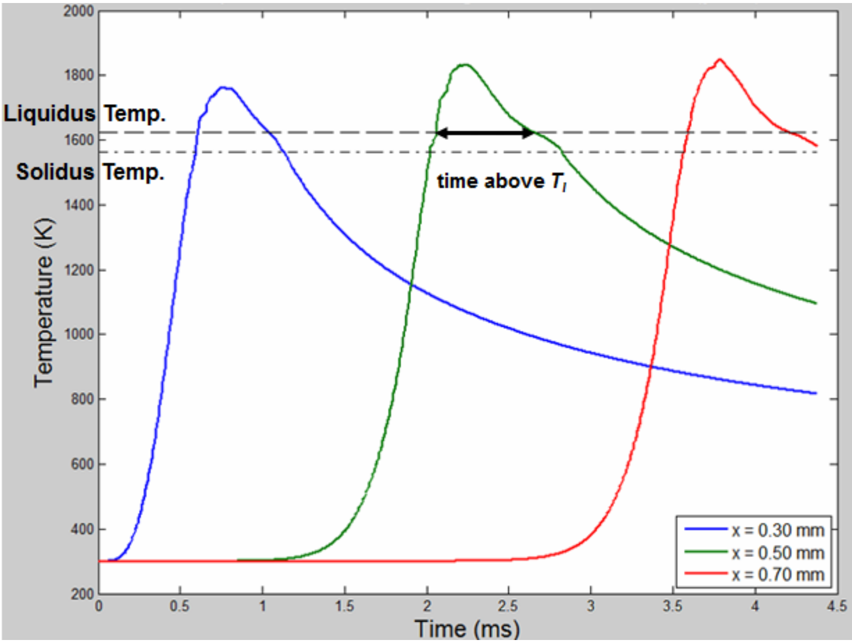

Figure 3.19. Temperature vs. time along the track centerline. (Criales et al., 2016)

The following table (Table 3.7) shows the mean value used in the base simulation, as well as the resulting value due to variation of -10% and +10% for each parameter. Each simulation was run by modifying a single parameter, e.g. -10% reflectivity, and leaving all other values equal to the mean. In this way, the effect of each parameter can be analyzed individually and independently.

Table 3.7. Sensitivity Analysis on Parameters for SLM of IN 625 (Yadroitsev et al., 2010)

Parameter	**-10%**	**Mean**	**+10%**
Bulk Density, ρ	7596	8440 kg/m^3	9284
Latent Heat of Fusion, L_f	204300	227000 J/kg	249700
Specific Heat, Cp	370.8	412 J/kg K	453
Thermal conductivity, k	8.847	9.83 W/mK	10.813
Reflectivity, R	0.63	0.7	0.77

Figure 3.20 shows how temperature varies with time while varying powder reflectivity for a fixed location in the powder bed. The x-coordinate is the midpoint of the track length (x=0.5 mm). The y-coordinate is the centerline of the track (y=0). The results show how variations of -10% and +10% affect peak temperature and time above T_l. In this particular case, the peak temperature and the time above T_l increase as the reflectivity decreases. By decreasing the reflectivity of the powder bed, more laser power is absorbed by the powder bed, which in turn leads to higher temperatures. The opposite is true when reflectivity increases: peak temperature and time above the melting temperature decrease.

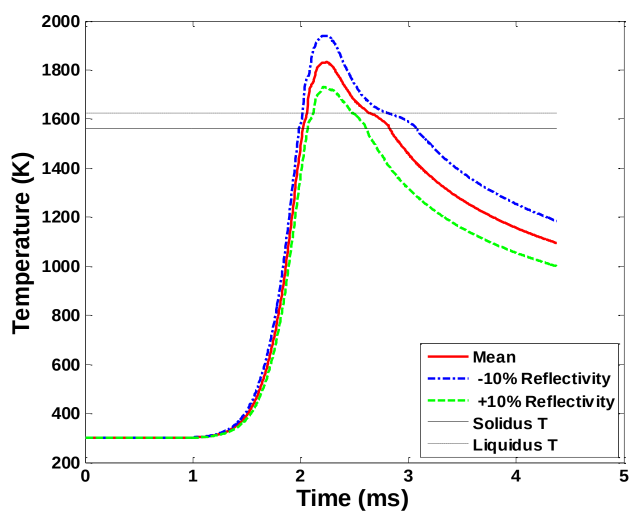

Figure 3.20. Temperature vs. Time for variation in reflectivity. (Criales et al., 2016)

3.6.2 Sensitivity of FEM model to Process Parameters

The following table (Table 3.8) shows the mean value used in the base simulation for SLM process parameters, as well as the resulting value due to variation of -10% and +10% for each parameter. Each simulation was run by modifying a single parameter, i.e. -10% laser power, and leaving all other values equal to the mean.

Table 3.8. Sensitivity Analysis on Process Parameters for SLM of IN 625 (Yadroitsev et al., 2010)

Parameter	**-10%**	**Mean**	**+10%**
Spot Size Diameter, *d*	63	70 μm	77
Laser Power, *P*	45	50 W	55
Scanning Speed, v_s	117	130 mm/s	143

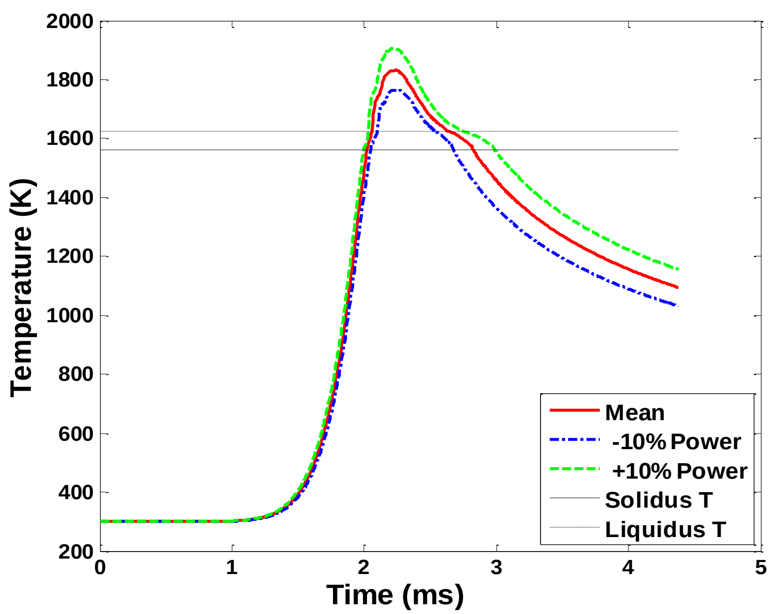

Figure 3.21. Temperature vs. Time for variation in laser power. (Criales et al., 2016)

A similar analysis is performed for material properties in place of laser process parameters. The evolution of temperature as a function of time at a fixed location is chosen to show the effect of varying laser power and scanning velocity (see Figures 3.21-3.22).

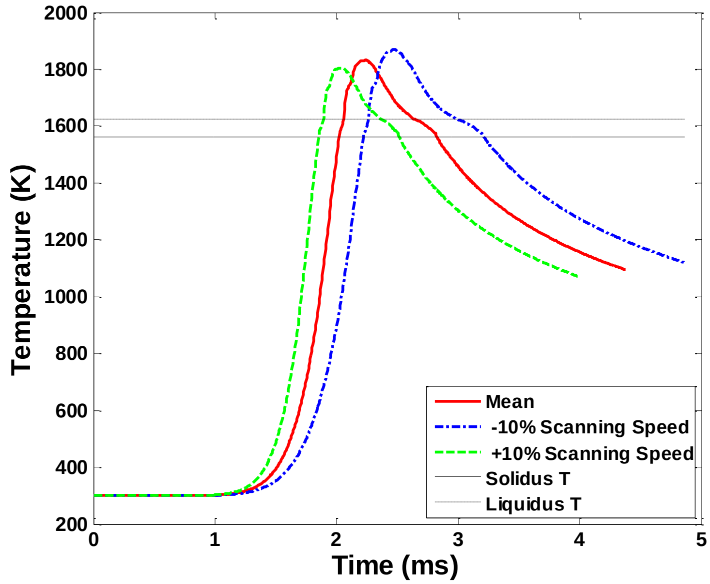

Figure 3.22. Temperature vs. Time for variation in laser scanning velocity. (Criales et al., 2016)

3.6.3 Effect of Powder Porosity on Simulation Results

A different set of simulations was executed to analyze the effects of powder porosity in the output variables described previously. For these simulations, only the porosity was modified. The value used in the control simulation was τ = 0.3, equivalent to 30% porosity or 70% dense material. 50% Dense and 90% dense material were also considered. Figure 3.23 shows the temperature rise as a function of time for multiple powder densities.

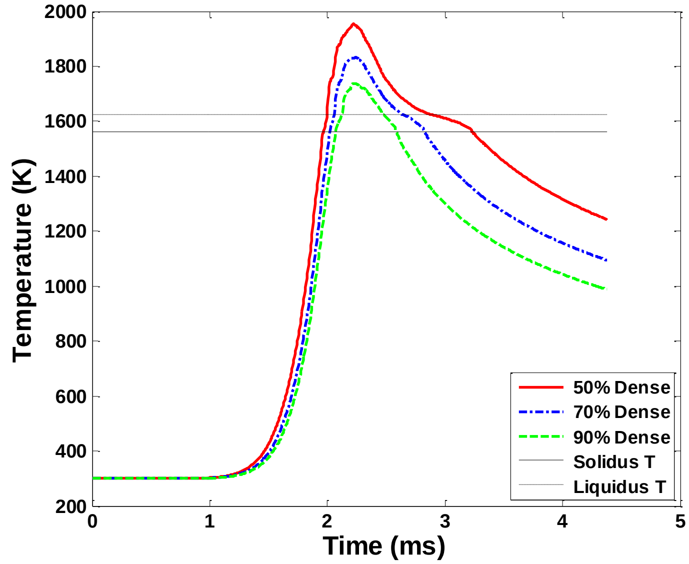

Figure 3.23. Temperature as a function of time for powder densities. (Criales et al., 2016)

3.6.4 Sensitivity Analysis Results Summary

The results of the sensitivity analysis can be summarized as follows. Figure 3.24 shows the effect of variation of each variable in the peak temperature at the center-point of the track. It can be seen that effect of latent heat is negligible, while the most variation occurs due to variation of reflectivity and laser power.

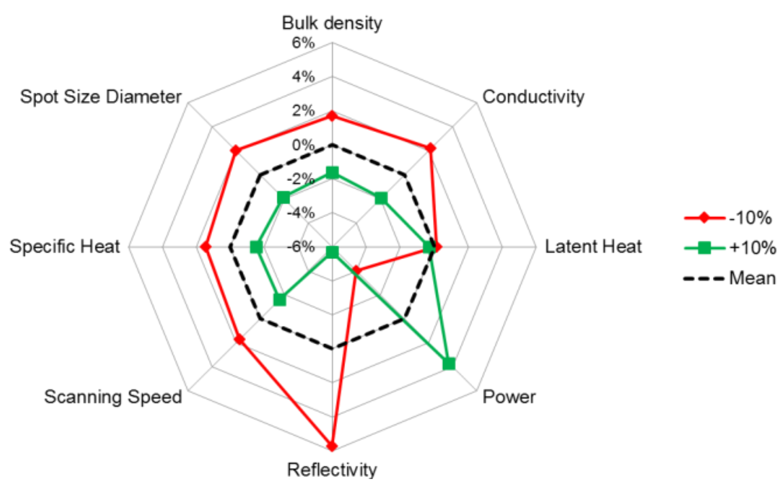

Figure 3.24. Variation of model parameters in peak temperature. (Criales et al., 2016)

Figure 3.25 shows how the melt pool length and the melt pool width change as parameters are varied one at a time. Note that variation of spot size diameter has very little incidence in melt pool geometry. Reflectivity, laser power, and scanning speed are the most relevant factors. Figure 3.26 shows the effect of variation of each parameter in the time above the liquidus temperature. Varying the scanning speed has a greater effect on the time above T_l than it does on melt pool geometry or peak temperature. As mentioned previously, the time above T_l, and the cooling time, will be critical to determine microstructure formation. Choosing appropriate ranges for scanning speed and laser power is vital for process optimization purposes, as further discussed in Chapter 7.

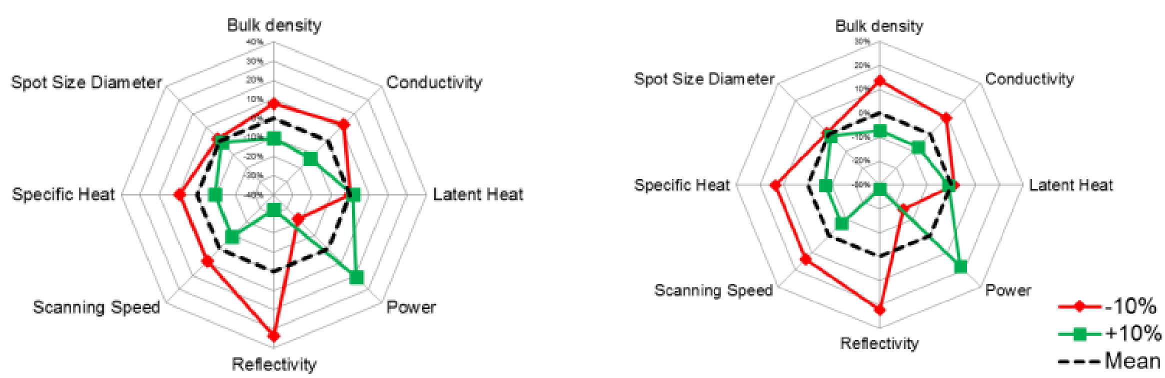

(a) (b)

Figure 3.25: Variation of model parameters in melt pool (a) length and (b) width. (Criales et al., 2016)

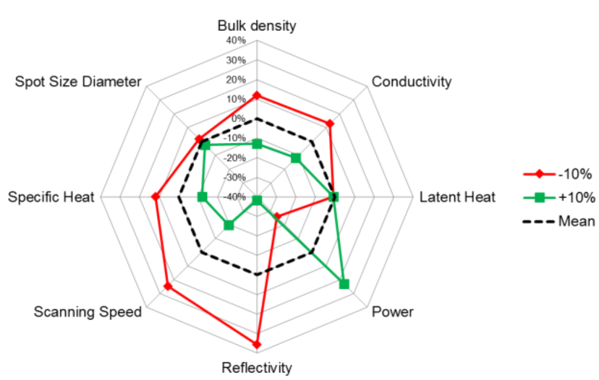

Figure 3.26. Variation of model parameters in time above T_l. (Criales et al., 2016)

To summarize, the objective of this sensitivity analysis was to obtain a better understanding of what occurs when a fixed, rigid value for a process parameter is not available. Perturbations to the material properties or the process parameters are introduced, which thereby affect the geometry of the melt pool, the peak temperature of the process, and the time spent by the material in liquid phase. This knowledge is extremely beneficial to the proper understanding of the SLM process; especially in cases where the nominal value of the parameter is not known with confidence (e.g. laser spot size) or in cases where the property itself changes constantly (e.g. specific heat). The modification of process parameters and the corresponding changes in the melt pool geometry, the peak temperature, and the time the material spends in liquid phase will provide qualitative and quantitative knowledge of how process parameters interact with each other during the SLM process. Furthermore, these results can be utilized to understand the effects of each individual parameter in the process output.

3.7 Summary and Conclusions

In this chapter, 2-D Finite Element-based thermal and melt pool models (on the XY- and XZ-planes) for single-track Selective Laser Melting of metal powders has been presented. Model results have been compared against the results published in the existing literature. Several published research results for SLM of powder metals have been utilized to investigate processing of titanium alloy Ti-6Al-4V, stainless steel 316L, and nickel-based alloy Inconel 625. Due to the two-dimensional nature of the FE simulation, temperature values were slightly higher, as conduction in the z-direction was not taken into account for the XY simulation. Additionally, a characterization of the melt pool shape and dimensions was provided based on the temperature distributions obtained through the FE simulation. This prediction of the melt pool shape and dimensions can be utilized for predicting layer geometry, and further on for optimization of process parameters such as stripe overlap factor based on dimensional quality. Finally, a complete temperature evolution plot showing how temperature changes with respect to time for a specific location on the surface was reported. Time above the liquidus temperature, t_m, was identified as a key parameter in the SLM process, as it may affect microstructure formation: texture, shapes and sizes of grains. Temperature distribution predictions in the XY- and XZ-planes were also provided in SLM of IN 625 alloy. A sensitivity analysis has been performed to quantify the effect of modifying process and material parameters by a set percentage (Criales et al., 2016). It was found that change in powder reflectivity produces the largest variation in the measurable outputs. Given the uncertainty in metal powder reflectivity measurements, a better understanding of how reflectivity changes as a function of powder porosity and temperature must be developed to improve the accuracy of predictive models.

Chapter 4 EXPERIMENTAL DESIGN AND MULTI-HATCH SIMULATIONS FOR SELECTIVE LASER MELTING OF INCONEL 625

4.1 Introduction

The previous chapter presented preliminary modeling for selective laser melting of a single track of metal powder. Although useful for documenting the effects of process parameters and material properties in the resulting temperature distribution, a single-track model does not fully capture the complex nature of the SLM process. In particular, the effects caused by processing of previous adjacent hatches are not observable in a single-track model. Cases in which the hatch overlap (the ratio between hatch distance and beam diameter) is more than one are of special interest, since such a design directly implies that powder bed locations that are never directly scanned by the laser footprint may exist. These areas are of particular importance because incomplete powder fusion may occur, as shown in Figure 4.1.

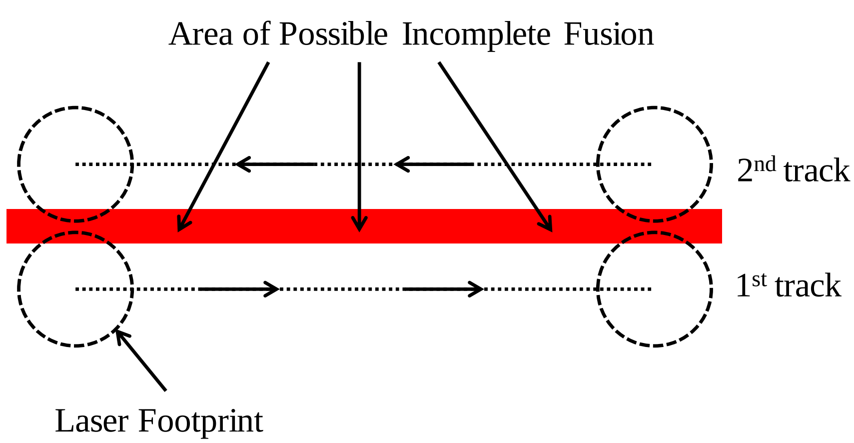

Figure 4.1. Surface view (XY) of two-hatch processing

Further investigation into the effect of process parameters in SLM of Inconel 625 was the subject of collaboration with the National Institute of Standards & Technology (**NIST**), located in Gaithersburg, Maryland, USA. An EOS M270 DMLS machine, similar to the one shown in Figure 4.2, was made available for processing of experimental test coupons. This machine has an IPG Photonics YLR-200-SM laser, which is a single-mode, continuous wave (CW) ytterbium fiber laser with maximum power of 200 W. The footprint of this laser is nearly Gaussian and can be modeled as such for simulation purposes.

Figure 4.2. EOSINT M 270 DMLS machine (EOS GmbH, Electro Optical Systems)

Modeling and experiments were designed in tandem to establish a relationship between process parameters and part quality. This chapter consists of three sections: experimental design, multi-hatch finite element modeling, and 3-D melt pool construction. During the experimental design phase, sets of process parameters to create test coupons were selected from a family of response surface methodology (RSM) designs.

4.2 Experimental Methodology

This study uses a Box-Behnken design to obtain response surface objectives. Response surface methodology (RSM) designs are often used to estimate interaction between factors using a quadratic model. Such designs excel at finding and improving optimal process settings, troubleshooting process problems and weak points, and improving process robustness. The use of RSM for process optimization will be further described in Chapter 5 and Chapter 7.

4.2.1 Selection of Variable Process Parameters

One of the objectives of this study is to understand the effect of energy intensity in the density/porosity of SLM-produced IN 625 test coupons. Energy intensity is a function of laser power (P), powder bed thickness (s), scanning speed or velocity (v_s), and hatch distance (h), as shown in Equation 4.1.

$$E = \frac{P}{v_s \times h \times s} \qquad (4.1)$$

Powder bed thickness is set at s=20 μm. From a practical point of view, it is extremely challenging to modify powder bed thickness by a few microns while maintaining accuracy. Therefore, powder bed thickness is fixed and remains unmodified for every treatment. Laser power, scanning velocity, and hatch distance were selected as the input variables to be modified in each treatment.

4.2.2 Scanning Strategy

In the SLM process, consecutive layers are built by processing powder material with a given bed thickness. As previously mentioned, powder bed thickness will be kept constant at ~20μm for all simulations and experimental designs. However, consecutive layers are processed slightly differently to ensure a robust built. More specifically, stripe orientation changes from layer to layer by a set margin. Two scan strategies are commonly utilized by SLM machines, such as the EOS M270: a) 90º counterclockwise (CCW) rotation, and b) 67º counterclockwise (CCW) rotation between consecutive layers. Figure 4.3 illustrates this concept for the 67º CCW rotation scanning strategy. The red parallel dashed lines indicate stripe boundaries, while the black arrows indicate the back-and-forth hatching action on a stripe.

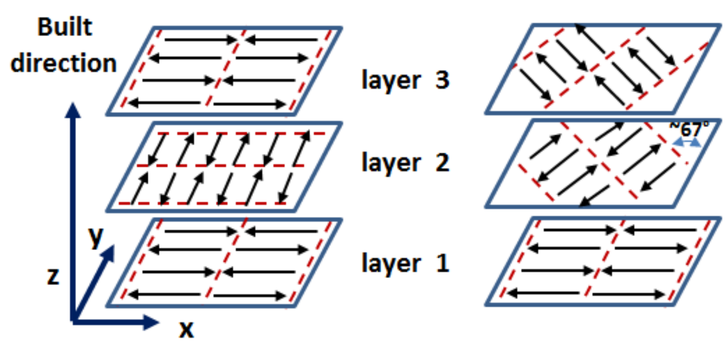

Figure 4.3. Schematic of a stripe scan pattern with 67º CCW rotation between consecutively built layers (Anam et al., 2014)

Scanning direction comes into play when considering multiple layers. For the remaining of this chapter, a single layer of material will be processed. Therefore, scanning strategy will not be observed in the results obtained through the finite-element simulation.

A specific set of process parameters is defined as the "default setting" for SLM of Inconel 625. In this "default setting", P=195 W, v_s=800 mm/s, and h=0.1 mm. The powder bed thickness is set to s=20 μm. This set of parameters was determined in conjunction by EOS, the machine manufacturer, and previous experiments performed by researchers at NIST. As such, these values act as reference points for establishing acceptable values for analysis.

4.2.3 Design of Experiments

An experimental design suitable for application of response surface methodology was selected. There were two limitations that restricted experimental design selection: i) a maximum of 36 test coupons could be fabricated due to size constraints in the build platform of the SLM machine, and ii) hatch distance could only be increased or decreased in intervals of 0.01 mm. The first limitation eliminated the possibility of a three-level factorial design for three factors and two scanning strategies, which would require a minimum of 54 treatments. The second limitation greatly reduced the applicability of Box-Wilson central composite design types, which require high resolution in between levels. Therefore, machine rounding error while input of process settings would have significantly altered the outcome of Box-Wilson type designs. Another alternative, the Box-Behnken design, offered an advantage by requiring comparatively less number of runs while maintaining rotatability. Figure 4.4 shows a schematic of the Box-Behnken design for three factors, in which the treatment combinations are at the midpoints of the edges of the process space cube, as well as at the center.

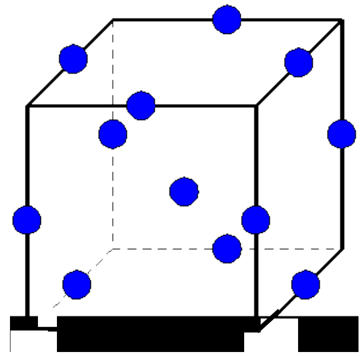

Figure 4.4. Box-Behnken Design (NIST)

The drawback of the Box-Behnken design is that it provides limited capability for orthogonal blocking when compared to central composite designs. Another drawback of this type of design is that it may contain regions of poor prediction quality. However, it is still possible to obtain rational response surface regression models for process input parameters and process response.

Table 4.1. General Structure of Box-Behnken Design for Three Factors

Exp #	**Factor 1**	**Factor 2**	**Factor 3**
1	-1	-1	0
2	+1	-1	0
3	-1	+1	0
4	+1	+1	0
5	-1	0	-1
6	+1	0	-1
7	-1	0	+1
8	+1	0	+1
9	0	-1	-1
10	0	+1	-1
11	0	-1	+1
12	0	+1	+1
13	0	0	0
14	0	0	0
15	0	0	0

The test coupons fabricated using these parameter settings are 16 x 16 mm at the base, and 15 mm in height. The final height of the coupons is less than 15 mm, as wire electrical discharge machining (EDM) is used to separate the built coupons from the platform, and some of the coupon remains attached to the platform. 16 mm was selected as the width and length of the coupons so that each processed layer of powder is composed of four 4-mm wide stripes. Stripe overlap, defined as the area of material in which laser scanning overlaps by consecutive stripes, is 0.1 mm (see Figure 4.5). Therefore, total stripe width is 4.1 mm.

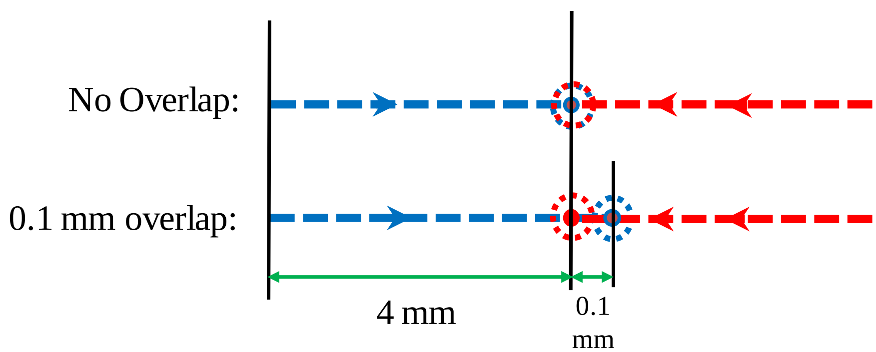

Figure 4.5. Stripe overlap definition

4.2.4 Selection of Process Parameter Sets

Numerical values for each process parameter were selected using the Box-Behnken design outlined previously. The range for each factor was selected so that resulting energy density for all sets fell within the limits calculated by Anam et al. (Anam et al., 2013) that showed acceptable builds. Each process parameter set along with energy intensity values are shown in Table 4.2. Three additional coupons were built at the "default settings" for control purposes.

Table 4.2. Box-Behnken Design of Experiments with three extra coupons at "default settings"

Exp #	Laser Power [W]	Scanning Speed [mm/s]	Hatch Distance [mm]	Energy Density [J/mm^3]
1	169	725	0.10	116.55
2	195	725	0.10	134.48
3	169	875	0.10	96.57
4	195	875	0.10	111.43
5	169	800	0.09	117.36
6	195	800	0.09	135.42
7	169	800	0.11	96.02
8	195	800	0.11	110.80
9	182	725	0.09	139.46
10	182	875	0.09	115.56
11	182	725	0.11	114.11
12	182	875	0.11	94.55
13	182	800	0.10	113.75
14	182	800	0.10	113.75
15	182	800	0.10	113.75
16	195	800	0.10	121.88
17	195	800	0.10	121.88
18	195	800	0.10	121.88

4.3 Multi-hatch Simulation of SLM for Inconel 625

Multi-hatch finite element simulation modeling of SLM is an extension of the physics-based finite element single-track model presented in Chapter 3. Hatch distance, *h*, is introduced to measure the distance between consecutive laser paths, as seen in Figure 4.6. To move the center of the laser from one hatch to the next during time step *i*, the *y*-

coordinate of the laser center is increased by h so that $y_{i+1} = y_i + h$. The laser is turned off for 0.042 ms while transitioning from one hatch to the next. This is accomplished by setting the heat input $\mathbf{q}$ = 0 during this time. The laser off time was measured at the EOSINT M 270 DMLS machine during the SLM IN625 experiments that will be described in Chapter 5.

YZ- and XZ-plane simulations consider a cross-section of the 3-D process space in which the *y*-coordinate is fixed. Therefore, multiple cross-sections must be considered to fully represent melt pool geometry throughout the process. XZ-plane simulations were executed at the center of each hatch, where the depth of the melt pool reaches its maximum value. YZ-plane simulations were ran at the edges of the stripe (*x* =0.05 mm and *x* = 4.05 mm) to observe how melt pool geometry may vary within a single hatch.

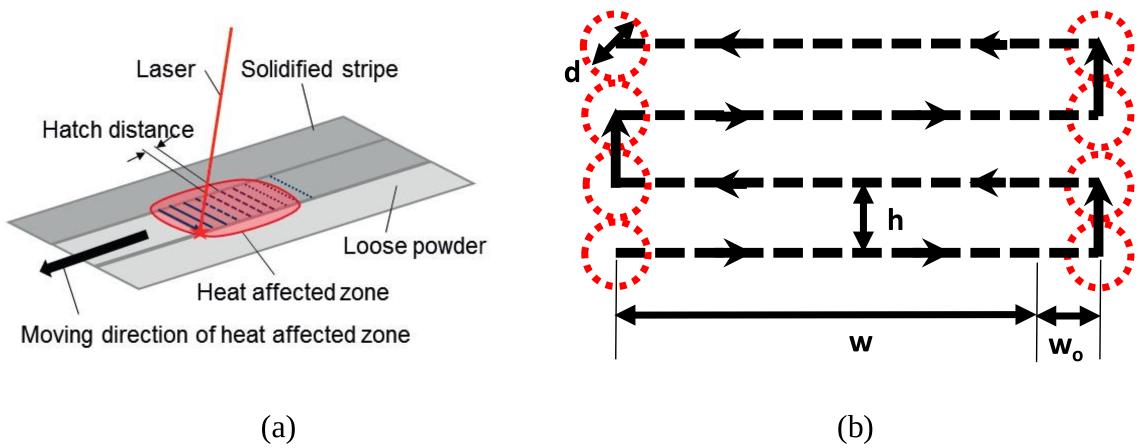

Figure 4.6. Overview of SLM a) process schematic (Krauss et al., 2014) b) XY view of a four-hatch simulation

4.3.1 Finite Element Method problem geometry and numerical limitations

Some modifications to the geometrical problem definition were necessary to more accurately represent the SLM process with finite element simulation modeling. The first modification was to increase mesh dimensions. To obtain the single-track results presented in Chapter 3, a relatively short laser-scanned length of 0.5 mm was considered. In reality, stripe width (the length of one continuously processed hatch) is usually 4 mm for parts whose dimensions exceed this value. Therefore, a new, larger workpiece is required to encapsulate full, multiple hatches. Mesh length (*x*-direction) was changed from 1 mm to 4.5 mm and mesh size in the *y*-direction remained unchanged at 0.6 mm, as shown in Figure 4.7. Single element size could be increased to reduce the number of total elements, but beam diameter and powder size remain in the order of tens of microns, and increasing element size above this threshold would lead to numerical divergence of the temperature solution. Therefore, the mesh used in multi-hatch simulations has the same resolution as the mesh used in single-track modeling, albeit with between 4 and 5 times more elements.

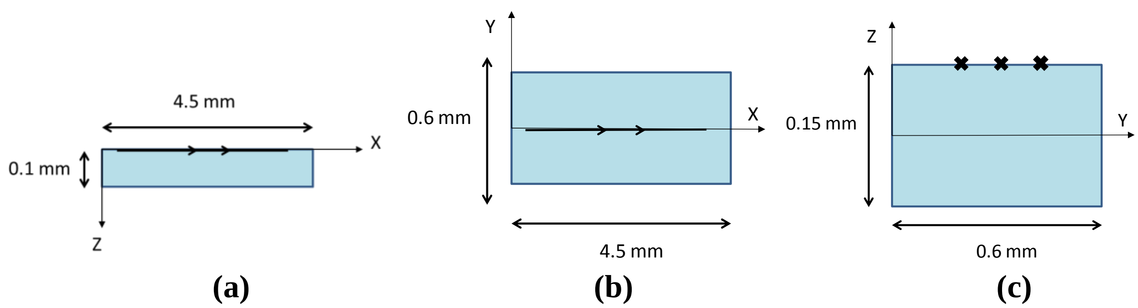

Figure 4.7. Workpiece dimensions in: a) XZ-plane, b) XY-plane, c) YZ-plane

Through a screening experiment while varying mesh size and dimensions, it was determined that the aforementioned described mesh was the largest mesh dimensions that could be solved by the program in a reasonable amount of time while maintaining solution converge. In summary, the main limitation that arises with modeling of multi-hatch SLM processing using the finite element method is the numerical constraint associated with having a large processed area relative to a small laser footprint.

4.3.2 FE Simulation of Single Hatch in XY-plane

A simulation of the SLM process using the finite element model was conducted for a single-track of IN 625 powder, for a stripe width of 4.1 mm. The process parameters and material properties are presented in Table 4.3. Laser power and scanning velocity are the "default setting" parameters for the EOS DMLS machine for processing of IN 625, as previously defined: P=195 W, v_s= 800 mm/s. Hatch distance does not need to be defined in a single-track simulation.

Table 4.3: Simulation parameters for SLM of single-hatch of IN 625

Parameter	**Value**	**Reference**
Liquidus Temperature, T_l [K]	1623	Special Metals DS
Solidus Temperature, T_s [K]	1563	Special Metals DS
Solid Density, ρ [kg/m^3]	8440	Special Metals DS
Latent Heat of Fusion, L_f [kJ/kg]	227	Special Metals DS
Specific Heat, C_p (T) [J/kg K]	$0.2437T + 338.98$	Special Metals DS
Thermal Conductivity, k (T) [W/m K]	$0.015T + 5.331$	Special Metals DS
Reflectivity, R	0.7	NIST
Powder Bed Thickness, s [μm]	20	NIST
Laser Power, P [W]	195	NIST
Spot Size Diameter, d [μm]	100	NIST
Scanning Speed, v_s [mm/s]	800	NIST

Two shapes are considered to represent the laser beam footprint in the XY-plane: a uniform beam shape and a Gaussian beam shape. When a uniform beam shape is utilized, the laser intensity is equally distributed and constant, as shown in Equation 4.2.

$$q(x,y) = (1-R)\frac{P}{\pi r^2} \tag{4.2}$$

Where R is the powder reflectivity, P is the laser power and r is the beam radius. As explained previously, laser intensity is not a function of (x,y) position.

The intensity of a Gaussian laser beam follows a Gaussian distribution in which the peak is at the center of the laser beam, as shown in Equation 4.3.

$$q(x,y) = (1-R)\frac{2P}{\pi w_o^2} e^{-2\left(\left((x-x_o)^2+(y-y_o)^2\right)/w_o^2\right)} \tag{4.3}$$

In Equation 4.3, (x,y) is the location of interest, (x_o,y_o) is the center of the laser beam, and w_o is the waist size of the laser beam, defined as the distance from the center at which the intensity reaches 1/e^2 of its peak value. The intensity profile of the built-in laser in the EOS DMLS machine is not known, but it is closer to a Gaussian than to a uniform distribution. To use the Gaussian distribution, it is assumed that the waist size is equal to the beam diameter. The radial distance from any location on the powder bed to the center of the laser beam is defined as:

$$r(x,y) = +\sqrt{(x-x_o)^2 + (y-y_o)^2} \tag{4.4}$$

The heat intensity is plotted as a function of radial distance from the laser beam center (Figure 4.8).

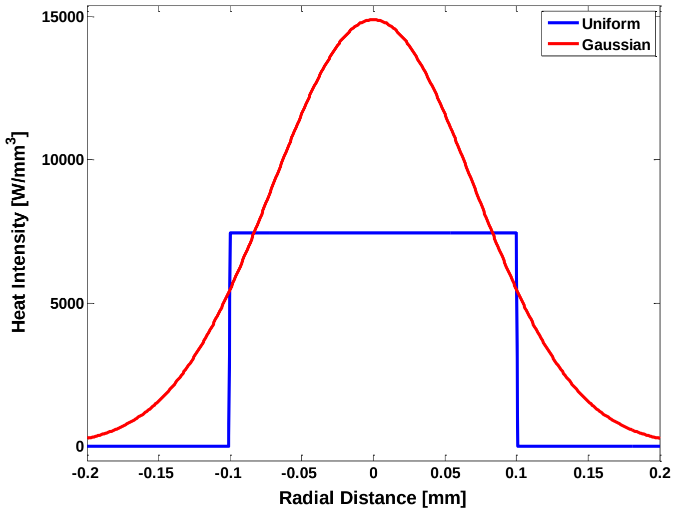

Figure 4.8. Heat Intensity as a function of radial distance from the center of the laser beam for Gaussian (red) and uniform (blue) beam profiles

The FE physics-based model was used to solve for both scenarios to illustrate the difference between the temperature distributions obtained using both laser profiles. To obtain the temperature profile at a specific location of the powder bed, it is sufficient to interpolate using the temperature of the nodes that surround the point of interest. Figure 4.9 shows the temperature vs. time plot for three different locations along the hatch, using a uniform laser beam profile and the process and material parameters given in Table 4.3. Figure 4.10 shows the equivalent temperature vs. time plot for a Gaussian-type laser profile using the same parameters and processing conditions.

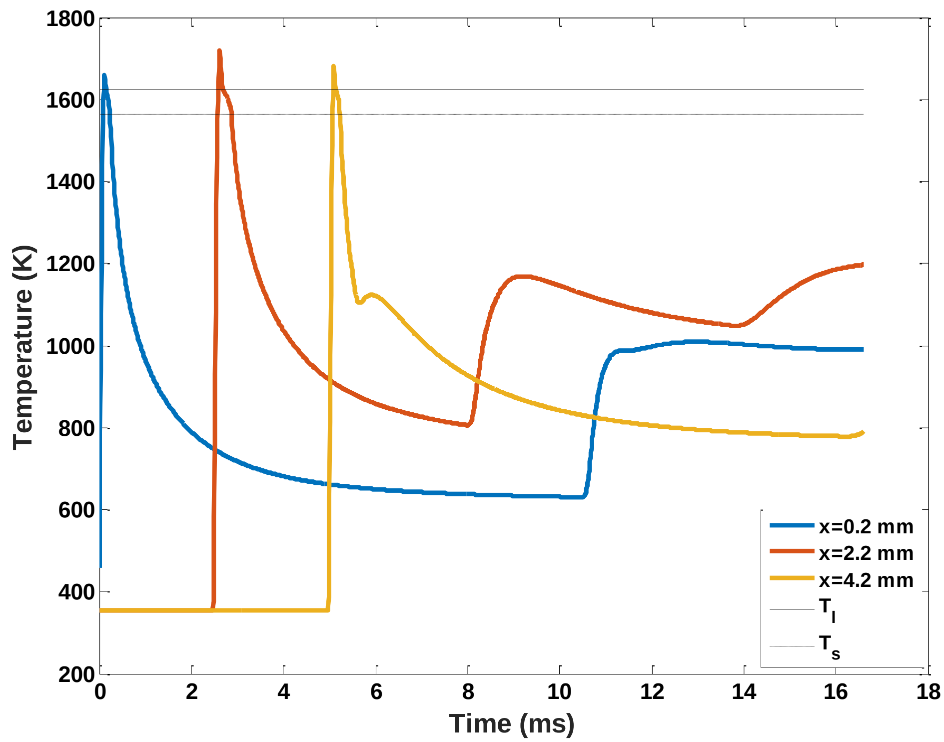

Figure 4.9. Temperature at specific locations along the first processed track (uniform beam).

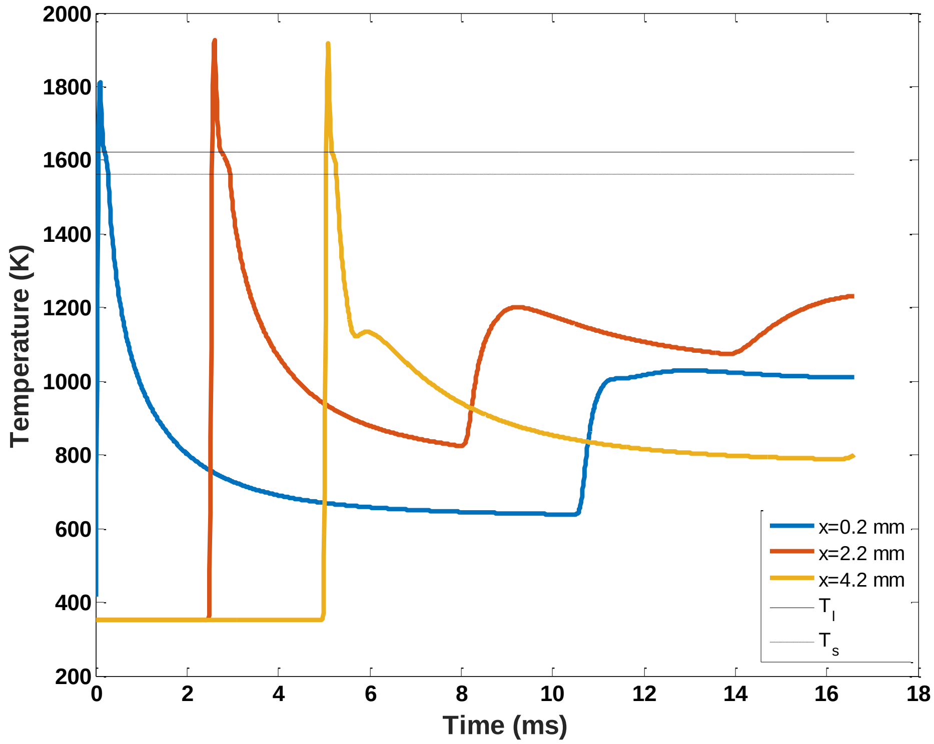

Figure 4.10. Temperature at specific locations along the first processed track (Gaussian beam).

As expected, the peak temperature is higher when using a Gaussian laser beam distribution (1926.8 K) than it is when using a uniform laser beam (1719.7 K). This is due to the higher laser intensity at the center of the beam in the Gaussian case. This ~200 K difference is quite significant, which indicates that establishing the correct laser beam shape is very important for accurate predictive modeling.

4.3.3 Results for three-hatch SLM simulation in XY

The simulation presented in the previous section was extended to the multi-hatch case by adding additional processing at different locations of the powder bed. In this case, a hatch distance of h=0.1 mm is considered. Three hatches are laser-processed in this simulation: the first hatch is processed at y= -0.10 mm, the second hatch at y= 0 mm, and the third hatch at y= 0.10 mm. The starting point of the laser beam center was lowered by 0.1 mm to maintain problem symmetry about the y-axis. All material and process parameters are given in Table 4.3. Only the Gaussian-shaped beam is considered, since this is a more accurate representation of reality. The temperature vs. time plot for the first hatch are identical to that presented in the previous section, Figure 4.10, since processing of the first hatch follows the same steps in both single-hatch and multi-hatch simulation. The only difference is the location of the track in reference to the y-axis (y = -0.1 mm vs. y = 0 mm), which leads to a very subtle difference in temperature due to the size and location of the elements in the mesh. Having a three-hatch simulation also allows the user to look at the temperature distribution along the centerline of the second and third hatch. The peak temperature along the centerline of the second hatch is 2127.3 K for the Gaussian-shaped beam, as seen in Figure 4.11.

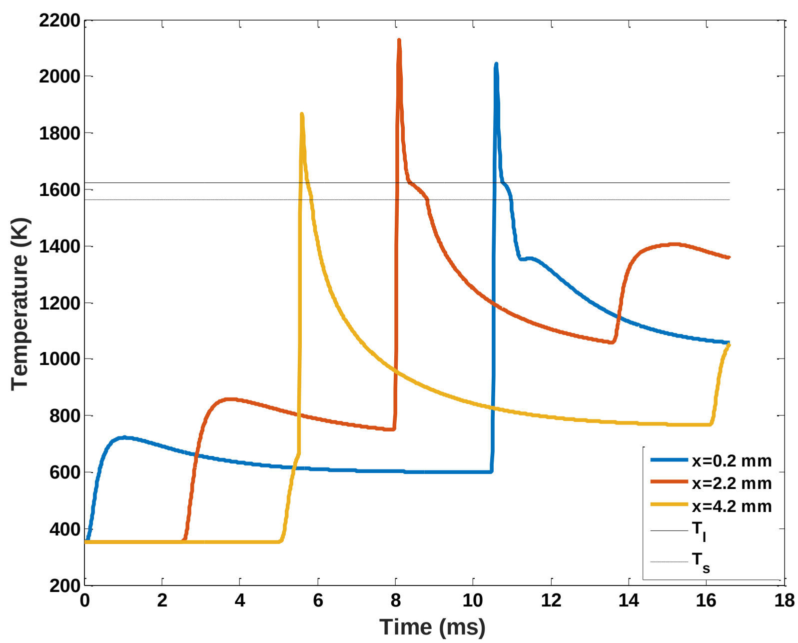

Figure 4.11. Temperature evolution at specific locations on second hatch (y=0 mm).

Even though the same stripe width is being processed under the same conditions, the peak temperature is higher when compared to the first hatch. This is due to heating of the powder bed as a result of processing of that first hatch. Consecutive hatches are close enough to each other, h=0.1 mm, that heat conduction through the powder bed heats the powder particles before they are actually processed. This effect is even more noticeable in the temperature history of the third hatch, as shown in Figure 4.12. Peak temperature reaches ~2300 K in the Gaussian case. Exposing the material to high temperatures above T_l leads to overheating, which significantly increase both the time above liquidus temperature, t_m, and the overall cooling time. By varying the hatch distance, it is possible to control overheating and its effects, as will be studied in Chapter 6.

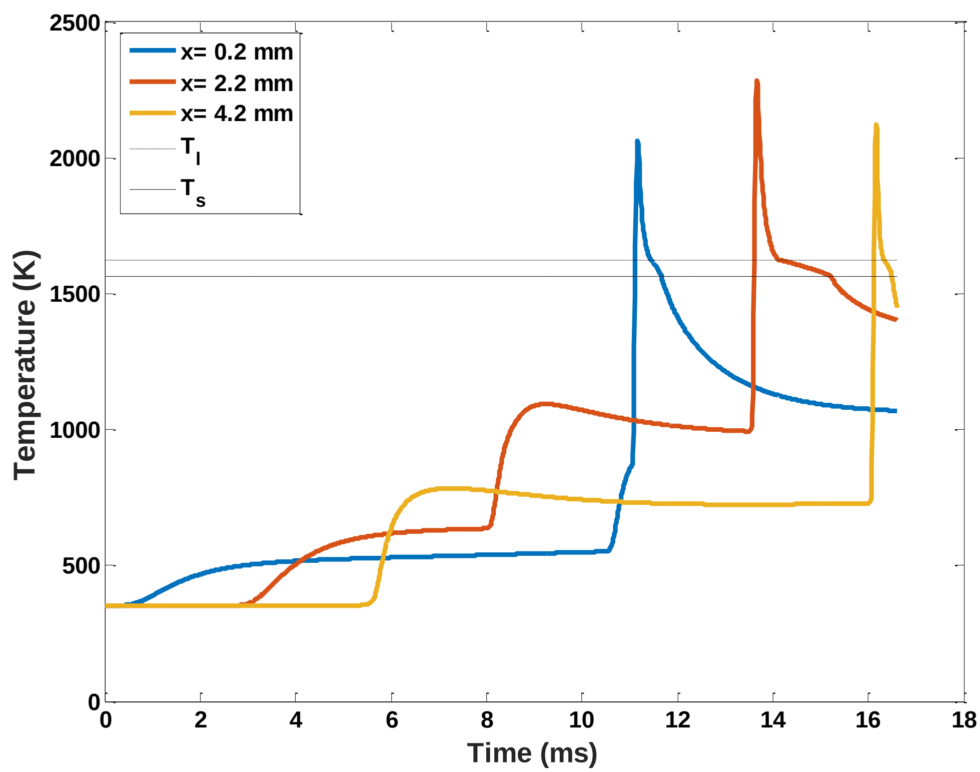

Figure 4.12. Temperature evolution at specific locations on the third hatch (y=0.1 mm).

Studying the hatch centerline gives a concrete measure of the increase in temperature in the region of the powder bed affected by the peak intensity of the laser source. Another location of interest is the line which receives the least amount of heat directly from the source, the midpoint between hatches. In the case of the current three-hatch simulation, there are two such locations: in between the first and second hatch centerline, and halfway between the second and third hatch centerline, as shown in Figure 4.13.

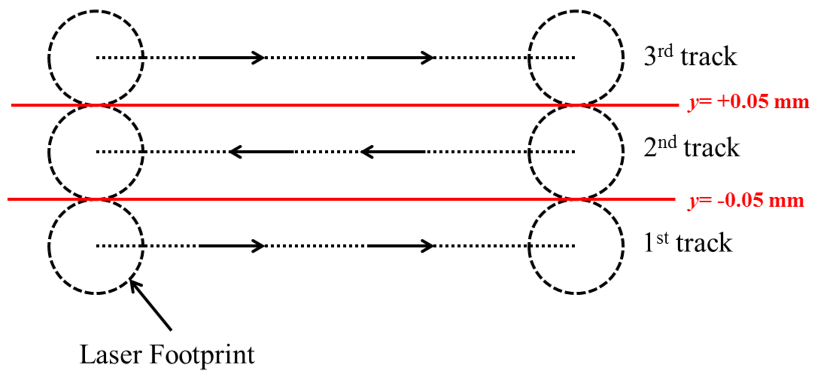

Figure 4.13. Location between hatches where possible incomplete fusion occurs.

At y=-0.05 mm, the halfway point between the first and second hatch, it can be seen that there is incomplete fusion of the powder, as the temperature does not reach the melting temperature of the material (see Figure 4.14).

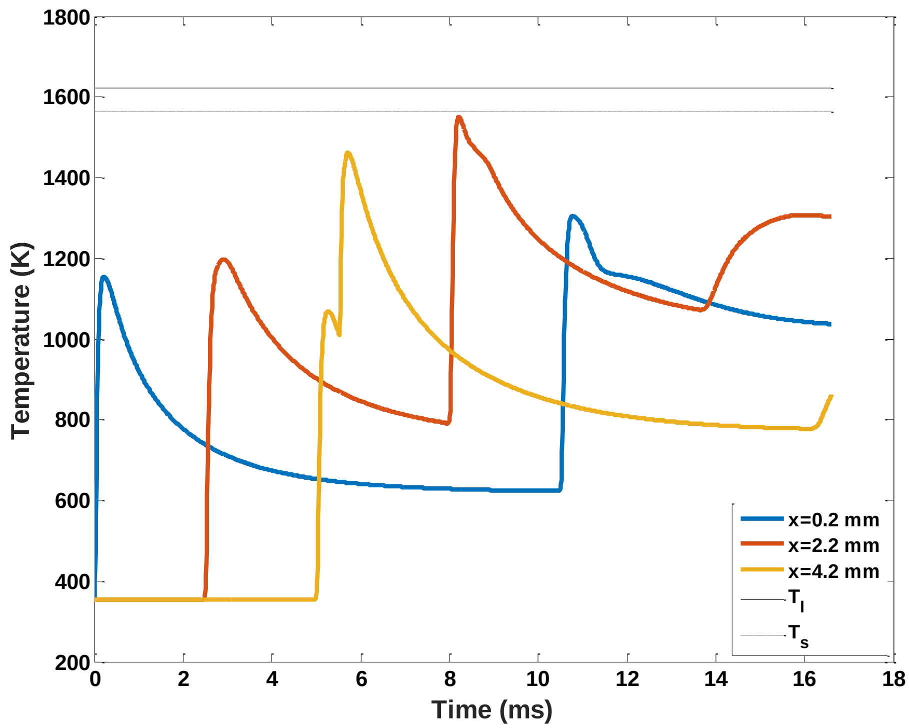

Figure 4.14. Temperature at specific locations between first and second hatch (*y*=-0.05 mm).

This same kind of behavior can be seen between the second and third hatch, where *y*=+0.05 mm. The peak temperature in this region is 1573.8 K when a Gaussian beam is used. Even though the peak temperature reaches the melting temperature of IN625, other locations along this *y*-axis present incomplete fusion, as shown in Figure 4.15.

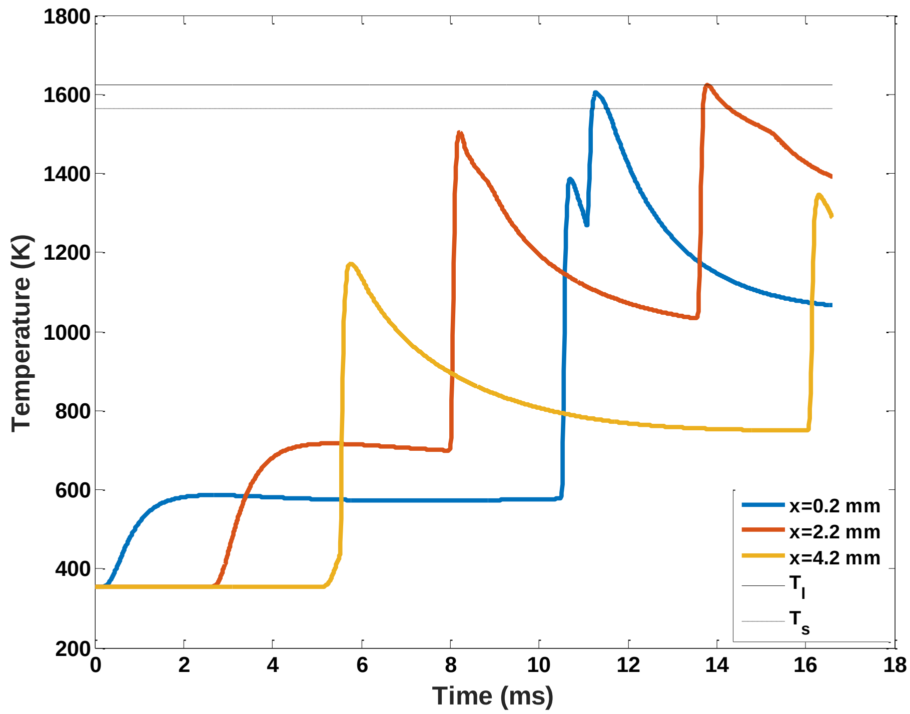

Figure 4.15. Temperature at specific locations between second and third hatch (y=+0.05 mm)

Another way of visualizing the results of the simulation to obtain a more complete understanding is by looking at the temperature profile for the entire powder bed at a specific moment in time. This can be represented in two ways. The first is to create a surface plot showing the temperature profile on the entire powder bed surface, as seen in Figure 4.16.

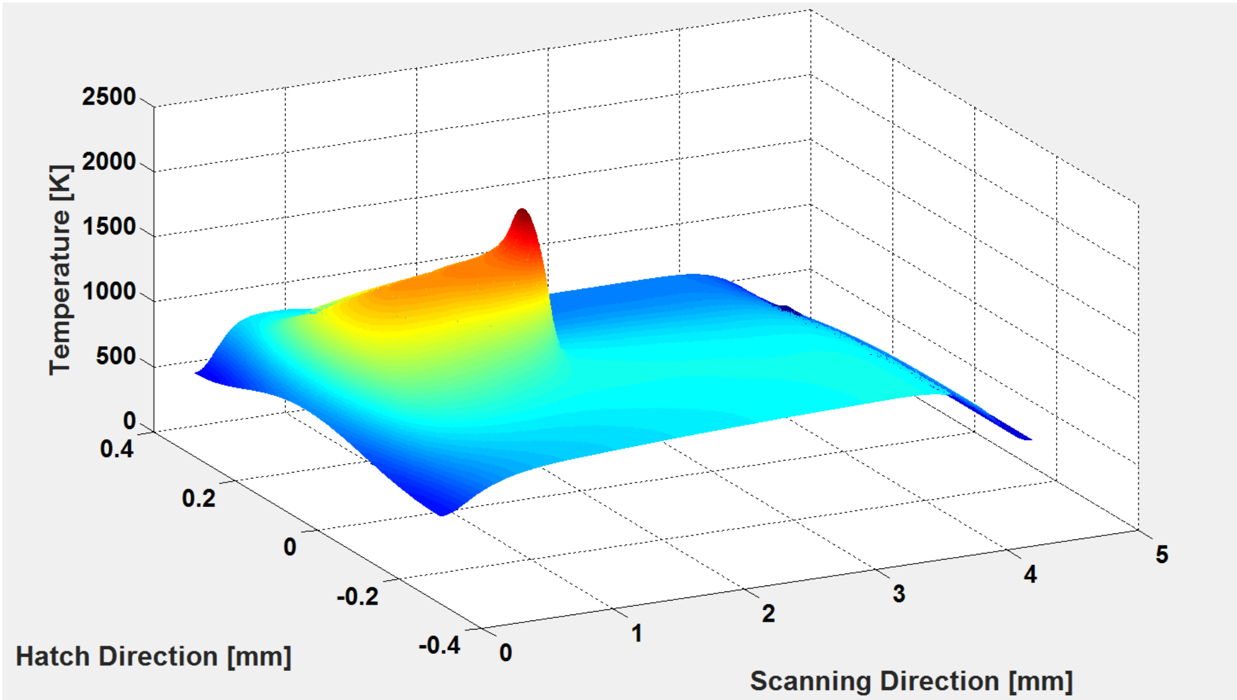

Figure 4.16. Temperature surface plot showing temperature along the powder bed surface

Alternatively, we can create a video that captures the evolution of temperature for the powder bed surface by piecing together contour maps of temperature at different times. The number of total frames in the video is limited by the time step used in the finite element model. Figure 4.17 shows several frames of the temperature evolution video at different steps of the process.

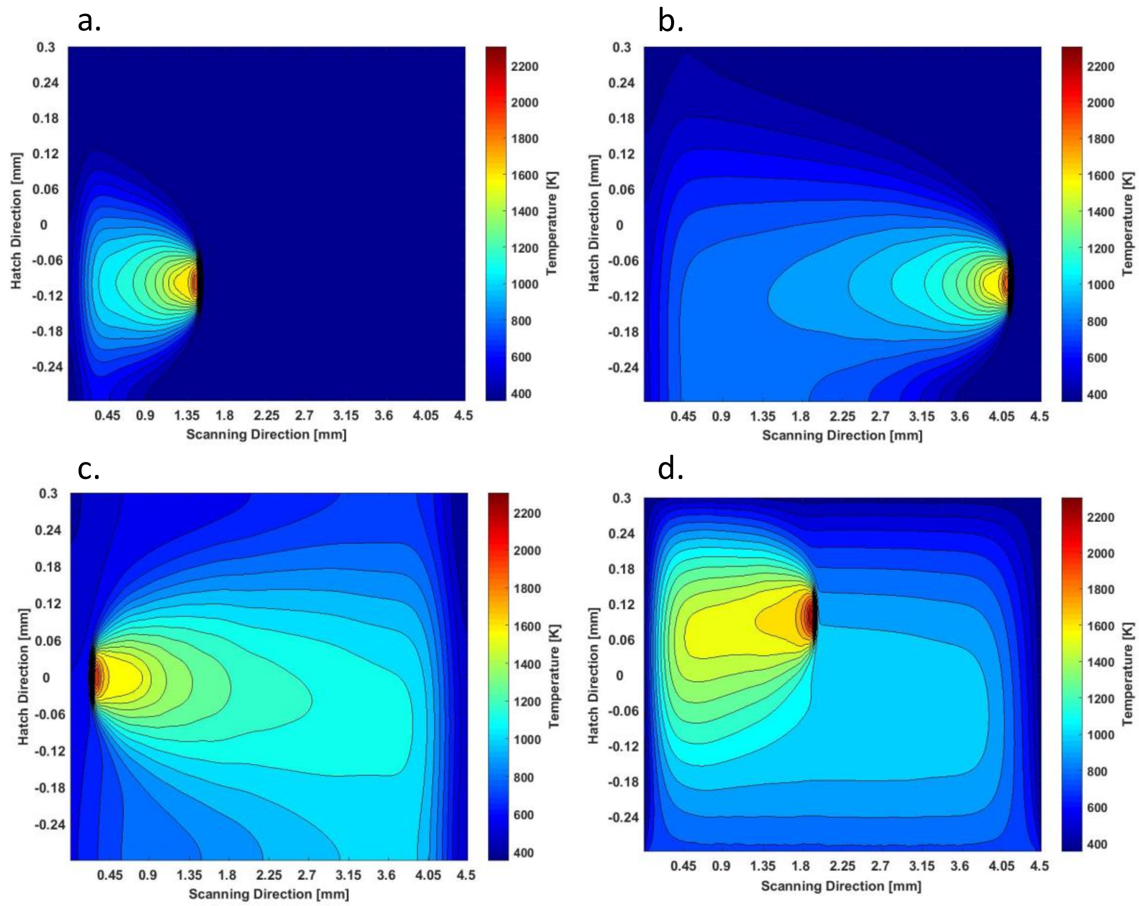

Figure 4.17. Temperature contour at a fixed time: a) t = 1.66 ms, b) t = 49.8 ms, c) t = 10.50 ms, d) t = 13.29 ms.

Instead of using temperature contours to visualize the powder bed, it may be more convenient to divide the workpiece into two clearly distinctive regions based on current temperature, T: i) locations where T is less than the liquidus temperature, indicating that either the material is still in powder form or has re-solidified, and ii) areas where T is greater than the liquidus temperature, indicating full melting of the material. Using this definition, it is possible to properly define the melt pool geometry, as shown in Figures 4.18 - 4.20. In these figures, the liquefied melt pool is shown in red, and each figure shows the melt pool at a different hatch. The increase in melt pool size due to heating of the powder bed by the laser source is clearly observable.

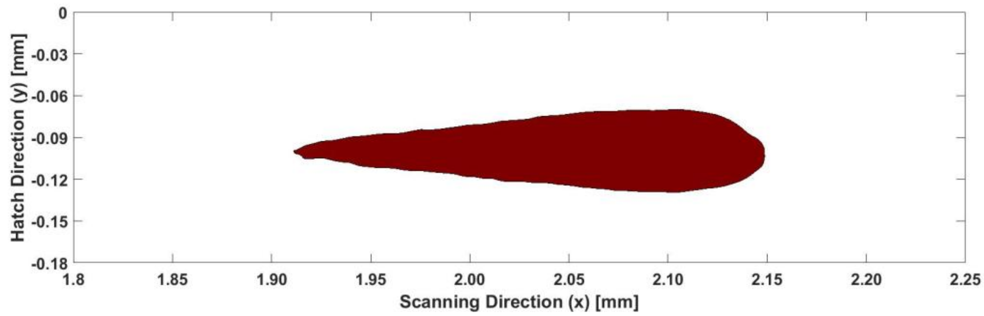

Figure 4.18. XY melt pool contour at a fixed time, first hatch (y = -0.1 mm). t= 2.49 ms.

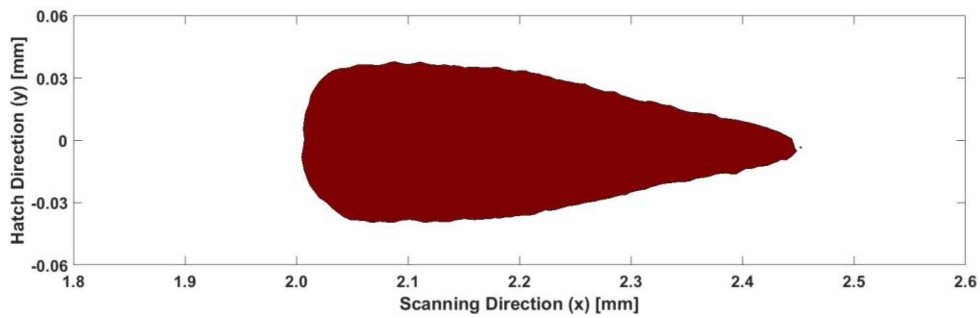

Figure 4.19. XY melt pool contour at a fixed time, second hatch (y = 0 mm). t= 8.32 ms.

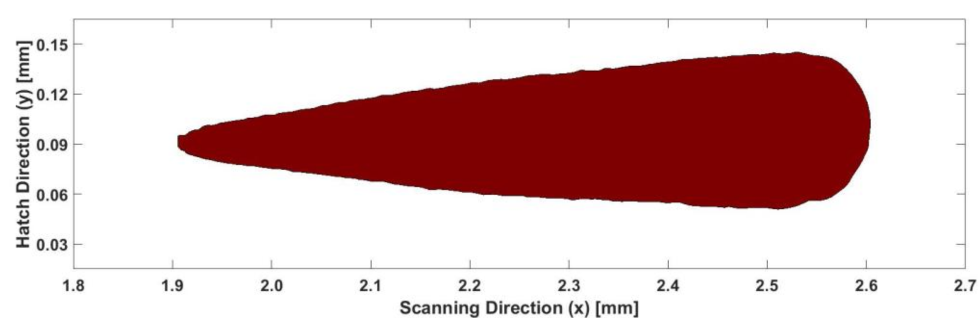

Figure 4.20. XY melt pool contour at a fixed time, third hatch (y = +0.1 mm). t= 14.12 ms.

Using this type of plot, it is easy to calculate the melt pool geometry by measuring length and width at its longest and widest points, respectively. Table 4.4 shows some sample values of melt pool length and width at 6 different positions of the laser beam center, obtained from the XY-plane 3-hatch simulation with “default” process parameters and Gaussian beam profile. It can be seen how melt pool width and depth increase as more heat is introduced by the laser source.

Table 4.4. Melt pool length (x_{MP}) and width (y_{MP}) at 6 different laser locations

	Laser Location		**Melt Pool Dimensions**	
	x [mm]	y [mm]	x_{MP} [μm]	y_{MP} [μm]
1	2.00	-0.10	150	85
2	4.00	-0.10	168	90
3	4.00	0.00	197	137
4	2.00	0.00	180	110
5	2.00	0.10	280	152
6	4.00	0.10	250	123

4.3.4 Results for three-hatch SLM simulation in XZ-plane

Corresponding 2-D temperature distribution simulations in the XZ-plane were executed by considering three cross-sections of the powder bed: one for each of the hatches (y = -0.10 mm, 0.0 mm, and 0.10 mm). To obtain temperature distributions in the XZ-plane, recall that this model considers the result of the XY simulation at the z=0 location as the equivalent of the heat source. Therefore, this simulation uses a profile of temperature vs. scanning direction (x) at a given y from the XY-simulation at each time step. Figure 4.21 provides one such temperature profile at the surface of the powder bed (z=0), for y = +0.10 mm, the second hatch. In this plot, temperature is represented at specific locations along the x-axis, instead of a continuous line. This is because the XZ-plane simulation requires matching the location of the nodes in the top boundary of the XZ-plane workpiece to temperature readings from the XY-simulation in a discrete, nodal manner.

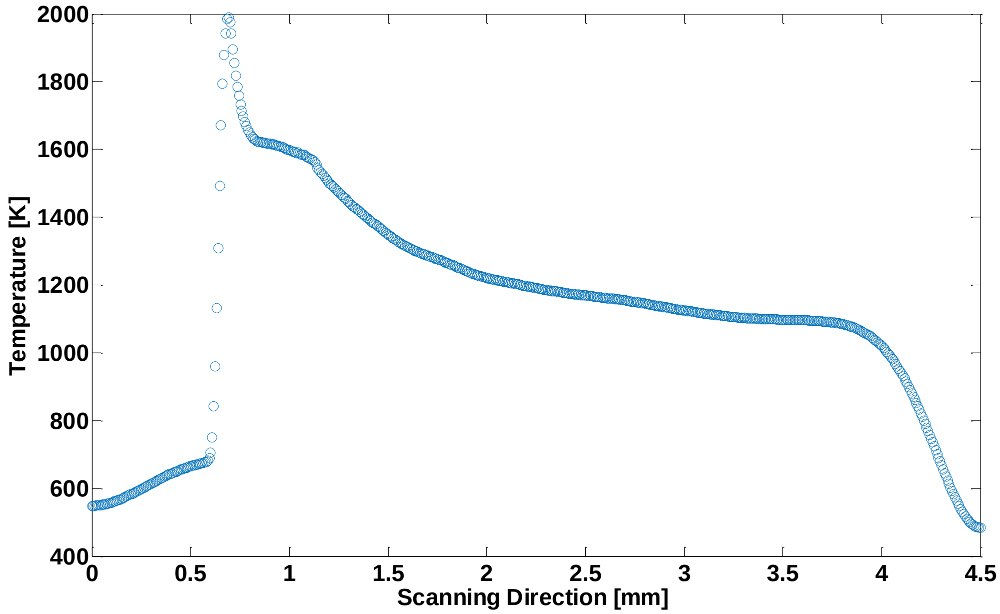

Figure 4.21. Temperature profile at y = +0.1 mm, z = 0. t = 14.12 ms.

Similar behavior is observed in the XZ-plane simulation as was the case in the XY-plane simulation. There is very little melting in the z-direction for the first hatch, with maximum temperature rising and melt pool depth increasing as further hatches are processed (see Figures 4.22-4.24). This is due to the increase in heat contained in the workpiece, which preheats the powder before it is scanned, leading to higher temperatures when scanning occurs.

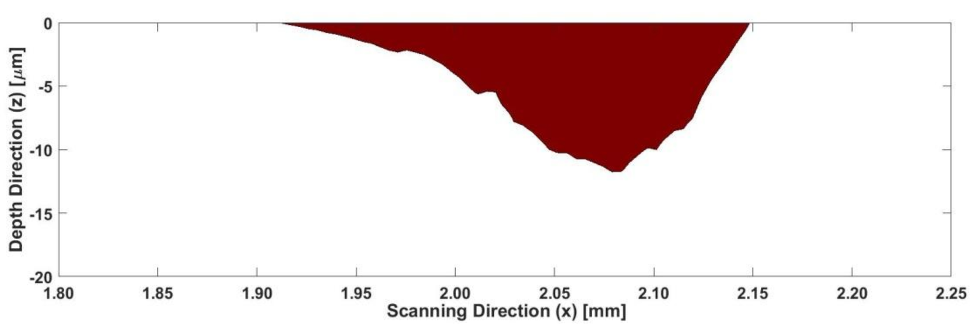

Figure 4.22. XZ melt pool contour at a fixed time, first hatch (y = -0.1 mm). t = 2.49 ms.

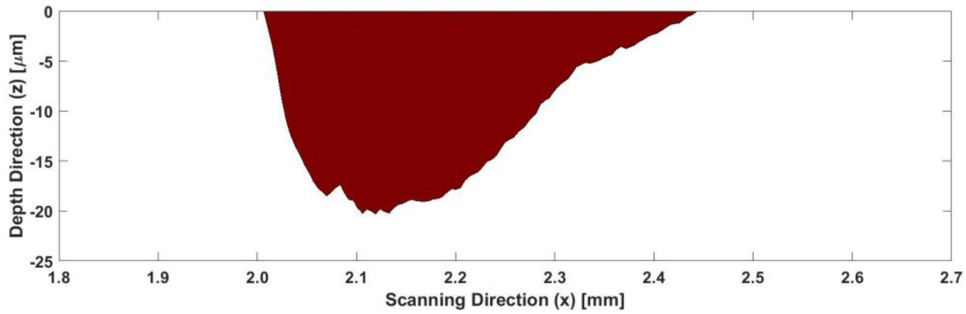

Figure 4.23. XZ melt pool contour at a fixed time, second hatch (y = 0 mm). t = 8.32 ms.

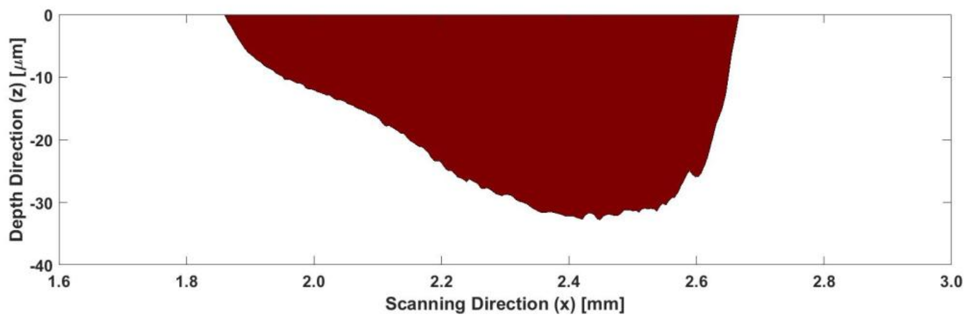

Figure 4.24. XZ melt pool contour at a fixed time, third hatch (y = +0.1 mm). t = 14.12 ms.

Analogously to the XY-plane simulation, a frame-by-frame video showing temperature distribution evolution as multiple hatches were scanned was created to better show how melt pool evolves through the SLM process. Table 4.5 gives melt pool length and depth for the same locations previously discussed in Table 4.4 for the XY-plane simulation.

Table 4.5. Melt pool length (x_{MP}) and depth (z_{MP}) at 6 different laser locations

	Laser Location		**Melt Pool Dimensions**	
	x [mm]	y [mm]	x_{MP} [μm]	z_{MP} [μm]
1	2.00	-0.10	150	5
2	4.00	-0.10	168	10
3	4.00	0.00	197	27
4	2.00	0.00	180	21
5	2.00	0.10	280	40
6	4.00	0.10	250	37

4.3.5 Results for three-hatch SLM simulation in YZ

Corresponding 2-D temperature distribution simulations in the YZ-plane were executed by considering two cross-sections of the powder bed: at each end of the stripes (x = 0.2 mm and 4.3 mm). Because this is a multi-hatch simulation, each of these cross-sections makes it possible to measure melt pool width and depth on each of the three different hatches at different points of the simulation. The time frame of interest is chosen by considering the time step where the peak temperature is the highest, as this corresponds to the moment when the laser beam is heating this section of the workpiece. This model considers the result of the XY simulation at the z=0 location as the equivalent of the heat source to obtain temperature distributions in the YZ-plane. Therefore, this simulation uses a profile of temperature vs. hatching direction (y) at a given x from the XY-simulation at each time step. Figure 4.25 provides one such temperature profile at the surface of the powder bed (z=0), for x = 0.2 mm and t = 11.30 ms. It should be noted that Δt= 0.01 ms. This time step corresponds to the moment when the laser is scanning the third hatch, which explains why the peak temperature is observed near y=+0.01 mm. Temperature is represented at specific locations along the y-axis, instead of a continuous line since YZ-plane simulation requires matching the location of the nodes in the top boundary of the YZ-plane workpiece to temperature readings from the XY-simulation in a discrete, nodal manner which requires interpolation.

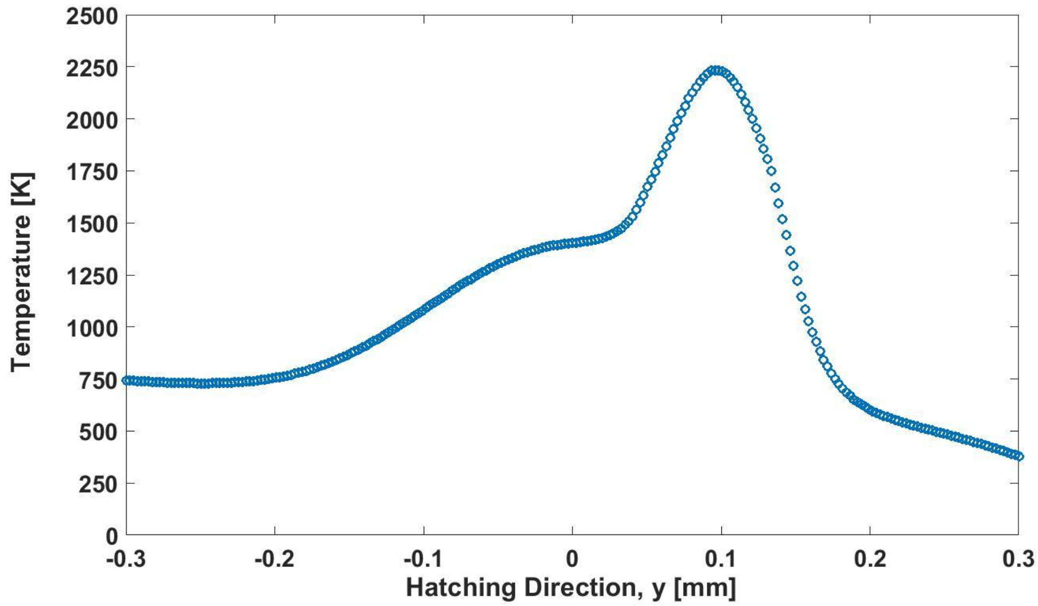

Figure 4.21. Temperature profile at x = 0.2 mm, z = 0. t =11.30 ms.

Similar behavior is observed in the YZ-plane simulation as was the case in the XZ-plane and XY-plane simulations. There is very little melting in both the y-direction and the z-direction for the first hatch, with maximum temperature rising and melt pool width and depth increasing as further hatches are processed (see Figures 4.22-4.24). This is due to the increase in heat contained in the workpiece, which preheats the powder before it is scanned, leading to higher temperatures when scanning occurs.

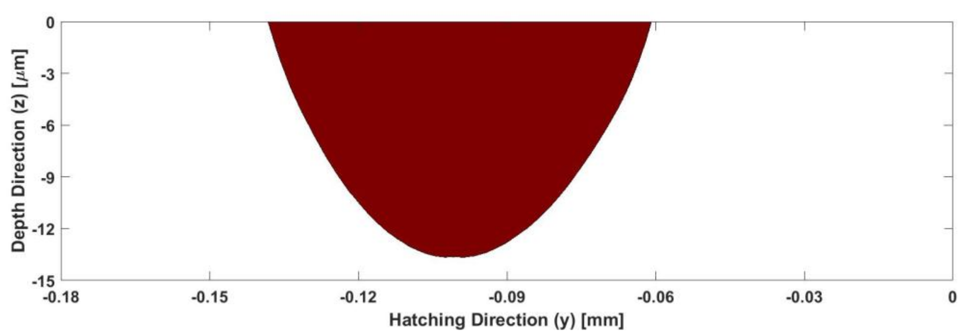

Figure 4.22. YZ melt pool contour at a fixed time, first hatch (x = 4.2 mm). t = 4.85 ms.

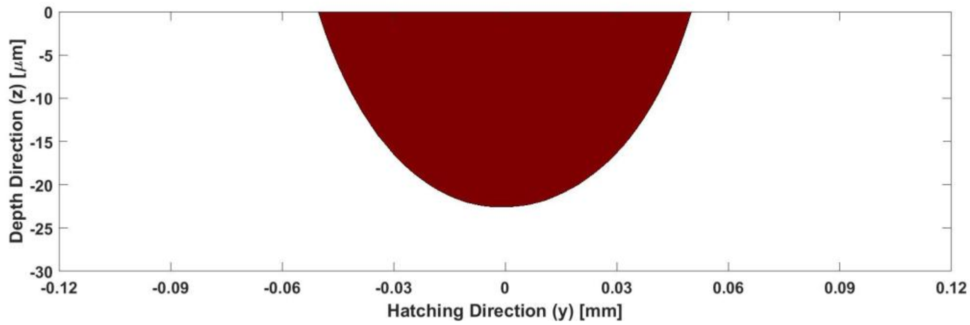

Figure 4.23. YZ melt pool contour at a fixed time, second hatch (x = 0.2 mm). t = 10.50 ms.

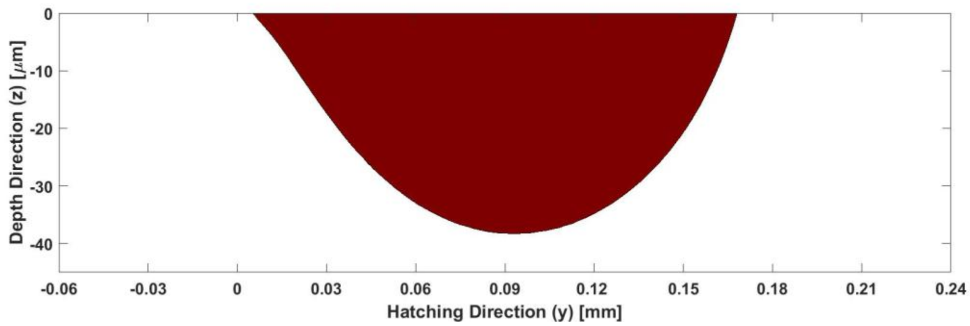

Figure 4.24: YZ melt pool contour at a fixed time, third hatch (x = 0.2 mm). t = 11.30 ms.

Analogously to the XY-plane simulation, a frame-by-frame video showing temperature distribution evolution as multiple hatches were scanned was created to better show how melt pool evolves through the SLM process. Table 4.6 gives melt pool length and depth for the same locations previously discussed in Table 4.4 for the XY-plane simulation.

Table 4.6: Melt pool width (y_{MP}) and depth (z_{MP}) at 6 different laser locations.

	Laser Location		**Melt Pool Dimensions**	
	x [mm]	y [mm]	y_{MP} [μm]	z_{MP} [μm]
1	0.20	-0.10	81	4
2	4.20	-0.10	95	14
3	4.20	0.00	140	28
4	0.20	0.00	108	20
5	0.20	0.10	157	42
6	4.20	0.10	120	35

4.4 Predicted Melt Pool Dimensions

To be able to obtain melt pool geometry in three dimensions, it is necessary to combine the planar melt pool geometry obtained from the XY-plane simulation with one or more simulations of the melt pool in both the XZ-plane and YZ-plane cross-sections. The XY simulation gives a 2-D view of the top surface of the melt pool, while the XZ-plane simulation along the hatch centerline gives a cross-section view of the melt pool at its maximum depth. The dimensions of the melt pool can be estimated by combining the melt pool length and width obtained from the XY-plane simulation with the melt pool length and depth obtained from the XZ-plane simulation. The melt pool width and depth can be cross-checked with the results of the YZ-simulation. Table 4.7 shows the resulting melt pool length, width, and depth obtained by combining the results previously presented in Tables 4.4 and 4.5, and confirmed with Table 4.6. It is evident that the melt pool grows in size as a track being processed in SLM process. It is also evident that the melt pool width and depth is different at the end of the second track and at the beginning of the third track leading to some interesting melt pool type definitions that will be discussed in more detail in Chapters 5 and 6.

Table 4.7. Melt pool length (x_{MP}), width (y_{MP}) and depth (z_{MP}) at various locations along the three-hatch processed as predicted with SLM finite element simulations

	Laser Location		**Melt Pool Dimensions**		
	x [mm]	y [mm]	x_{MP} [µm]	y_{MP} [µm]	z_{MP} [µm]
1	2.00	-0.10	150	85	5
2	4.00	-0.10	168	90	10
3	4.00	0.00	197	137	27
4	2.00	0.00	180	110	21
5	2.00	+0.10	280	152	40
6	4.00	+0.10	250	123	37

4.5 Summary and Conclusions

This chapter focused on introducing preliminary results of physics-based finite element modeling of selective laser melting of IN 625 nickel-based alloy powder. Especial emphasis was made on the approach used to capture the complex nature of this process for multi-hatch processing, and in showing how measurable parameters could be obtained from simulation results for posterior analysis. In particular, it was shown that melt pool geometry can be calculated from the temperature distribution for XY-plane, XZ-plane, and YZ-plane simulations. Melt pool geometry changes from hatch to hatch and also within each hatch, meaning that melt pool dimensions vary while scanning a track. This dynamic behavior is confirmed and formally defined in Chapter 5.

Chapter 5 EXPERIMENTAL ANALYSIS OF ADDITIVELY FABRICATED INCONEL 625 TEST COUPONS VIA SELECTIVE LASER MELTING

5.1 Introduction

The purpose of this chapter is to define and apply a methodology to analyze a set of IN 625 test coupons additively fabricated via SLM using an EOS M270 machine, following the Box-Behnken experimental design described in Chapter 4. These coupons were analyzed with two objectives in mind: i) to determine coupon density, and ii) to determine melt pool dimensions (length, width, and depth) and shape for each coupon. Coupon density, relative to that of bulk Inconel 625, is useful to determine how porous (or non-porous) the resulting parts are. Other analysis, such as microstructural analysis and mechanical testing for strength and hardness are beyond the scope of this thesis.

5.2 Analysis of Experimental Results: IN 625 Test Coupons

Test coupons fabricated with IN 625 nickel-based alloy in powder form were manufactured using an EOS M270 DMLS machine at the National Institute for Standards & Technology (NIST) facility located in Gaithersburg, MD. A total of 36 coupons were fabricated following the Box-Behnken design of experiments presented in Chapter 4. The Box-Behnken design calls for 15 experimental units for a 3-factor analysis, plus an additional 3 experimental units at the "default setting" for a total of 18 experimental units. By implementing two different scanning strategies (90° rotation and 67° rotation layer-to-layer), the total of 36 coupons is obtained. The location of the 36 coupons in the design platform was randomized, and is shown in Figure 5.1. The process parameters associated with each coupon are referenced in Table 5.1.

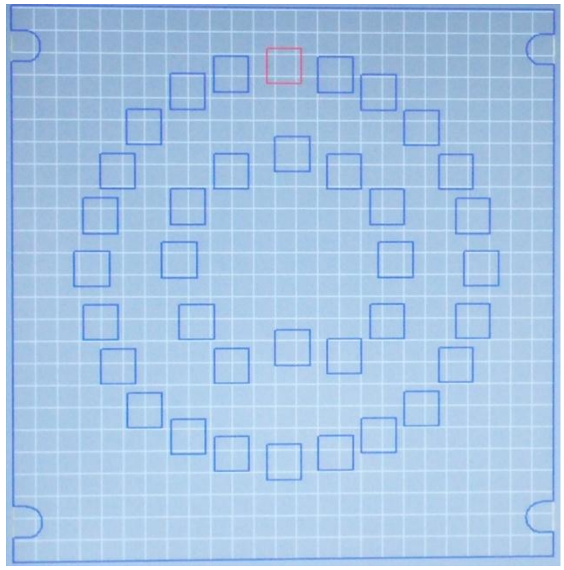

Figure 5.1. Build layout, as shown in the EOS M270 software

Originally, the experimental plan called for all 36 coupons to be built simultaneously. However, an unforeseen limitation in the number of unique process parameter combinations that could be handled in a single build by the SLM machine's software forced the research team to divide the build into two. Scanning strategy was the selected single criterion to divide the build: first, a set of 18 coupons were fabricated using 90º rotation in scanning direction between layers. A second set of coupons, following the same experimental design as the first set, was processed using the default scanning rotation setting of the EOS machine, which is estimated to be ~67º rotation.

Table 5.1. Test coupons and process parameters

Coupon #	Power P [W]	Scanning Velocity v_s [mm/s]	Hatch Distance h [mm]	Scanning Rotation SR [°]
1	169	875	0.10	90°
2	169	725	0.10	67°
3	195	725	0.10	67°
4	195	875	0.10	90°
5	169	800	0.09	67°
6	182	875	0.09	90°
7	182	800	0.10	67°
8	182	725	0.11	90°
9	195	800	0.11	90°
10	182	725	0.11	67°
11	169	875	0.10	67°
12	182	725	0.09	90°
13	195	800	0.09	67°
14	182	800	0.10	90°
15	182	800	0.10	90°
16	195	725	0.10	90°
17	182	800	0.10	90°
18	182	875	0.11	90°
19	195	875	0.10	67°
20	169	725	0.10	90°
21	169	800	0.09	90°
22	182	800	0.10	67°
23	169	800	0.11	90°
24	182	800	0.10	67°
25	195	800	0.11	67°
26	182	875	0.09	67°
27	182	725	0.09	67°
28	182	875	0.11	67°
29	195	800	0.09	90°
30	169	800	0.11	67°
31	195	800	0.10	67°
32	195	800	0.10	67°
33	195	800	0.10	67°
34	195	800	0.10	90°
35	195	800	0.10	90°
36	195	800	0.10	90°

5.2.1 Relative Density of IN 625 test coupons

Both sets of coupons, built with 90º and 67º scanning rotation between layers, were measured and weighed to determine the density of each coupon. The objective is to determine how close to fully dense each coupon is. For this purpose, relative density is defined as shown in Equation 5.1.

$$\rho_{rel} = \frac{\rho_{coupon}}{\rho_{bulk}} \times 100\% = \frac{m/_{V}}{\rho_{bulk}} \times 100\% \qquad (5.1)$$

Where m and V are the mass and the volume of the coupon, respectively, and ρ_{bulk} is the density of solid IN 625. The mass of the coupon was calculated using a weighing scale. The mass was measured 5 times for each coupon, which provides an average and standard deviation. The volume of the coupon was calculated by measuring the length, width, and height of the coupon using a Browne & Sharpe Coordinate Measurement Machine (CMM). Similarly, multiple measurements of each dimension were taken to find the average volume. The bulk density of IN 625 is 8.440 g/cm^3. Relative density values are summarized in Tables 5.2 and 5.3.

Further analysis of the relationship between process parameters and coupon relative density using Response Surface Methodology (RSM) is presented in consequent sections.

Table 5.2. Box-Behnken design of experiments for 90° rotation scan strategy with three extra coupons at "default settings"

Coupon #	Laser Power P [W]	Scanning Velocity v_s [mm/s]	Hatch Distance h [mm]	Energy Intensity, E [J/mm^3]	Relative Density, ρ_{rel} [%]
01	169	875	0.10	96.57	95.23
04	195	875	0.10	111.43	98.30
06	182	875	0.09	115.56	97.03
08	182	725	0.11	114.11	95.97
09	195	800	0.11	110.80	98.47
12	182	725	0.09	139.46	97.14
14	182	800	0.10	113.75	98.10
15	182	800	0.10	113.75	98.05
16	195	725	0.10	134.48	97.50
17	182	800	0.10	113.75	98.13
18	182	875	0.11	94.55	96.50
20	169	725	0.10	116.55	96.38
21	169	800	0.09	117.36	97.50
23	169	800	0.11	96.02	96.60
29	195	800	0.09	135.42	99.01
34	195	800	0.10	121.88	98.64
35	195	800	0.10	121.88	98.53
36	195	800	0.10	121.88	98.69

Table 5.3. Box-Behnken design of experiments for 67° rotation scan strategy with three extra coupons at "default settings"

Coupon Number	Laser Power P [W]	Scanning Velocity v_s [mm/s]	Hatch Distance h [mm]	Energy Intensity, E [J/mm^3]	Relative Density, ρ_{rel} [%]
02	169	875	0.10	96.57	96.00
03	195	875	0.10	111.43	98.70
05	182	875	0.09	115.56	97.40
07	182	725	0.11	114.11	96.17
10	195	800	0.11	114.11	98.52
11	182	725	0.09	139.46	97.29
13	182	800	0.10	113.75	98.21
19	182	800	0.10	113.75	98.19
22	195	725	0.10	134.48	97.74
24	182	800	0.10	113.75	98.30
25	182	875	0.11	94.55	96.75
26	169	725	0.10	116.56	96.52
27	169	800	0.09	117.36	97.91
28	169	800	0.11	96.02	96.78
30	195	800	0.09	135.42	99.23
31	195	800	0.10	121.88	98.86
32	195	800	0.10	121.88	98.75
33	195	800	0.10	121.88	98.81

5.2.2 Calculation of Melt Pool Geometry for IN 625 test coupons

Melt pool width and depth can be measured via digital optical microscopy of the planes that allow a cross-sectional view of the melt pool, i.e. XZ and YZ. Images were taken using a VHX-5000 Digital Microscope, manufactured by Keyence. Image resolution is 1600 x 1200 pixels. The length of the melt pool at any specific time cannot be measured due to the continuous nature of the laser scanning process. Therefore, one single continuous track can be observed in the x-direction, as shown in Figure 5.2. Due to the 90° scanning strategy between layers, XZ and YZ become interchangeable when analyzing melt pool dimensions. Melt pool width and depth can be measured every other layer due to the change in orientation of the scanning direction, which allows a view of the cross-section of the melt pool every other layer.

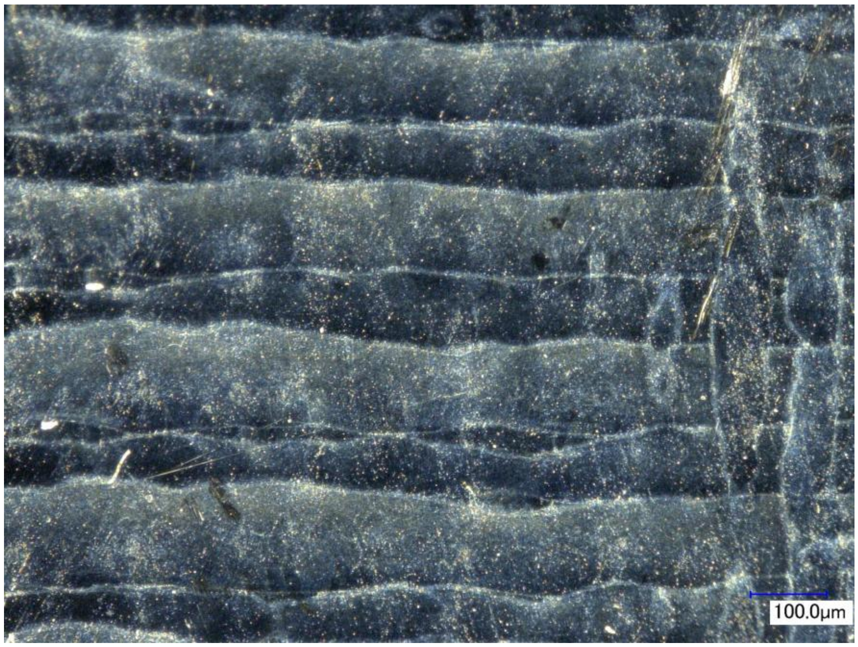

Figure 5.2. XY view of Coupon 35 (P=195 W, v_s=800 mm/s, h=0.1 mm)

This same type of analysis could be replicated for other quantifiable responses, such as melt pool length, width, and depth after completing the measurements in melt pool marks in XY and XZ as shown in Figures 5.3 and 5.4.

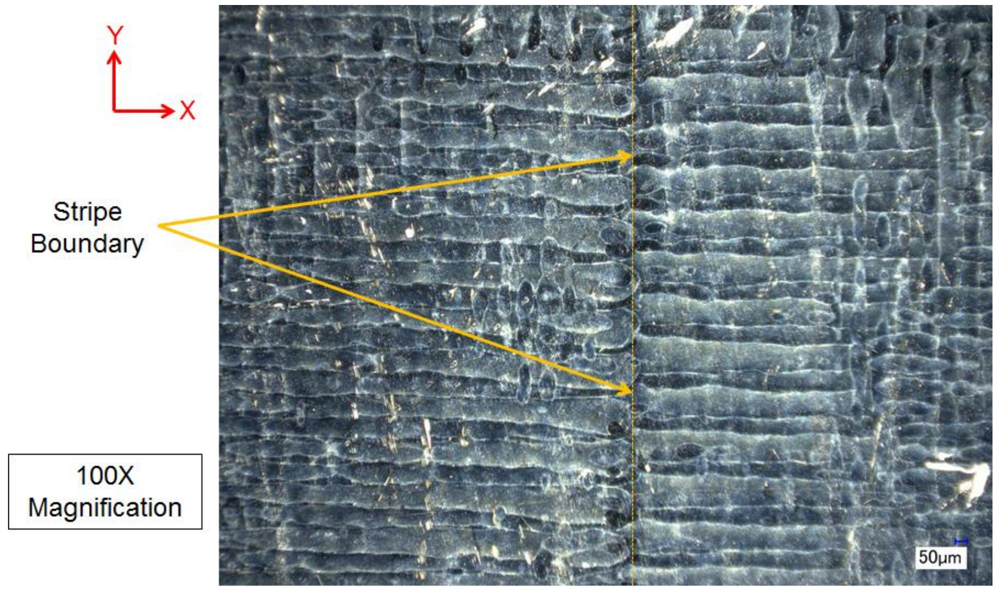

Figure 5.3. A sample optical image of the electro-polished surface of Coupon 35 (XY-plane)

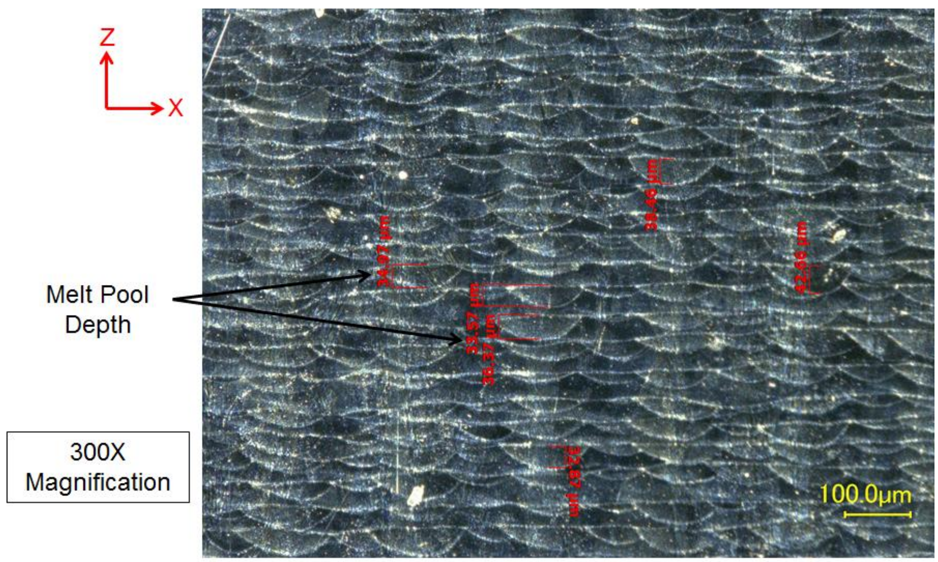

Figure 5.4. A sample optical image of the electro-polished surface of Coupon 35 (XZ-plane)

In order to obtain images where the melt pools could be measured, three of the coupon faces corresponding to XY-, XZ-, and YZ-plane, were electro-polished a total of 50 μm deep. Therefore, melt pool measurements were taken at a cross-section very close to the edge of the coupon (see Figure 5.5).

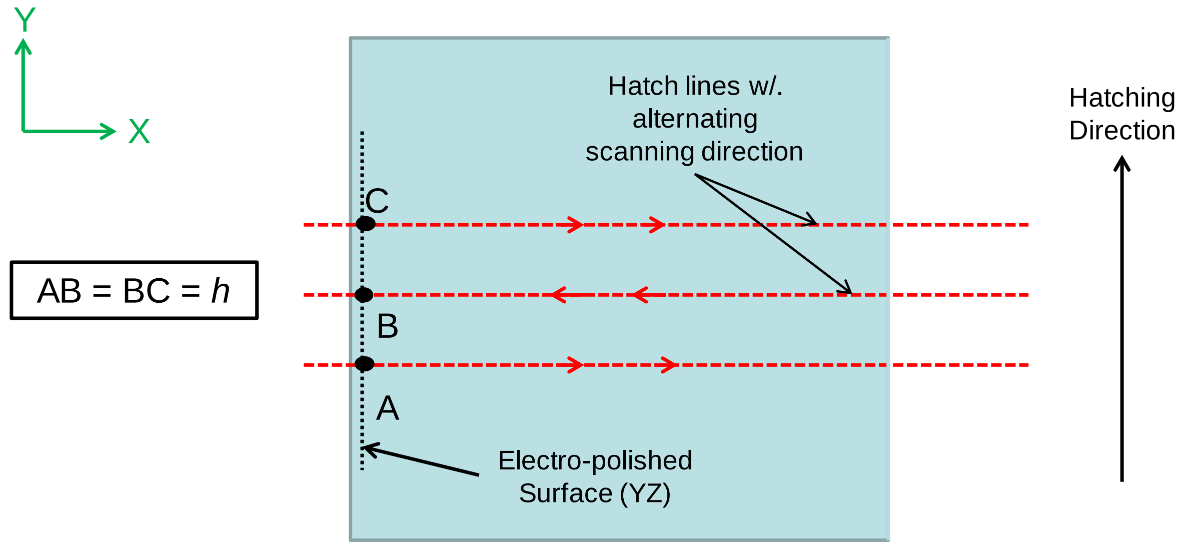

Figure 5.5. Location of electro-polished surface relative to XY-plane

Note that points A, B, and C will represent consecutive melt pools observed in an image taken of the YZ-plane. The distance between A-B and B-C is the same, and equivalent to one hatch distance. However, there is a discrepancy between the time necessary for the laser to arrive at point B from point A, and the time required to reach point C from point B. Assuming that the laser off-time between hatches is 0.042 ms, as measured during coupon building, and the scanning velocity is 800 mm/s for a 4 mm stripe, it follows that:

$$t_{AB} \approx \frac{2w}{v} = \frac{2(4\,mm)}{800\,mm/s} = 10\,ms \tag{5.2}$$

$$t_{BC} \approx laser\ off\ time = 0.042\,ms \tag{5.3}$$

Therefore, it takes approximately 10 ms longer for the laser to reach the same *x*-coordinate location on consecutive hatches, depending on whether this particular location of interest constitutes the beginning or the end of a scanned hatch. This difference in time is considerable, because it allows the powder bed to cool about 10 ms and has an effect on the melt pool dimensions, as shown next.

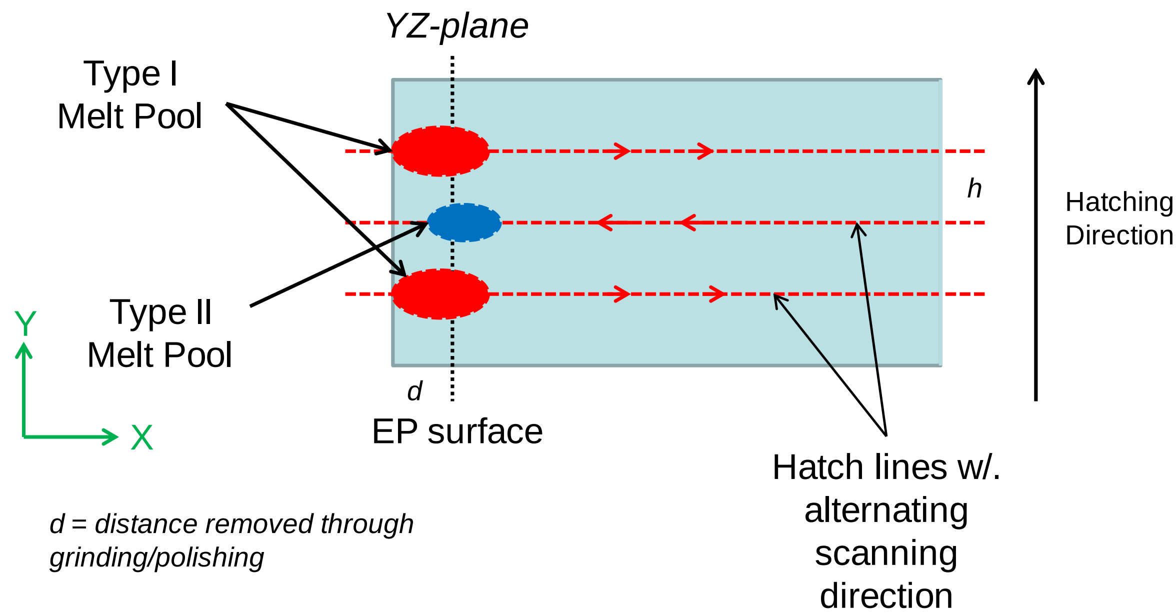

Figure 5.6. Definition of Type I and Type II melt pools

Two different sizes of melt pools were observed due to the characteristics of the laser scanning process described previously: i) a Type I melt pool, where the area being processed (points A and C in Figure 5.5 and Figure 5.6) is still within the heat-affected zone of the previous hatch scanning, and ii) a type II melt pool, where the area currently being processed (location B in Figure 5.5 and Figure 5.6) is no longer affected by the heat from the laser scanning of the previous hatch.

Type I and Type II melt pools can be formally defined as follows: define an YZ-plane at a specific *x*-location (*x* is fixed). The time elapsed between two consecutive passes of the laser footprint through this plane will vary as a function of *x*. For locations very close to the stripe boundaries, the difference in time elapsed is the largest. This leads to different sized melt-pools along this particular YZ-plane. The size of the melt pool will depend on the scanning direction. Melt pools at a location at the beginning of the stripe will be larger (Type I) and melt pools at a location at the end of a processed stripe will be smaller

(Type II). The difference in melt pool sizes can be attributed to the presence of a heat-affected zone (HAZ) and rapid cooling times. Digital microscopy imaging and thermal camera imaging were then utilized to corroborate these results.

5.2.2.1 Methodology for Melt Pool Width and Depth measurements

A digital optical microscope was utilized to obtain images of the electro-polished surfaces from which the melt pool width and depth were measured. All the images utilized for analysis were captured in 1600 x 1200 pixel resolution and 500X magnification. The images were measured using a built-in scale provided by the optical microscope, as seen in Figure 5.7.

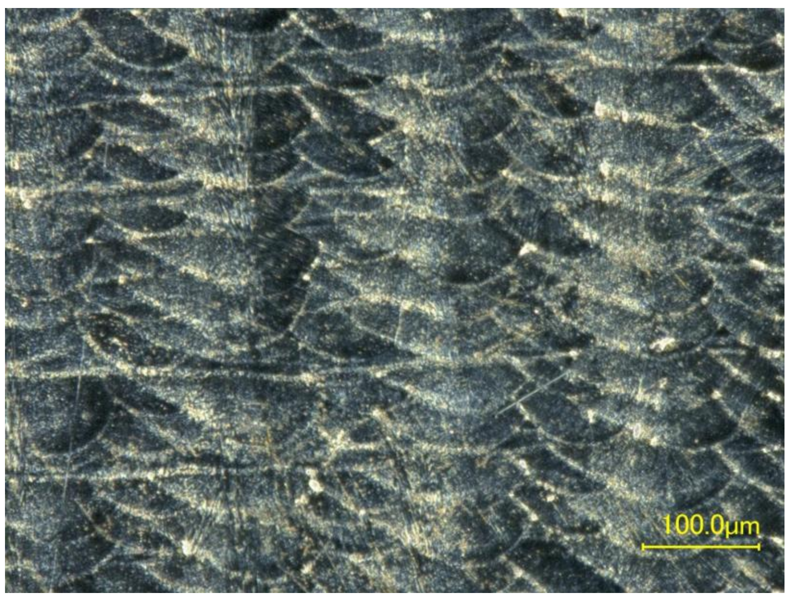

Figure 5.7. Unprocessed image of XZ-face of Coupon 29

First, the number of pixels that makes up the length of the scale (100 μm) was counted to obtain a pixel-to-μm conversion ratio. Then, the width and depth of the melt pools were measured by drawing color-coded lines on the images and counting the number of pixels spanned by each individual line. Then, the measurements were converted to micro-meters using the scale. The width of Type I and Type II melt pools were marked using red (RGB = 255-0-0) and blue (RGB = 0-0-255), respectively (see Figure 5.8).

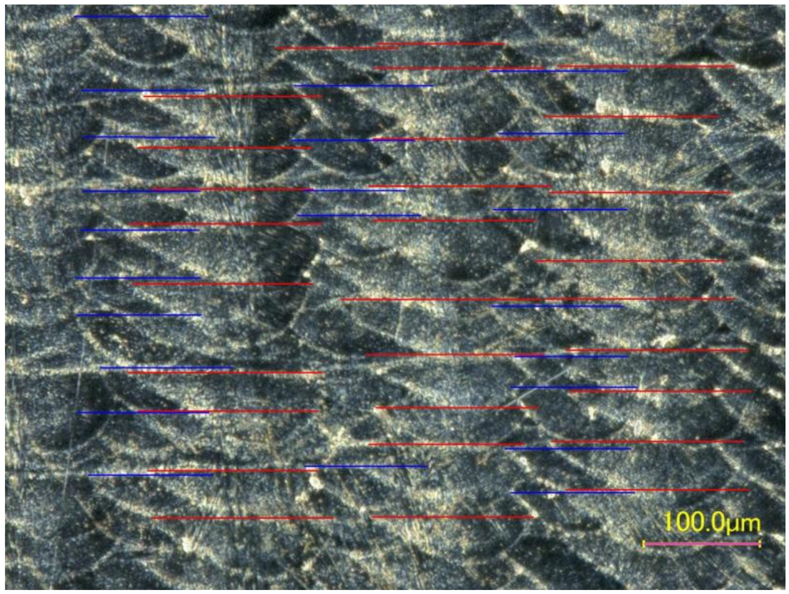

Figure 5.8. Marked melt pool width of Coupon 29 (XZ-plane)

The depth of Type I and Type II melt pools were marked using green (R-G-B = 0-0-255) and cyan (R-G-B = 0-0-255), respectively (see Figure 5.9). A Matlab computer code was then used to automatically detect the colored lines and obtain the width and depth of each individual marked melt pool using the scale as a reference.

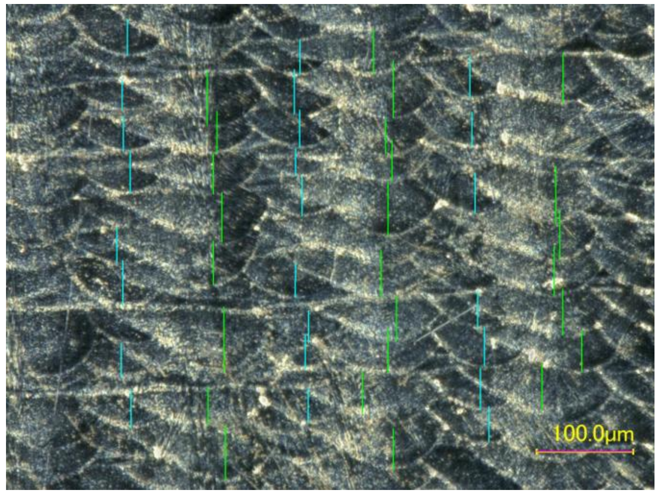

Figure 5.9. Marked melt pool depth of Coupon 29 (XZ-plane)

Multiple optical images of each coupon were analyzed following this methodology, and the results were compiled to obtain an average melt pool width and depth, with corresponding standard deviation. Figure 5.10 shows a histogram for melt pool width and depth for Coupon 29.

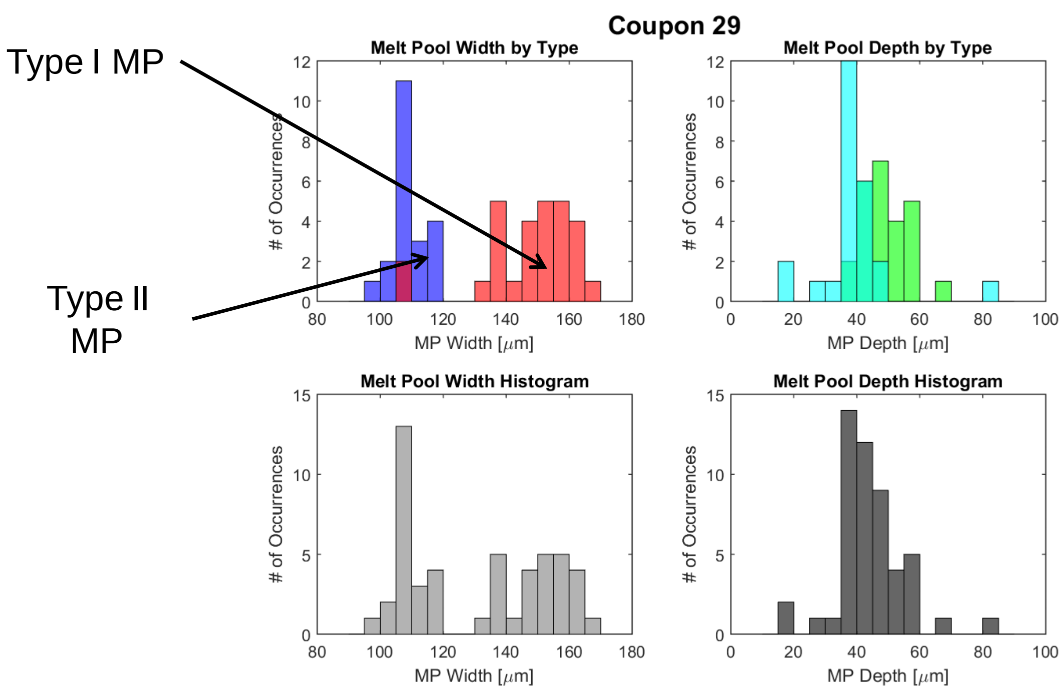

Figure 5.10. Histogram of melt pool depth and width for Coupon 29

From the histogram, it is clear that melt pool width changes considerably based on the type of melt pool. Melt pool depth also varies slightly between types. Table 5.4 summarizes all melt pool width and depth by type for each coupon, with the respective standard deviation. A complete list of measured coupon images and histograms can be found in Appendix A. Additionally, the effect of process parameters on melt pool dimensions can be analyzed via main effect plots, as shown in Figure 5.11, Figure 5.12 and Figure 5.13.

Table 5.4. Summary of melt pool dimensional measurements

	Melt Pool Width Avg [μm]		**Melt Pool Width Std Dev. [μm]**		**Melt Pool Depth Avg [μm]**		**Melt Pool Depth St. Dev. [μm]**	
Coupon	**Type I**	**Type**	**Type I**	**Type**	**Type I**	**Type**	**Type I**	**Type**
01	134	92	12	9	35	31	6	5
04	170	111	25	7	49	46	7	8
06	149	101	17	16	45	38	7	5
08	153	107	25	12	48	39	8	9
09	143	109	13	9	44	42	7	7
12	134	113	18	11	45	36	7	10
14	132	109	11	10	44	38	7	6
15	128	105	12	11	40	33	9	6
16	152	114	13	11	52	42	18	10
17	143	112	10	7	48	38	6	7
18	134	110	13	15	47	32	7	7
20	159	106	13	8	51	42	8	6
21	154	107	14	9	47	45	8	9
23	150	96	28	11	43	33	6	6
29	149	103	15	16	49	39	7	12
35	155	112	11	15	50	41	6	7

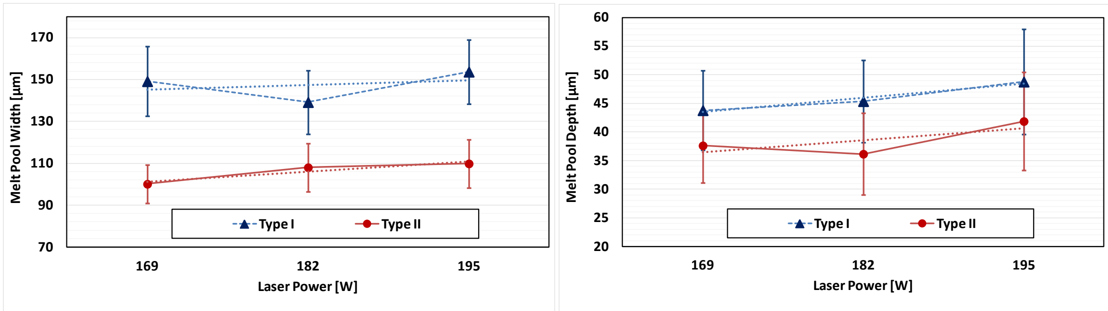

(a) **(b)**

Figure 5.11. Effect of laser power on melt pool (a) width, (b) depth

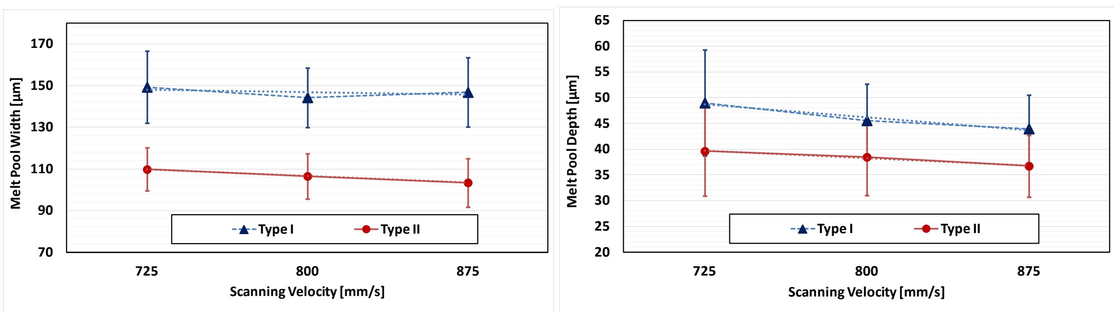

(a) **(b)**

Figure 5.12. Effect of scanning velocity on melt pool (a) width, (b) depth

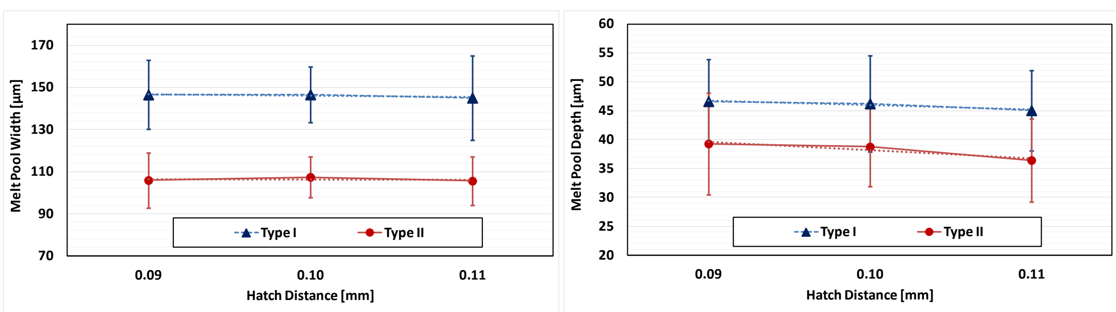

(a) **(b)**

Figure 5.13. Effect of hatch distance on melt pool (a) width, (b) depth

One way to analyze these results is to consider the behavior of melt pool depth and width as a function of laser energy intensity. We define energy intensity as the amount of energy applied to the powder bed per unit volume. Energy intensity is then a function of laser power, scanning speed, layer thickness, hatch distance, as shown in Equation 5.4.

$$E = \frac{P}{v_S \cdot h \cdot s} \qquad (5.4)$$

Using this definition, it is possible to generate plots of melt pool width and depth as a function of energy intensity, as shown in Figure 5.14.

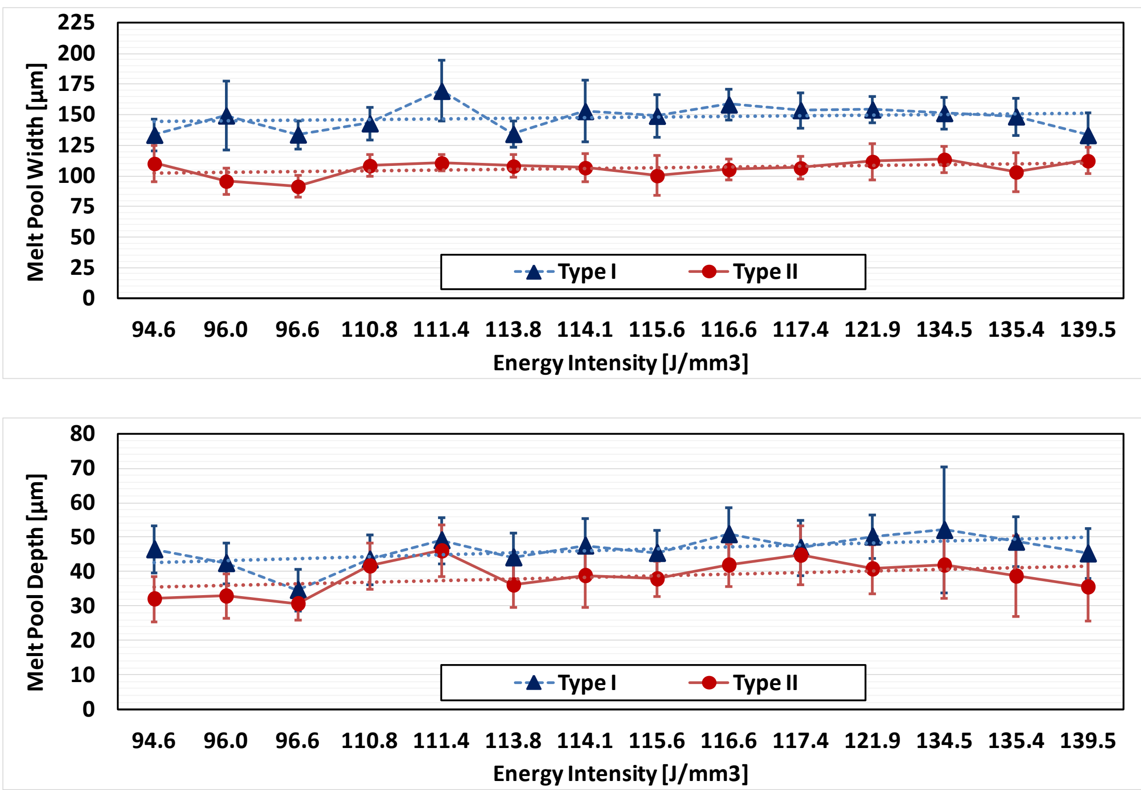

Figure 5.14. Effect of process energy intensity (E) on melt pool a) width, b) depth.

The trend lines on Figure 5.14 show that melt pool size increases slightly as energy intensity increases. This behavior is more noticeable in melt pool depth than in melt pool width. Furthermore, there is no appreciable difference in behavior between Type I and Type II melt pool size when considering energy intensity as an all-inclusive factor.

Another method to analyze melt pool size is to keep one of the three factors (laser power, scanning speed, or hatch distance) constant and study how melt pool width and depth change as a factor of the other two. Figure 5.15 and Figure 5.16 show how melt pool width and depth, respectively, vary as a function of scanning speed for the three laser power levels considered in the Box-Behnken experimental design.

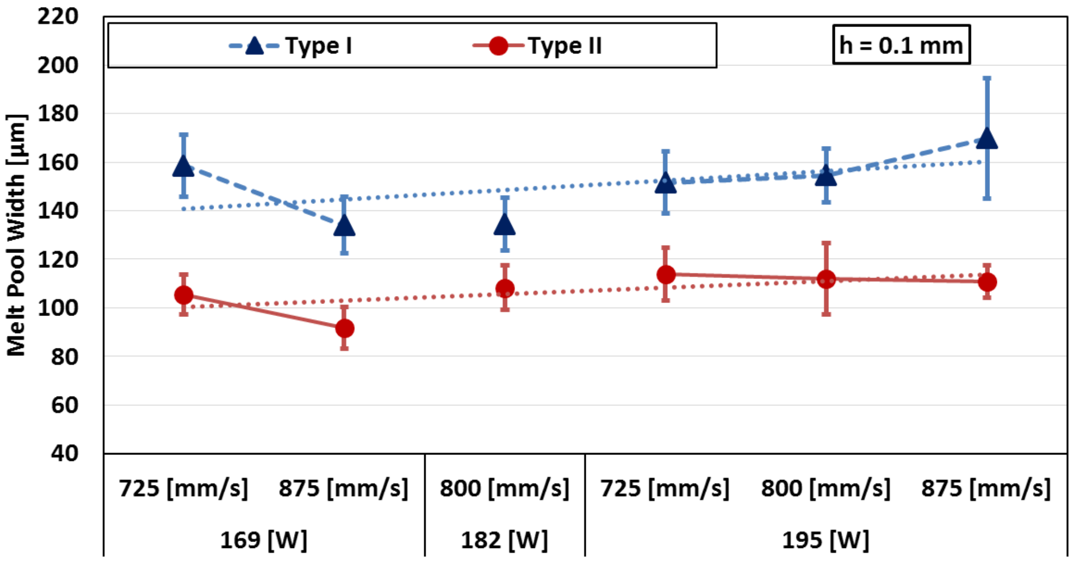

Figure 5.15. Effect of scanning speed on MP width for three laser power levels (h = 0.1 mm)

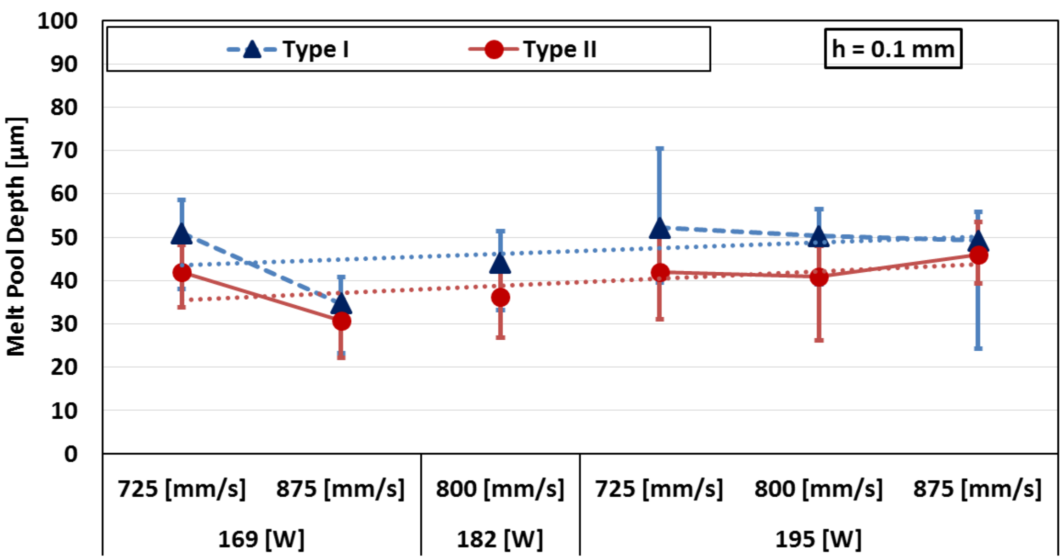

Figure 5.16. Effect of scanning speed on MP depth for three laser power levels (h = 0.1 mm)

The same data points, for test coupons additively fabricated with hatch distance h = 0.1 mm, can be utilized to analyze melt pool width and depth as a function of laser power for three levels of scanning velocity (Figure 5.17 and Figure 5.18). These figures, along with Figure 5.15 and Figure 5.16, indicate that melt pool size increases with increasing laser power and decreasing scanning speed. However, the behavior is clearly non-linear.

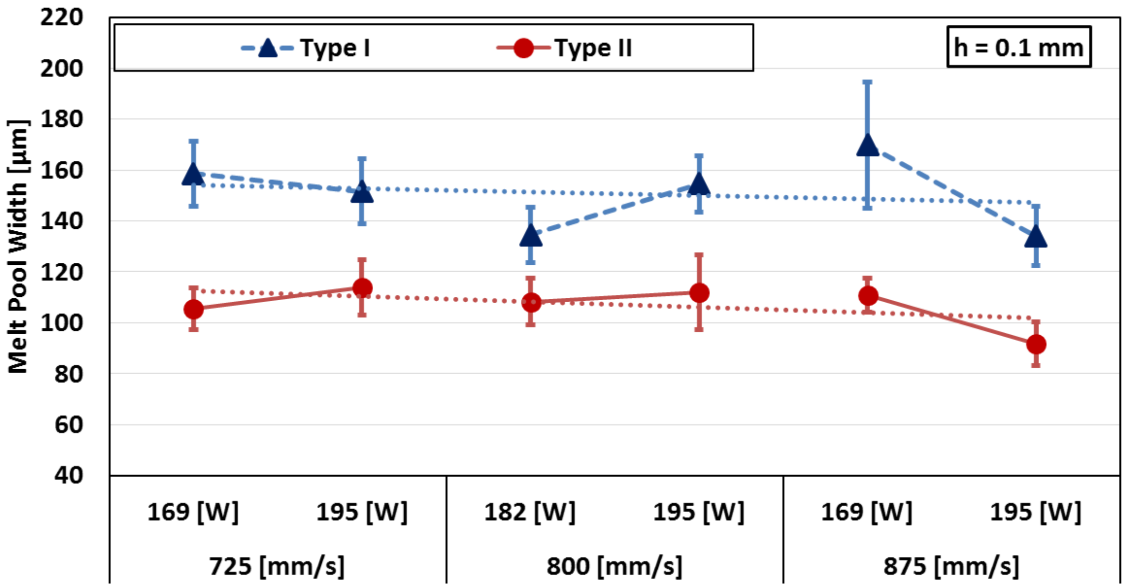

Figure 5.17. Effect of laser power on MP width for three scanning speed levels (h = 0.1 mm)

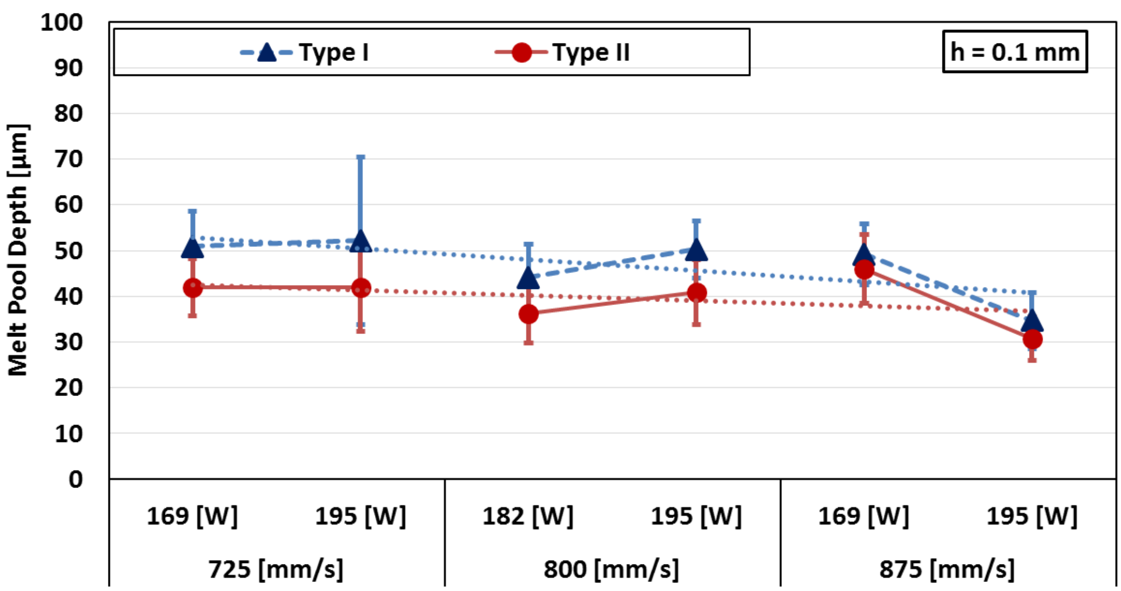

Figure 5.18. Effect of laser power on MP depth for three scanning speed levels (h = 0.1 mm)

Additionally, the melt pool width and depth measurements taken indicate that there is a large difference between Type I and Type II melt pool width (approx. 50 μm). This is in contrast with the difference between Type I and Type II melt pool depth, which does not appear to vary significantly (approx. 10 μm). Figure 5.19 and Figure 5.20 show how melt pool size varies for coupons fabricated with scanning speed, v_s = 800 mm/s.

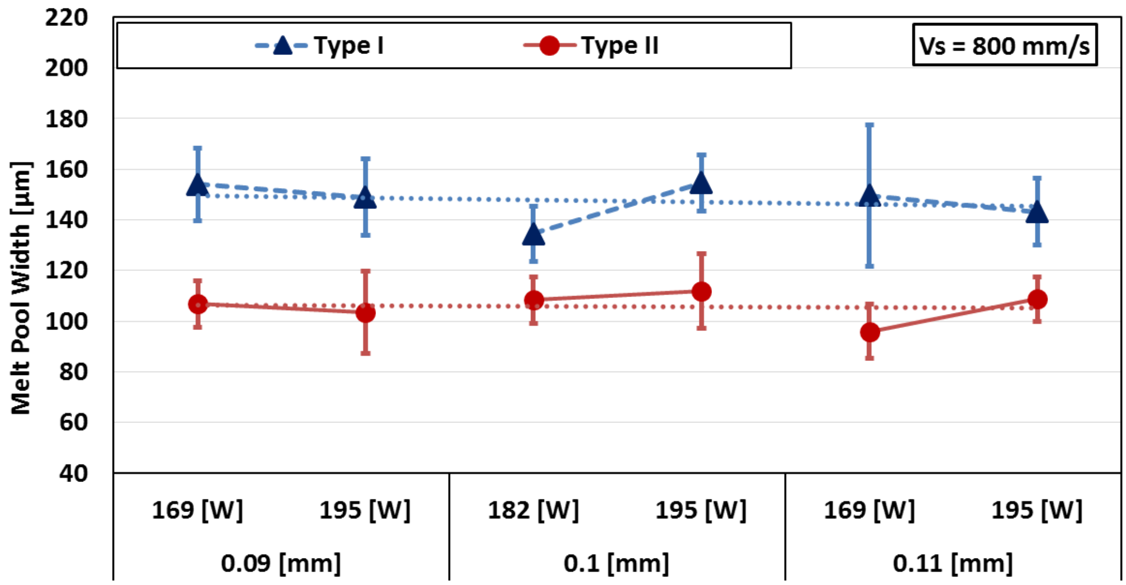

Figure 5.19. Effect of laser power on MP width for three hatch distance levels (v_s = 800 mm/s)

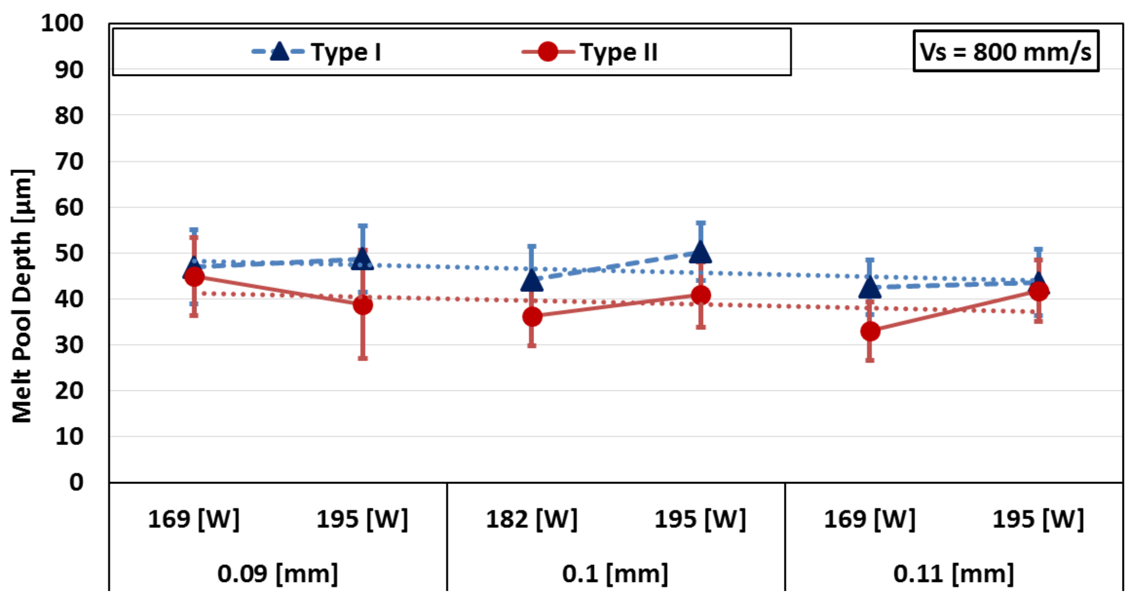

Figure 5.20. Effect of laser power on MP Depth for three hatch distance levels (v_s = 800 mm/s)

Melt pool width and depth decrease with increasing hatch distance, especially for Type I melt pools. This is in agreement with what is intuitively expected, since a larger hatch distance causes the heat affected zone from a previously scanned track to be further away from the following track. Additionally, the difference in depth between Type I and Type II melt pools is greatly reduced with increasing hatch distance, leading to more evenly sized melt pools, as shown in Figure 5.21 and Figure 5.22.

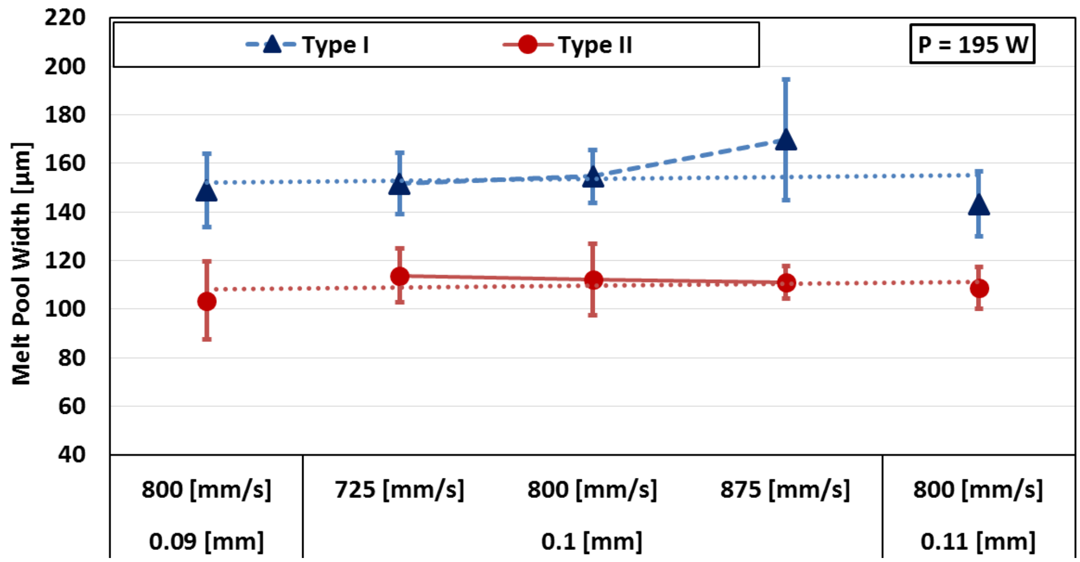

Figure 5.21. Effect of scanning speed on MP width for three hatch distance levels (*P* = 195 W)

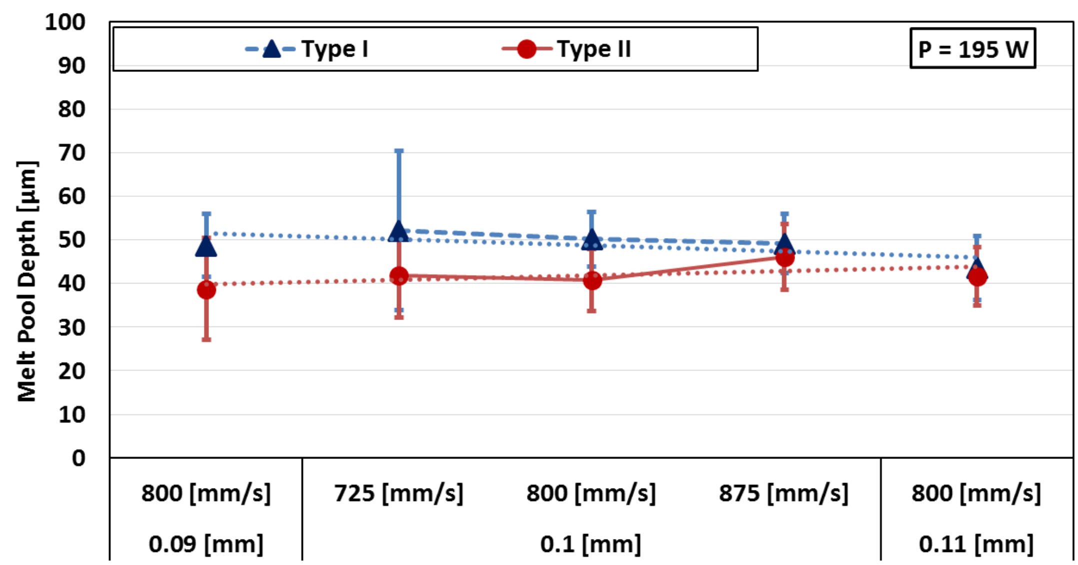

Figure 5.22. Effect of scanning speed on MP depth for three hatch distance levels (*P* = 195 W)

In summary, the measurements taken for melt pool width and depth give very significant insight into the dynamic nature of melt pool size. Figure 5.13 and Figure 5.14 show how melt pool size varies as a function of energy intensity, a term that compounds laser power, scanning speed, and hatch distance, and corresponds to the linear energy applied to the power bed. Additionally, Figure 5.15 to Figure 5.22 show how melt pool size changes according to both type and varying processing parameters (three levels), when one of the processing parameters is held constant. Furthermore, the change in melt pool size is non-linear. To fully understand how melt pool size is defined as a function of process parameters, it is necessary to consider second-order behavior and inter-factor interactions. This analysis is presented in Section 3 of this Chapter.

5.2.2.2 Melt Pool Shape Analysis

The laser heating effect described in the previous section produces a notable effect on the geometrical shape of the melt pool as well. In particular, by analyzing the images obtained via optical microscopy, it was observed that the location along the *y*-axis at which the maximum melting depth occurs does not necessarily lie on the hatch centerline. To quantify this effect, a measure of the melt pool shape was developed and will be explained next.

For this analysis, we will consider once again the cross-sectional (YZ-plane) view of the melt pool. The melt pool width, *w*, and the distance from the edge of the melt pool farthest away from the previous hatch to the location at which the maximum melted depth is observed, *a*, are measured using the same methodology as before (see Figure 5.23).

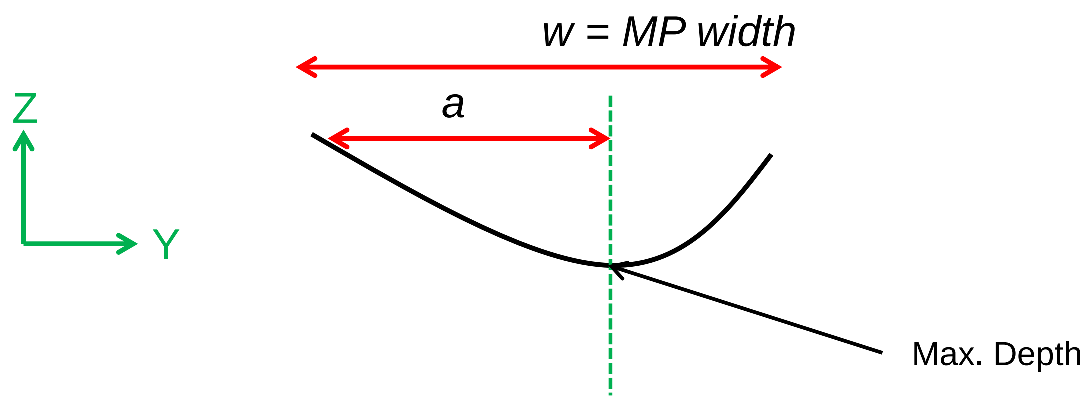

Figure 5.23. Location of maximum depth of melted material

Then, a measure for the melt pool shape is defined as follows:

$$\varphi(a,w) = \frac{a - {}^{w}/_{2}}{{}^{w}/_{2}} = \frac{2a-w}{w} \qquad (5.5)$$

With this definition, a way to determine how skewed the melt pool is has been established. If the melt pool is perfectly symmetrical about the *z*-axis, then $a = w/2$ and $\varphi = 0$, or 0%. On the contrary, if the melt pool is completely skewed towards the previous processed hatch due to the heat-affected zone, then $a \rightarrow w/2$, in which case $\varphi \rightarrow 1$, or 100%. In summary, this measure gives a value between 0 and 1 (or 0 and 100%) that quantifies how non-symmetrical the melt pool geometry is. To further illustrate how this measure is employed, consider the following example taken from the optical image obtained of Coupon 29, previously shown in Figure 5.7. In this example we consider only a single melt pool. Note that *w* and *a* have been measured in pixels and have not been converted to micrometers to avoid rounding error (see Figure 5.24).

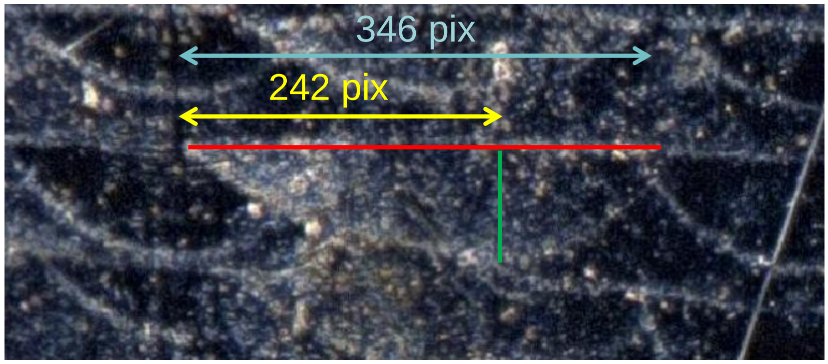

Figure 5.24. Measurements for calculation of melt pool shape

The melt pool shape can then be determined using Equation 5.5:

$$\varphi(242{,}346) = \frac{242 - {}^{346}/_{2}}{{}^{346}/_{2}} = 0.3988 = 39.88\% \qquad (5.6)$$

This value of φ close to 40% indicates that the melt pool is considerably non-symmetrical, indicating a strong effect of the already-processed scanned hatch. By repeating this process for all melt pools previously measured, it is possible to obtain an average measure (and standard deviation) of the melt pool shape for a specific set of process parameters and present those results in a histogram (see Figure 5.25). Then, the melt pool shape measure for different process parameters can be tabulated and presented for comparison, as shown in Table 5.5.

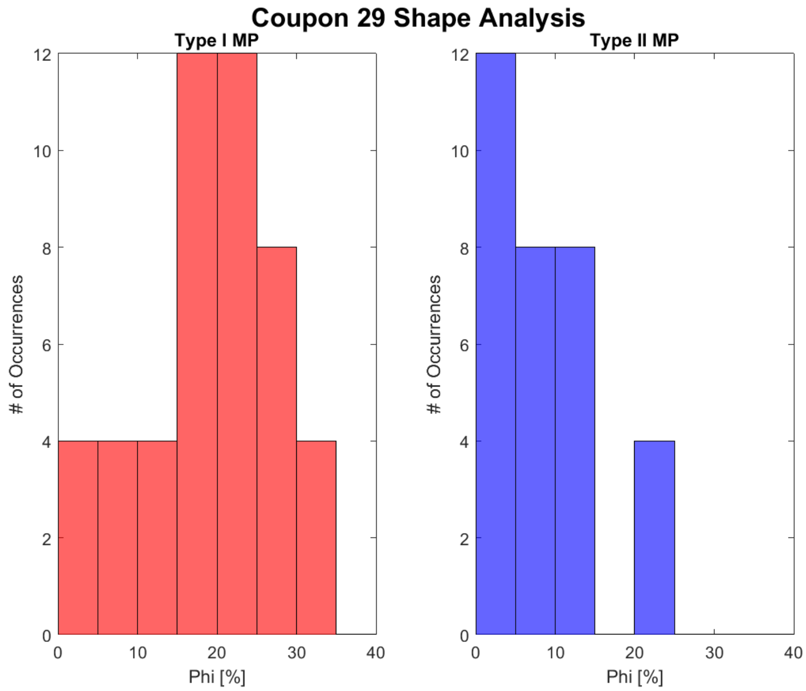

Figure 5.25. Histogram for shape analysis of Coupon 29 by melt pool type

Table 5.5. Summary of melt pool shape measurements

	Shape Avg [%]		Shape Std Dev. [%]	
Coupon	**Type I**	**Type II**	**Type I**	**Type II**
01	10.0	2.2	3.1	2.9
04	16.1	13.4	2.5	2.4
06	19.4	15.3	3.1	2.7
08	12.6	12.7	4.3	4.7
09	11.8	10.5	4.2	4.0
12	15.0	2.7	3.2	4.7
14	10.9	1.0	4.0	4.1
15	16.3	6.7	3.7	4.5
16	9.5	11.5	3.6	4.1
17	8.6	0.4	2.7	4.5
18	7.1	0.1	2.4	3.1
20	11.0	2.6	3.6	6.1
21	23.4	11.5	5.1	6.4
23	9.1	0.2	2.8	6.4
29	21.0	6.0	5.2	5.5
35	5.4	3.5	2.5	3.3

The main conclusion from this analysis is that beyond the variation in melt pool shape, Type I and Type II melt pools obtained via the same processing conditions have different shapes. The effect of processing parameters on melt pool shape can be represented via main effect plots, as seen in Figure 5.26, Figure 5.27 and Figure 5.28. Notice the considerable effect of low hatch distance in Type I melt pools and of high laser power in Type II melt pools.

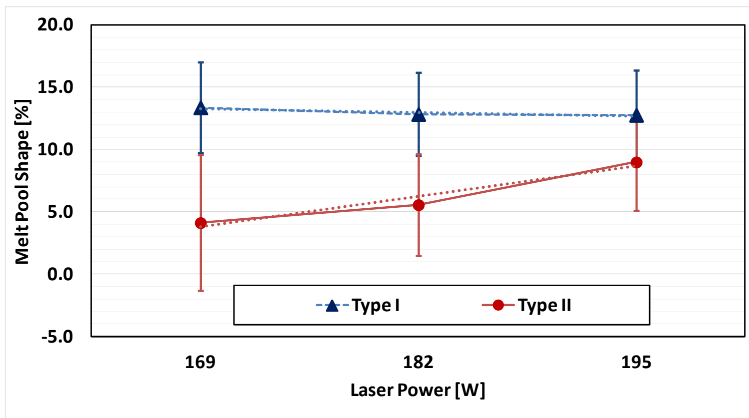

Figure 5.26. Effect of laser power on melt pool shape

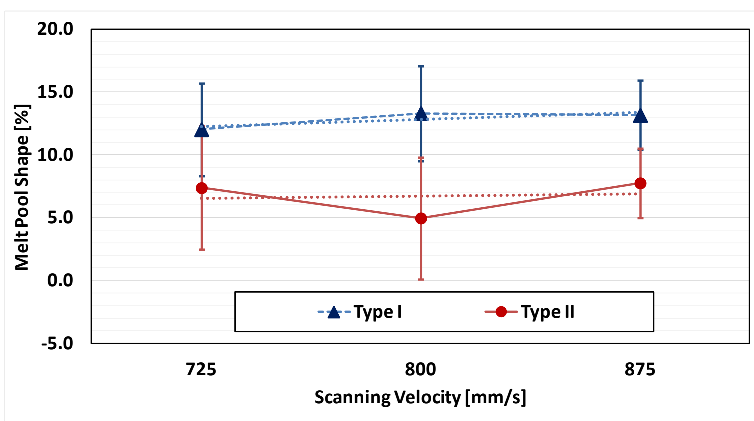

Figure 5.27. Effect of scanning velocity on melt pool shape

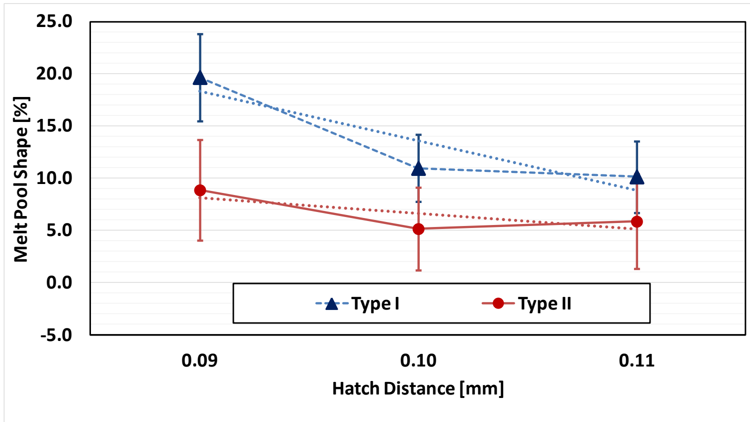

Figure 5.28. Effect of hatch distance on melt pool shape

It is possible to consider how melt pool shape changes as a function of laser energy intensity, using the definition introduced in Equation 5.4. Recall that energy intensity is a function of laser power, scanning speed, layer thickness, and hatch distance. It is then possible to generate plots of melt pool shape, by type, as a function of energy intensity, as shown in Figure 5.29.

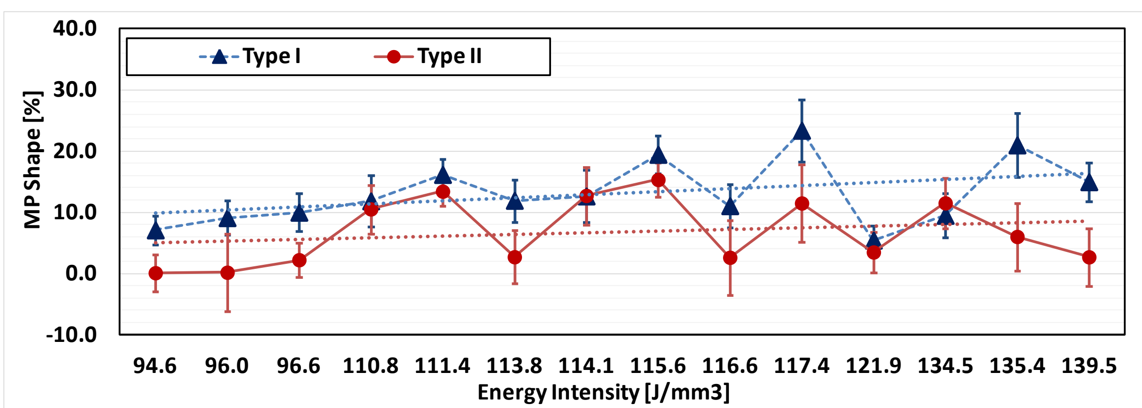

Figure 5.29. Effect of process energy intensity (*E*) on melt pool shape

The trend line on Figure 5.29 shows that melt pool shape is more asymmetrical as energy intensity increases. This behavior is more noticeable in Type I melt pool than in Type II melt pools. Another method to analyze the variation in melt pool shape due to changing process parameters is to keep one of the three factors (laser power, scanning speed, or hatch distance) constant and study how melt pool shape for each melt pool type changes as a result of changes in the other two. Figure 5.30 and Figure 5.31 show how melt pool shape vary for constant hatch distance, both as a function of scanning speed for three laser power levels and as a function of laser power for three levels of scanning speed. The three levels considered are those selected in the Box-Behnken experimental design.

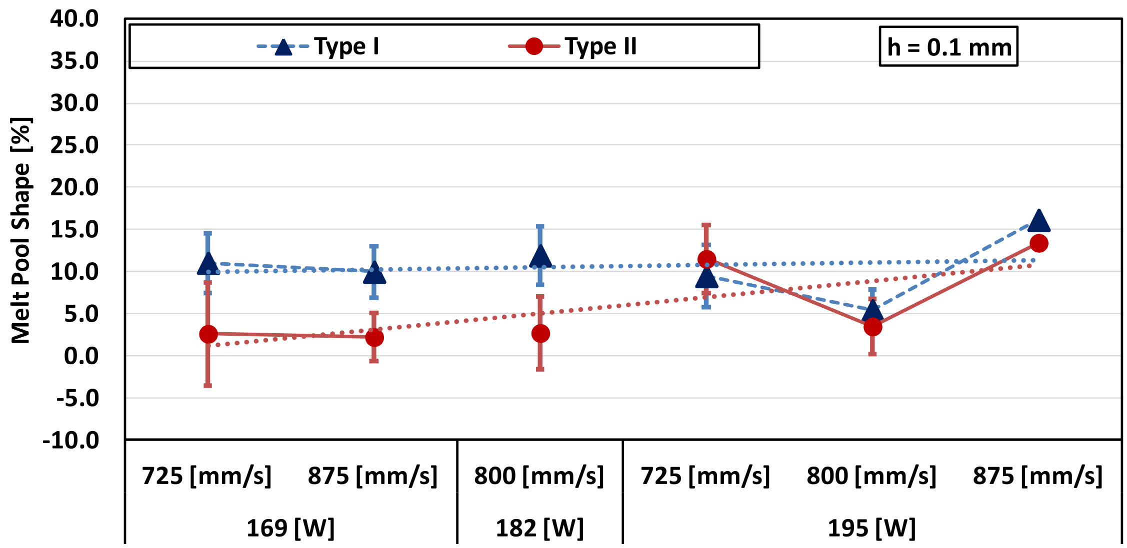

Figure 5.30. Effect of scanning speed on MP shape for three laser power levels (h = 0.1 mm)

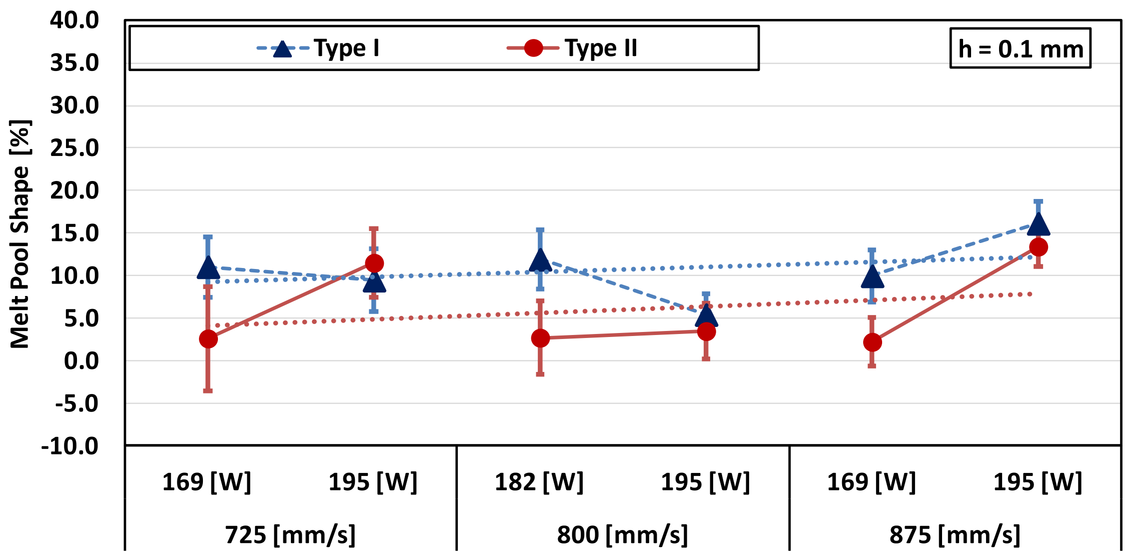

Figure 5.31. Effect of laser power on MP shape for three scanning speed levels (h = 0.1 mm)

These figures indicate that the melt pool tends to be more asymmetric with increasing laser power and increasing scanning speed, especially for Type II melt pools. However, the behavior is clearly non-linear. Melt pool shape measurements taken indicate that there is a considerable difference between Type I and Type II melt pool shapes. Type I melt pools are considerably more asymmetric than Type II melt pools. This behavior is more easily observable at lower scanning speeds. To observe how hatch distance affects melt pool shape, it is possible to consider either constant scanning speed or constant laser power. Figure 5.32 shows how melt pool size varies for coupons fabricated with constant scanning speed, v_s = 800 mm/s. Figure 5.31 shows how melt pool shape varies for coupons additively fabricated with constant laser power, P = 195 W.

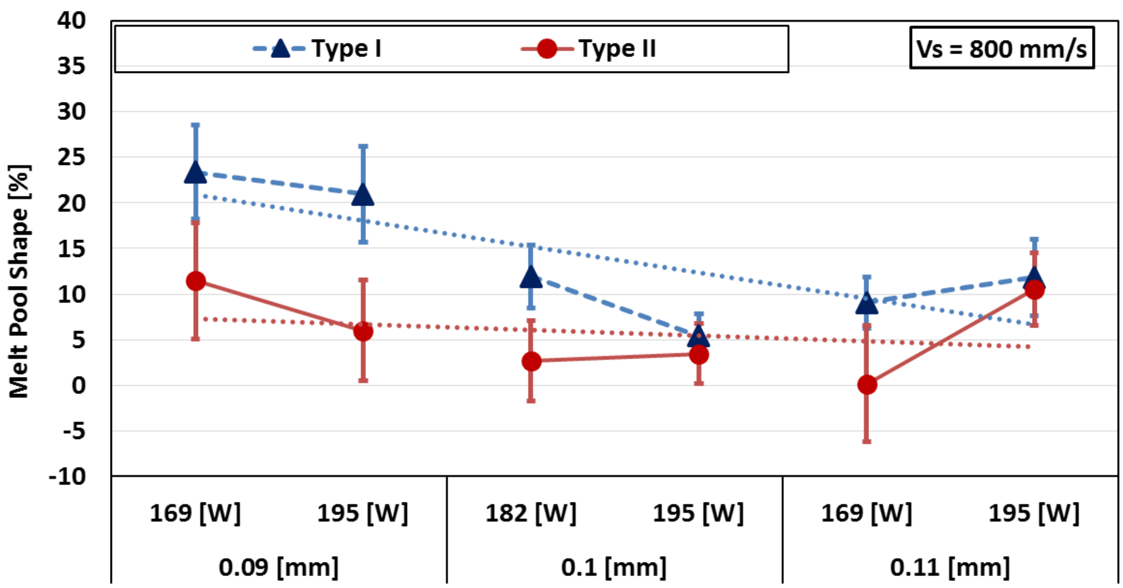

Figure 5.32. Effect of laser power on MP shape for three hatch distance levels (v_s = 800 mm/s)

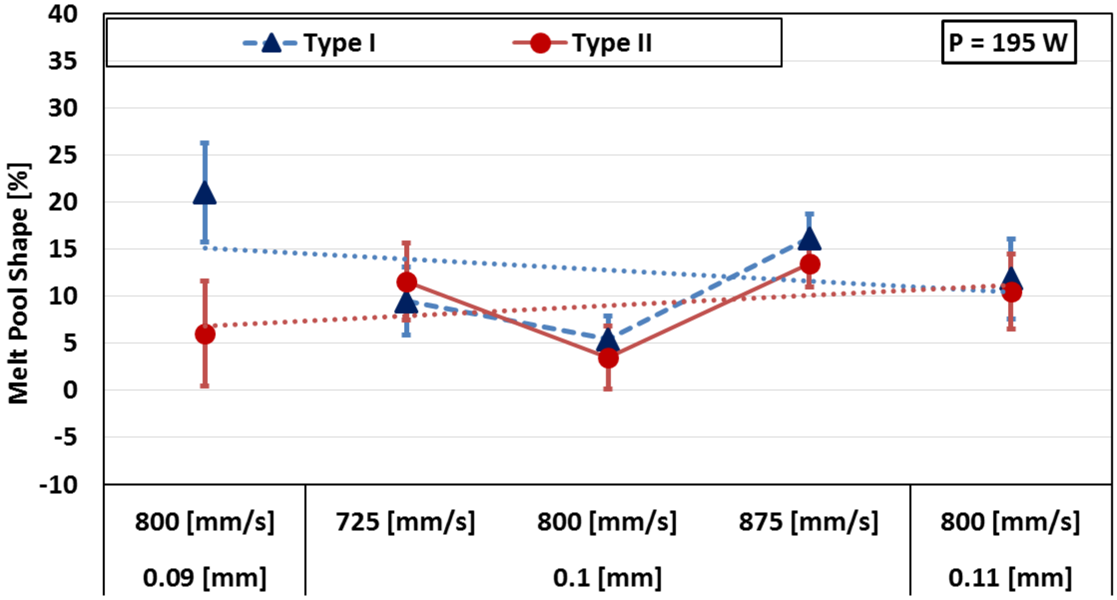

Figure 5.33. Effect of scanning speed on MP shape for three scanning speed levels (*P* = 195 W)

Notice that Type I melt pools tend to be more symmetric when the highest level of hatch distance is utilized. This is intuitive from the fact that a higher hatch distance, the distance between consecutive scanned tracks, results in the melt pool being further removed from the heat affected zone due to melting of the previous track. In summary, the difference in melt pool shape for Type I and Type II melt pools can be mostly attributed to the effect of the heat-affected zone from the previous scanned track. Therefore, hatch distance is the most relevant factor, as hypothesized initially.

5.3 Response Surface Methodology for Predictive Modeling of SLM

The Box-Behnken experimental design presented in Chapter 4 was chosen for two reasons: i) strict limitations in possible values of process parameters introduced by the EOS SLM machine and the restriction in the number of experimental units (i.e. coupons) that could be built, and ii) this design fit the criteria necessary to be able to obtain a meaningful second-order response using Response Surface Methodology (RSM).

5.3.1 Definition of Response Surface Methodology (RSM)

RSM is a methodology used to design, improve, and optimize processes based on an assortment of mathematical and statistical tools, as defined by Myers et al. (Myers et al., 2009). In a nutshell, RSM provides a strategy for exploration of the space of the process or independent variables (e.g. laser power, scanning velocity, hatch distance); builds a mathematical relationship between the process variables and the measured output (e.g. part density, melt pool geometry) through statistical analysis, and also allows for optimization of the aforementioned process parameters based on desired output values. In particular, second-order response models are desirable for the following reasons:

- Flexibility. A second-order model is easy to modify to adjust into a wide variety of response surfaces. True response surfaces usually exhibit curvature near the optimum point, which cannot be represented with a first-order model.
- Estimation of the process parameters in a second-order model is not overly complex, and simple statistical concepts like the method of least squares can be used effectively.
- There is good experimental correlation between second-order models and the "true" response surface.

The general form of the second order model for *k* process variables is given by Equation 5.7.

$$\eta = \beta_0 + \sum_{i=1}^{k} \beta_i x_i + \sum_{i=1}^{k} \beta_{ii} x_i^2 + \sum\sum_{i<j=2}^{k} \beta_{ij} x_i x_j + \epsilon \tag{5.7}$$

In Equation 5.7, η is the output variable (e.g. density), β_0's are the estimated parameters in the response, and x_i's are the process variables, ϵ is the residual error. In the proposed experiment design, three process parameters are taken into consideration (k=3): laser power, scanning velocity, and hatch distance.

The first step in RSM is to identify process variables that may affect the response, usually as part of a screening experiment. The second step would be to determine levels of the process variables which are close to the optimum desired response. The "default setting" described in Chapter 4 (P=195 W. v=800 mm/s, h=0.1 mm) has been identified by EOS, the machine manufacturer, as close to the optimal setting for SLM of IN 625. Therefore, the region of interest has been defined based on these values. It is important to note that 195 W is the maximum power setting of the fiber-laser used by the EOS M270 machine, so the "laser power" variable is bounded above by this value.

5.3.2 Results of RSM analysis of coupon density

For this preliminary analysis, the coupons described in Section 3 of this Chapter are used to create a response model. Three levels were considered for each of the three factors: laser power (P), scanning velocity (v_s), and hatch distance (h). The response variable is relative density, defined as the density of the coupons divided by the density of bulk IN 625. The density of each coupon was calculated by dividing the mass of the coupon by its volume. The mass was measured using a sensitive scale, while the volume was measured using a Coordinate Measurement Machine (CMM). As previously described, from the 18 coupons built, 15 correspond to the Box-Behnken design of experiments and the 3 remaining coupons correspond to repetitions at the "default setting". To avoid design imbalance, these last 3 coupons have not been considered in the RSM analysis.

5.3.2.1 Results of RSM analysis of coupon density (90º rot. scanning strategy)

Table 5.6. Box-Behnken design of experiments with process variables and response (90º rotation)

Random Order	**Laser Power P [W]**	**Scanning Velocity v_s [mm/s]**	**Hatch Distance h [mm]**	**Relative Density, ρ_{rel} [%]**
1	169	875	0.10	95.23
2	195	875	0.10	98.30
3	182	875	0.09	97.03
4	182	725	0.11	95.97
5	195	800	0.11	98.47
6	182	725	0.09	97.14
7	182	800	0.10	98.10
8	182	800	0.10	98.05
9	195	725	0.10	97.50
10	182	800	0.10	98.13
11	182	875	0.11	96.50
12	169	725	0.10	96.38
13	169	800	0.09	97.50
14	169	800	0.11	96.60
15	195	800	0.09	99.01

The RSM analysis and omnibus ANOVA were performed using R statistical software for data analysis. Figure 5.34 shows the output of the analysis in R-Studio, where the estimate, the standard error, the value of the t-distribution and the p-value are given.

```
            Estimate Std. Error    t value   Pr(>|t|)
(Intercept) 98.0933333  0.1057802 927.3320 2.768e-14 ***
P            0.9462500  0.0647769  14.6078 2.715e-05 ***
v            0.0087500  0.0647769   0.1351  0.897819
h           -0.3925000  0.0647769  -6.0593  0.001767 **
P:v          0.4875000  0.0916083   5.3216  0.003136 **
P:h          0.0900000  0.0916083   0.9824  0.370999
v:h          0.1600000  0.0916083   1.7466  0.141146
P^2         -0.0029167  0.0953490  -0.0306  0.976780
v^2         -1.2379167  0.0953490 -12.9830 4.833e-05 ***
h^2         -0.1954167  0.0953490  -2.0495  0.095705 .
---
Signif. codes:  0 ‘***’ 0.001 ‘**’ 0.01 ‘*’ 0.05 ‘.’ 0.1 ‘ ’ 1

Multiple R-squared:  0.9891,   Adjusted R-squared:  0.9694
F-statistic: 50.36 on 9 and 5 DF,  p-value: 0.0002254

Analysis of Variance Table

Response: Density
             Df Sum Sq Mean Sq F value    Pr(>F)
FO(P, v, h)   3 8.3962 2.79873  83.374 0.0001088
TWI(P, v, h)  3 1.0854 0.36181  10.778 0.0127140
PQ(P, v, h)   3 5.7325 1.91082  56.923 0.0002752
Residuals     5 0.1678 0.03357
Lack of fit   3 0.1646 0.05486  33.587 0.0290517
Pure error    2 0.0033 0.00163

Stationary point of response surface:
        P         v         h
-0.380505 -0.451051 -3.067583

Stationary point in original units:
       Power     Velocity        Hatch
 179.05343343 741.17120412   0.06932417

Eigenanalysis:
$values
[1]  0.05749216 -0.20494221 -1.28879995

$vectors
       [,1]        [,2]        [,3]
P 0.9535018 -0.23894157  0.18368805
v 0.1936760  0.01880602 -0.98088528
h 0.2309198  0.97085182  0.06420883
```

Figure 5.34. Output of RSM analysis for 90º rotation coupon density in RStudio software.

In the output given in Figure 5.34, “FO” corresponds to the first-order response of the system, “TWI” represents the two-term interactions, and “PQ” corresponds to the quadratic term. The model shows that power and velocity are significant contributors to relative density of coupons fabricated with 90º scanning strategy. Especially, scanning velocity appears to be the most significant term, as both the linear and quadratic terms are significant. It is also worth noting that the laser power-scanning velocity interaction is significant. The model also provides the estimates for the β_i's in Equation 5.7, where i = 1, 2, and 3 correspond to laser power, scanning speed, and hatch distance, respectively. These coefficients are presented in Table 5.7. The R^2 value for this model is 0.9891, which indicates that the data is very close to the fitted model. Finally, the stationary, or optimal, point that maximizes density for coupons fabricated with 90º rotation scanning strategy, is given by P=179 W, v_s=741 mm/s, h=0.07 mm.

Table 5.7. Summary of second order model approximation (90º rotation coupon density)

	Estimate	***p*-value**
β_0	98.093333	0.000000
β_1	0.946250	0.000027
β_2	0.008750	0.897819
β_3	-0.392500	0.001767
β_{11}	-0.002917	0.976780
β_{22}	-1.237917	0.000048
β_{33}	-0.195417	0.095705
β_{12}	0.487500	0.003136
β_{13}	0.090000	0.370999
β_{23}	0.160000	0.141146

Additionally, contour and response surface plots can be generated using this model using Matlab. In order to create 3-D response surface plots, one of the process parameters must be held constant throughout. Then, the output can be plotted against the other two process parameters. Figures 5.35-5.37 show response surface plots obtained by fixing one of the process parameters and varying the other two: Figure 5.35 is a plot of relative density for varying hatch distance and laser power when scanning velocity, v_s = 800 mm/s. Analogously, Figures 5.36 and 5.37 show response surface plots for varying hatch distance and scanning velocity for laser power, P = 195 W and for varying power and velocity for hatch distance, h = 0.1 mm, respectively. It can be seen that the most dense coupons are obtained at a non-linear combination of power, velocity and hatch distance. Least dense coupons are obtained by implementing low laser power, highest laser power, and the largest hatch distance.

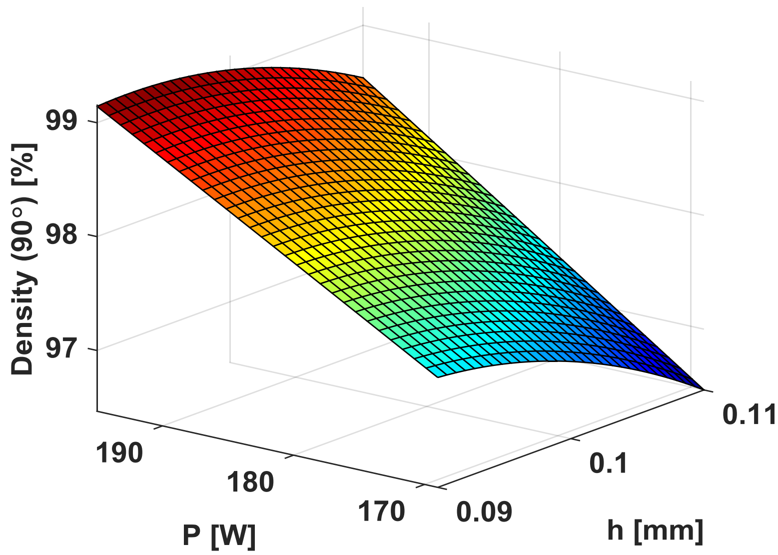

Figure 5.35. Surface plot for rel. density (90º) vs. hatch distance and power (v_s = 800 mm/s).

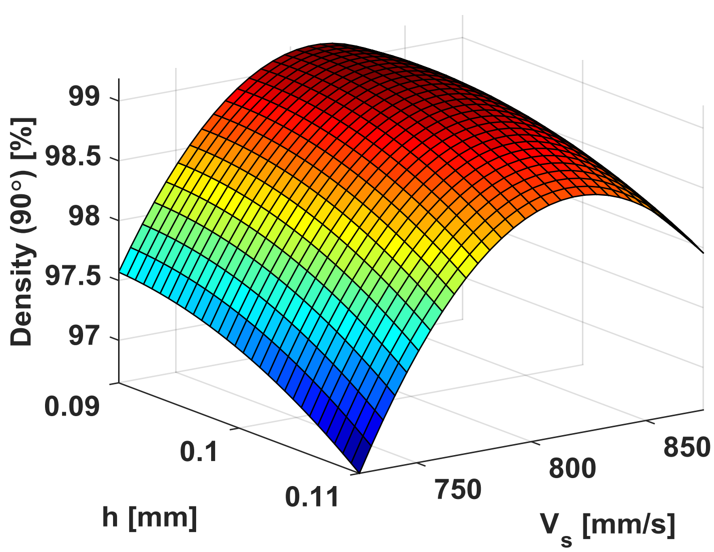

Figure 5.36. Surface plot for rel. density (90º) vs. hatch distance and speed (P = 195 W).

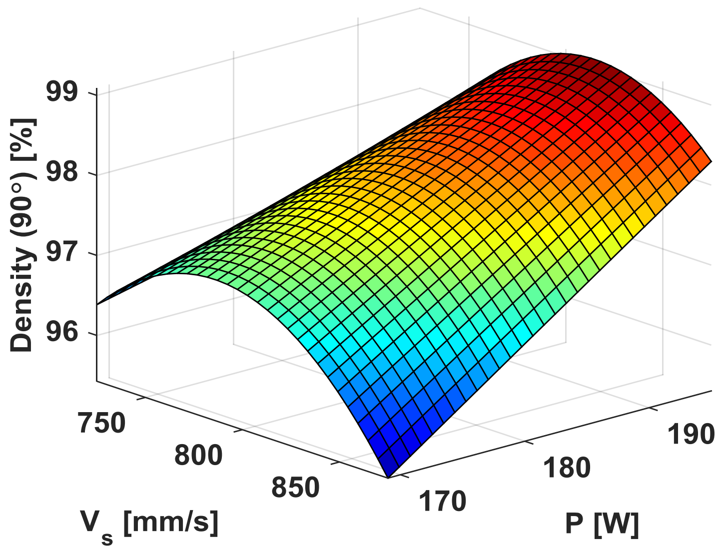

Figure 5.37. Surface plot for rel. density (90º) vs. scanning speed and power (h = 0.1 mm).

5.3.2.2 Results of RSM analysis of coupon density (67º rot. scanning strategy)

Table 5.8. Box-Behnken design of experiments with process variables and response (67º rotation)

Random Order	Laser Power P [W]	Scanning Velocity v_s [mm/s]	Hatch Distance h [mm]	Relative Density, ρ_{rel} [%]
1	169	875	0.10	96.00
2	195	875	0.10	98.70
3	182	875	0.09	97.40
4	182	725	0.11	96.17
5	195	800	0.11	98.52
6	182	725	0.09	97.29
7	182	800	0.10	98.21
8	182	800	0.10	98.19
9	195	725	0.10	97.74
10	182	800	0.10	98.30
11	182	875	0.11	96.75
12	169	725	0.10	96.52
13	169	800	0.09	97.91
14	169	800	0.11	96.78
15	195	800	0.09	99.23

The RSM analysis and omnibus ANOVA were performed using R statistical software for data analysis. The model shows that power, velocity, and hatch distance are all significant factors in final coupon density. Especially, scanning velocity appears to be the most significant term, as both the linear and quadratic terms are significant. It is also worth noting that the laser power-scanning velocity interaction is significant. This matches what was reported previously for 90º scanning rotation. Therefore, the difference in scanning strategy does not significantly affect the relationship between process parameters when it comes to coupon density. The model also provides the estimates for the β_i's in Equation 5.7, where i = 1, 2, and 3 correspond to laser power, scanning speed, and hatch distance, respectively. These coefficients are presented in Table 5.9. The R^2 value for this model is 0.9919, which indicates an excellent fit between the data and the model. Finally, the stationary, or optimal, point that maximizes coupon density, is given by P=169 W, v_s=766 mm/s, h=0.08 mm.

Table 5.9. Summary of second order model approximation (67º rotation coupon density)

	Estimate	***p*-value**
β_0	98.23333	9.073e-15
β_1	0.872500	1.361e-05
β_2	0.141250	0.0416946
β_3	-0.451250	0.0003329
β_{11}	0.107083	0.2199178
β_{22}	-1.100417	2.908e-05
β_{33}	-0.230417	0.0295457
β_{12}	0.370000	0.0039632
β_{13}	0.105000	0.2119534
β_{23}	0.117500	0.1703002

Figures 5.38-5.40 show response surface plots obtained by keeping one of the process parameters constant. Figure 5.38 is a plot of relative density of IN 625 coupons built

following a 67º rotation between layers scanning strategy, for varying hatch distance and laser power when the scanning velocity is v_s = 800 mm/s. Analogously, Figures 5.39 and 5.40 show response surface plots for varying hatch distance and scanning velocity when laser power, P = 195 W, and for varying power and velocity when hatch distance, h = 0.1 mm, respectively. It can be seen that the densest coupons are obtained at a non-linear combination of power, velocity and hatch distance. Least dense coupons are obtained by implementing a low laser power, the highest laser power, and the largest hatch distance.

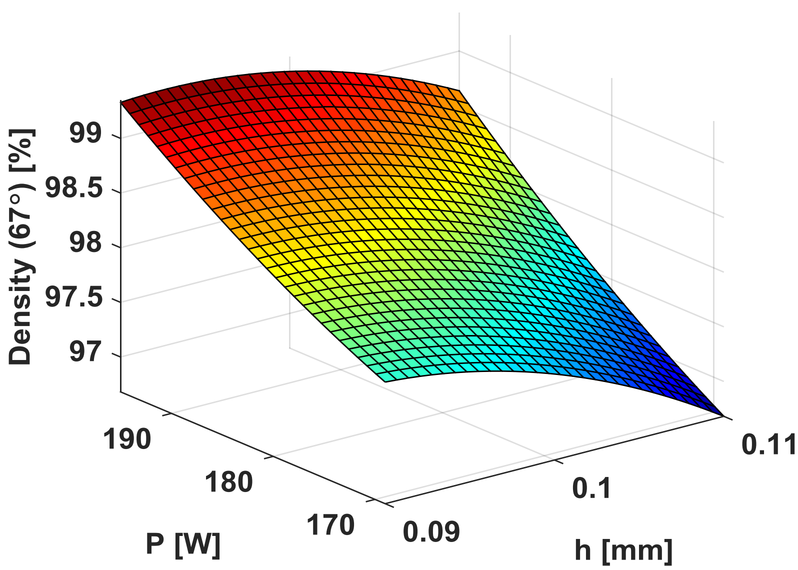

Figure 5.38. Surface plot for rel. density (67º) vs. hatch distance and power (vs = 800 mm/s)

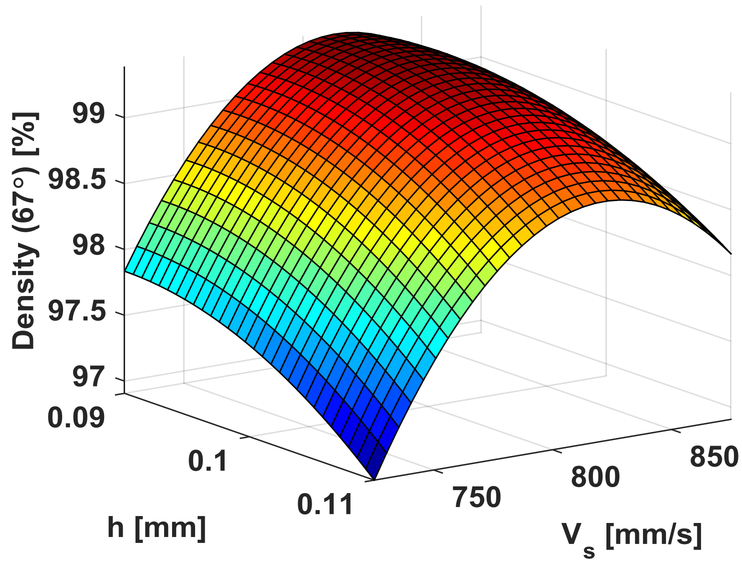

Figure 5.39. Surface plots for rel. density (67º) vs. hatch distance and speed (P = 195 W)

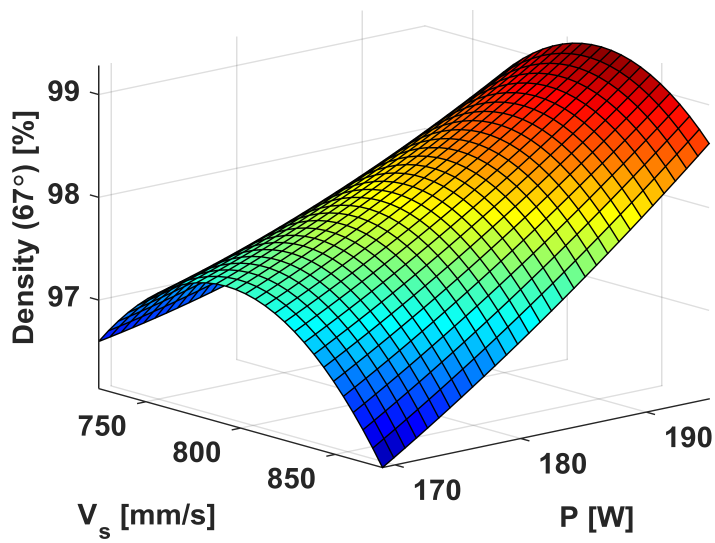

Figure 5.40. Surface Plot for Rel. Density (67º) vs. scanning speed and power (h = 0.1 mm)

5.3.3 Results of RSM Analysis for Melt Pool Dimensions

The following subsections provide a complete analysis using response surface methodology for the four measured outputs that describe the size of the melt pool: melt pool width (Types I and II) and melt pool depth (Types I and II). A table providing the estimated coefficients from fitting a quadratic model with interactions to the measured data is provided for each of the measured outputs, along with the specific process parameters that maximize said output within the explored range.

5.3.3.1 Results of RSM Analysis for Melt Pool Width – Type I

Table 5.10 provides the estimated coefficients and the associated *p*-value when fitting a second-order response model (Equation 5.7) to the observed measurements for Type I melt pool width.

Table 5.10. Summary of second order model approximation: melt pool width (Type I)

	Estimate	***p*-value**
β_0	134.3333	1.177e-06
β_1	2.1250	0.50836
β_2	-1.3750	0.66440
β_3	-0.7500	0.81162
β_{11}	12.9583	0.03191
β_{22}	6.4583	0.20155
β_{33}	1.7083	0.71343
β_{12}	10.7500	0.05148
β_{13}	-0.5000	0.91033
β_{23}	-8.5000	0.10020

The ANOVA results show that power-squared and power-velocity interaction are the only significant factors in determining width for Type I melt pools, using a p-value less than 0.1 as reference. The R^2 value for this model is 0.812, which indicates that the measured data is in good agreement with the fitted model. The stationary, or optimal point, which maximizes Type I melt pool width within the given range of process parameters is given by P=183 W, v_s=774 mm/s, h=0.09 mm. Figures 5.39-5.41 show response surface plots obtained by keeping constant one of the process parameters: Figure 5.41 is a plot of Type I melt pool width for varying hatch distance and laser power with scanning velocity, v_s = 800 mm/s. Analogously, Figures 5.42 and 5.43 show response surface plots for varying hatch distance and scanning velocity when P = 195 W, and for varying power and velocity with hatch distance, h = 0.1 mm, respectively. From these plots, the quadratic behavior of the process can be seen clearly.

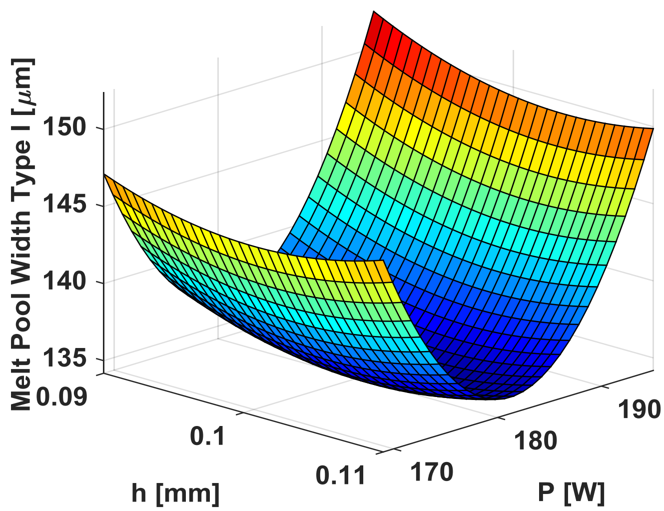

Figure 5.41. Surface plot for MP width (Type I) vs. hatch distance and power (vs =800 mm/s).

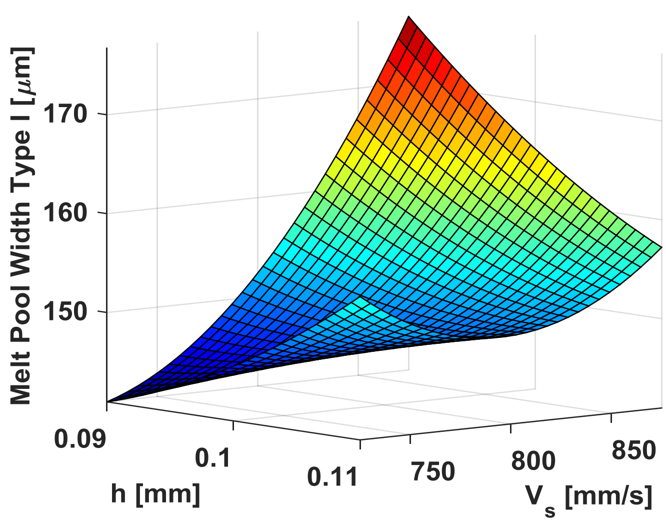

Figure 5.42. Surface plot for MP width (Type I) vs. hatch distance and speed (P = 195 W).

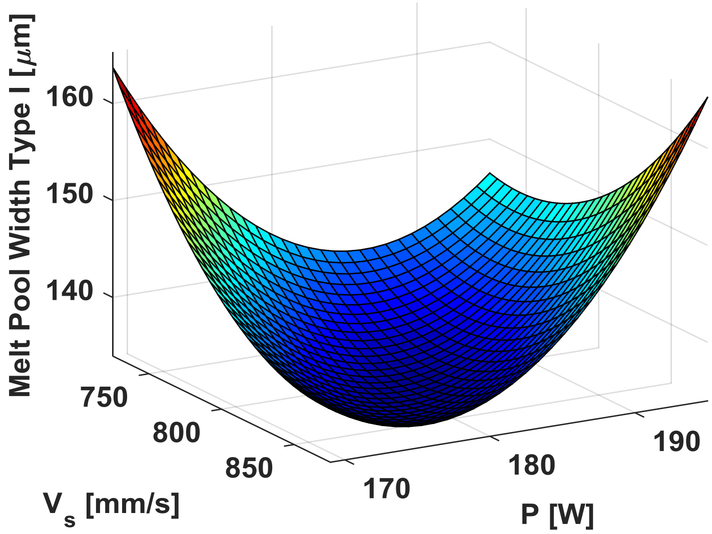

Figure 5.43. Surface plot for MP width (Type I) vs. scanning speed and power (h = 0.1 mm).

5.3.3.2 Results of RSM Analysis for Melt Pool Width – Type II

Table 5.11 provides the estimated coefficients and the associated *p*-value when fitting a second-order response model (Equation 5.7) to the observed measurements for Type II melt pool width.

Table 5.11. Summary of second order model approximation: melt pool width (Type II)

	Estimate	***p*-value**
β_0	108.66667	8.49e-08
β_1	4.50000	0.02512
β_2	-3.25000	0.07140
β_3	-0.25000	0.86757
β_{11}	-3.48533	0.15999
β_{22}	0.54167	0.80645
β_{33}	-1.45833	0.51773
β_{12}	2.75000	0.23044
β_{13}	4.25000	0.08866
β_{23}	3.75000	0.12174

The R^2 value for this model is 0.8495, which indicates that the model is a good fit for the measured data. The width of Type II melt pools behaves significantly different to that of Type I reported in the previous section. In this case, power and velocity and the power-hatch distance interactions are reported as significant according to the ANOVA analysis. Therefore, not only does melt pool geometry showcase a dynamic behavior, but the characteristics of this behavior, as described by process parameters, change based on the location of the melt pool along the scanned track. The stationary, or optimal point, which maximizes Type II melt pool width within the given range of process parameters is given by P=192 W, v_s=767 mm/s, h=0.10 mm. Figures 5.44-5.46 show response surface plots obtained by keeping constant one of the process parameters: Figure 5.44 is a plot of Type II melt pool width for varying hatch distance and laser power with scanning velocity, v_s = 800 mm/s. Analogously, Figures 5.45 and 5.46 show response surface plots for varying hatch distance and scanning velocity when P = 195 W, and for varying power and velocity with hatch distance, h = 0.1 mm, respectively. From these plots, the quadratic behavior of the process can be observed, especially near the boundaries of the set.

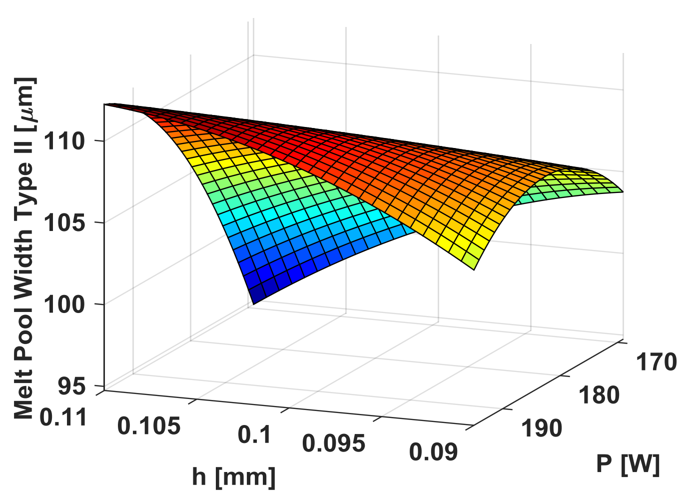

Figure 5.44. Surface plot for MP width (Type II) vs. hatch distance and power (vs = 800 mm/s)

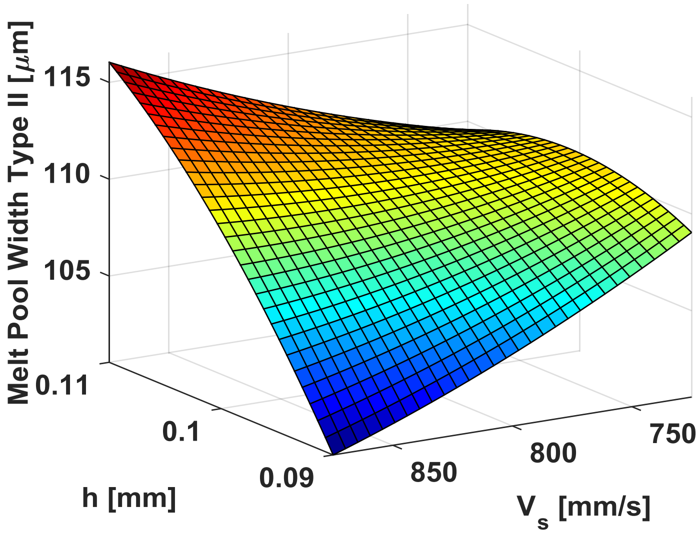

Figure 5.45. Surface plot for MP width (Type II) vs. hatch distance and speed (P = 195 W)

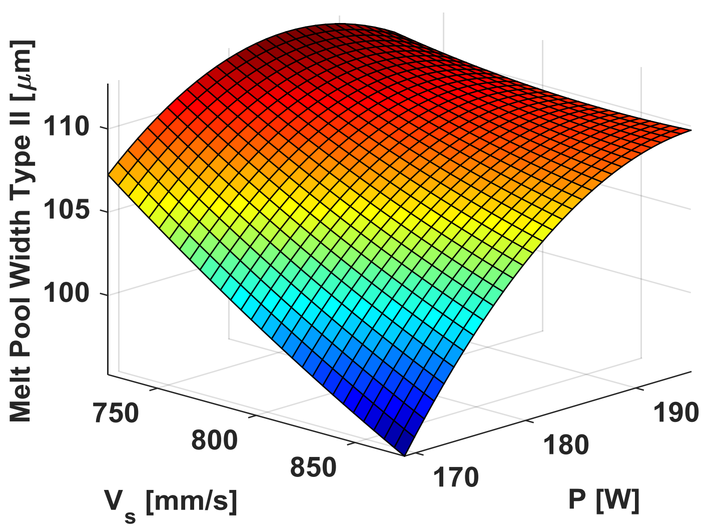

Figure 5.46. Surface plot for MP width (Type II) vs. scanning speed and power (h = 0.1 mm)

By comparing Figures 5.41-5.43 and Figures 5.44-5.46, it can be readily seen that melt pool width behavior varies significantly from Type I and Type II. This is one clear indicator of the *dynamic nature of the melt pool* and its dependence on process parameters.

5.3.3.3 Results of RSM Analysis for Melt Pool Depth – Type I

Table 5.12 provides the estimated coefficients and the corresponding *p*-value when fitting a quadratic response model with interactions (Equation 5.7) to the observed measurements for Type I melt pool depth. The R^2 value for this model is 0.5651, which indicates that the model is not a very good fit for the data.

Table 5.12. Summary of second order model approximation: MP depth (Type I)

	Estimate	***p*-value**
β_0	44.0000	1.796e-05
β_1	2.2523	0.2419
β_2	-2.500	0.2004
β_3	-0.500	0.7799
β_{11}	1.1250	0.6710
β_{22}	1.6250	0.5437
β_{33}	0.6250	0.8122
β_{12}	3.2500	0.2333
β_{13}	-0.2500	0.9203
β_{23}	-0.2500	0.9210

The ANOVA results show that there are no significant factors in this quadratic model, based on *p*-value. Therefore, it cannot be determined accurately which interactions among process parameters are more crucial to Type I melt pool depth. Figures 5.47-5.49 show response surface plots obtained by keeping constant one of the process parameters: Figure 5.47 is a plot of Type I melt pool depth for varying hatch distance and laser power with scanning velocity, v = 800 mm/s. Analogously, Figures 5.48 and 5.49 show response surface plots for varying hatch distance and scanning velocity when P = 195 W, and for varying power and velocity with hatch distance, h = 0.1 mm, respectively. From these plots, the quadratic behavior of the process can be observed, especially near the boundaries of the set. It is obvious that shallow (least deep) melt pools occur when low power and high velocity are utilized. Conversely, high power and low hatch distance lead to the deepest melt pools.

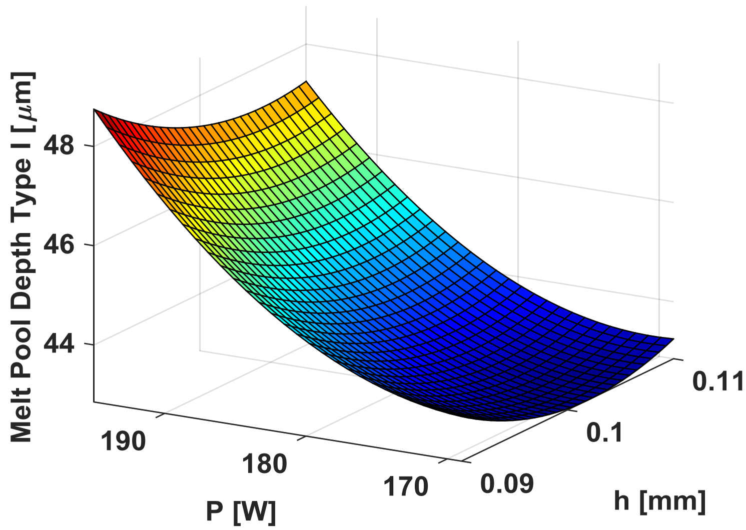

Figure 5.47. Surface plot for MP depth (Type I) vs. hatch distance and power (v_s = 800 mm/s).

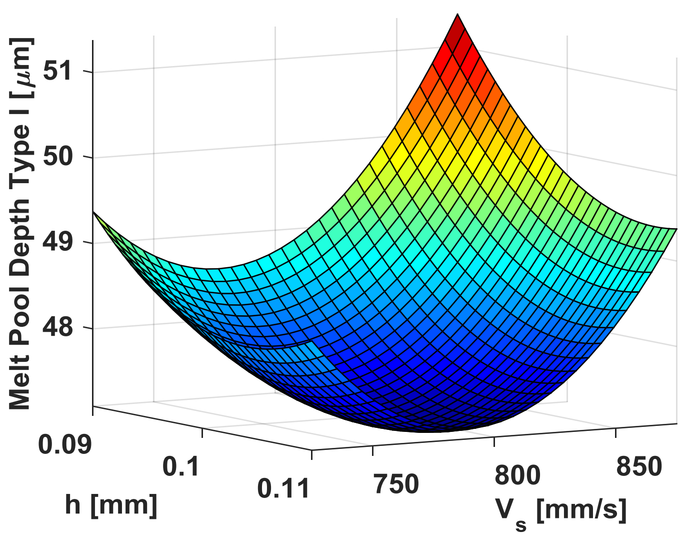

Figure 5.48. Surface plot for MP depth (Type I) vs. hatch distance and speed (P = 195 W).

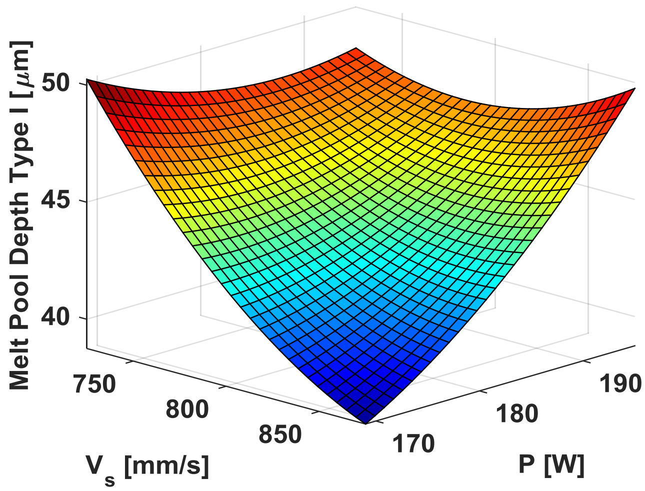

Figure 5.49. Surface plot for MP depth (Type I) vs. scanning speed and power (h = 0.1 mm).

5.3.3.4 Results of RSM Analysis for Melt Pool Depth – Type II

Table 5.13 provides the estimated coefficients and the corresponding p-value when fitting a quadratic response model with interactions (Equation 5.7) to the observed measurements for Type II melt pool depth.

Table 5.13. Summary of second order model approximation: melt pool depth (Type II)

	Estimate	p-value
β_0	36.3333	3.337e-06
β_1	2.2500	0.07340
β_2	-1.500	0.19234
β_3	-1.500	0.19253
β_{11}	3.70833	0.05254
β_{22}	0.20833	0.89253
β_{33}	-0.29167	0.85012
β_{12}	3.7500	0.04473
β_{13}	3.7500	0.04358
β_{23}	-2.2500	0.17101

Unlike Type I melt pool depth, ANOVA results show that laser power, laser power squared, and laser power-scanning velocity and laser power-hatch distance interactions are all significant. Therefore, it can be concluded that laser power is the predominant factor in determining resulting melt pool depth for Type II melt pools. This result makes intuitive sense since Type II melt pools, those occurring at the end of the scanned track, are the result of heating an area of the powder bed that has not been processed recently. Therefore, the effect of scanning velocity and hatch distance (previously scanned hatches) should be minimal. The R^2 value for this model is 0.8682, which indicates that the model fits the measured data very well. Figures 5.50-5.52 show response surface plots obtained by keeping constant one of the process parameters: Figure 5.50 is a plot of Type II melt pool depth for varying hatch distance and laser power with scanning velocity, v_s = 800 mm/s. Analogously, Figures 5.51 and 5.52 show response surface plots for varying hatch distance and scanning velocity when P = 195 W, and for varying power and velocity with hatch distance, h = 0.1 mm, respectively. From these plots, the quadratic behavior of the process can be observed, especially near the boundaries of the set. Also the quadratic behavior is most noticeable in the power-hatch distance and power-scanning velocity interactions. The velocity-hatch distance interaction is quasi-linear.

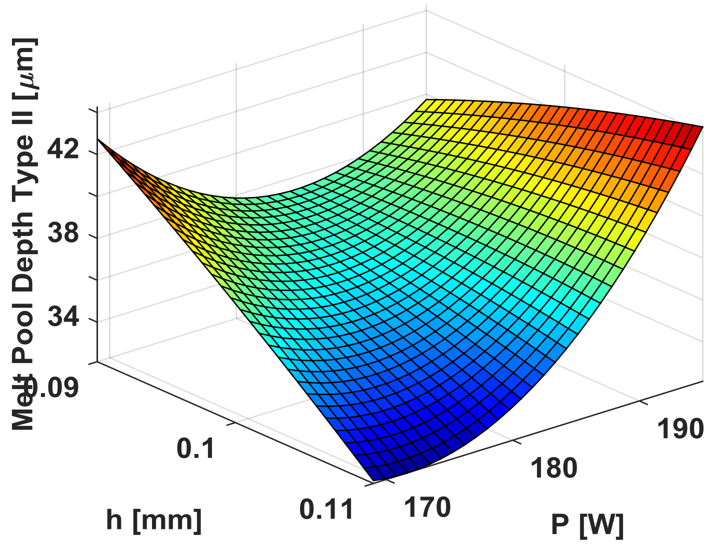

Figure 5.50. Surface plot for MP depth (Type II) vs. hatch distance and power (v_s = 800 mm/s).

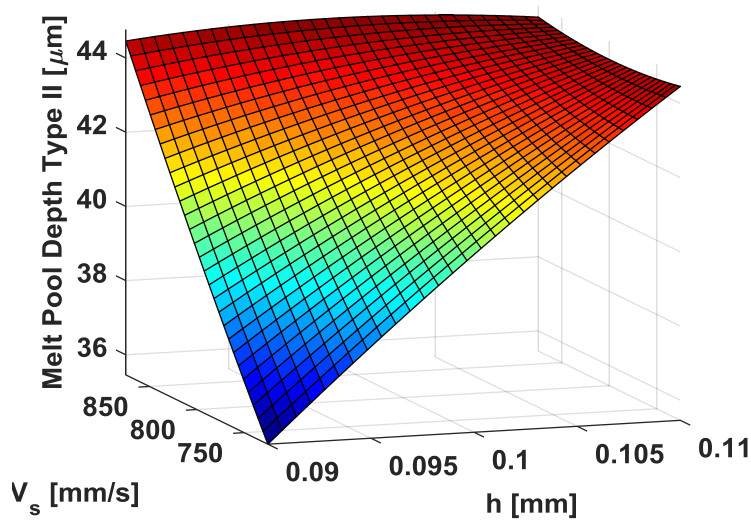

Figure 5.51. Surface plot for MP depth (Type II) vs. hatch distance and speed (P = 195 W).

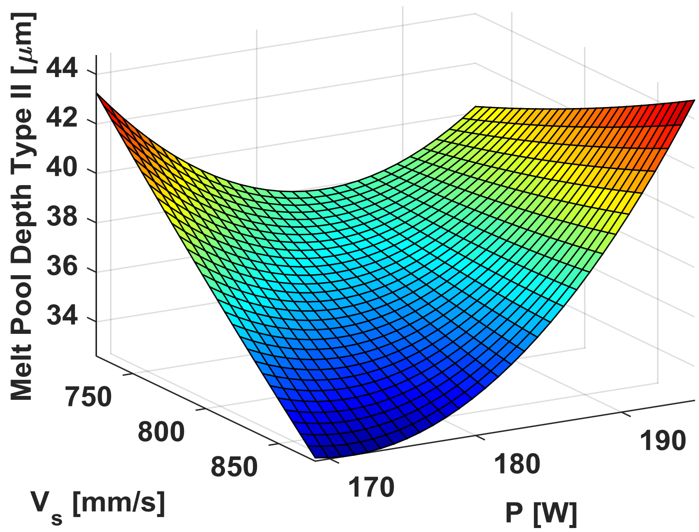

Figure 5.52. Surface plot for MP depth (Type II) vs. scanning speed and power (h = 0.1 mm)

5.3.4 Results of RSM analysis for melt pool shape

To analyze melt pool shape, the same methodology applied to analyze melt pool dimensions is followed. The first step is to separate results by melt pool type: Type I and Type II, based on whether the melt pool being analyzed is located at the beginning of the scanned track or at the end. Melt pool shape is calculated using the methodology described in Section 2.2.2 of this Chapter.

5.3.4.1 Results of RSM Analysis for Melt Pool Shape – Type I

Table 5.14 provides the estimated coefficients and the corresponding p-value when fitting a quadratic response model with interactions (Equation 5.7) to the observed measurements for Type I melt pool shape.

Table 5.14. Summary of second order model approximation: melt pool shape (Type I)

	Estimate	***p*-value**
β_0	11.92000	0.001190
β_1	0.61875	0.599289
β_2	0.56625	0.629810
β_3	-4.76500	0.007593
β_{11}	1.26125	0.472699
β_{22}	-1.52875	0.389957
β_{33}	3.13375	0.111673
β_{12}	1.93750	0.269599
β_{13}	1.28500	0.447878
β_{23}	-2.50500	0.169465

ANOVA results show that hatch distance is the most significant factor in Type I melt pool shape. This result makes intuitive sense, since the deformation of the melt pool's shape is due to the heat affected zone generated by the scanning of the previous track. Therefore, it can be concluded that hatch distance is the predominant factor in determining resulting melt pool depth for Type I melt pools. The effect of scanning velocity and laser power should be minimal. The R^2 value for this model is 0.8547, which indicates that the model is a reasonable fit for the data. Figures 5.53-5.55 show response surface plots obtained by keeping constant one of the process parameters: Figure 5.53 is a plot of Type I melt pool shape for varying hatch distance and laser power with scanning velocity, vs = 800 mm/s. Analogously, Figures 5.54 and 5.55 show response surface plots for varying hatch distance and scanning velocity when P = 195 W, and for varying power and velocity with hatch distance, h = 0.1 mm, respectively.

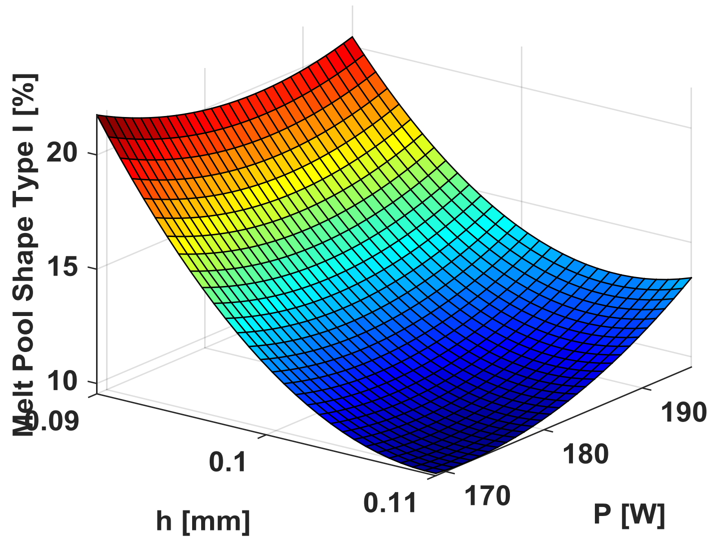

Figure 5.53. Surface plot for MP shape (Type I) vs. hatch distance and power (v_s = 800 mm/s).

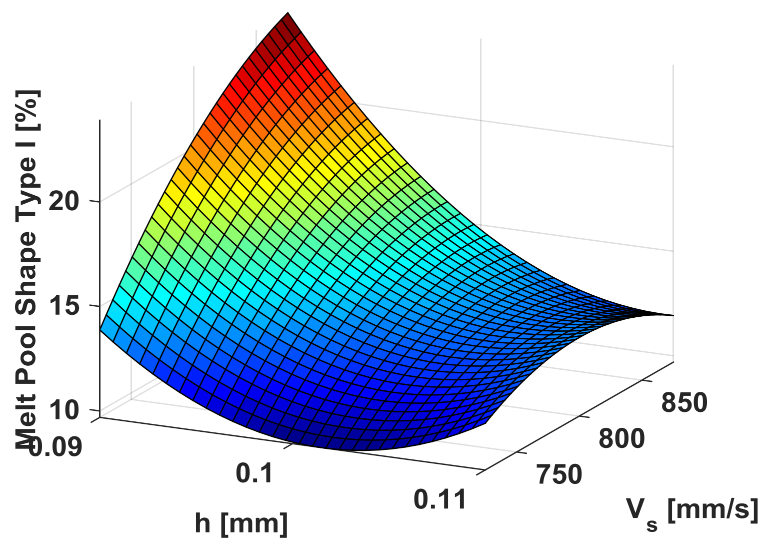

Figure 5.54. Surface Plot for MP Shape (Type I) vs. hatch distance and speed (P = 195 W).

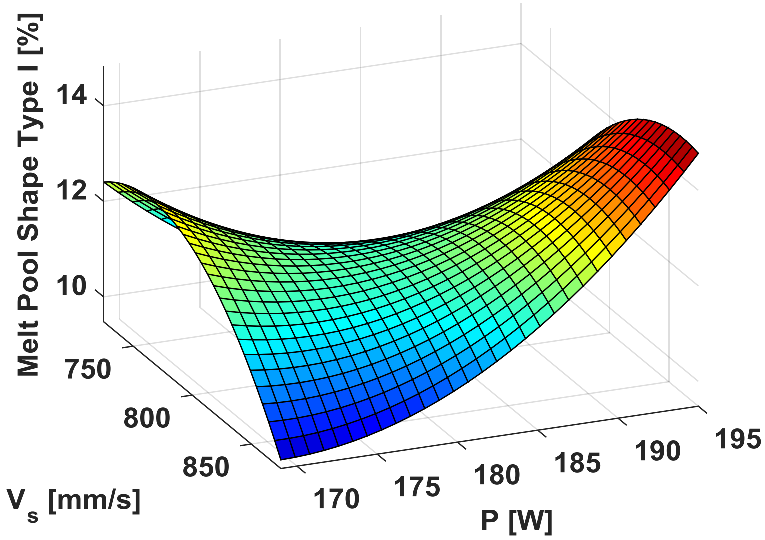

Figure 5.55. Surface Plot for MP Shape (Type I) vs. scanning speed and power (h = 0.1 mm).

5.3.4.2 Results of RSM Analysis for Melt Pool Shape – Type II

Table 5.15 provides the estimated coefficients and the corresponding p-value when fitting a quadratic response model with interactions (Equation 5.7) to the observed measurements for Type II melt pool shape. The R^2 value for this model is 0.8734, which indicates a good fit.

Table 5.15. Summary of second order model approximation: melt pool shape (Type II)

	Estimate	***p*-value**
β_0	2.70000	0.21477
β_1	3.12375	0.04365
β_2	0.19125	0.87594
β_3	-1.50250	0.25328
β_{11}	2.03750	0.28781
β_{22}	2.69750	0.17626
β_{33}	2.30500	0.23637
β_{12}	0.58000	0.73898
β_{13}	3.95750	0.06133
β_{23}	-6.32250	0.01212

ANOVA results show that scanning velocity-hatch distance interaction is the most significant factor in Type II melt pool shape. Other significant factors include laser power and laser power-hatch distance interaction. None of the quadratic terms are reported as significant, indicating that a linear model may be sufficient to characterize Type II melt pool shape. By comparing to the Type I melt pool shape results from the previous section, it can be seen that the large deformations in melt pool shape seen in Type I melt pools are not present in type II melt pools. Since Type II melt pools are not occurring near a heat affected zone from a previous track, these melt pools exhibit a almost nearly symmetrical shape, more in line with what would be expected initially of this process. Figures 5.56-5.58 show response surface plots obtained by keeping constant one of the process parameters: Figure 5.56 is a plot of Type II melt pool shape for varying hatch distance and laser power with scanning velocity, v_s = 800 mm/s. Analogously, Figures 5.57 and 5.58 show response surface plots for varying hatch distance and scanning velocity when P = 195 W, and for varying power and velocity with hatch distance, h = 0.1 mm, respectively.

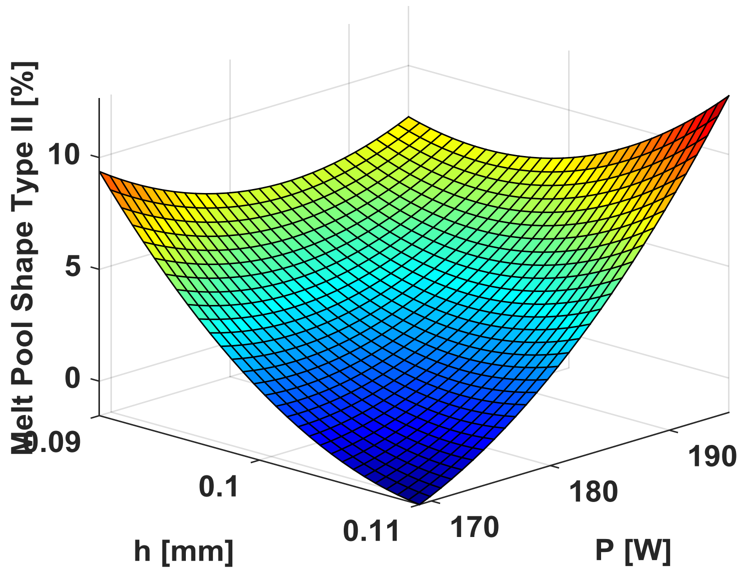

Figure 5.56. Surface plot for MP shape (Type II) vs. hatch distance and power (v_s = 800 mm/s).

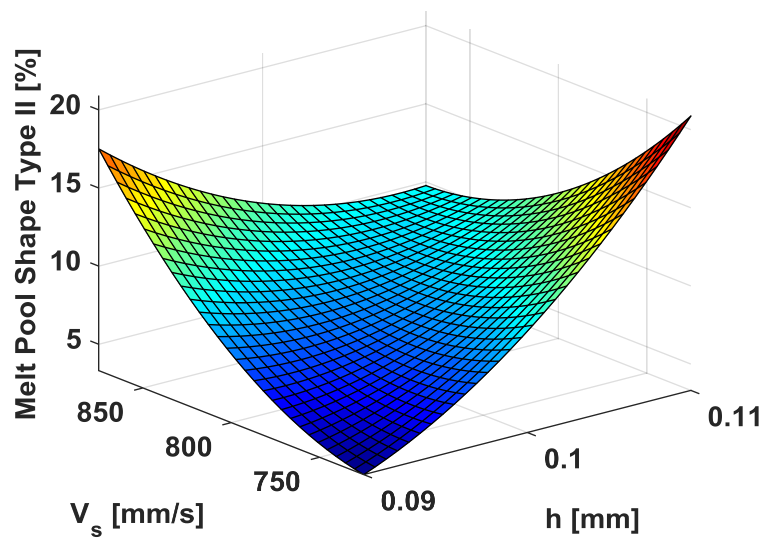

Figure 5.57. Surface Plot for MP Shape (Type II) vs. hatch distance and speed (P = 195 W).

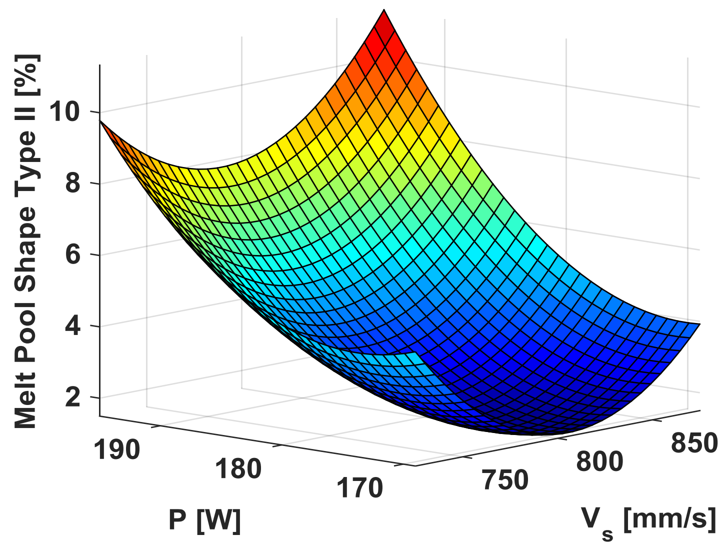

Figure 5.58. Surface plot for MP Shape (Type II) vs. scanning speed and power (h = 0.1 mm)

5.4 Summary & Conclusions

In this chapter, a complete and thorough analysis of IN 625 coupons additively fabricated using selective laser melting has been presented. A methodology was defined and applied to analyze a set of IN 625 test coupons fabricated using an EOS M270 machine, following a Box-Behnken experimental design. These coupons were analyzed with two objectives in mind: i) to determine coupon density/porosity, and ii) to determine melt pool dimensions (width, and depth) and shape for each coupon. Selecting the Box-Behnken design for design of experiments allowed the development of second-order (quadratic) models for prediction of melt pool geometry and coupon density, using Response Surface Methodology. Model coefficients are summarized in Table 5.16. ANOVA results showed which factors and factor interactions were significant for each of the design objectives.

Table 5.16. Summary of second order model coefficients with R^2 values.

	Density (90º)	Density (67º)	MP Width Type I	MP Width Type II	MP Depth Type I	MP Depth Type II	MP Shape Type I	MP Shape Type II
β_0	98.0933	98.2333	134.3333	108.6667	44.0000	36.3333	11.92000	2.70000
β_1	0.94625	0.87250	2.1250	4.5000	2.2523	2.2500	0.61875	3.12375
β_2	0.00875	0.14125	-1.3750	-3.2500	-2.5000	-1.500	0.56625	0.19125
β_3	-0.39250	-0.4513	-0.7500	-0.2500	-0.5000	-1.500	-4.76500	-1.50250
β_{11}	-0.0029	0.10708	12.9583	-3.4853	1.1250	3.70833	1.26125	2.03750
β_{22}	-1.2379	-1.1004	6.4583	0.54167	1.6250	0.20833	-1.52875	2.69750
β_{33}	-0.1954	-0.2304	1.7083	-1.4583	0.6250	-0.29167	3.13375	2.30500
β_{12}	0.4875	0.3700	10.7500	2.7500	3.2500	3.7500	1.93750	0.58000
β_{13}	0.0900	0.1050	-0.5000	4.2500	-0.2500	3.7500	1.28500	3.95750
β_{23}	0.1600	0.1175	-8.5000	3.7500	-0.2500	-2.2500	-2.50500	-6.32250
R^2	0.9891	0.9919	0.812	0.8495	0.5651	0.8682	0.8547	0.8734

The main conclusion of this chapter is the identification and definition of a dynamic melt pool, a condition which indicates that melt pool geometry is constantly changing as the laser scans a single track. The presence of melt pools of varying size may prove key in future research for microstructure characterization and the calculation of structural properties of finished parts. Last but not least, the experimental results presented in this chapter serve as one of the necessary and primary sources for validation of the finite element physics-based model introduced in Chapter 3 and Chapter 4. Validation of the finite element simulation model is the subject matter of Chapter 6 and process optimization using the predictive models presented in this chapter will be discussed in Chapter 7.

Chapter 6 MODEL VALIDATION AND SIMULATION EXPERIMENTS FOR SELECTIVE LASER MELTING OF INCONEL 625

6.1 Introduction

The research presented in Chapter 6 initially focuses on validation of the Finite Element simulation model for Selective Laser Melting of Inconel 625 presented in Chapters 3 and 4 for single track and multi-track processing, respectively. Two sources of experimental data will be used for validation purposes: melt pool width and depth measurements from optical image analysis and temperature readings obtained using a thermal camera.

Using the temperature field obtained from the simulation results, it is possible to estimate melt pool geometry, i.e. melt pool width and depth, and compare these values to the data obtained from the experimental analysis of IN 625 test coupons presented in Chapter 5. The Box-Behnken design of experiments used to produce the test coupons utilizes 13 unique combinations of process parameters. Additionally, three coupons were also built using the "default" settings corresponding to P = 195 W, v_s = 800 mm/s, h = 0.01 mm. Therefore, the results presented in Chapter 5 contain melt pool width and depth measurements for 14 unique combinations of process parameters. Melt pool width and depth was estimated for each of these 14 combinations of process parameters by using the physics-based finite element simulation model and results will be compared to those obtained via optical imaging. These results are presented in Section 2.1 of this chapter.

Furthermore, temperature predictions from the finite element model can be directly compared to data obtained from temperature readings using a thermal camera. A thermal camera was utilized to capture light intensity on the surface of the powder bed during the production of a test coupon using the "default" settings. Light intensity can be translated to temperature readings, which can then be compared to the temperature field obtained via FE simulation on the surface of the powder bed (XY-plane, z = 0). This technique offers further validation of the temperature field estimated using the physics-based simulation model, albeit for only one combination of process parameters.

Once the FE simulation model has been deemed to be a good representation of the SLM process, the model is used as a predictive tool to calculate variables which cannot be observed or measured experimentally in a reliable manner. In particular, the focus is on estimating peak temperature at the surface of the powder bed, T_{peak}, and the time spent by a particular location of the powder bed as part of the melt pool, t_m. These two criteria have been identified previously in Chapter 3 as possible key parameters to understand how microstructure of an SLM-produced part varies with changes in process parameters. For this purpose, simulation experiments following the Box-Behnken design is considered. Response surface methodology is used in a similar manner to that employed in Chapter 5 to analyze the effect of process parameters on T_{peak} and t_m, and develop a predictive second-order model.

Finally, a multi-objective optimization problem is portrayed, in which minimizing processing time and maximizing part density are two conflicting objectives. Constrains in the selection of process parameters suitable for SLM of IN 625 using the EOS M270 SLM machine are included in the formulation. The optimization technique utilized to solve the multi-objective constrained problem is explained, and the solution, i.e. the sets of process parameters in the Pareto front, is presented and discussed.

6.2 Validation of FE Model for SLM using Experimental Results

6.2.1 Validation of Temperature Predictions using Melt Pool Geometry

The first set of 18 coupons with 90º scanning rotation was analyzed using optical microscopy, as reported in Chapter 5. From these images and the melting marks left on the surfaces of IN 625 coupons, it was possible to measure melt pool geometry (width and depth) and melt pool shape. This data can be used to validate the finite element model, since melt pool geometry is a direct result of the temperature field. Recall that we define the melt pool as the convex hull of the powder-bed locations where the material is currently in liquid phase ($T > T_l$). Specifically, melt pool width and depth at a specific moment of the process can be obtained by looking at the corresponding time step of the YZ-plane temperature field in the FE simulation.

6.2.1.1 Experiment vs. Simulation Comparison – Melt Pool Geometry

Finite element simulations were executed matching the process parameters utilized to build the IN 625 coupons. The Box-Behnken design calls for 15 experimental units. However, note that Coupons 14, 15, and 17 used the same processing conditions (P = 182 W, v_s = 800 mm/s, h = 0.10 mm), corresponding to the center point of the Box-Behnken design. Therefore, it is not necessary to run the simulation with the same process parameters three times, as the finite element thermal model is deterministic and will show no variation regardless of how many times the process is simulated. By eliminating two repetitions, the total number of simulations decreases from the 15 originally stipulated by the Box-Behnken design to 13. Additionally, it is necessary to ensure that the analysis considers the melt pool at the same YZ-plane in order to match the observed plane in Optical Imaging. In other words, the x-coordinate at which the melt pool cross-section will be measured must match the amount of material that was removed due to electro-polishing of the coupons. This is crucial due to the dynamic nature of the melt pool explained in Chapter 5. Choosing the wrong *x*-coordinate would result in comparing two inherently different melt pools and would reflect negatively in the melt pool geometry comparison. Since a thin layer of 50 μm of material was removed via electro-polishing, this analysis measures the melt pool geometry for the YZ-planes corresponding to x = 0.05 mm and x = 4.05 mm, where x is a relative coordinate frame in which x = 0 is the beginning of the track and x = 4.1 mm is the end. There is uncertainty based on both the accuracy of the electro-polishing process, which will be reflected in the comparison.

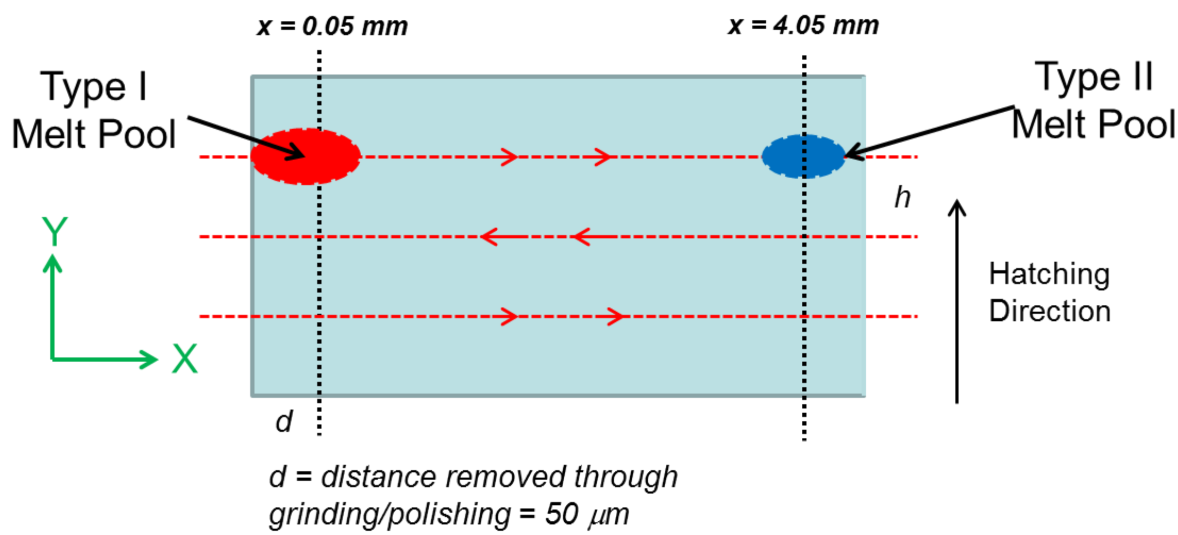

Figure 6.1. Location of electro-polished surface for melt pool geometry comparison.

Using the methodology explained in Chapter 3, the melt pool width and depth are calculated from the FE-based temperature profile for the second and third hatch of a 3-hatch simulation, at x = 0.05 mm and x = 4.05 mm, as shown in Figure 6.1. This provides a width and depth estimation for Type I and Type II melt pools, as reflected in Tables 6.1 and 6.2. Images of melt pool cross-section simulations are included in Appendix B.

Table 6.1. Simulated melt pool width measurements

Coupon #	Laser Power [W]	Scanning Velocity [mm/s]	Hatch Distance [mm]	Energy Intensity, E [J/mm^3]	Sim. MP Width – Type I [μm]	Sim. MP Width – Type II [μm]
01	169	875	0.10	96.57	132	102
04	195	875	0.10	111.43	148	110
06	182	875	0.09	115.56	143	108
08	182	725	0.11	114.11	156	117
09	195	800	0.11	110.80	155	116
12	182	725	0.09	139.46	167	118
14-15-17	182	800	0.10	113.75	146	112
16	195	725	0.10	134.48	160	122
18	182	875	0.11	94.55	138	107
20	169	725	0.10	116.55	148	111
21	169	800	0.09	117.36	142	108
23	169	800	0.11	96.02	136	107
29	195	800	0.09	135.42	162	118
34-35-36	195	800	0.10	121.88	157	117

Table 6.2. Simulated melt pool depth measurements

Coupon #	Laser Power [W]	Scanning Velocity [mm/s]	Hatch Distance [mm]	Energy Intensity, E [J/mm^3]	Sim. MP Depth - Type I [μm]	Sim. MP Depth - Type II [μm]
01	169	875	0.10	96.57	48	33
04	195	875	0.10	111.43	53	38
06	182	875	0.09	115.56	52	36
08	182	725	0.11	114.11	57	42
09	195	800	0.11	110.80	56	42
12	182	725	0.09	139.46	59	43
14-15-17	182	800	0.10	113.75	54	40
16	195	725	0.10	134.48	62	45
18	182	875	0.11	94.55	49	35
20	169	725	0.10	116.55	54	39
21	169	800	0.09	117.36	50	37
23	169	800	0.11	96.02	49	37
29	195	800	0.09	135.42	57	42
34-35-36	195	800	0.10	121.88	57	42

It is now possible to compare the optical imaging analysis results with the simulation results. A straight forward way of comparing results is to look at melt pool geometry by type with respect to energy intensity. All simulation predictions for Type I melt pool width are within one standard deviation of the average, except for the experimental unit processed with the highest energy intensity, as shown in Figure 6.2a.

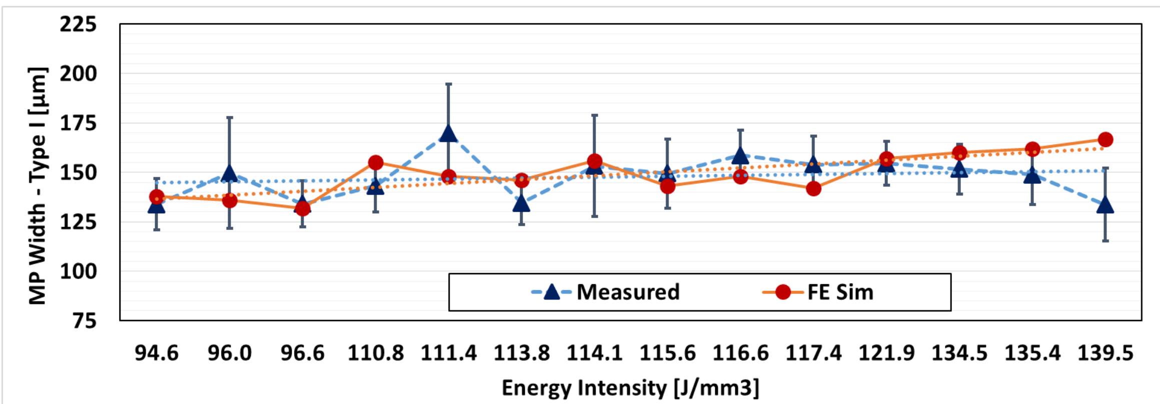

(a)

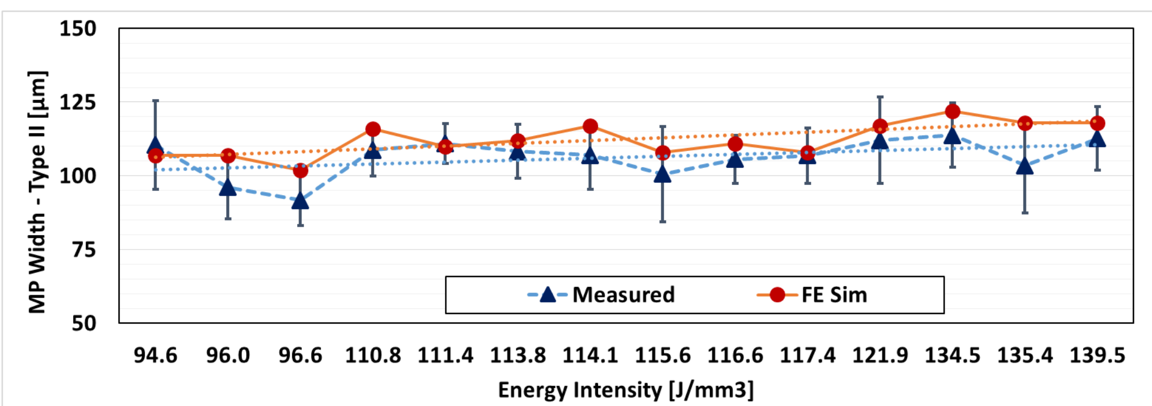

(b)

Figure 6.2. Measured and predicted melt pool width vs. energy intensity: a) Type I, b) Type II

Figure 6.2b indicates that Type II melt pool width is over-estimated by the simulation, but well within one standard deviation of the measured average using optical imaging. The linear fit for the measured data and the simulation results are essentially parallel to one another, which shows the accuracy of the prediction. Effect of increasing energy intensity on the melt pool depth is shown in Figure 6.3 where measured and simulated melt pool depth values at various energy intensity levels obtained from experimental design are compared yielding to very good agreement for especially Type II melt pools.

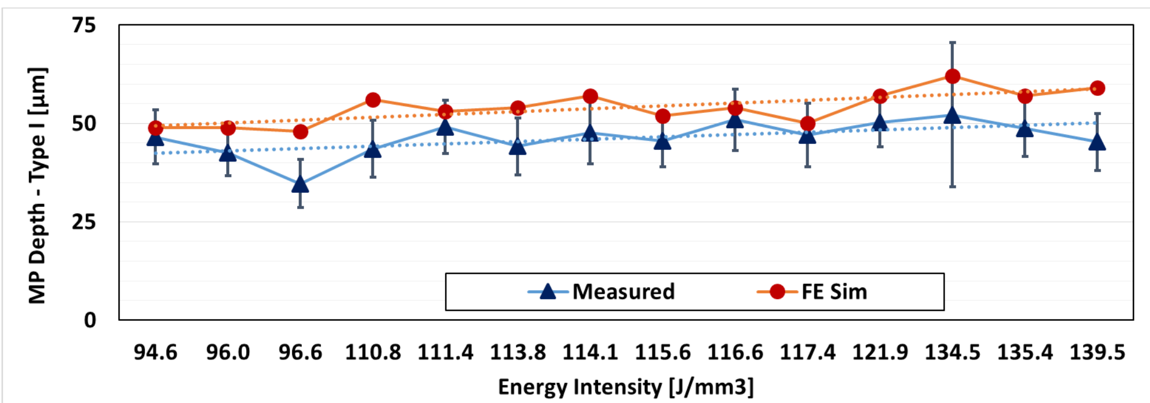

(a)

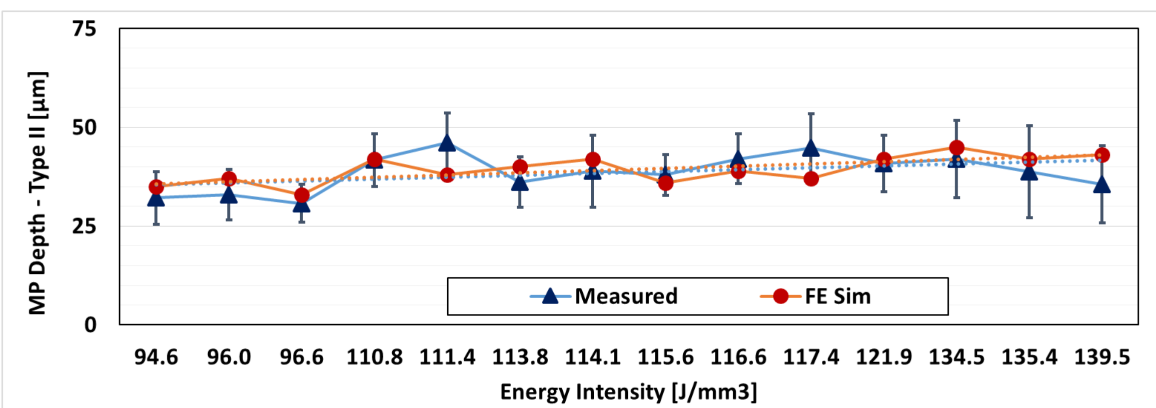

(b)

Figure 6.3. Measured and predicted melt pool depth vs. energy intensity: a) Type I, b) Type II

6.2.2 Validation of Temperature Predictions using Thermal Camera

A thermal camera was used to capture temperature readings while building one of the coupons, Coupon #35, using the default process parameter settings: P = 195 W, v_s = 800 mm/s, h = 0.10 mm. An IRC912 infrared camera was utilized in this set-up.

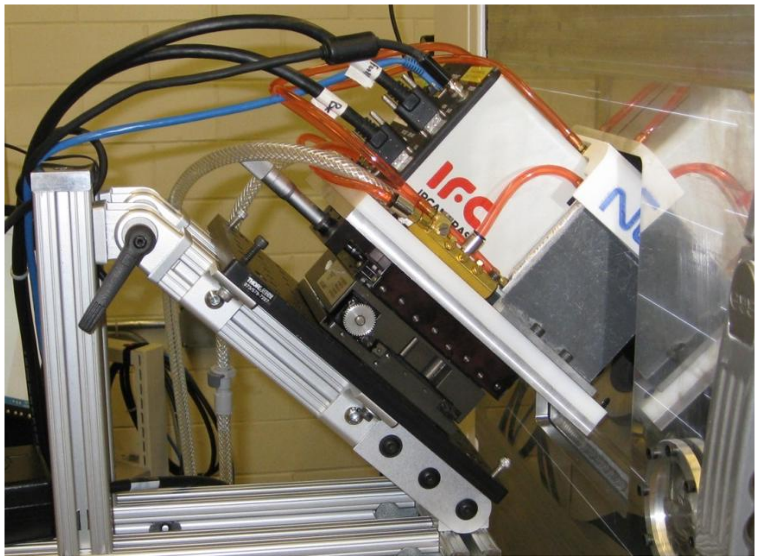

Figure 6.4. Side-view of the EOS machine, custom door, and thermal camera (Source: NIST)

The thermal camera was mounted to a specially-modified door of the EOS M270 SLM machine, as shown in Figure 6.4 (Lane et al., 2015). The camera was inclined at a 43.7º angle (see Figure 6.5a) and the pixel size of the resulting images is 36 μm. This pixel size corresponds to a scenel size of 36 μm in the x-direction and 52 μm in the y-direction, as seen in Figure 6.5b.

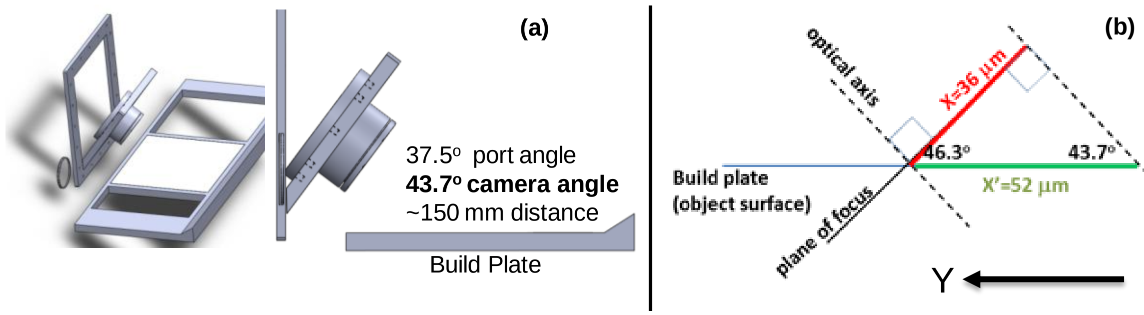

Figure 6.5. a) SolidWorks model of EOS build chamber and custom viewpoint, b) Optical axis and plane of focus. (Source: NIST)

The thermal camera captures a raw signal that must be processed and converted to temperature readings based on the material's emissivity. Uniform emissivity values of ε = 0.2, 0.5, and 1 were used to calculate the apparent temperature. Limitations introduced by the black body used for calibration of the thermal camera limit the reliability of the apparent temperature readings to the 700 – 1400 K range, as shown in Figure 6.6. The numerical precision associated with this conversion is 0.1°C.

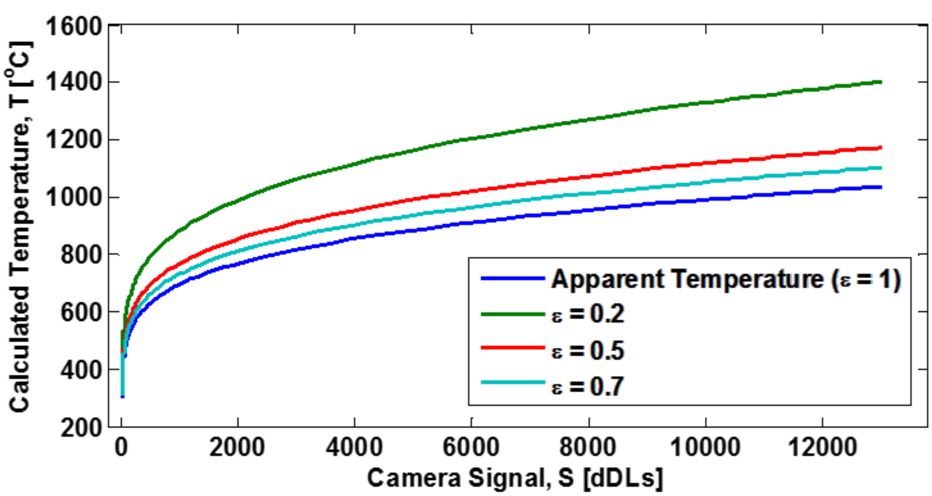

Figure 6.6. Calibration curve for Signal-to-Temperature conversion (Source: NIST)

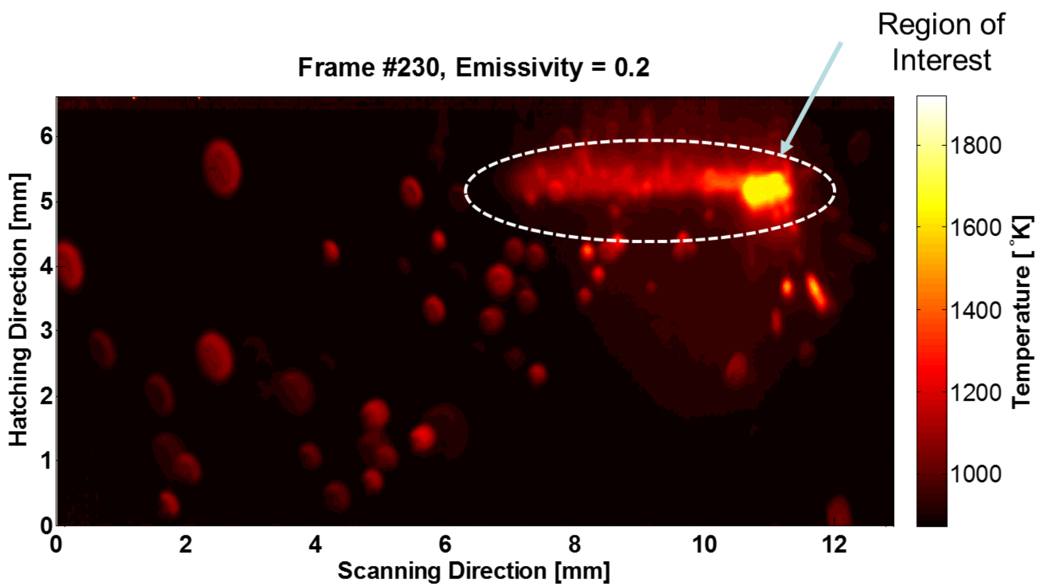

Figure 6.7. Temperature Contour from Thermal Camera at a fixed frame (Emissivity, ε = 0.2)

The camera captures 1800 frames per second, which corresponds to one frame each 0.555 ms. Therefore, the video captured by the camera provides a full temperature field once every 0.555 ms. A contour plot of the powder-bed's temperature field is shown in Figure 6.7. This figure provides an overview of the SLM process, as the general location of the scanned track, and specifically the melt pool, can be identified. Spattering can also be seen as hotter spots picked up by the thermal camera as they float across the lens. To visualize more data related to the temperature readings of specific locations, it is possible to plot temperature vs. time at a specific (x,y) coordinate on the powder bed, as shown in Figure 6.8.

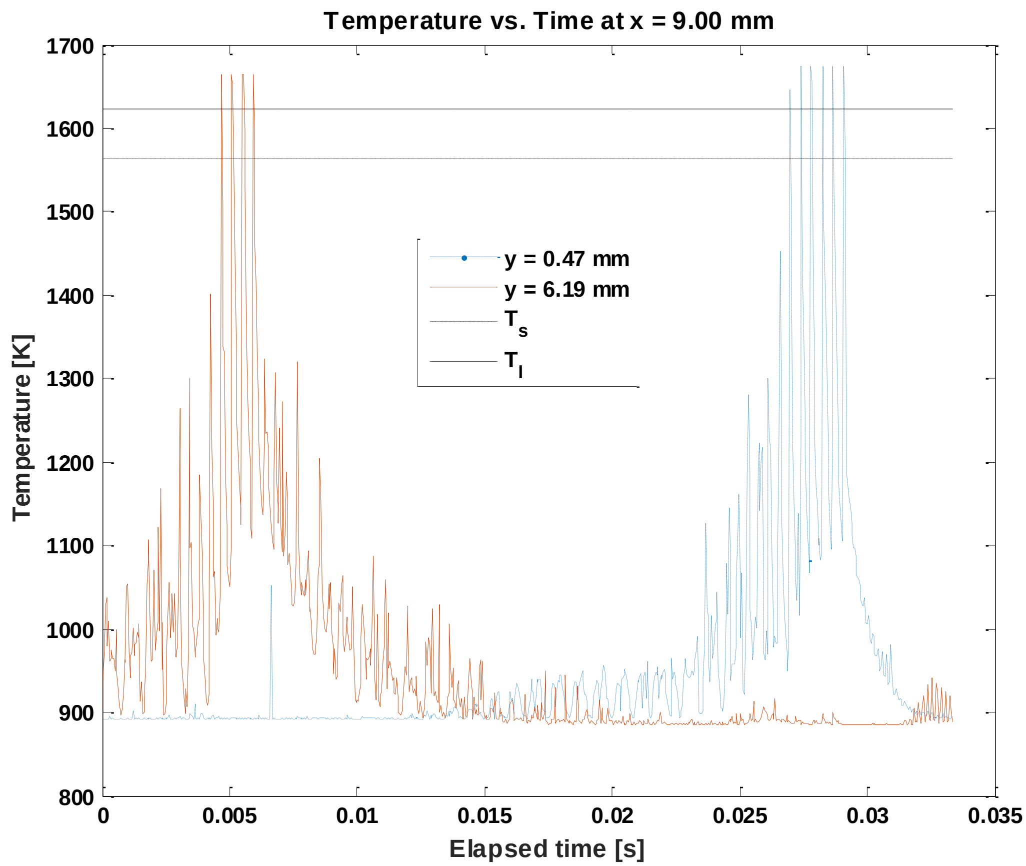

Figure 6.8. Temperature vs. Time at two fixed locations (Emissivity, ε = 0.2).

Similarly, it is possible to plot the temperature profile along a chosen hatch (fixed *y*-location) at a given moment in time, as shown in Figure 6.9. By fixing time, it is possible to predict the location of the center of the beam, as this would be the hottest point in the field. This way, we can determine the corresponding time to match against the simulation results. The obvious obstacle to overcome is the inability to determine the exact coordinates along the powder bed from the thermal camera data.

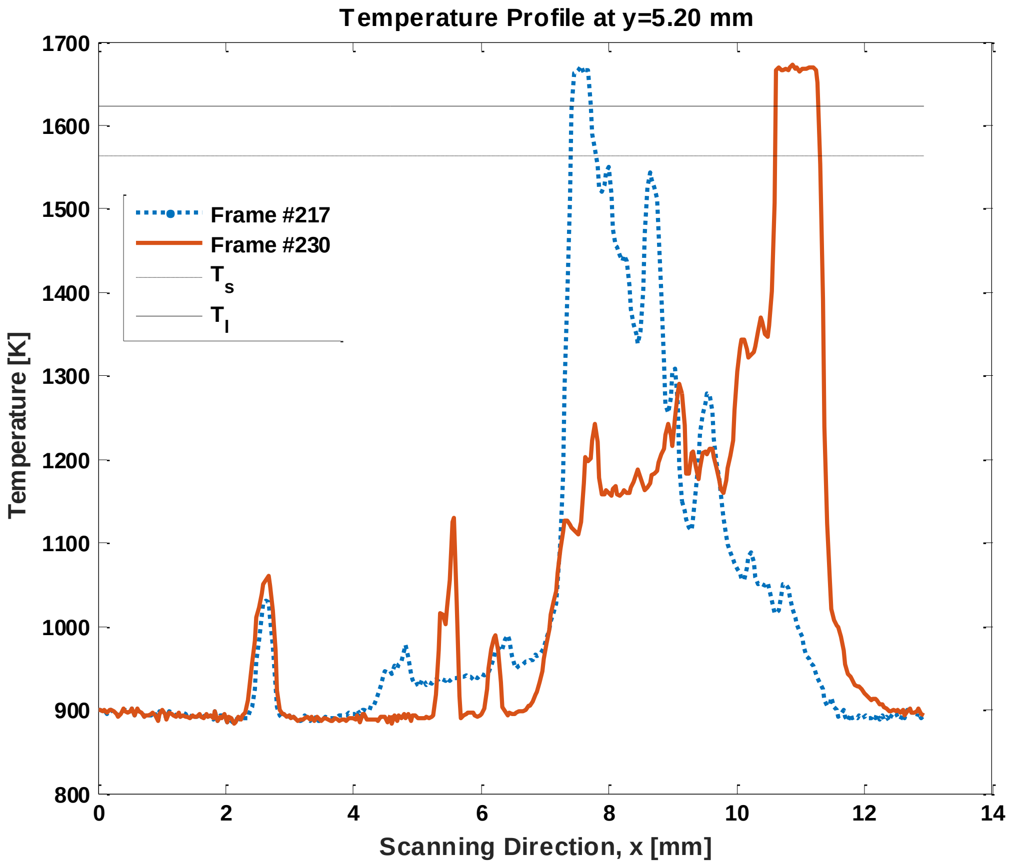

Figure 6.9. Temperature Profile at a fixed time and hatch location (Emissivity, ε = 0.2)

Temperature profiles for fixed frames can be compared against each other by synchronizing the images obtained from the camera with the corresponding time in the simulation, as shown in Figure 6.10 and Figure 6.11. This type of comparison allows the distinction between Type I and Type II melt pools to be observed. This comparison also includes the two available emissivity values: 0.2 and 0.5, as the true emissivity is somewhere in this range. This is more readily achievable than the fixed location scenario described in the previous paragraph, because it is easier to determine the moment where a hatch is completed and a new hatch scanning begins. However, the temperature readings obtained by the camera are reliable in a range that does not include the solidus/liquidus temperature. Therefore, the thermal camera images cannot be used to predict melt pool dimensions or to estimate peak temperatures.

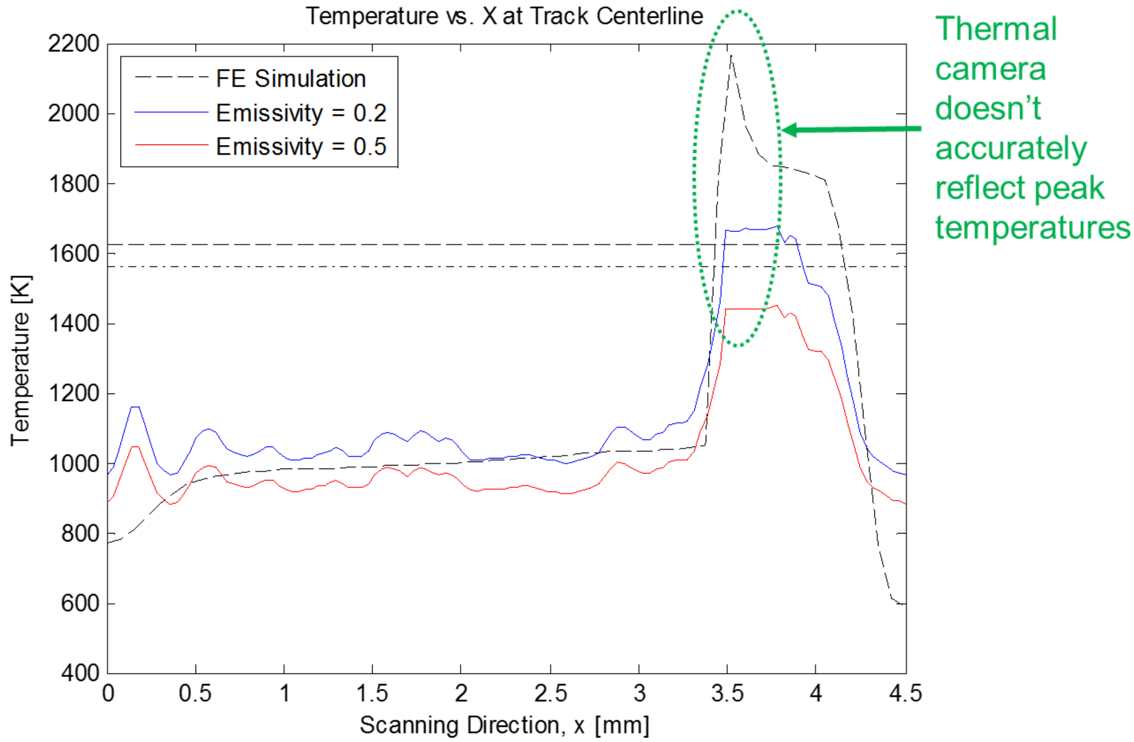

Figure 6.10. Temperature comparison: Thermal Imaging vs. FE Simulation (Type I)

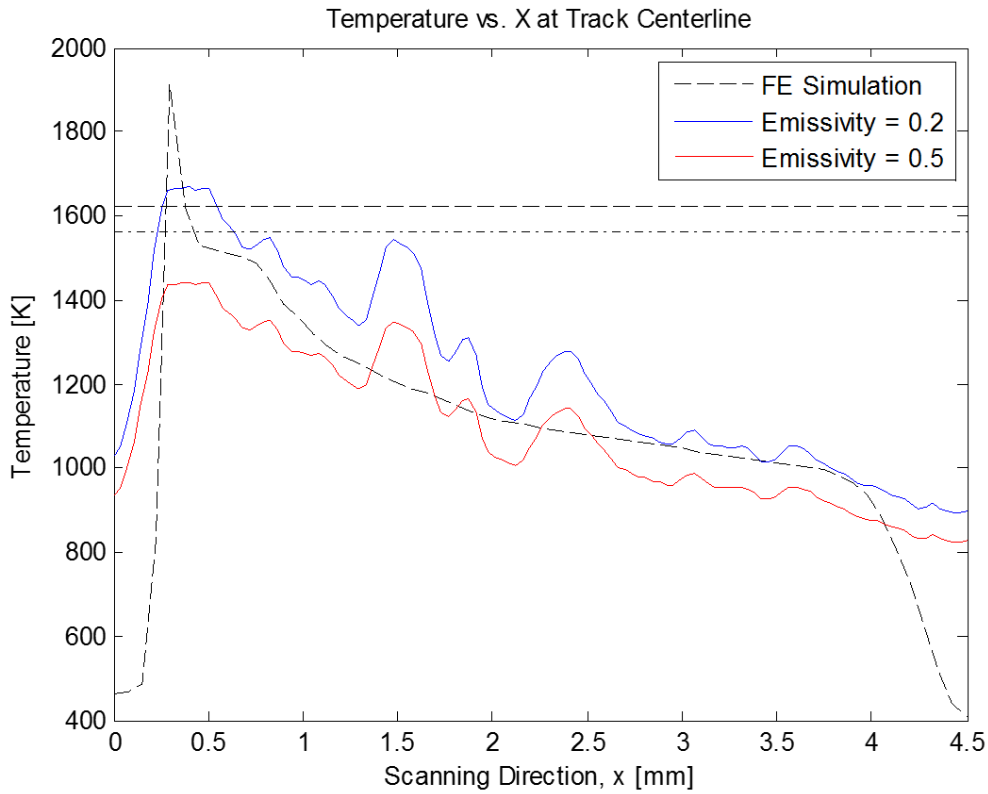

Figure 6.11. Temperature comparison: Thermal Imaging vs. FE Simulation (Type II)

6.3 Simulation Experiments

The purpose of the simulation experiments is to provide information that cannot be measured accurately during the SLM process. Two specific examples are peak temperature (the maximum temperature of the melt pool), and time above melting (amount of time a powder-bed location remains in liquid form, $T > T_l$). These parameters are relevant in this analysis because they are tightly connected to the resulting mechanical properties of the part. Therefore, the ability to predict and control maximum temperature and heating and cooling rates will prove beneficial to process efficiency.

6.3.1 Peak Temperature Prediction and Analysis

Peak temperature (T_{peak}) was defined as the maximum temperature achieved by a location of the powder bed during the 3-hatch simulation. The location where the peak temperature is achieved corresponds to the beginning of the 3rd track, where a Type I melt pool is observed. The peak temperatures reflected in Table 6.3 are obtained from the XY-plane simulation, i.e. on the surface of the powder bed.

Table 6.3. Predicted peak temperature at all experimental processing conditions

Coupon #	Laser Power P [W]	Scanning Velocity v_s [mm/s]	Hatch Distance h [mm]	Energy Intensity, E [J/mm^3]	Peak Temperature T_{peak} [K]
01	169	875	0.10	96.57	1985.7
04	195	875	0.10	111.43	2182.4
06	182	875	0.09	115.56	2124.1
08	182	725	0.11	114.11	2291.8
09	195	800	0.11	110.80	2280.2
12	182	725	0.09	139.46	2311.0
14-15-17	182	800	0.10	113.75	2226.7
16	195	725	0.10	134.48	2421.7
18	182	875	0.11	94.55	2076.8
20	169	725	0.10	116.55	2190.3
21	169	800	0.09	117.36	2121.6
23	169	800	0.11	96.02	2083.0
29	195	800	0.09	135.42	2338.5
34-35-36	195	800	0.10	121.88	2302.9

A better way to visualize how the maximum temperature behaves is to plot peak temperature as a function of energy intensity, as shown in Figure 6.12. The general trend shows that peak temperature increases as energy intensity increases.

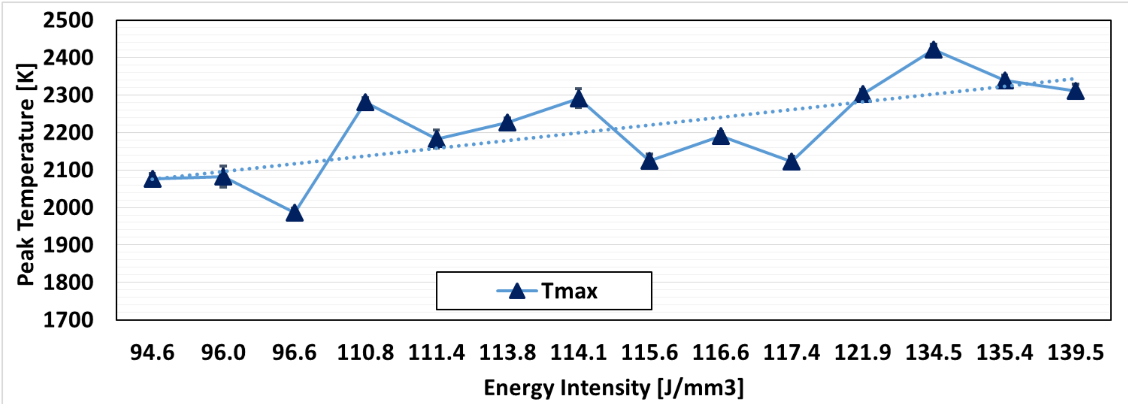

Figure 6.12. Predicted peak temperature, T_{peak}, as a function of energy intensity, E.

Notice that peak temperature's behavior is non-linear, so it is also useful to look at how peak temperature changes based on the three factors considered in the experimental design. Figures 6.13-6.15 show effect plots for peak temperature relative to laser power, scanning speed, and hatch distance.

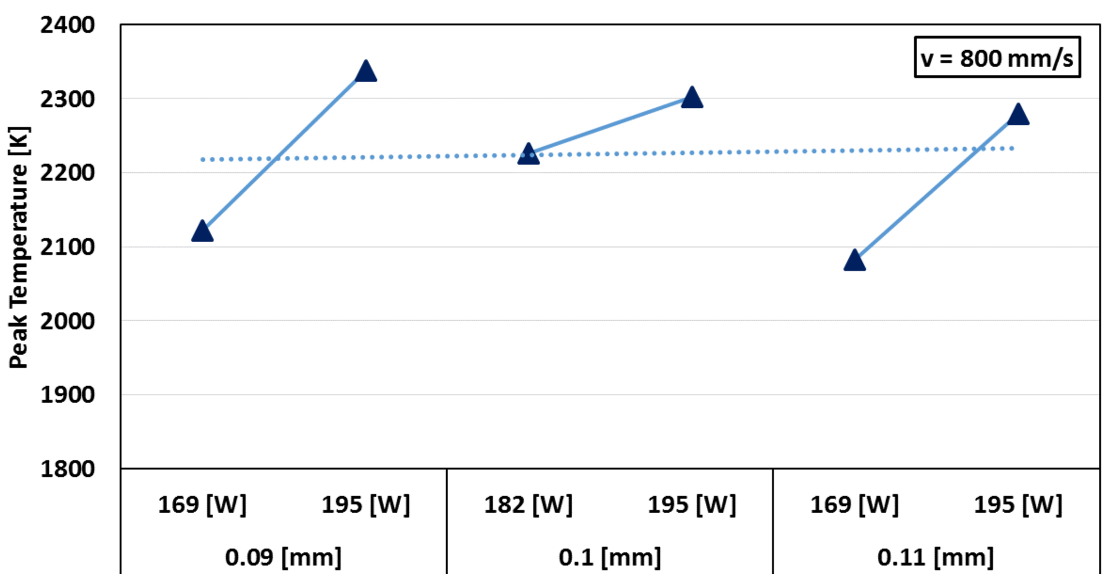

Figure 6.13. Predicted peak temperature, T_{peak}, vs. laser power, P, and hatch distance, h, for constant scanning speed (v_s = 800 mm/s).

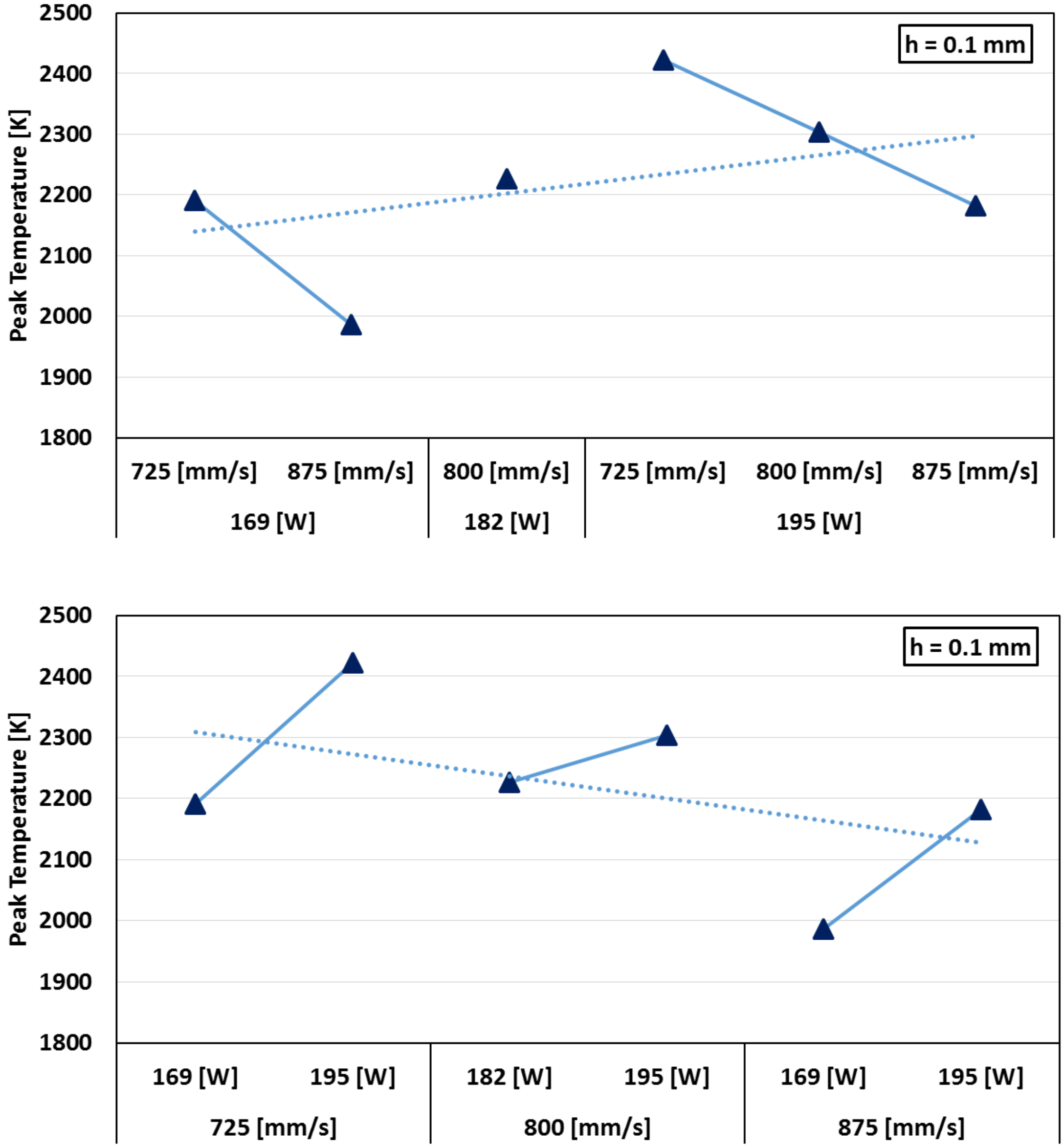

Figure 6.14. Predicted peak temperature, T_{peak}, vs. laser power, P, and scanning velocity, v_s, for constant hatch distance (h = 0.10 mm)

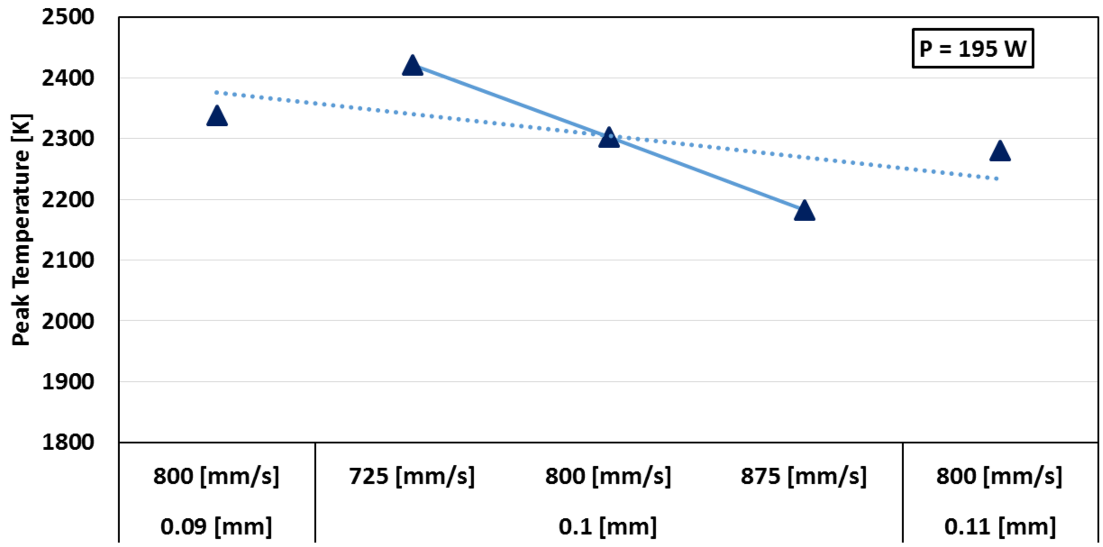

Figure 6.15. Predicted peak temperature, T_{peak}, vs. scanning speed and hatch distance, for constant laser power (P = 195 W)

The effect plots show that peak temperature increases with increasing power and decreases with increasing scanning speed and hatch distance. Since the Box-Behnken design of experiments was used, it is possible to fit a second order response model to the data. This model can then be used to predict peak temperature for any combination of laser power, scanning speed, and hatch distance.

The RSM analysis and omnibus ANOVA were performed using R statistical software for data analysis. Recall that the general form of the second order model for k process variables is given by Equation 6.1.

$$\eta = \beta_0 + \sum_{i=1}^{k} \beta_i x_i + \sum_{i=1}^{k} \beta_{ii} x_i^2 + \sum \sum_{i<j=2}^{k} \beta_{ij} x_i x_j + \epsilon \qquad (6.1)$$

The model provides the estimates for the β_i's in Equation 6.1, where i = 1, 2, and 3 correspond to laser power, scanning speed, and hatch distance, respectively, with the associated p-values. These coefficients are presented in Table 6.4. The R^2 value for this model is 0.998, which indicates that the data is very close to the fitted model.

Table 6.4. Summary of second order model approximation (Peak Temperature)

	Estimate	***p*-value**
β_0	2226.7	9.819e-13
β_1	105.2750	3.549e-07
β_2	-105.7250	3.474e-07
β_3	-20.4250	0.001045
β_{11}	-13.3875	0.029099
β_{22}	-18.2875	0.009012
β_{33}	-7.4875	0.150970
β_{12}	-8.6750	0.096470
β_{13}	-4.9250	0.298426
β_{23}	-7.0250	0.158908

Significant factors are those whose p-value is less than 0.1. Laser power and scanning velocity appear to be the most significant terms, as both the linear and quadratic terms are significant. The only non-significant factors are the quadratic hatch distance factor and the scanning velocity-hatch distance interaction. Additionally, response surface plots can be generated using this model. Figures 6.16-6.18 show response surface plots obtained by fixing one of the process parameters and varying the other two: Figure 6.16 is a plot of relative density for varying hatch distance and laser power when scanning velocity, v = 800 mm/s. Analogously, Figures 6.17 and 6.18 show response surface plots for varying hatch distance and scanning velocity and constant laser power (P = 195 W), and for varying power and velocity for constant hatch distance (h = 0.1 mm), respectively. It can be seen that the highest peak temperature is obtained at a non-linear combination of power, velocity and hatch distance. Low peak temperatures are obtained by implementing low laser power, highest laser power, and the largest hatch distance, but incomplete fusion may occur.

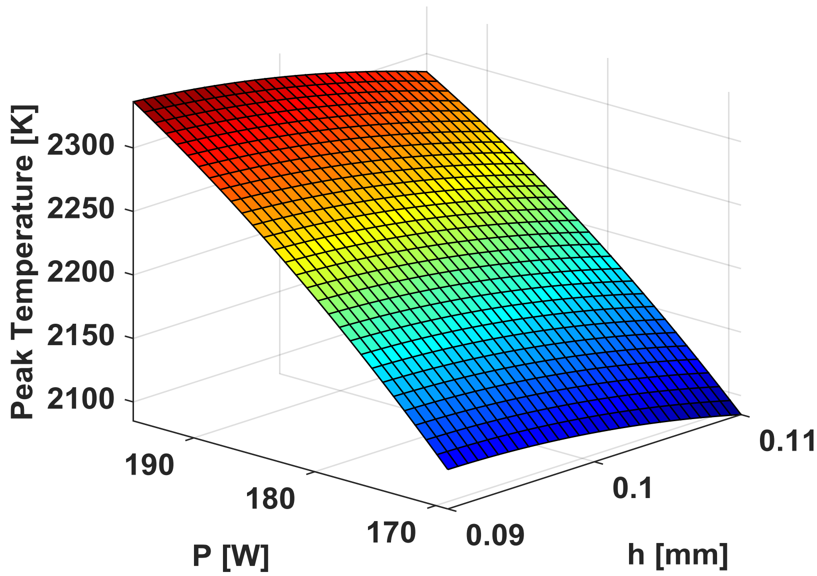

Figure 6.14. Response surface plot for peak temperature vs. hatch distance and power (v_s = 800 mm/s)

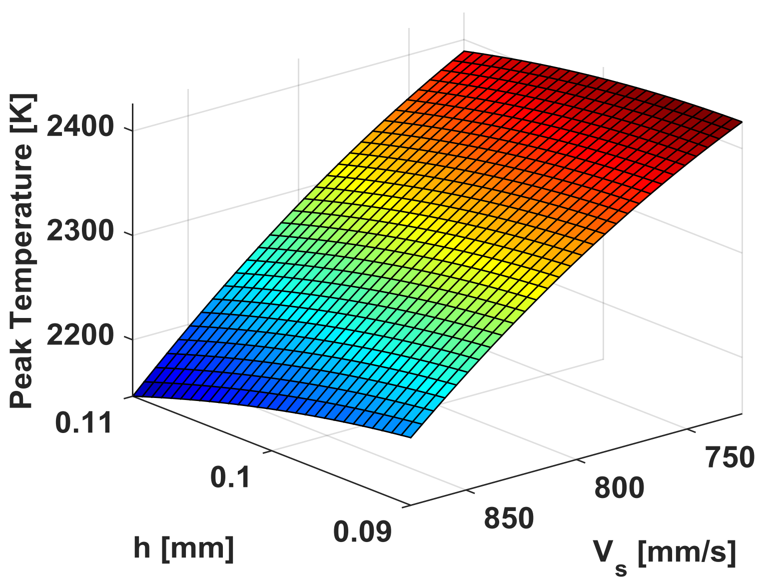

Figure 6.15. Response surface plot for peak temperature vs. hatch distance and velocity (P = 195 W)

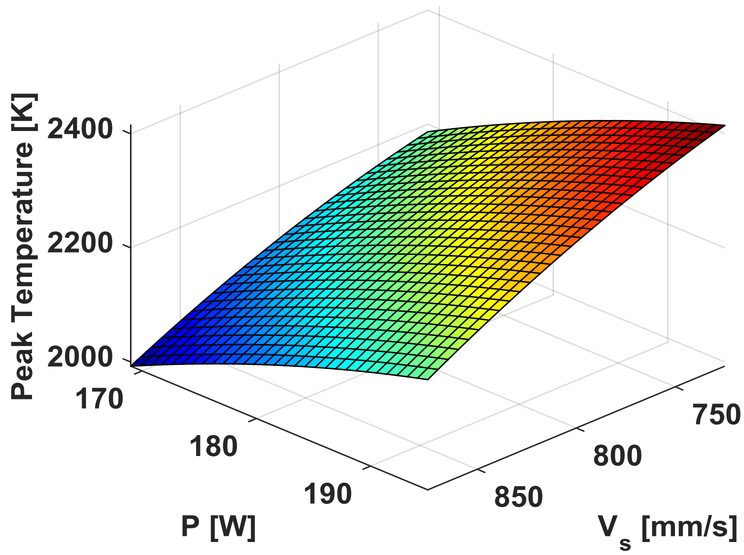

Figure 6.16. Response surface plot for peak temperature vs. velocity and power (h = 0.1 mm)

Note that the surfaces in all three previous figures tend to be planar in nature. Therefore, a first-order model with interactions may suffice to accurately predict peak temperature as a function of laser power, scanning velocity, and hatch distance.

6.3.2 Time above Melting Temperature Prediction and Analysis

Time above melting temperature, t_m, is defined as the amount of time that a location of the powder bed remains uninterruptedly in fully liquid state, or $T > T_l$. In other words, this is the length of time during which this specific location is part of the melt pool. This term must not be confused with time of melting, which is the time necessary to go from solid (powder) to liquid state ($T_s < T < T_l$) and corresponds to the time elapsed in the solidus-liquidus region. Due to the dynamic nature of melt pool geometry, it is of interest to analyze time above melting temperature for different locations along the scanned track. The locations studied in this analysis correspond to the beginning of the 3rd track (x_{rel} = 0.05 mm), where a Type I melt pool is observed, and the end of the 2nd track (x_{rel} = 4.05

mm), where a Type II melt pool is observed. The times above the melting temperature shown in Table 6.5 are obtained from the XY-plane simulation, i.e. on the surface of the powder bed (z = 0).

Table 6.5. Predicted time above melting at all experimental processing conditions

Coupon Number	**Laser Power P [W]**	**Scanning Velocity v_s [mm/s]**	**Hatch Distance h [mm]**	**Energy Intensity, E [J/mm^3]**	**Time above melting, t_m Type I [ms]**	**Time above melting, t_m Type II [ms]**
01	169	875	0.10	96.57	0.25	0.13
04	195	875	0.10	111.43	0.43	0.22
06	182	875	0.09	115.56	0.34	0.17
08	182	725	0.11	114.11	0.60	0.30
09	195	800	0.11	110.80	0.56	0.27
12	182	725	0.09	139.46	0.61	0.30
14-15-17	182	800	0.10	113.75	0.47	0.21
16	195	725	0.10	134.48	0.78	0.39
18	182	875	0.11	94.55	0.33	0.17
20	169	725	0.10	116.55	0.49	0.25
21	169	800	0.09	117.36	0.34	0.18
23	169	800	0.11	96.02	0.36	0.18
29	195	800	0.09	135.42	0.56	0.27
34-35-36	195	800	0.10	121.88	0.57	0.28

A better way to visualize how time above melting temperature changes as a function of process parameters is to plot t_m as a function of energy intensity, E, as shown in Figure 6.19. The general trend seen is similar to the one observed for peak temperature, where t_m increases as energy intensity increases.

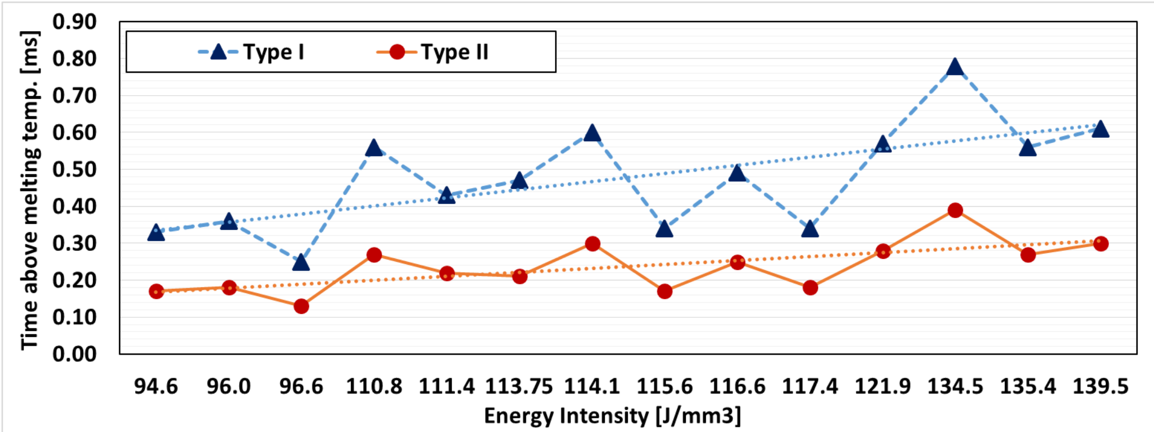

Figure 6.19. Predicted time above melting temperature, t_m, as a function of energy intensity, E

Notice that time above melting temperature's behavior is non-linear, so it is necessary to look at how it changes based on the three factors considered in the experimental design. Figures 6.20-6.22 show effect plots for peak temperature relative to laser power, scanning speed, and hatch distance.

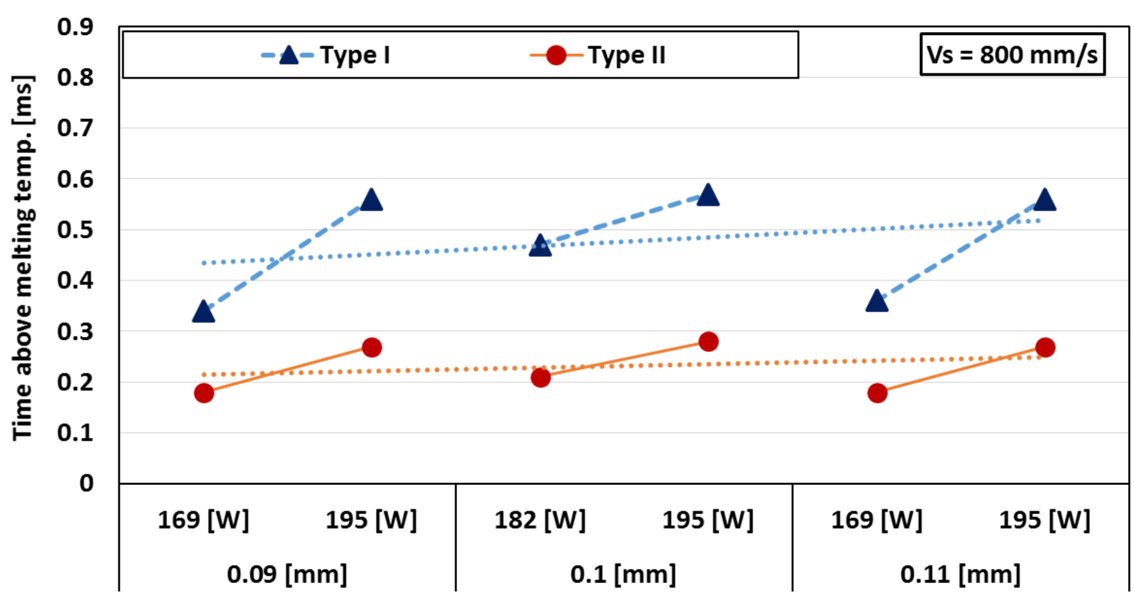

Figure 6.20. Predicted time above melting temp vs. laser power and hatch distance.

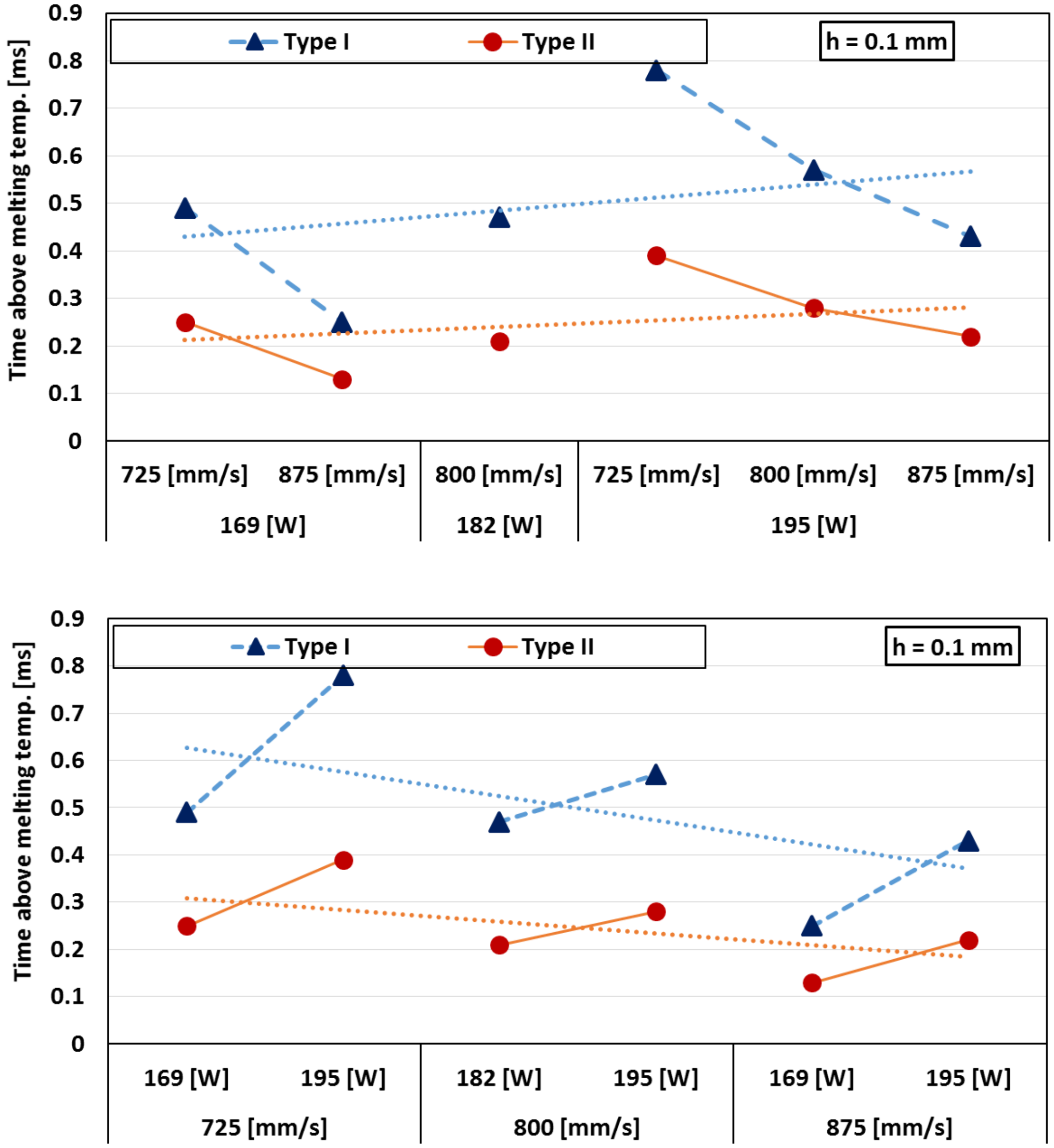

Figure 6.21. Predicted time above melting temp vs. laser power and scanning speed.

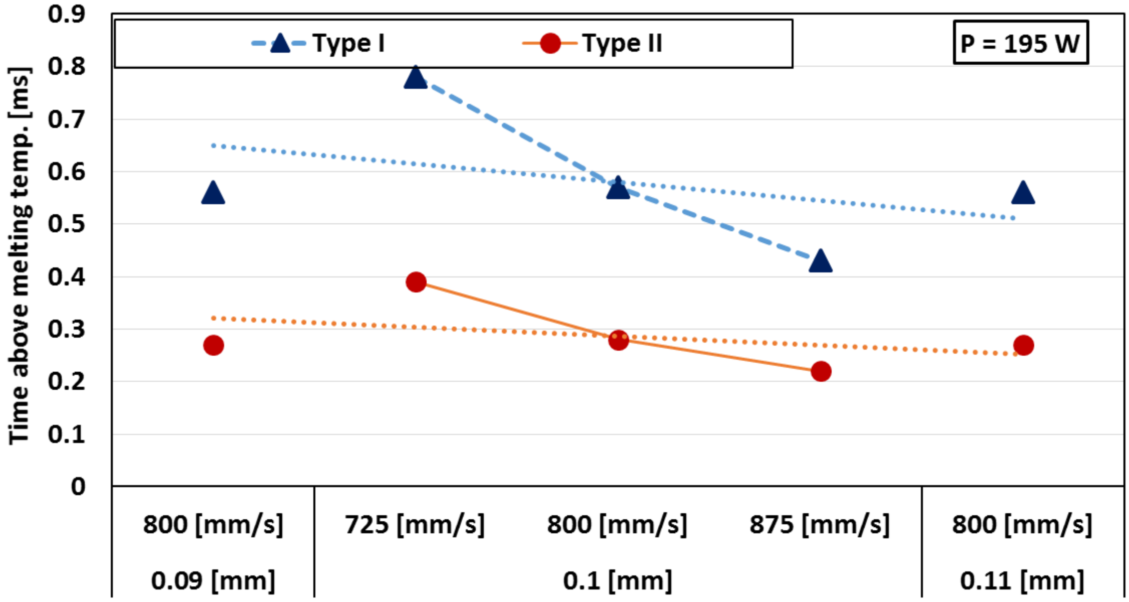

Figure 6.22. Predicted time above melting temp vs. scanning speed and hatch distance.

The effect plots show that time above melting temperature increases with increasing power and decreases with increasing scanning speed and hatch distance, and behaves in the same way as peak temperature for both Type I and Type II melt pools.

6.4 Summary and Conclusions

In this chapter, the finite element simulation model developed in Chapters 3 and 4 was validated by comparing temperature-based melt pool geometry predictions with measured melt pool width and depth obtained from the optical image analysis presented in Chapter 5. Additionally, thermal camera data recorded during the build of a coupon was used to further confirm that temperature predictions of particles in powder/solid phase fall within the temperature range estimated by the thermal camera.

After validation of the physics-based finite element model was presented, the model was used to execute simulation experiments following the same design of experiments approach as for validation purposes, the Box-Behnken design. From the simulation results, the peak temperature and the time above melting for specific locations of the powder bed was calculated. Second order models were obtained and the behavior of these key characteristics was described in terms of process parameters: laser power, scanning speed, and hatch distance.

The second-order response models obtained from experimental analysis in Chapter 5 and from finite element simulations in Chapter 6 can be used as a basis for process optimization. The development and application of a multi-objective optimization algorithm for selective laser melting of Inconel 625 powder material will be the focus of discussion of the next chapter, Chapter 7.

Chapter 7 MULTIPLE-OBJECTIVE OPTIMIZATION FOR SELECTIVE LASER MELTING OF INCONEL 625

7.1 Introduction

The work presented in Chapter 7 is aimed at determining the optimal process parameters that generate certain desirable outputs of the selective laser melting process for IN 625 powder material. For example, identifying process parameters and scanning strategy that produces nearly fully dense parts which requires optimization of process parameters for maximizing relative density. Another example could be obtaining energy efficient processing conditions which require optimizing process parameters for minimizing energy intensity while maintaining high relative part density. These objectives can be constructed by using the response surface regression models obtained through experimental analysis and finite element based simulation results.

Response, or objective, functions in a given process can be in conflict with each other, meaning that a variation to a process parameter can have a positive effect in one of the outputs, but a negative effect in one of the others. This trade-off between objectives is the focus of multi-objective optimization studies.

There are several well-known techniques for multi-objective optimization, such as the family of Genetic Algorithms (GAs), Reactive Search Optimization (RSO), Normal Boundary Intersection (NBI), and Particle Swarm Optimization (PSO), among others. For this study, Multi-Objective Particle Swarm Optimization (MOPSO) and a Multi-Objective Genetic Algorithms (MOGA) were selected as the optimization techniques to be implemented to find the best solution in the available process space.

7.1.1 Multiple-objective Particle Swarm Optimization (MOPSO)

Particle Swarm Optimization (PSO) is a population-based stochastic optimization technique developed by Kennedy and Eberhart (Kennedy and Eberhart, 1995). PSO is a robust and efficient technique for solving complex optimization problems by modeling the solution space and identifying potential solutions as individual particles of a swarm. These particles move through the solution space seeking a “best” solution. The position of a particle is modified by using its current location and its velocity: the rate at which their position of the particle changes between iterations. As the model is iterated, the swarm focuses more and more on an area of the solution space, which contains these “best” solutions (Blum and Li, 2008). PSO algorithms have been applied to optimization problems across many disciplines. In recent years, PSO has become a popular optimization technique in advanced manufacturing processes (Ciurana et al., 2009, Karpat and Özel, 2007, Vazquez et al., 2011).

In PSO, the velocity of each particle is modified iteratively using its own best position (i.e., the best position found by the particle so far), and the best position found by particles in its neighborhood, as given by Equation 7.1 and Equation 7.2:

$$\boldsymbol{v}_i^{k+1} = w\boldsymbol{v}_i^k + c_1\boldsymbol{R}_1\left(\boldsymbol{p}_i - \boldsymbol{x}_i^k\right) + c_2\boldsymbol{R}_2\left(\boldsymbol{p}_g - \boldsymbol{x}_i^k\right) \tag{7.1}$$

$$\boldsymbol{x}_i^{k+1} = \boldsymbol{x}_i^k + \boldsymbol{v}_i^{k+1} \tag{7.2}$$

Where $\boldsymbol{v}_i^k$ denotes the velocity of particle i at iteration k, $\boldsymbol{x}_i^k$ denote its current position in space, $\boldsymbol{p}_i$ denotes the personal best position of particle i, $\boldsymbol{p}_g$ denotes the best position found by particles in particle i’s neighborhood, w represents an inertia weight, c_1 and c_2 are acceleration coefficients, and $\boldsymbol{R}_1$ and $\boldsymbol{R}_2$ are two vectors of random numbers generated uniformly in the range [0, 1] to introduce stochastic behavior. Each individual particle searches for a new best solution in a region defined by these two criteria: its personal best position and the best position from its neighborhood.

Different information propagation techniques will have unique effects in the PSO algorithm. Limiting the information propagation by using small neighborhood topologies has been shown to perform better on complex problems, whereas larger neighborhoods generally perform better on simpler problems, as described by Mendes (Mendes et al., 2004). A PSO implementation that selects $\boldsymbol{p}_g$ from within a limited local neighborhood is referred to as an ***lbest*** PSO, whereas choosing $\boldsymbol{p}_{\mathrm{g}}$ from all available solutions results in a ***gbest*** PSO.

The following algorithm summarizes a PSO implementation:

- *Step 0:* initial swarm position and velocities are randomly generated. The current position of each particle is set as $\boldsymbol{p}_i$. The $\boldsymbol{p}_i$ with best value is set as $\boldsymbol{p}_{\mathrm{g}}$.
- *Step 1:* Evaluate the objective function for each particle. If any particle achieves a better objective value, $\boldsymbol{p}_i$ is replaced by the current position $\boldsymbol{x}_i$.
- *Step 2:* Set $\boldsymbol{p}_{\mathrm{g}}$ equal to the best collected $\boldsymbol{p}_i$ values.
- *Step 3:* Update the velocity and position of each particle using Equations 7.1-7.2.
- *Step 4:* Repeat *Steps 1-3* until completion.

This MOPSO algorithm will be implemented in Matlab and will be used to determine the best combination of laser power, scanning velocity, and hatch distance that leads to optimization of key objectives in the fabrication of IN 625 test coupons.

7.1.2 Multiple-objective Genetic Algorithms (MOGA)

Evolution and the natural selection process seen in nature is the basis of Genetic Algorithms (GA), a programming method for optimization purposes. Starting with an initial population, individuals of the population mate and evolve towards the optimal solution. Each individual in the population has a chromosome that represents the current values of the decision variables for that individual. The next generation of individuals, containing the offspring, is obtained from the current generation, the parents. The algorithm relies on three main operations: Selection, Crossover and Mutation. A child, or offspring, must be the product of either crossover, or mutation. Typical control parameters of GAs include (i) population size, (ii) selection strategy, (iii) generation gap, (iv) crossover, (v) mutation, and (vi) scaling (Grefenstette, 1986). Population based algorithms such as Genetic Algorithms (Mitchell, 1996) are superior to single-solution algorithms such as Tabu Search and Simulated Annealing in terms of locating the global optimum. The drawback is a loss of convergence speed. When more than one objective is considered, especially when considering objectives that are in conflict with each other, multi-objective optimization can be utilized to reveal a set of best optimal solutions known as the Pareto front. Multi-objective Genetic Algorithm optimization (MOGA) (Deb, 2011, Konak et al., 2006) is used for multi-objective optimization problems. The MOGA algorithm will be implemented using a built-in function in Matlab and used to find the optimal combination of laser power, scanning velocity, and hatch distance that leads to optimization of key objectives in the fabrication of IN 625 test coupons.

7.2 Optimization of Process Parameters for Relative Density, Processing Rate, and Energy Intensity

The first set of optimization problems that will be studied in this chapter utilizes objective functions obtained via predictive modeling of the selective laser melting process using the results of the experimental analysis presented in Chapter 5.

7.2.1 Definition of the Multi-objective Optimization Problem Set for Part Density, Processing Rate, and Energy Intensity

One of the key objectives of selective laser melting is to obtain fully-dense parts. For this purpose, a measure of relative density to that of bulk Inconel 625, ρ_{rel}, was described in Chapter 5. With this measure, a relative part density of 100% would be fully-dense and ideal. This objective can also be stated as minimizing the porosity of resulting parts. The predictive model for relative density of test coupons built with two scanning strategies was obtained from the experimental analysis presented in Chapter 5. The model is summarized in Equation 7.3 and Equation 7.4 for 90º and 67º scanning strategy, respectively.

$$\rho_{rel,90} = 30.2 - 0.39P + 0.2399v_s + 55h + 0.000017P^2 - 0.00022v_s^2 - 1954h^2 + 0.0005Pv_s + 0.692Ph + 0.213v_sh$$

$$\rho_{rel,67} = 44.3 - 0.548P + 0.2302v_s + 143h + 0.000634P^2 - 0.000196v_s^2 - 2304h^2 + 0.000379Pv_s + 0.808Ph + 0.1567v_sh \qquad (7.4)$$

A second key objective of concern to industry and researchers alike is the need to minimize processing time, as selective laser melting is currently a very time-consuming process, limited by the relatively low scanning speeds. However, processing time is geometry-dependent and cannot be calculated reliably, especially for 67º rotation scanning strategy. Alternatively, processing rate can be used as a measure to evaluate the performance of the SLM process. We define the response processing rate, R_p, as the volume of powder material processed per second [mm3/s], and given in Equation 7.6.

$$R_p = v_s \times h \times s \tag{7.5}$$

The powder layer thickness, s, is constant and equal to 0.02 mm for all cases. Finally, the large amount of energy required by the selective laser melting process is also of concern to researchers. Therefore, energy intensity applied can be used to control the amount of energy utilized by the process. Recall that energy intensity, E [J/ mm^3] is a function of laser power, scanning velocity, hatch distance and layer thickness, and is given in Equation 7.7. Energy intensity is a way to measure how much power and energy is utilized to process a volume (mm^3) of metal powder. Notice that in this case, we are trying to minimize energy consumption, so it makes intuitive sense to minimize energy intensity.

$$E = \frac{P}{v_s \times h \times s} \tag{7.6}$$

Notice how these objectives are conflicting: maximum part density (and minimum porosity) can be obtained for parts with low hatch distance and low scanning velocity. Similarly, processing rate is maximized with high scanning velocity and high hatch distance. Furthermore, utilizing higher laser power results in higher part density, but also results in higher energy consumption. Therefore, a multi-objective optimization problem can be stated to address the optimization of conflicting objectives. In total, two multi-objective optimization problems, jointly referred to as optimization set #1, are constructed as follows:

- Maximize the relative density of test coupons built with 90º scanning strategy, maximize processing rate (R_p), and minimize energy intensity (E):

$$\text{Min.} \qquad \left\{-\rho_{rel,90}(P, v_s, h), -R_p(v_s, h), E(P, v_s, h)\right\} \tag{7.7}$$

- Maximize the relative density of test coupons built with 67º scanning strategy, maximize processing rate, and minimize energy intensity:

$$\text{Min.} \qquad \left\{-\rho_{rel,67}(P, v_s, h), -R_p(v_s, h), E(P, v_s, h)\right\} \tag{7.8}$$

Furthermore, constraints in the decision variables, i.e. process parameters, are defined to include the limitations of the predictive model, and are given by Equation 7.9.

$$\begin{aligned} &169 \leq P \leq 195\, W \\ &725 \ \leq v_s \leq 875\, mm/s \\ &0.09 \leq h \leq 0.11\, mm \end{aligned} \tag{7.9}$$

The optimization problem is solved using both a Multi-Objective Genetic Algorithm (MOGA) and a Multi-Objective Particle Swarm Optimization (MOPSO) algorithm, as described in Sections 1.1 and 1.2.

7.2.2 Solution for the Multi-objective Optimization Problem Set for Part Density, Processing Rate, and Energy Efficiency

The multi-objective problem set presented in the previous section is solved using two approaches. The first approach considers using the MOGA function *gamultiobj* in Matlab. This function uses a variant of the Non-dominated Sorting Genetic Algorithm-II

(NSGA-II) (Deb et al., 2002). Table 7.1 summarizes the solver parameters chosen to obtain the Pareto front. “Population size” is the number of individuals, the number of “generations” is the maximum number of steps until the process is terminated (if convergence is not reached), “constraint tolerance” is the convergence tolerance that must be met to proceed to the next generation, the “crossover fraction” is the fraction of genes swapped between individuals, “elite count” is the number of best individuals that survive to the next generation without any change, and the “Pareto fraction” is the fraction of population present in the front. The solver parameter values were chosen from the default options of the *gaoptimset* function in Matlab, with the exception of the population size, which was chosen based on a brief sensitivity study. The initial range for the solutions is only limited by the constraints on the decision variables, as given by Equation 7.9.

Table 7.1. Solver parameters for MOGA for Optimization Set #1

Parameter	Setting
Population Size	500
Max. Generations	1000
Const. Tolerance	1e-6
Crossover Fraction	0.8
Elite Count	50
Pareto Fraction	0.35

A second approach to solving the optimization problem consists of using Matlab to implement the MOPSO algorithm of Section 7.1.1. Table 7.2 summarizes the process parameters utilized in the implementation. Notice that the number of particles and the number of iterations are equivalent to those used in MOGA. Particle acceleration constant values were selected after a brief sensitivity analysis.

Table 7.2. Solver parameters for MOPSO for Optimization Set #1

Parameter	Setting
Particles	500
Iterations	1000
Const. Tolerance	1e-6
Particle Accel. 1	2.02
Particle Accel. 2	2.02
Pareto Fraction	0.35

Multi-objective optimization results obtained with MOGA and MOPSO using the parameters in Table 7.1 and Table 7.2 are shown in Figure 7.1 to Figure 7.4. In each figure, each point represents an optimal solution that forms part of the Pareto front.

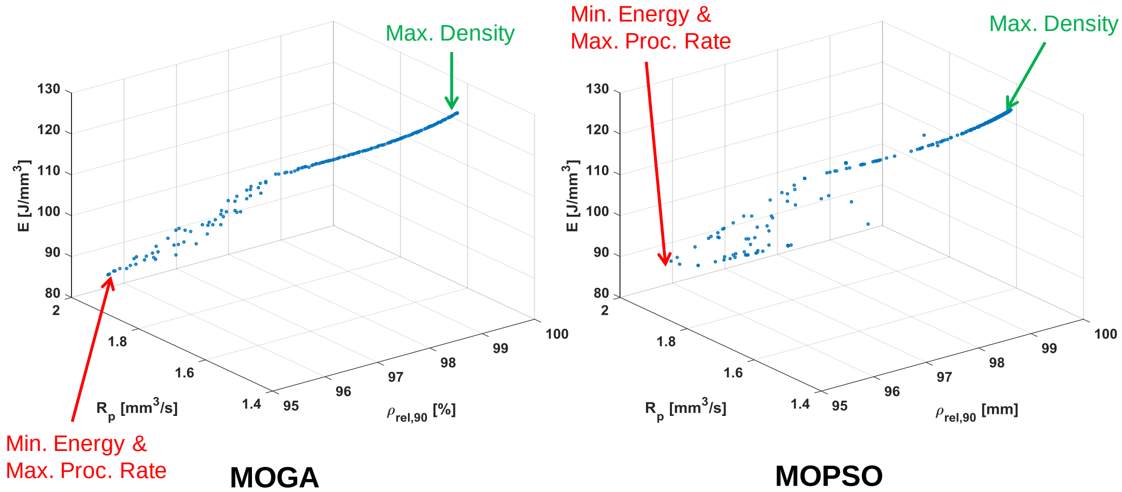

Figure 7.1. Objective function value solution space for optimization of $\rho_{\mathrm{rel,90}}$, R_p, and E using MOGA (left) and MOPSO (right).

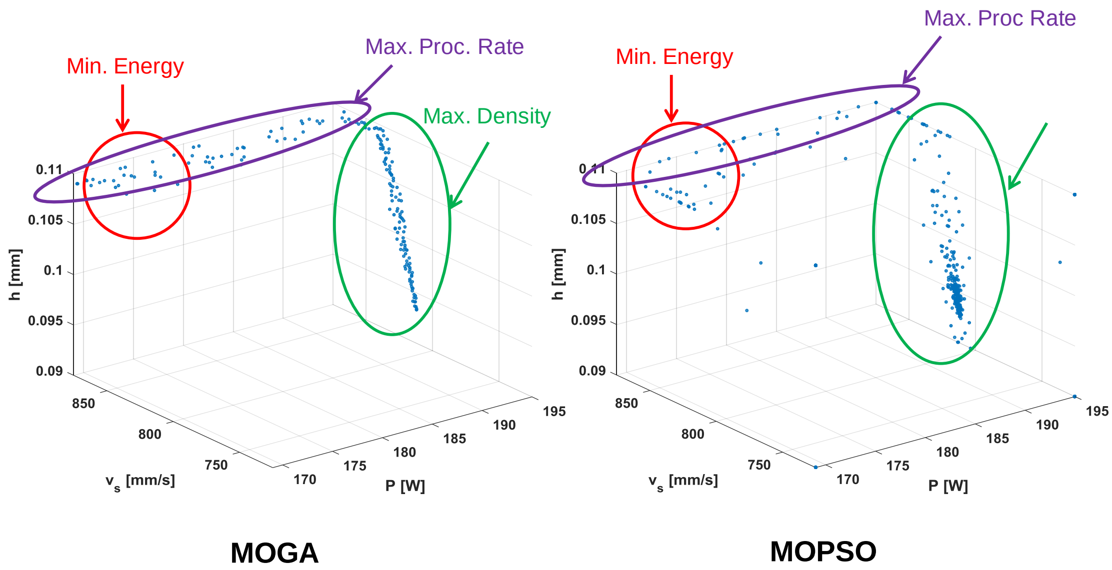

Figure 7.2. Decision variable solution space for optimization of $\rho_{\mathrm{rel},90}$, R_p, and E using MOGA (left) and MOPSO (right).

Figure 7.1 and Figure 7.2 show the solution to the problem described in Equation 7.7., where $\rho_{rel,90}$ is maximized, R_p is maximized, and E is minimized. In particular, Figure 7.1 indicates the optimized objective values and Figure 7.2 indicates the decision variables used to obtain those optimized objective values. The results indicate that R_p achieves its optimal value (max value) at high hatch distance and high scanning velocity combinations. Meanwhile, E achieves its optimal value (min value) for a smaller range, where high scanning velocity (v_s = 875 mm/s), high hatch distance (h = 0.01 mm) and low power (P < 180 W) are utilized. Maximum part density is obtained at maximum laser power, P = 195 W.

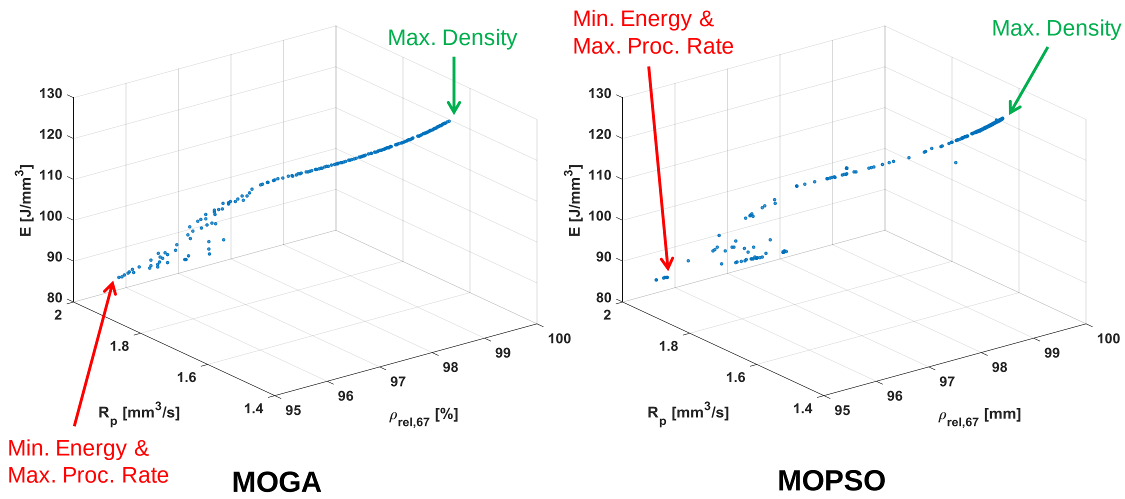

Figure 7.3. Objective function value solution space for optimization of $\rho_{rel,67}$, R_p, and E using MOGA (left) and MOPSO (right).

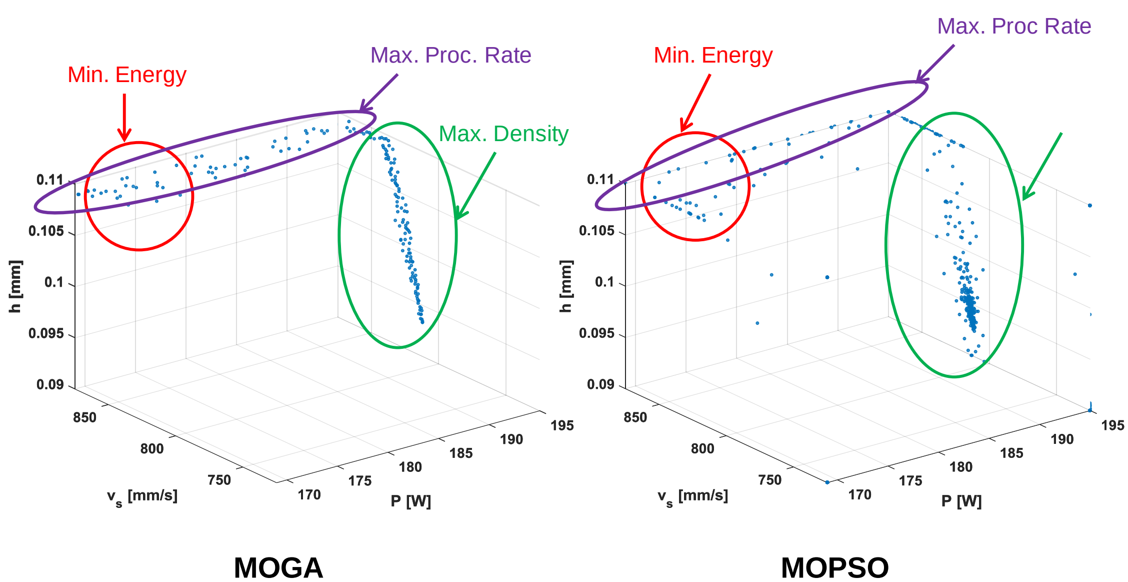

Figure 7.4. Decision variable solution space for optimization of $\rho_{rel,67}$, R_p, and E using MOGA (left) and MOPSO (right).

Figure 7.3 and Figure 7.4, which show the solution to the problem in Equation 7.8, shows a similar trend, indicating that there is no distinction between 67º and 90º scanning strategy. In general, notice that the solutions obtained using MOGA and MOPSO are very similar to each other. However, it is obvious that the solution obtained with MOPSO can be improved to eliminate straggler points. Additionally, it is important to note that the MOGA implementation using the built-in function in Matlab is between 50 and 60 times faster than the MOPSO implementation that requires a user-created routine.

7.3 Optimization of Process Parameters for Relative Density, Peak Temperature, and Time above the Melting Temperature

The second set of optimization problems that will be studied in this chapter utilizes objective functions obtained via predictive modeling using both the results from the experimental analysis of Chapter 5 and the results of the FE simulation analysis presented in Chapter 6.

7.3.1 Definition of the Multi-objective Optimization Problem Set for Part Density, Peak Temperature, and Time above the Melting Temperature

As explained in the previous section, one of the key objectives of selective laser melting is to obtain fully-dense parts (100% relative density). The same predictive models to calculate the relative density of parts processed with 90º and 67º rotation between layers will be used in this analysis (Equation 7.3 and Equation 7.4).

During the presentation of the FE-based simulation model in Chapter 6, two key parameters were introduced: the peak temperature at the surface of the powder bed (T_{peak}) and the time spent by a particular location of the powder bed in liquid phase (t_m). These two parameters, along with heating and cooling times, have been identified as the keys to understanding how microstructure (and therefore, the mechanical properties) of SLM-produced parts vary with process parameters. The predictive model for peak temperature and time above the melting temperature of test coupons built with two scanning strategies was obtained from the simulation analysis presented in Chapter 6. These predictive second-order models are given by Equation 7.10 and Equation 7.11.

$$T_{peak} = 2226 + 105.275P - 105.725v_s - 20.425h - 13.3875P^2 - 18.2875v_s^2 - 7.4875h^2 - 8.675Pv_s - 4.925Ph - 7.025v_sh \quad (7.10)$$

$$t_m = 0.47 - 0.11125P - 0.14125v_s - 2.82 \times 10^{-17}h + 0.00125P^2 + 0.01625v_s^2 - 0.01625h^2 - 0.0275Pv_s - 0.005Ph - 1.54 \times 10^{-18}v_sh \quad (7.11)$$

It is important to note here that the peak temperature must always be above the liquidus temperature of the material. Otherwise, full-melting of the powder material does not occur and incomplete fusion of powder material takes place.

Please note that the time above melting calculated by Equation 7.11 corresponds exclusively to Type I melt pools. The time above melting varies as a function of the location of the point of interest along the powder bed. Peak temperature and time above melting

Notice how the three chosen objectives for this analysis are conflicting: maximum part density (and minimum porosity) can be obtained for parts with low hatch distance and low scanning velocity. Similarly, peak temperature is minimized with low power, high scanning velocity and high hatch distance. Furthermore, utilizing higher laser power results in higher part density, but also results in larger melt pools. Therefore, a location of the powder bed belongs to the melt pool for a longer period of time and t_m increases as more laser power is utilized. A multi-objective optimization problem can be stated to address the optimization of conflicting objectives. In total, two multi-objective optimization problems, jointly referred to as optimization set #2, are constructed as follows:

- Maximize the relative density ($\rho_{rel,90}$) of test coupons built with 90º scanning strategy, minimize peak temperature (T_{peak}), and minimize time above melting temperature (t_m):

$$\text{Min.} \quad \{-\rho_{rel,90}(P, v_s, h), T_{peak}(v_s, h), t_m(P, v_s, h)\} \tag{7.12}$$

- Maximize the relative density of test coupons built with 67º scanning strategy, minimize peak temperature, and minimize time above the melting temperature:

$$\text{Min.} \quad \{-\rho_{rel,67}(P, v_s, h), T_{peak}(P, v_s, h), t_m(P, v_s, h)\} \tag{7.13}$$

Furthermore, constraints in the decision variables, i.e. process parameters, are defined to include the limitations of the predictive model, and are given by Equation 7.14.

$$\begin{aligned} &169 \leq P \leq 195\, W \\ &725 \ \leq v_s \leq 875\, mm/s \\ &0.09 \leq h \leq 0.11\, mm \end{aligned} \tag{7.14}$$

An additional constraint could be added to the optimization problem forcing $T_{peak} > T_l$. However, this is not necessary as all combinations of process parameters in the aforementioned problem space produce peak temperatures larger than T_l = 1623K.

The optimization problem is solved using both the Multi-Objective Genetic Algorithm (MOGA) and the Multi-Objective Particle Swarm Optimization algorithm used to find the solution front to the first optimization problem set in Section 2 of this chapter.

7.3.2 Solution for the Multi-objective Optimization Problem Set for Part Density, Peak Temperature, and Time above the Melting Temperature

The multi-objective problem set presented in the previous section is solved using two approaches. The first approach considers using the MOGA function *gamultiobj* in Matlab. Table 7.3 summarizes the solver parameters chosen to obtain the Pareto front. The second approach uses a Matlab implementation of MOPSO with the parameters shown on Table 7.4. The initial range for the solutions is only limited by the constraints on the decision variables, as given by Equation 7.14.

Table 7.3. Solver parameters for MOGA for Optimization Set #2

Parameter	Setting
Population Size	500
Max. Generations	1000
Const. Tolerance	1e-6
Crossover Fraction	0.8
Elite Count	50
Pareto Fraction	0.35

Table 7.4. Solver parameters for MOPSO for Optimization Set #2

Parameter	Setting
Particles	500
Iterations	1000
Const. Tolerance	1e-6
Particle Accel. 1	2.02
Particle Accel. 2	2.02
Pareto Fraction	0.35

Multi-objective optimization results obtained with MOGA and MOPSO using the parameters in Table 7.3 and Table 7.4 are shown in Figure 7.5 to Figure 7.8. In each figure, each point represents an optimal solution that forms part of the Pareto front.

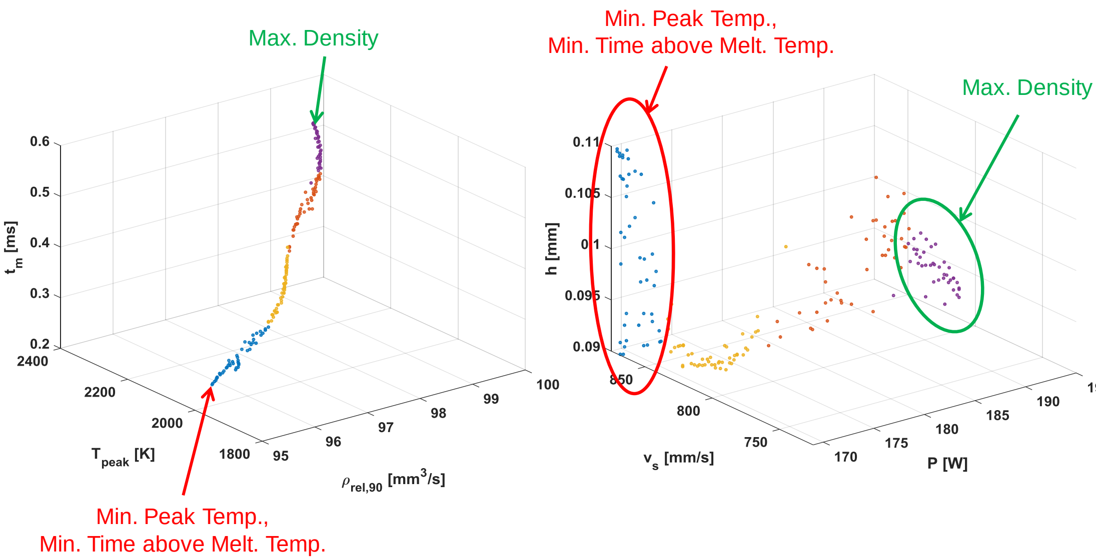

Figure 7.5. MOGA solution for optimization of $\rho_{\text{rel},90}$, T_{peak}, and t_m showing the objective function value space (left) and the decision variable space (right).

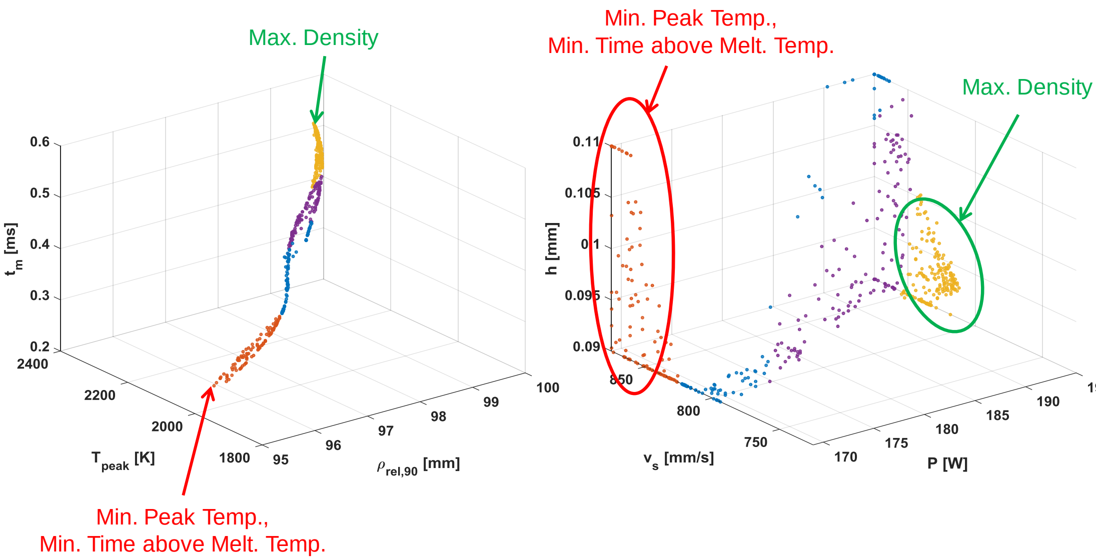

Figure 7.6. MOPSO solution for optimization of $\rho_{\text{rel},90}$, T_{peak}, and t_m showing the objective function value space (left) and the decision variable space (right).

Figure 7.5 and Figure 7.6 show the solution to the problem described in Equation 7.12, where $\rho_{rel,90}$ is maximized, R_p is maximized, and E is minimized. In particular, Figure 7.5

was obtained using MOGA and Figure 7.6 using MOPSO. The results indicate that T_{peak} achieves its optimal value (min value) at high hatch distance and high scanning velocity combinations. Similarly, t_m achieves its optimal value (min value) for the same range of process parameters, where high scanning velocity (v_s = 875 mm/s), high hatch distance (h = 0.01 mm) and low power (P < 175 W) are utilized. Maximum part density is obtained at maximum laser power, P = 195 W. A k-means clustering approach with k = 4 was used to color-code each solution in the Pareto front.

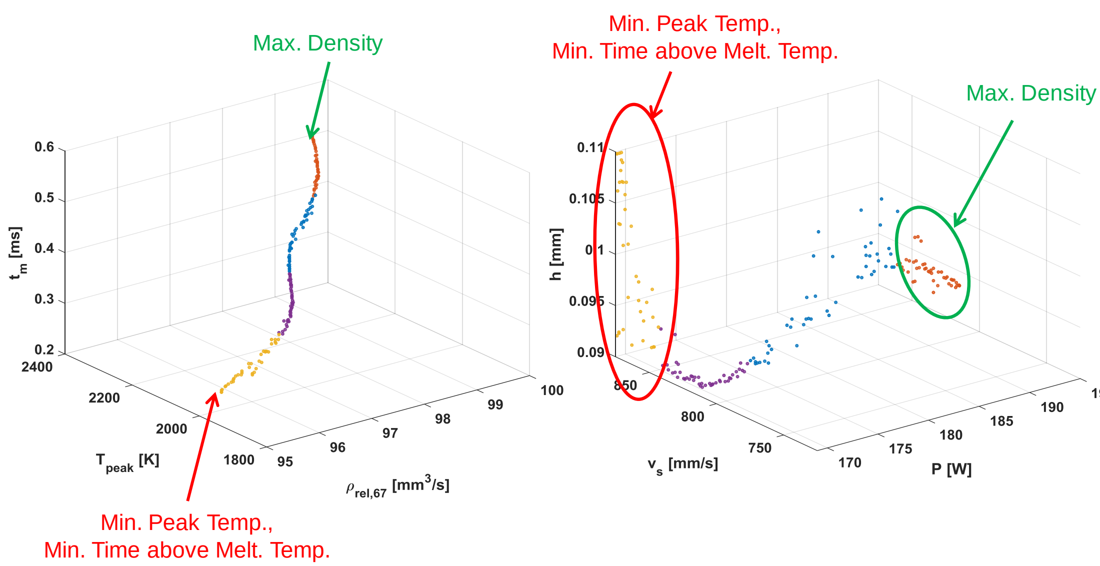

Figure 7.7. MOGA solution for optimization of $\rho_{\mathrm{rel},67}$, T_{peak}, and t_m showing the objective function value space (left) and the decision variable space (right).

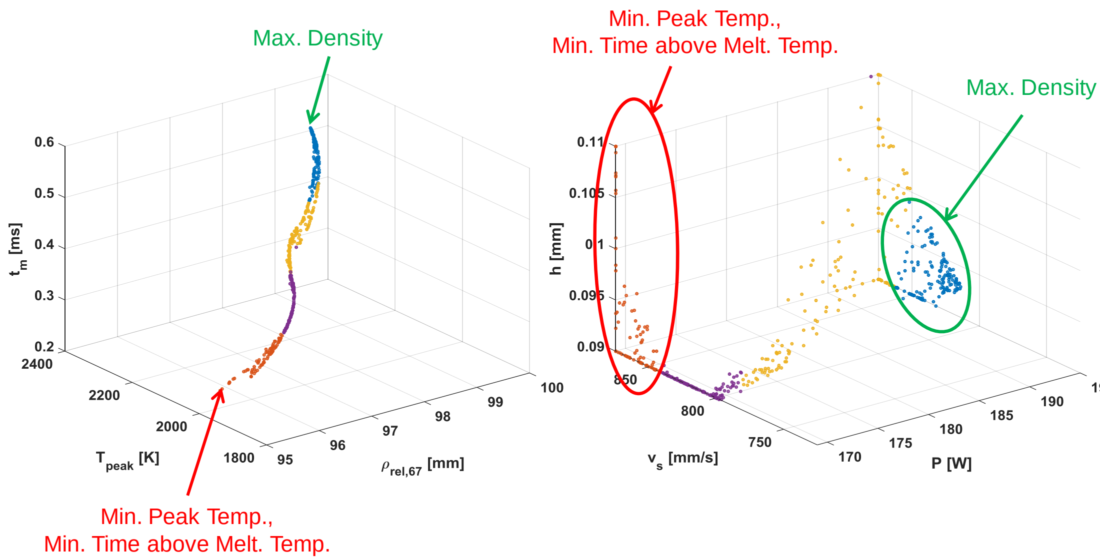

Figure 7.8. MOPSO solution for optimization of $\rho_{\mathrm{rel},67}$, T_{peak}, and t_m showing the objective function value space (left) and the decision variable space (right).

Figure 7.7 and Figure 7.8, which show the solution to the problem in Equation 7.13, portray a similar trend, indicating that there is no inherent difference in the optimization problem between 67° and 90° scanning strategy beyond the predicted values. In general, notice that the solutions obtained using MOGA and MOPSO are very similar to each other. However, the solution obtained with MOPSO contains a larger number of solutions in the intermediary region, the region between optimization of a single objective.

7.4 Summary and Conclusions

In this chapter, two sets of multi-objective optimization problems have been solved. The first set considered a combination of experimental analysis results i.e. measured relative density, with industrial considerations of the SLM process: processing rate and energy consumptions. The second set of optimization problems was centered around once again maximizing part density, but this time conflicting against physical properties of the process obtained through simulations, such as the peak temperature on the powder bed and the time above melting temperature near the edge of the stripe (Type I melt pools). Results show that processing rate, energy consumption, and the amount of heat that builds up in the material can be optimized by increasing scanning velocity and hatch distance, but at a cost of resulting part density.

For each optimization problem, combinations of process parameters were identified that provided insight into how laser power, scanning velocity, and hatch distance alongside scanning strategy interact to produce SLM built parts based on the desired process characteristics. Additionally, it was also reported that the behavior of the Pareto front for scanning strategies of 67º and 90º rotation between layers is nearly identical. Therefore, scanning strategy is not a significant factor in determining with process parameters to prioritize based on the optimization objectives. These results were confirmed by using two separate approaches to solve the multi-objective optimization problem: a multi-objective genetic algorithm (MOGA) and a multi-objective particle swarm optimization (MOPSO) implementation.

In both cases, the optimization objectives conflicted with each other and were assigned equal value. Based on the requirements of the user, e.g. high density parts preferred, the weight assigned to each individual objective can be set and process parameters may be obtained that prioritize the specific objective of interest.

Chapter 8 CONTRIBUTIONS AND FUTURE WORK

The objective of this dissertation was to provide new knowledge regarding two specific types of laser processing of dissimilar materials: UV nanosecond pulsed laser micro-machining of transparent polymers and selective laser melting (SLM) of powder metals. The theoretical framework and literature review utilized in the development of the dissertation was introduced in Chapter 1.

Chapter 2 provided an experimental analysis on the feasibility of UV nanosecond pulsed laser micro-machining of polydimethylsiloxane (PDMS) for the creation of micro-channels for micro-fluidics applications. A full factorial experimental design was utilized to determine the effect of fluence and pulse overlapping in micro-channel geometry. The experimental work was complemented with a physics-based 1-D finite element model to predict ablation depth and a shape model to predict micro-channel geometry.

In Chapter 3, a 2-D physics-based finite element model was used to simulate selective laser melting of a single track of material for three powder metals: Ti-6Al-4V titanium alloy, 316L stainless steel, and Inconel 625 nickel based alloy. The resulting temperature distribution was utilized to determine key variables such as melt pool geometry, peak temperature, and time above melting temperature. A sensitivity analysis for SLM of Inconel 625 was performed to obtain a better understanding of the effect of process parameters and material properties in the resulting temperature profile.

Chapter 4 extended the single track model to include multi-track simulations, with an emphasis on the use of Inconel 625 powder material. An experimental design following the Box-Behnken design of experiments was introduced for manufacturing of Inconel 625 test coupons.

In Chapter 5, test coupons fabricated at the National Institute of Standards & Technology (NIST) were analyzed. The density of the test coupons was measure and compared to the density of bulk Inconel 625 material. Additionally, melt pool width, depth, and shape were measured from electro-polished coupon surfaces using digital optical microscopy. These results were analyzed using response surface methodology (RSM) and utilized to develop predictive models for melt pool width, depth, and shape. It was found that melt pool geometry is dynamic and varies based on the scanning direction and the location on the powder bed.

Melt pool geometry measurements were used to validate the model in Chapter 6. Further validation was possible utilizing thermal data on the surface of one of the powder bed, gathered during the test coupon fabrication process. After model validation, a suit of simulation experiments was executed, following the same Box-Behnken design, to determine peak temperature and time above the melting temperature.

Finally, two sets of multi-objective optimization problems were presented and solved in Chapter 7. The first set used maximizing relative density of the test coupons, maximizing processing rate of the material, and minimizing energy consumption during the process as conflicting objectives to optimize process parameters: laser power, scanning velocity, and hatch distance. The second optimization problem set aimed at maximizing part density, minimizing peak temperature and minimizing time above the melting temperature as key objectives. Results obtained multi-objective genetic algorithms (MOGA) and multi-objective particle swarm optimization (MOPSO) implementations were compared and contrasted.

This dissertation contains both experimental and computational work, which relies heavily on knowledge from various fields: materials science, statistics, applied mathematics, industrial engineering, and mechanical engineering, among others. Therefore, the regions for improvement are vast. On the computational side, the models used for estimating the thermal field for both laser processing of polymers and for SLM of metal powders can be enhanced significantly by considering more complex 3-D models. Furthermore, a phase field solidification model that uses the thermal history of the powder bed to predict the resulting micro-structure would be of great interest to researchers. Being able to pinpoint possible regions of cracking or fracture are critical for the continued development of SLM as a widely-applied production process.

Additionally, stochastic processes could be used to account for modeling of other physical conditions present in laser processing, such as spattering in SLM and gas bubble formation in PDMS ablation. On the experimental side, more complex controlled experiments can be executed to obtain more comprehensive predictive models for both UV nanosecond-pulsed laser processing of PDMS and SLM of powder metals. Further experimentation would also provide additional information regarding the underlying physics for each process, with critical optimization objectives in mind.

APPENDIX A: OPTICAL IMAGE ANALYSIS – MELT POOL GEOMETRY

Figure A.1. Analysis of SLM-fabricated IN 625 test coupons for melt pool width, depth, and shape measurements – Coupon 01

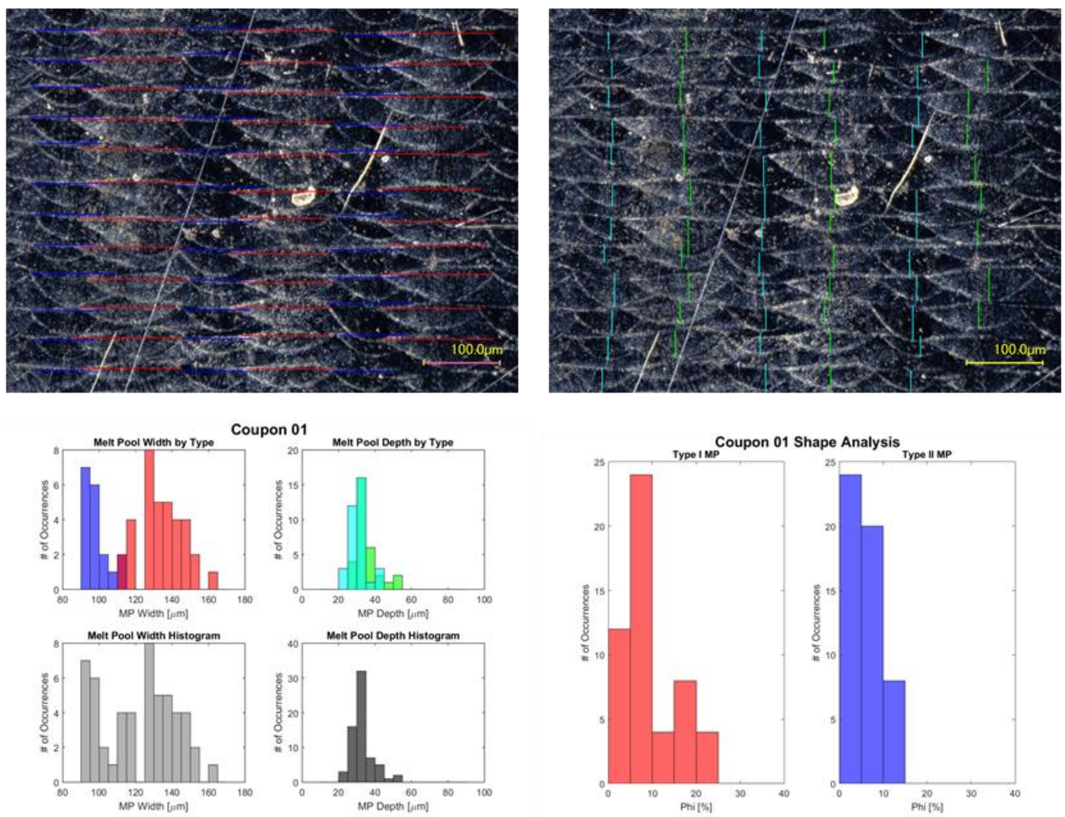

Figure A.2. Analysis of SLM-fabricated IN 625 test coupons for melt pool width, depth, and shape measurements – Coupon 04

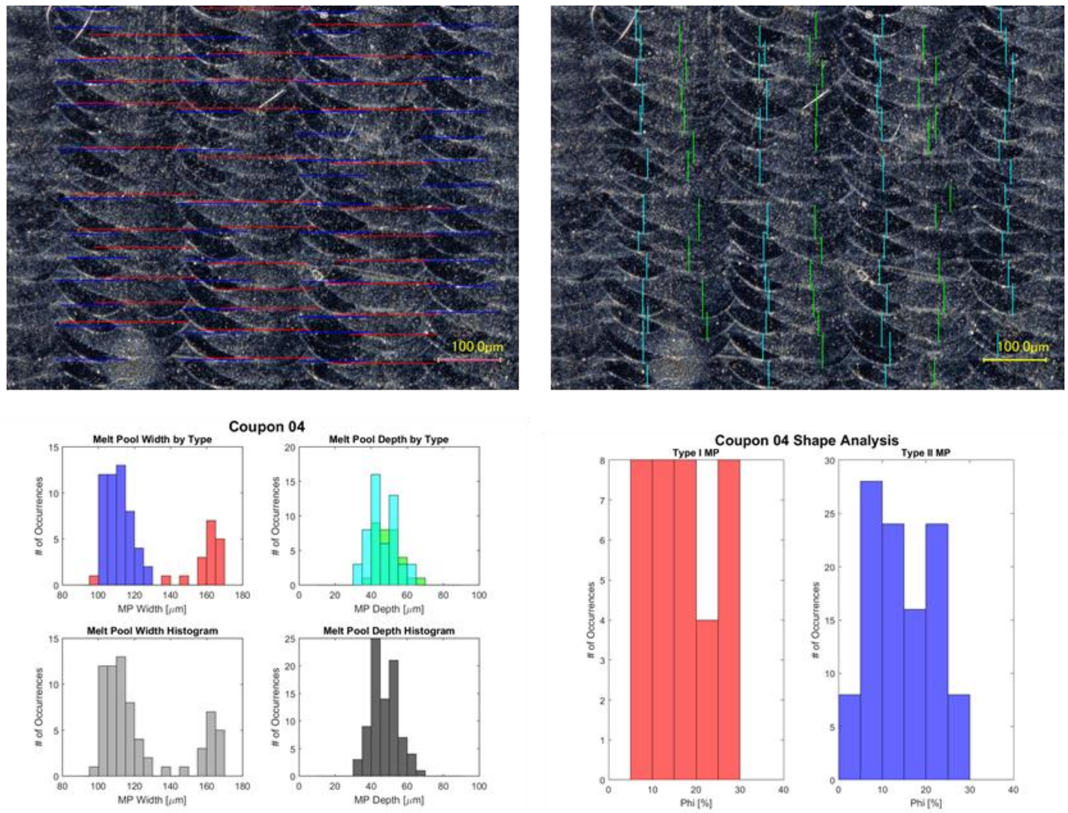

Figure A.3. Analysis of SLM-fabricated IN 625 test coupons for melt pool width, depth, and shape measurements – Coupon 06

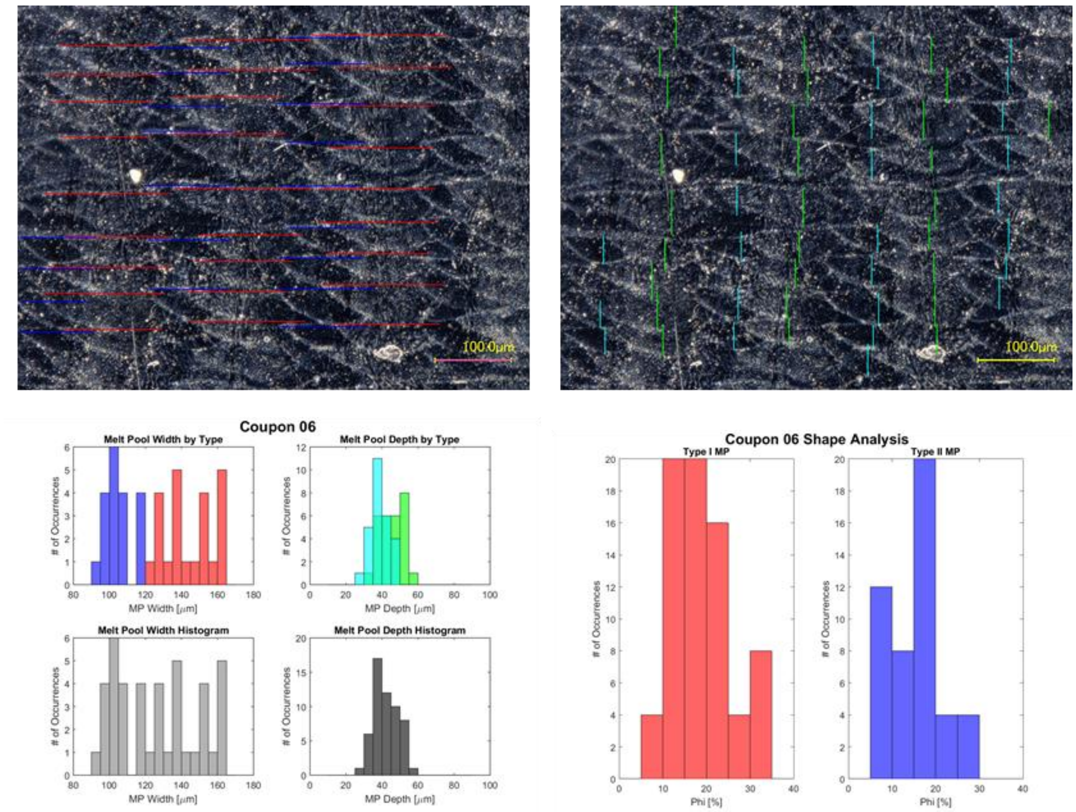

Figure A.4. Analysis of SLM-fabricated IN 625 test coupons for melt pool width, depth, and shape measurements – Coupon 08

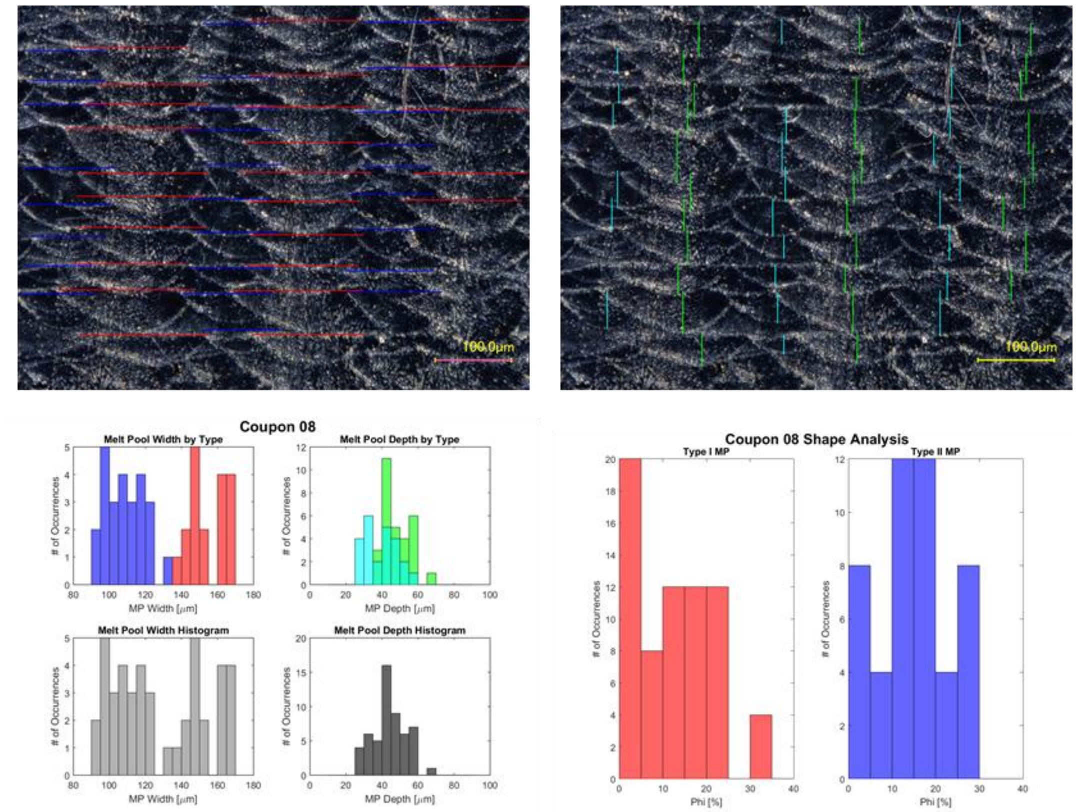

Figure A.5. Analysis of SLM-fabricated IN 625 test coupons for melt pool width, depth, and shape measurements – Coupon 09

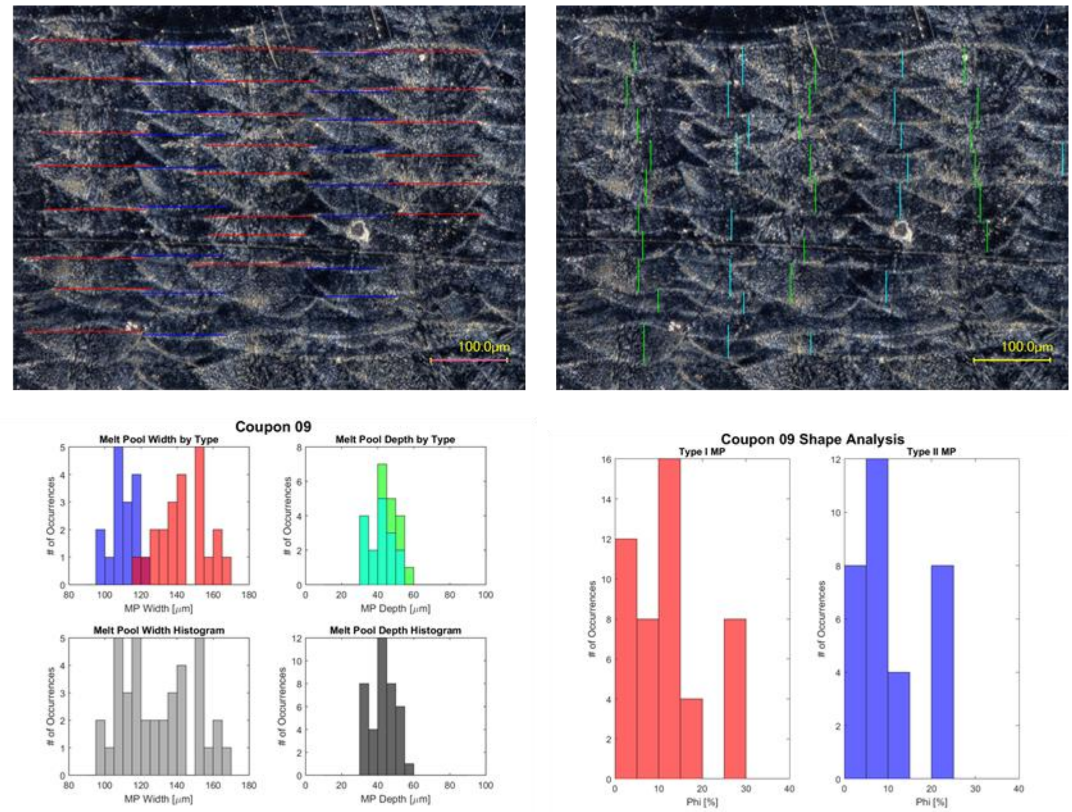

Figure A.6. Analysis of SLM-fabricated IN 625 test coupons for melt pool width, depth, and shape measurements – Coupon 12

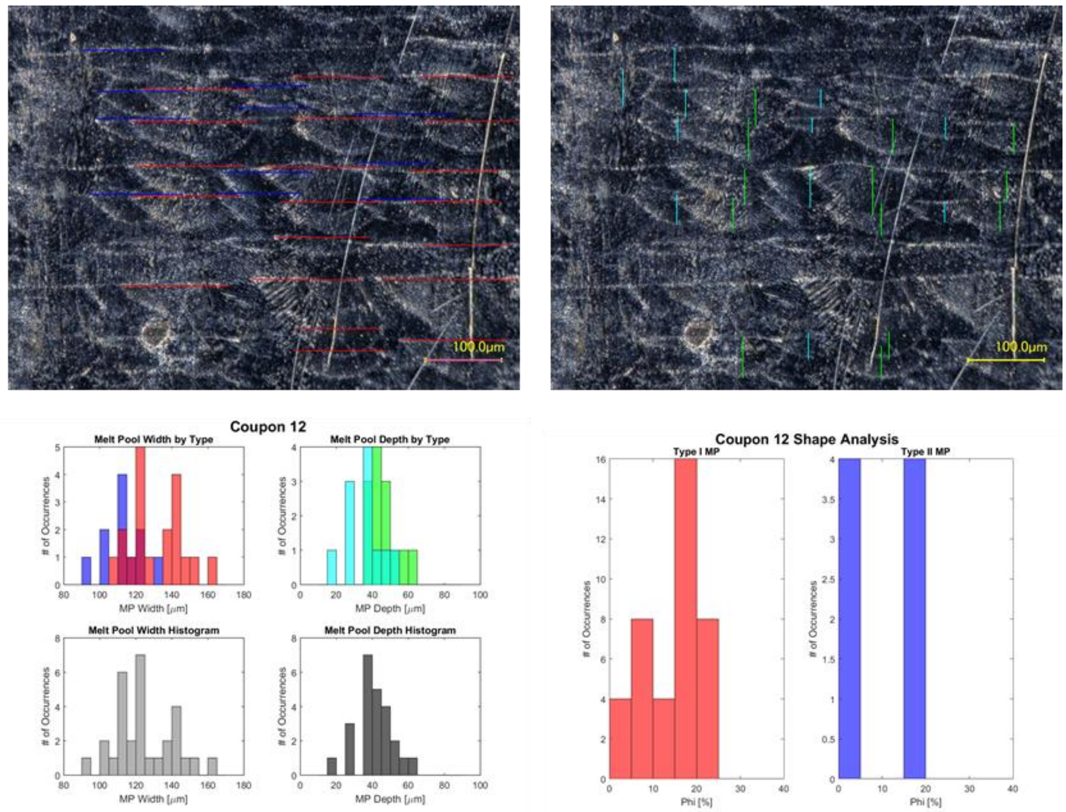

Figure A.7. Analysis of SLM-fabricated IN 625 test coupons for melt pool width, depth, and shape measurements – Coupon 14

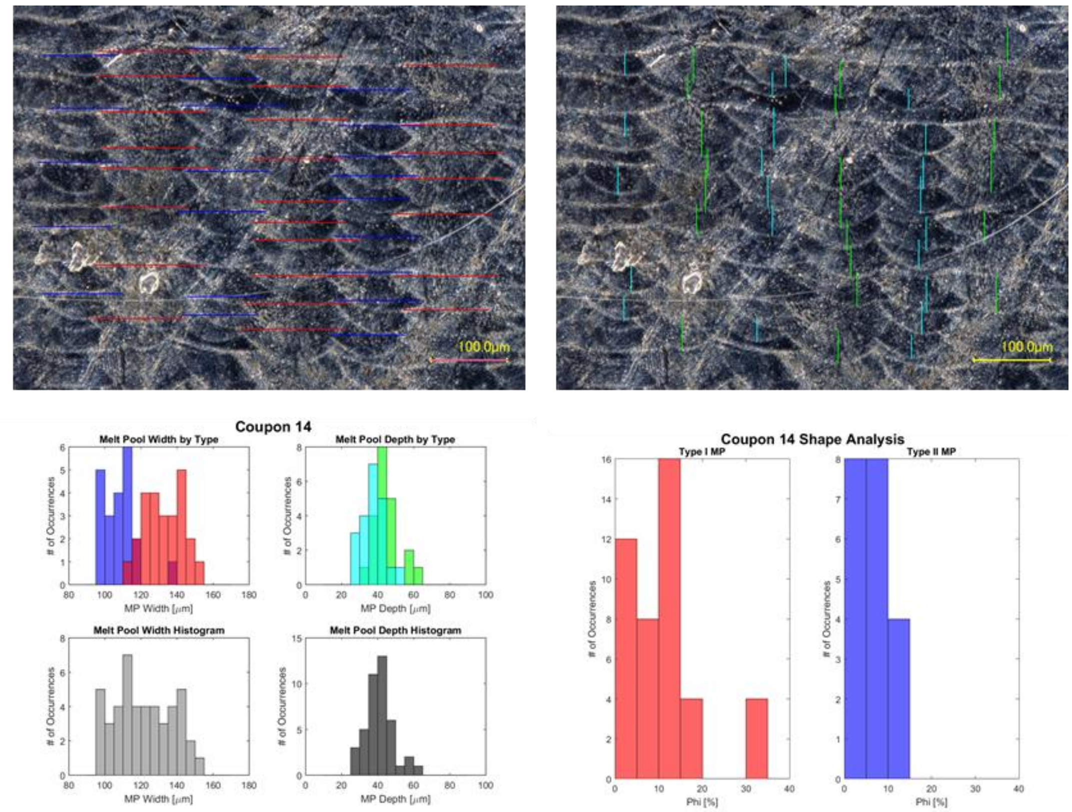

Figure A.8. Analysis of SLM-fabricated IN 625 test coupons for melt pool width, depth, and shape measurements – Coupon 15

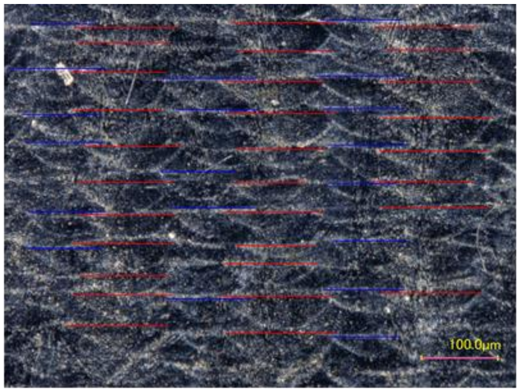

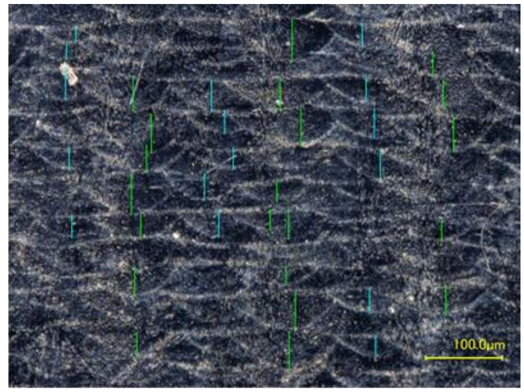

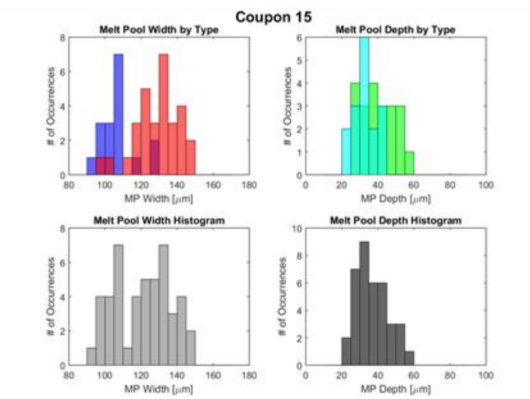

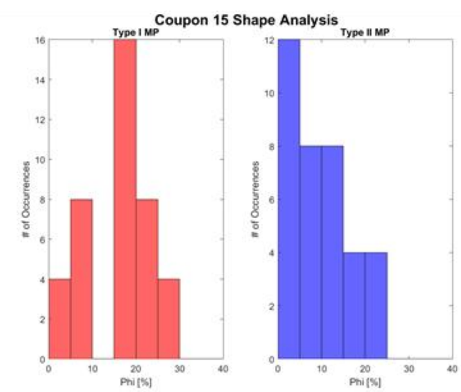

Figure A.9. Analysis of SLM-fabricated IN 625 test coupons for melt pool width, depth, and shape measurements – Coupon 16

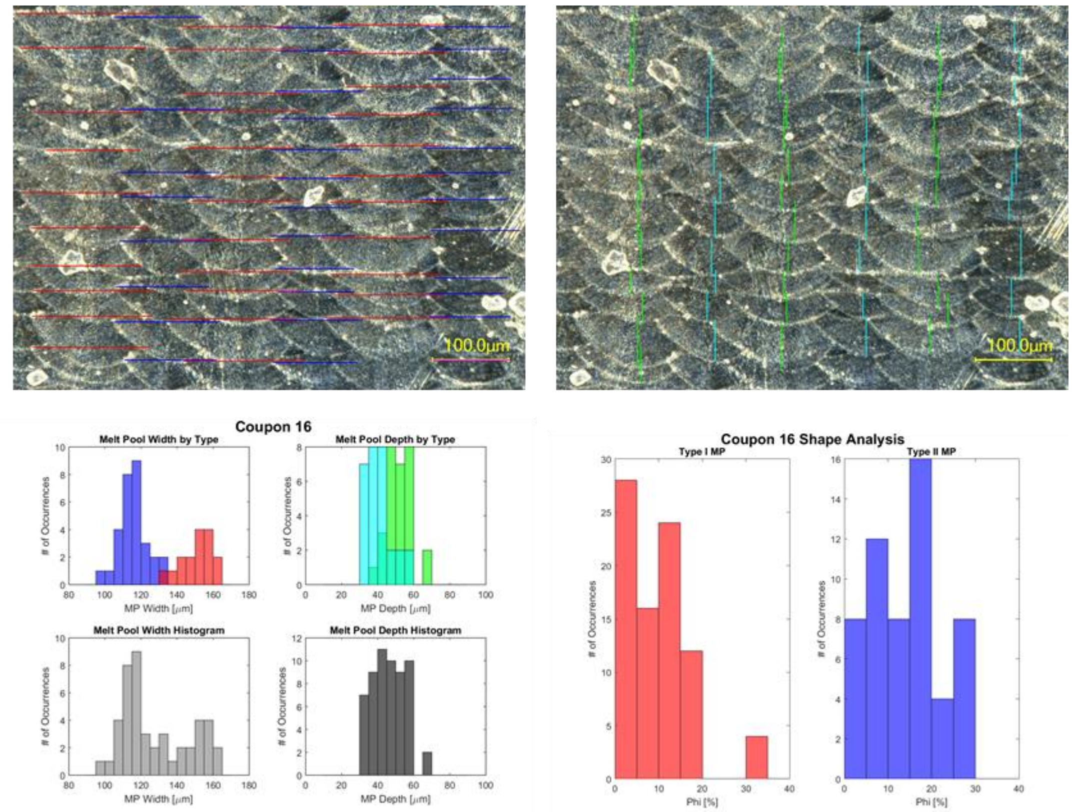

Figure A.10. Analysis of SLM-fabricated IN 625 test coupons for melt pool width, depth, and shape measurements – Coupon 17

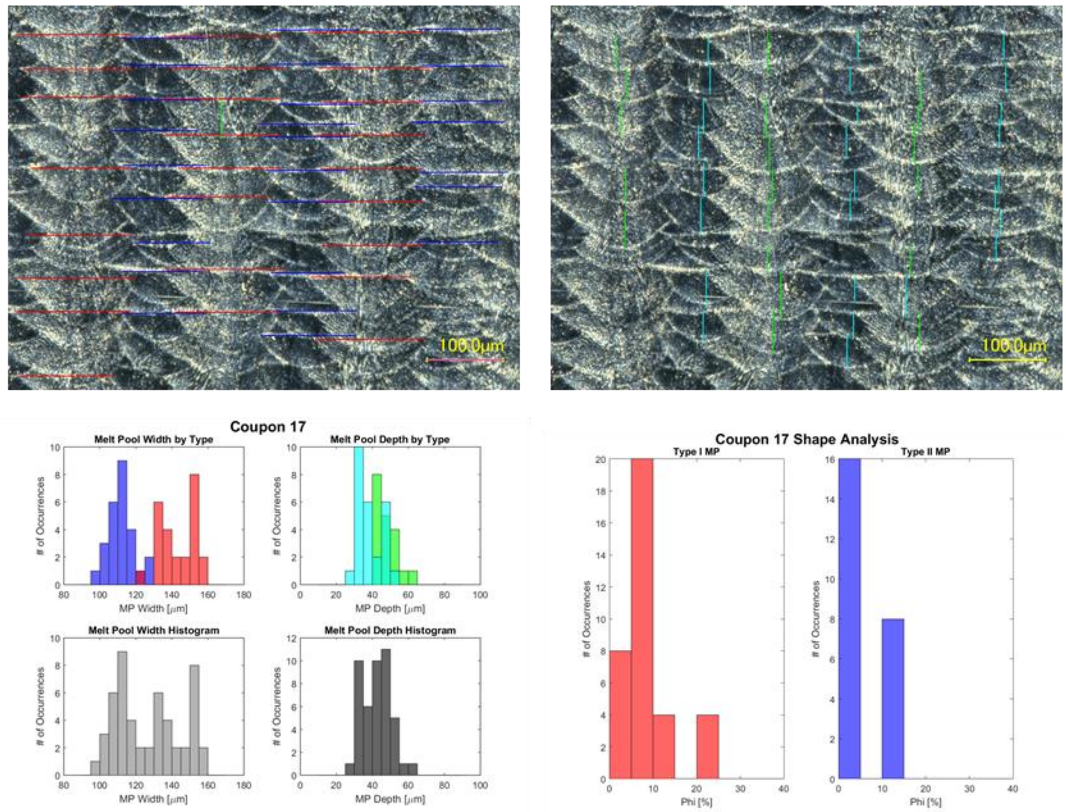

Figure A.11. Analysis of SLM-fabricated IN 625 test coupons for melt pool width, depth, and shape measurements – Coupon 18

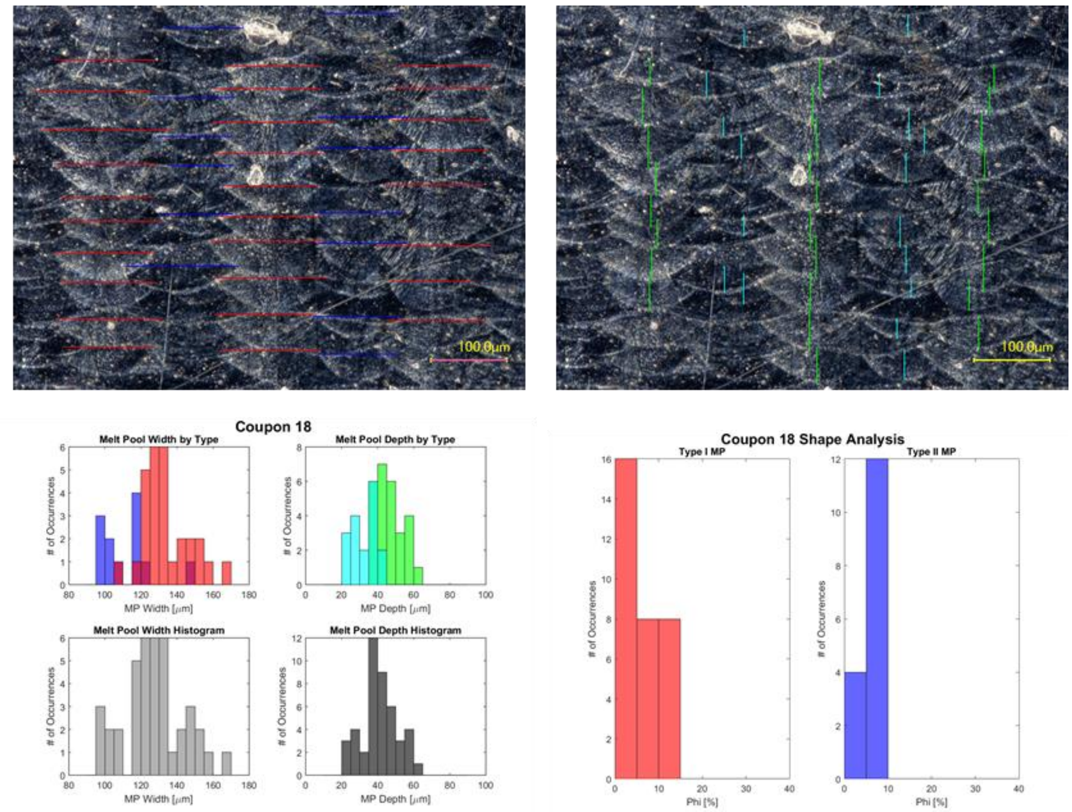

Figure A.12. Analysis of SLM-fabricated IN 625 test coupons for melt pool width, depth, and shape measurements – Coupon 20

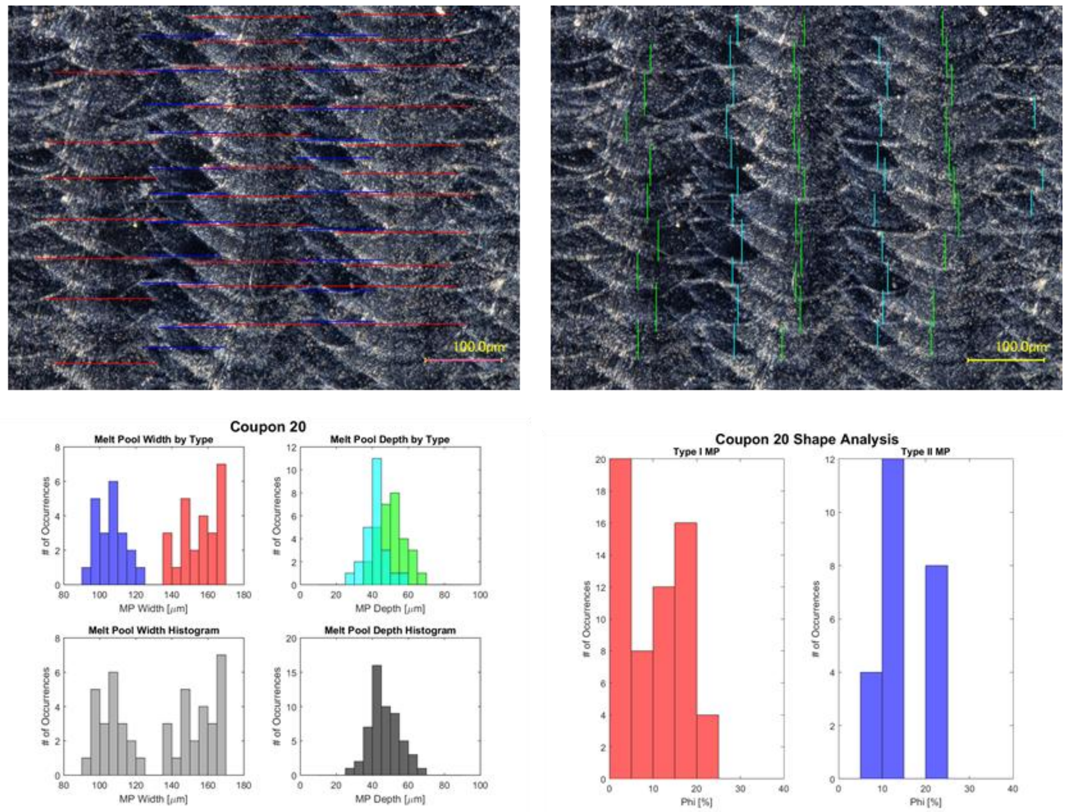

Figure A.13. Analysis of SLM-fabricated IN 625 test coupons for melt pool width, depth, and shape measurements – Coupon 21

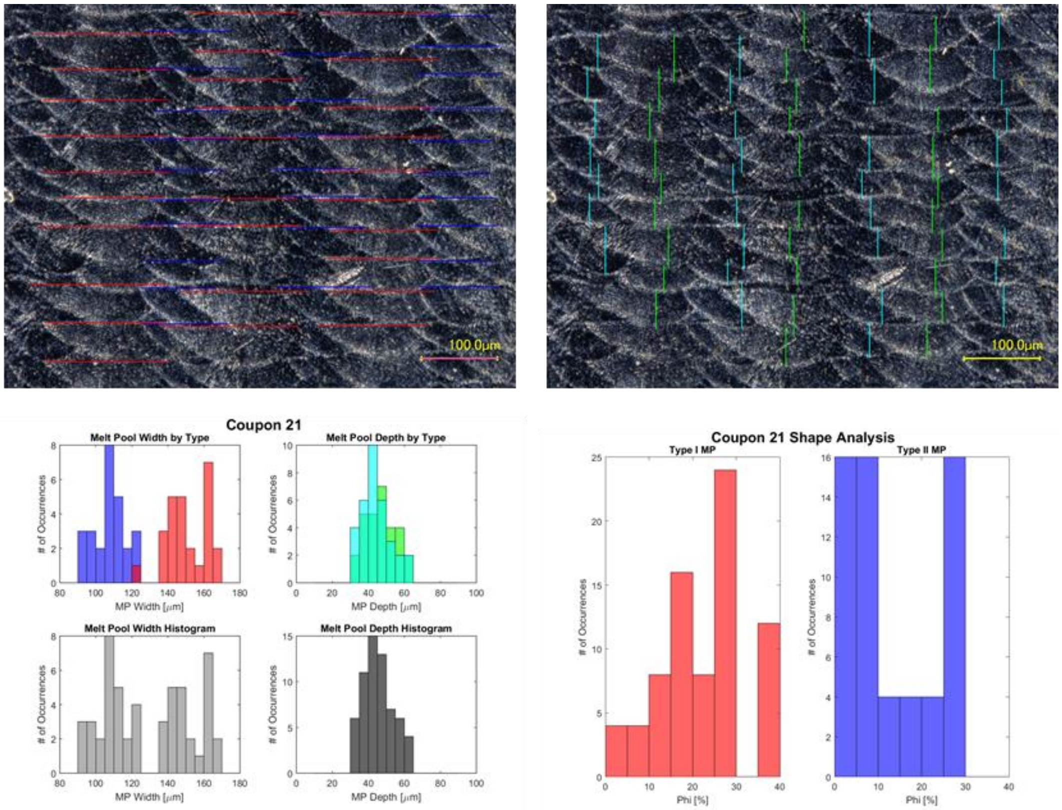

Figure A.14. Analysis of SLM-fabricated IN 625 test coupons for melt pool width, depth, and shape measurements – Coupon 23

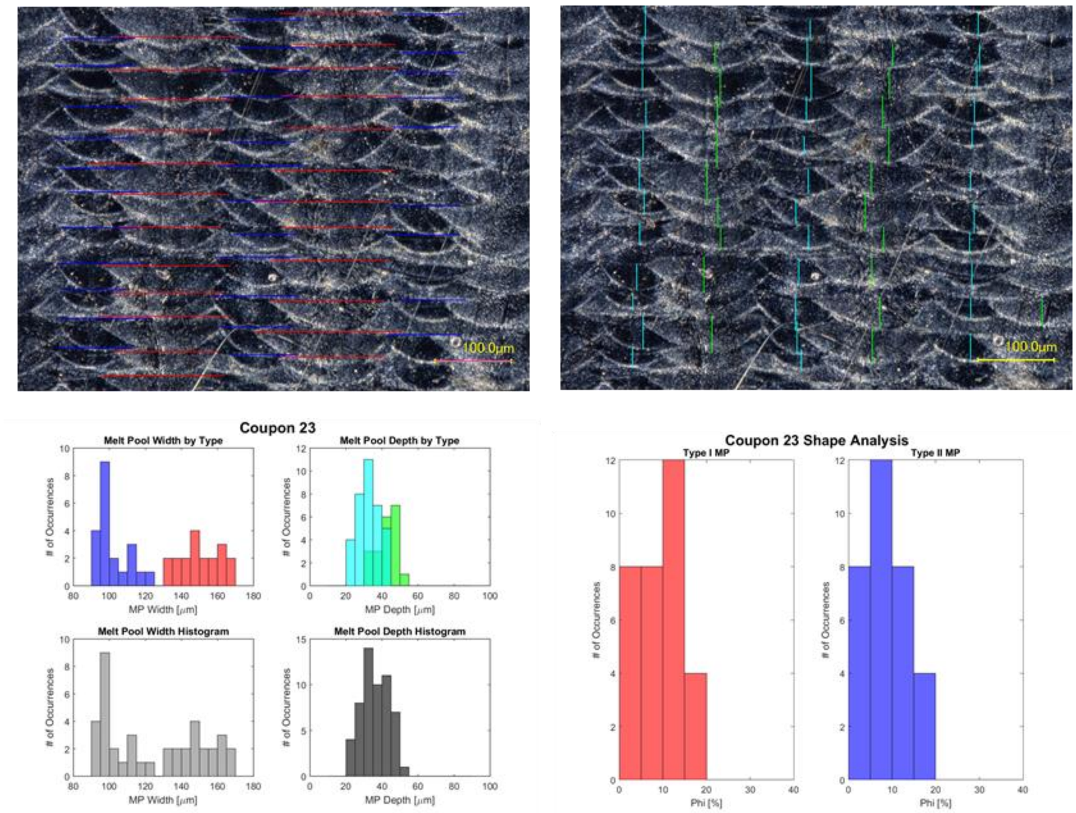

Figure A.15. Analysis of SLM-fabricated IN 625 test coupons for melt pool width, depth, and shape measurements – Coupon 29

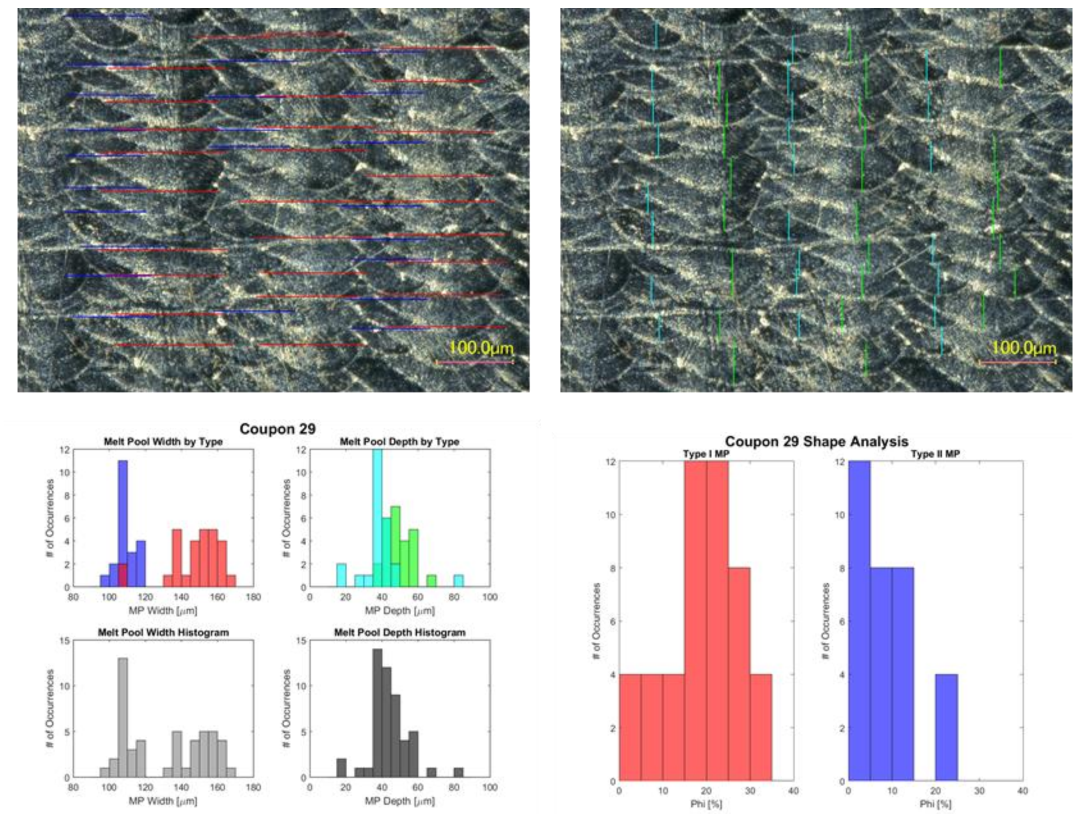

APPENDIX B: WIDTH AND DEPTH MELT POOL PREDICTIONS OBTAINED FROM FINITE-ELEMENT SIMULATED TEMPERATURE FIELD

The cross-section of the melt pool is calculated at a distance of 50 μm from the edge of the edge of the stripe, for the 2^{nd} and 3^{rd} scanned tracks. This distance matches the amount of material removed from the additively fabricated test coupons via electro-polishing. Therefore, these results can be compared directly to the melt pool width and depth measured using the optical microscopy images from Appendix A.

Figure B.1. YZ-cross section of the melt pool at 50 μm from the edge of the stripe (2^{nd} and 3^{rd} track) – Coupon 01

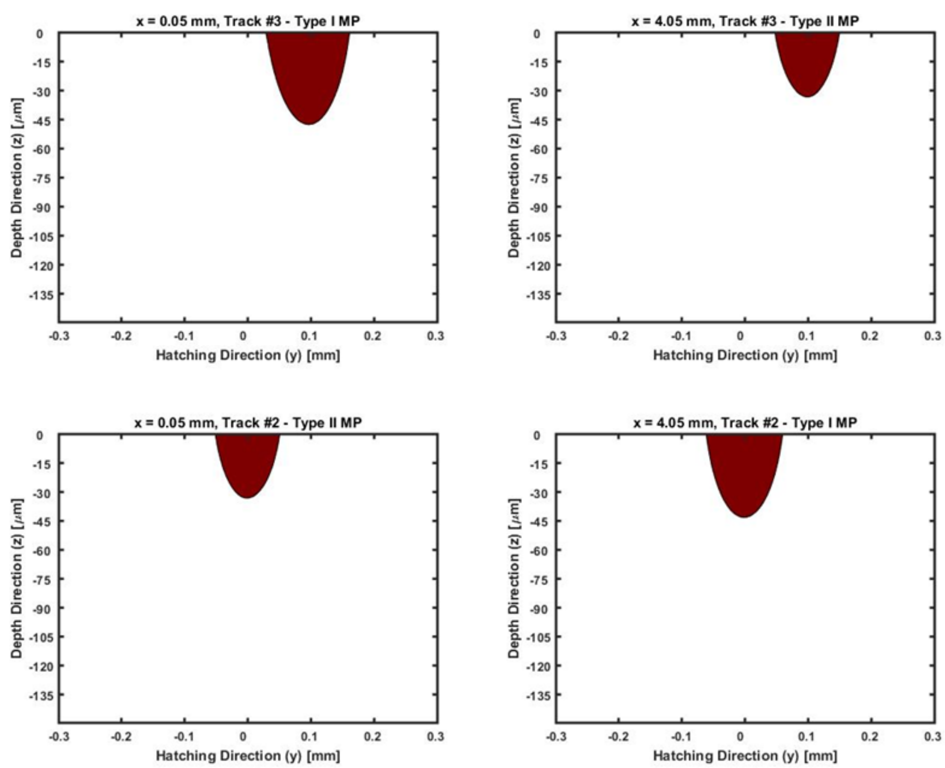

Figure B.2. YZ-cross section of the melt pool at 50 μm from the edge of the stripe (2nd and 3rd track) – Coupon 04

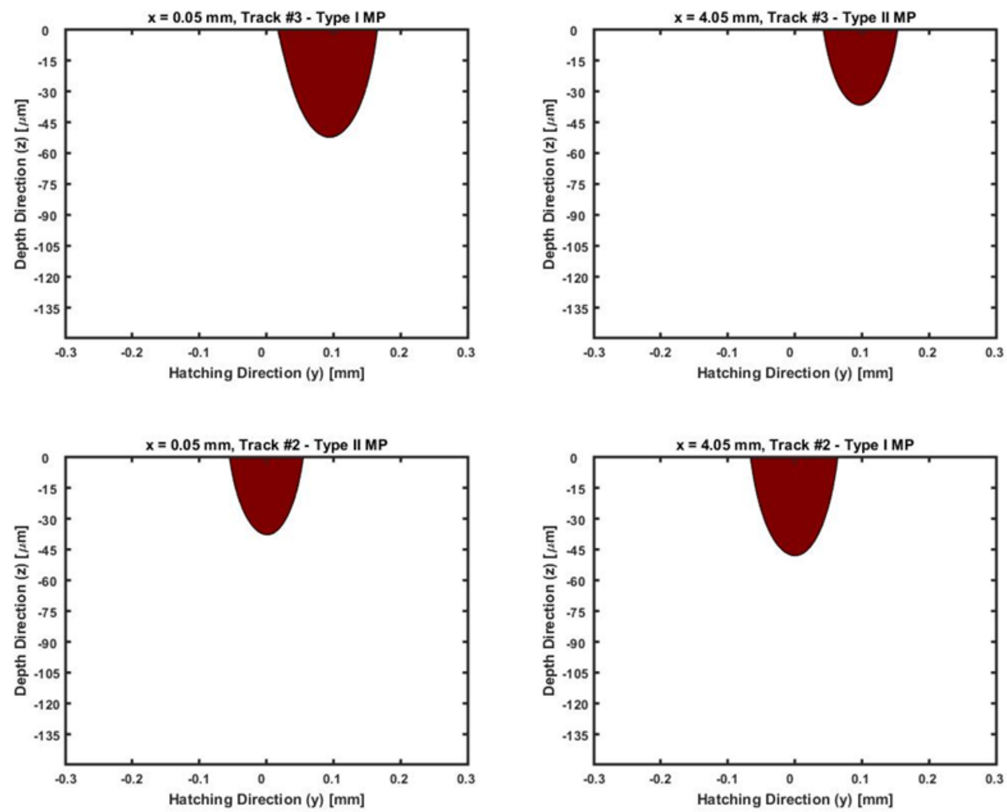

Figure B.3. YZ-cross section of the melt pool at 50 μm from the edge of the stripe (2nd and 3rd track) – Coupon 06

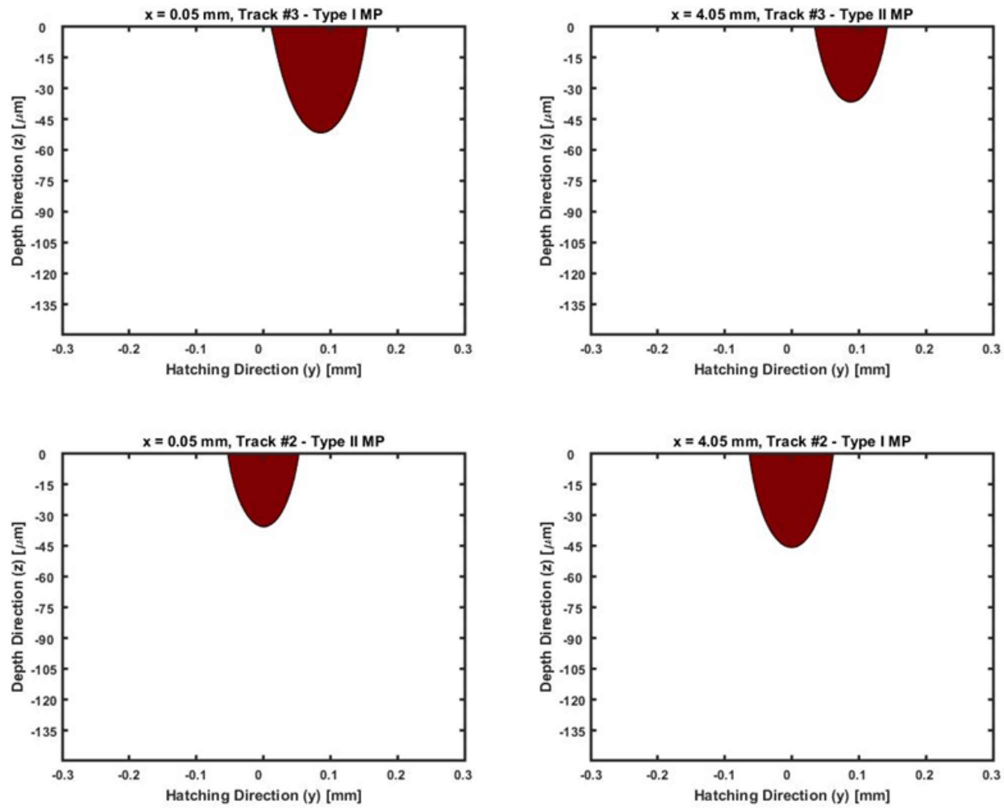

Figure B.4. YZ-cross section of the melt pool at 50 μm from the edge of the stripe (2nd and 3rd track) – Coupon 08

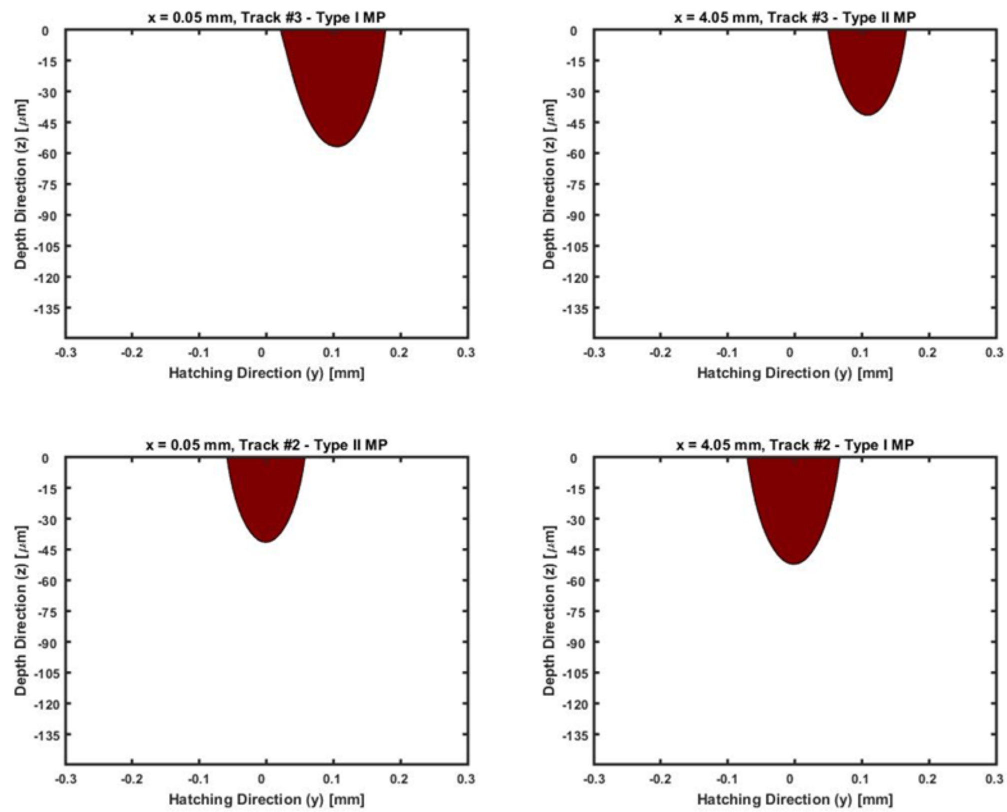

Figure B.5. YZ-cross section of the melt pool at 50 μm from the edge of the stripe (2nd and 3rd track) – Coupon 09

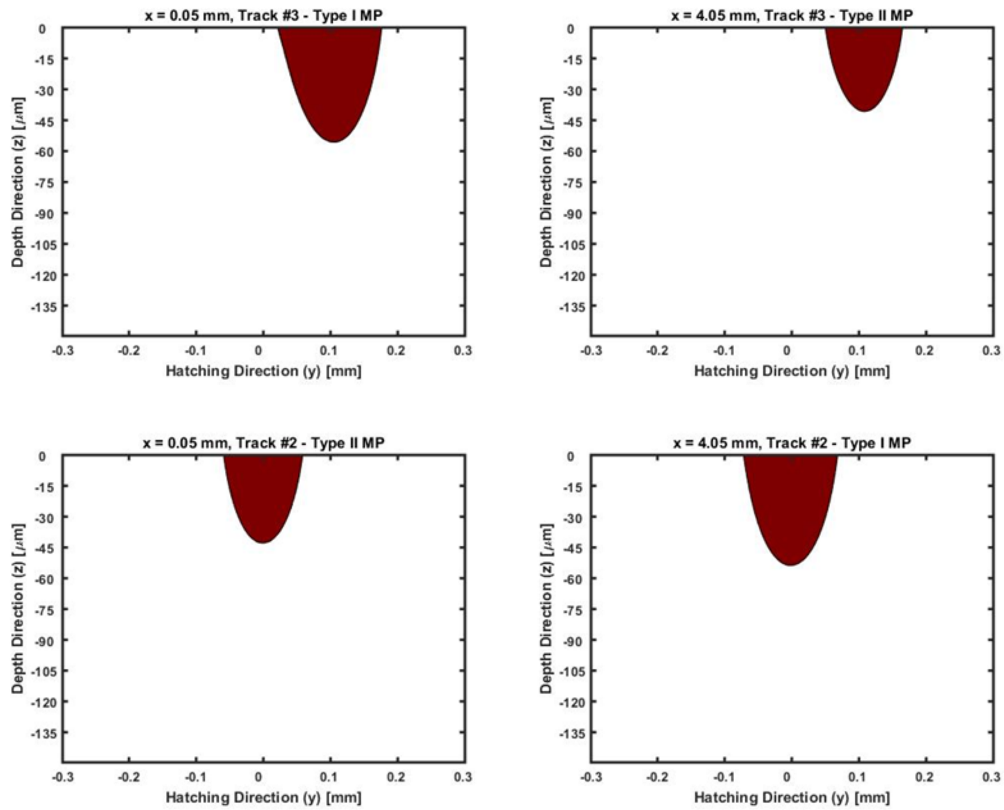

Figure B.6. YZ-cross section of the melt pool at 50 μm from the edge of the stripe (2nd and 3rd track) – Coupon 12

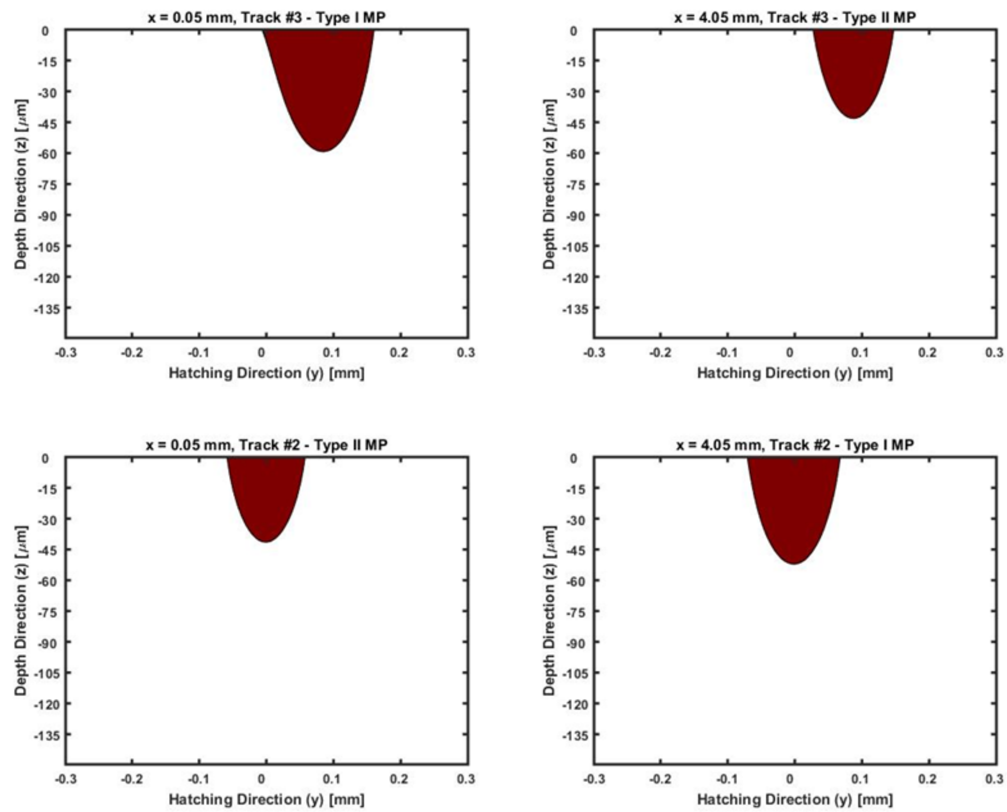

Figure B.7. YZ-cross section of the melt pool at 50 μm from the edge of the stripe (2nd and 3rd track) – Coupons 14, 15, and 17

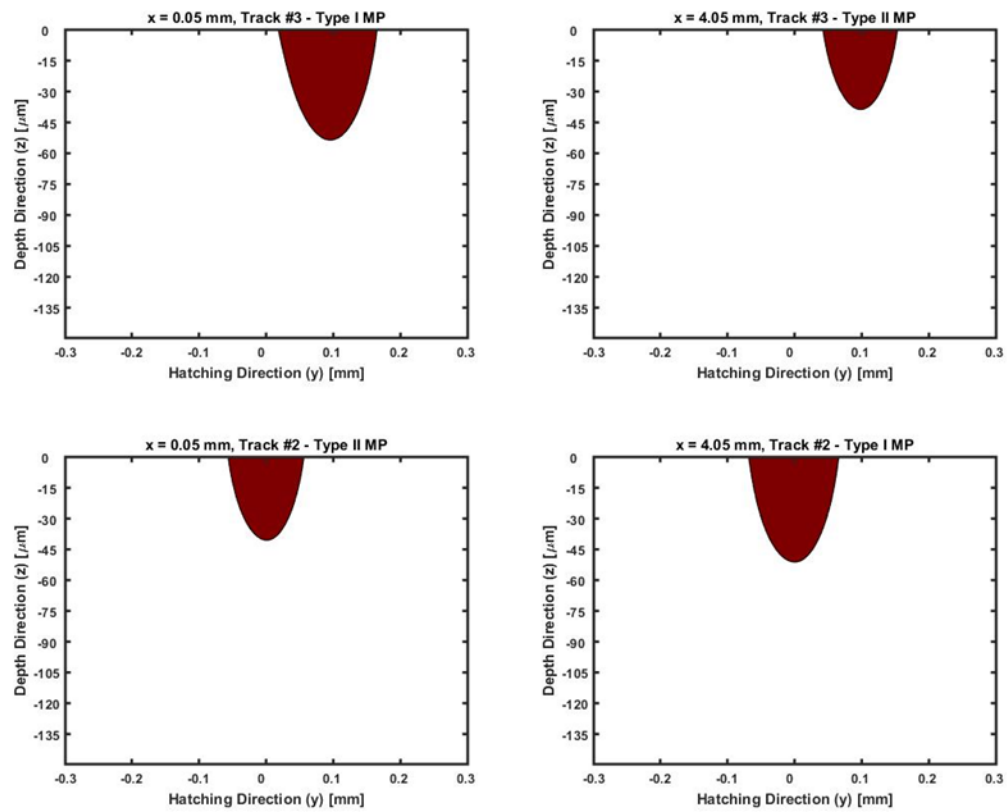

Figure B.8. YZ-cross section of the melt pool at 50 μm from the edge of the stripe (2nd and 3rd track) – Coupon 16

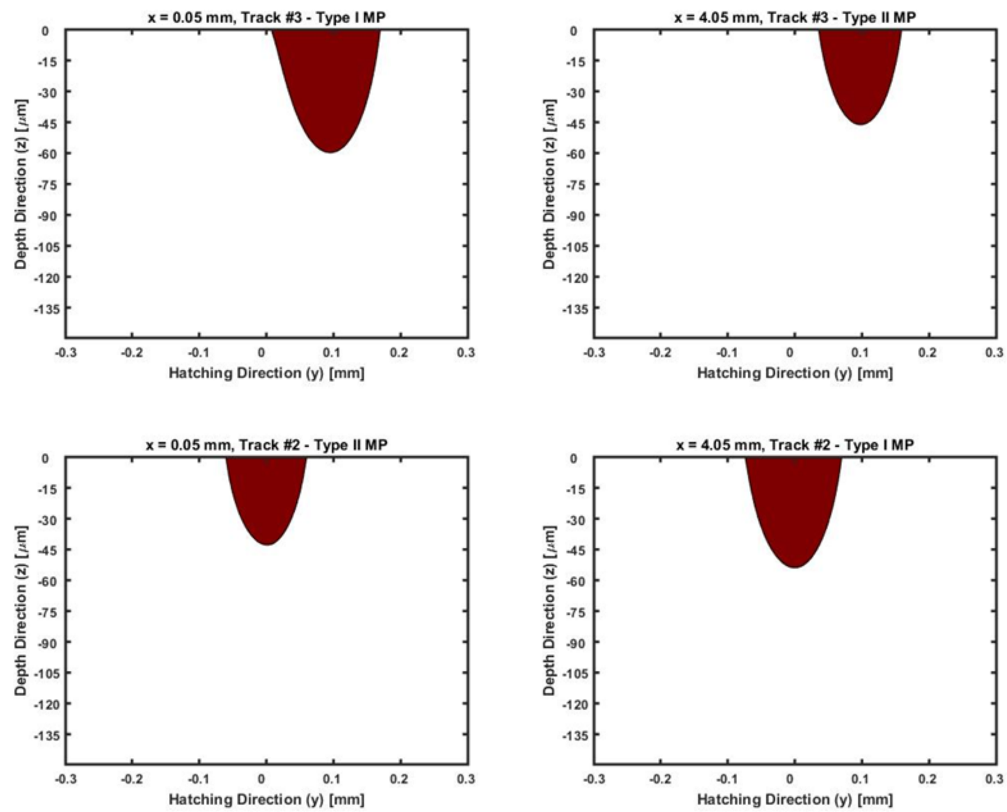

Figure B.9. YZ-cross section of the melt pool at 50 μm from the edge of the stripe (2nd and 3rd track) – Coupon 18

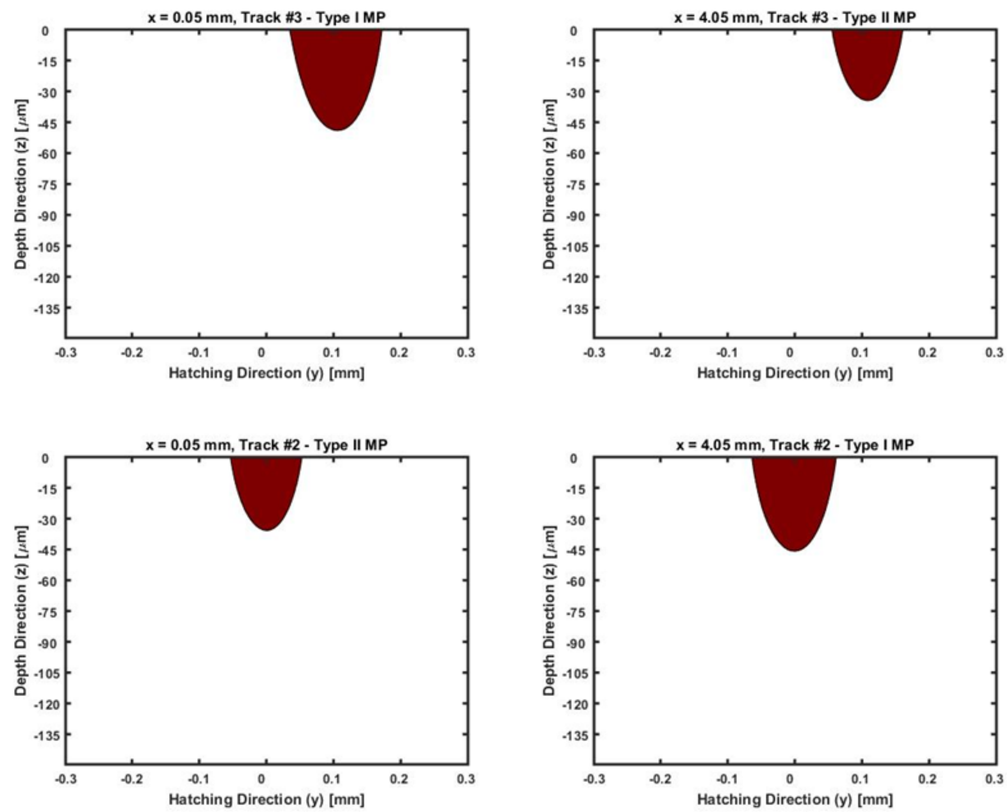

Figure B.10. YZ-cross section of the melt pool at 50 μm from the edge of the stripe (2nd and 3rd track) – Coupon 20

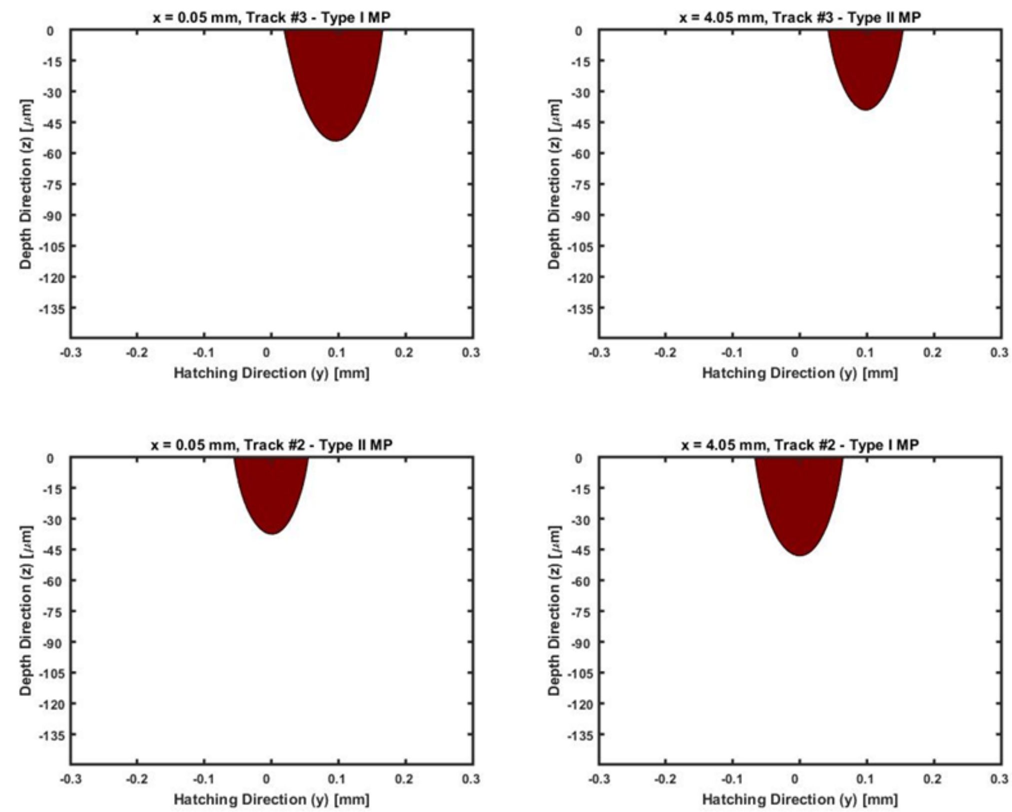

Figure B.11. YZ-cross section of the melt pool at 50 μm from the edge of the stripe (2^{nd} and 3^{rd} track) – Coupon 21

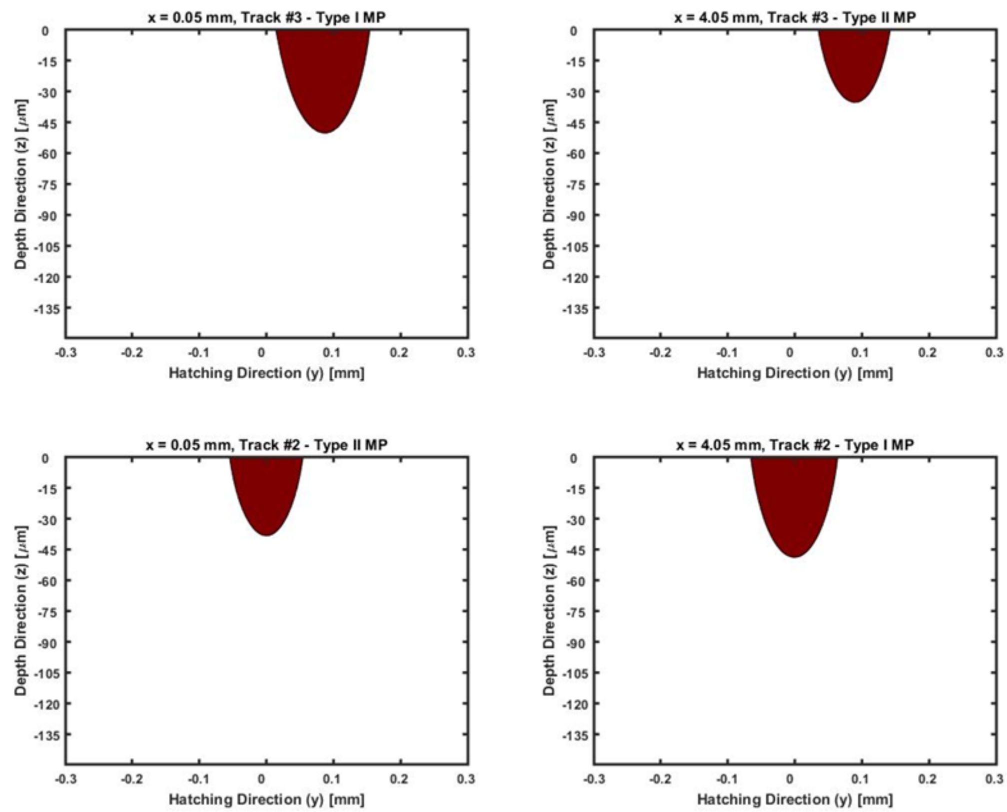

Figure B.12. YZ-cross section of the melt pool at 50 μm from the edge of the stripe (2nd and 3rd track) – Coupon 23

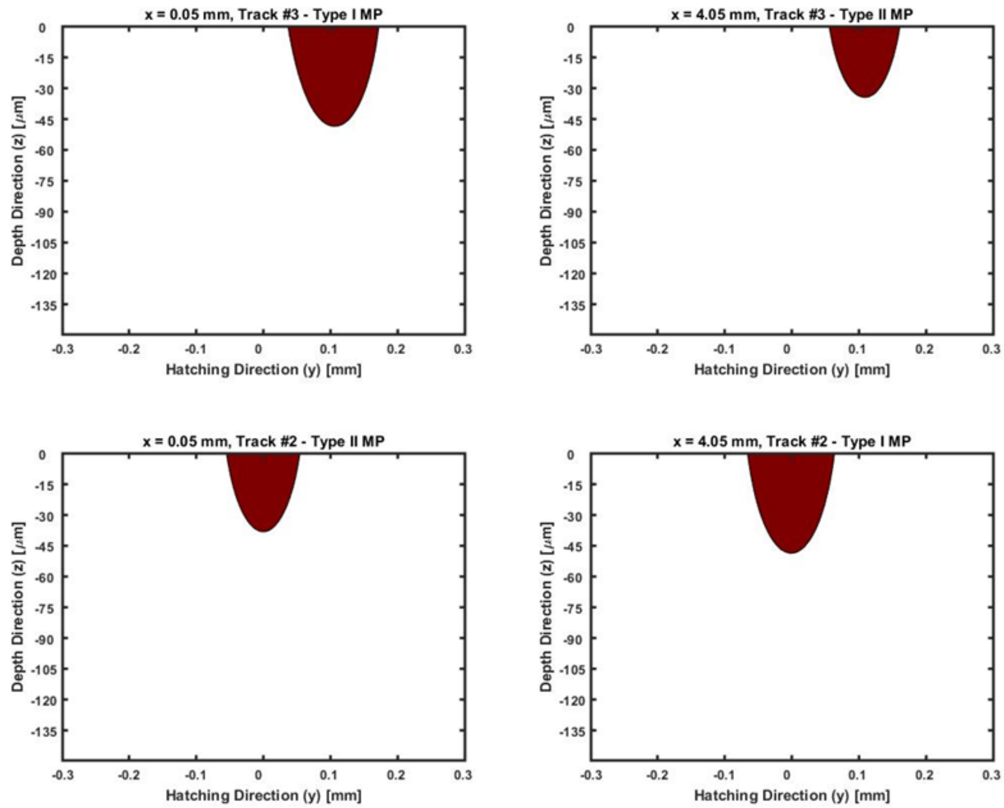

Figure B.13. YZ-cross section of the melt pool at 50 μm from the edge of the stripe (2nd and 3rd track) – Coupon 29

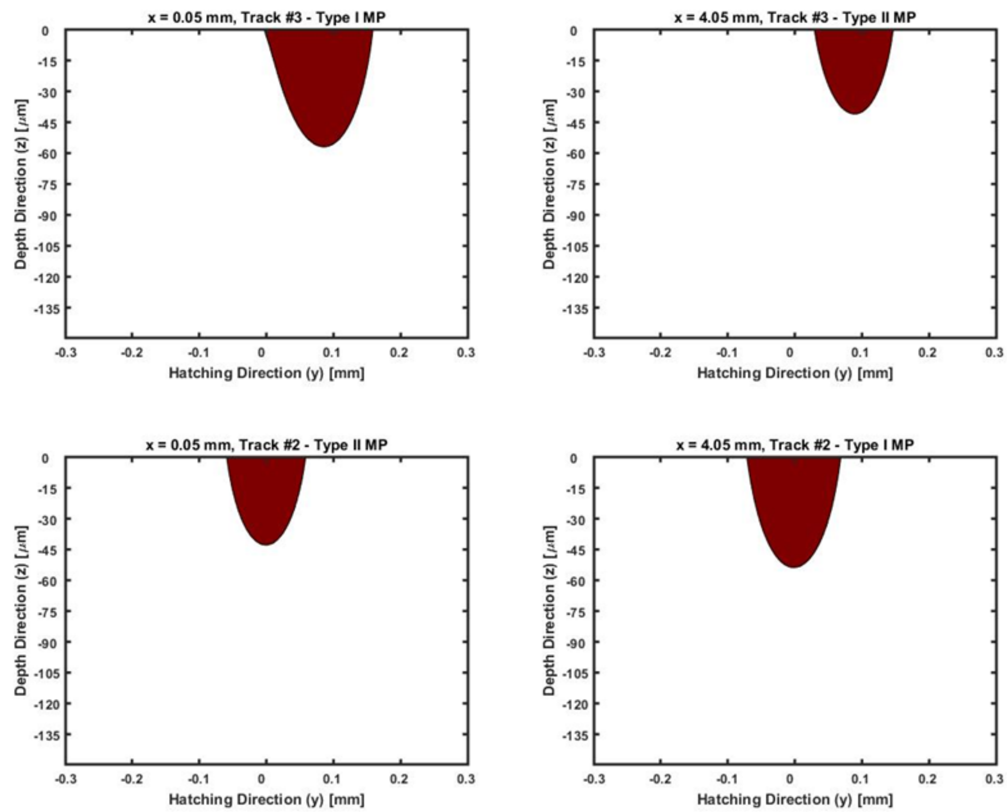

Figure B.14. YZ-cross section of the melt pool at 50 μm from the edge of the stripe (2nd and 3rd track) – Coupon 35

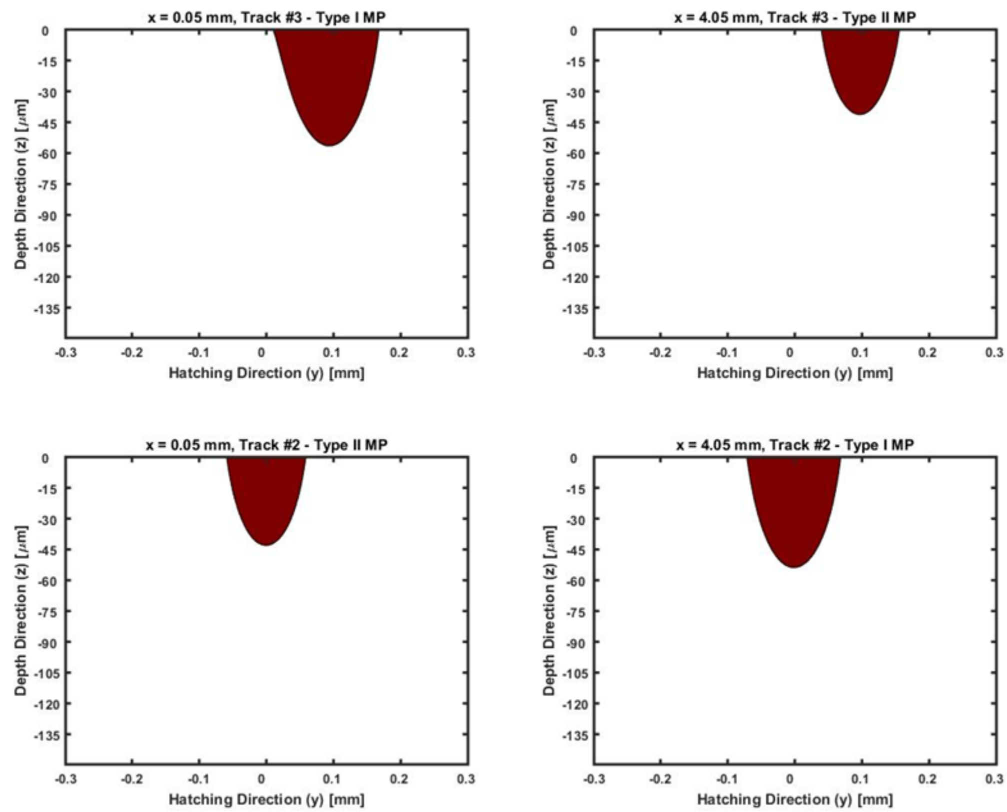

REFERENCES

AGGARANGSI, P., BEUTH, J. L. & GRIFFITH, M. Melt pool size and stress control for laser-based deposition near a free edge. Solid Freeform Fabrication Proceedings, 2003. University of Texas, Austin, TX, 196-207.

AMATO, K., GAYTAN, S., MURR, L., MARTINEZ, E., SHINDO, P., HERNANDEZ, J., COLLINS, S. & MEDINA, F. 2012. Microstructures and mechanical behavior of Inconel 718 fabricated by selective laser melting. *Acta Materialia,* 60**,** 2229-2239.

ANAM, M. A., DILIP, J., PAL, D. & STUCKER, B. Effect of Scan Pattern on the Microstructural Evolution of Inconel 625 during Selective Laser Melting. SFF Symposium 2014 proceedings, 2014 Austin, TX, USA.

ANAM, M. A., PAL, D. & STUCKER, B. Modeling and Experimental validation of Nickel-based super alloy (Inconel 625) made using Selective Laser Melting. Proc. 24th Annual Int. Solid Freeform Fabrication Symp.–An Additive Manufacturing Conf., Austin, TX, USA, 2013. 463-473.

BERTOL, L. S., JÚNIOR, W. K., DA SILVA, F. P. & AUMUND-KOPP, C. 2010. Medical design: direct metal laser sintering of Ti–6Al–4V. *Materials & Design,* 31**,** 3982-3988.

BLUM, C. & LI, X. 2008. *Swarm intelligence in optimization*, Springer.

BOIVINEAU, M., CAGRAN, C., DOYTIER, D., EYRAUD, V., NADAL, M.-H., WILTHAN, B. & POTTLACHER, G. 2006. Thermophysical properties of solid and liquid Ti-6Al-4V (TA6V) alloy. *International journal of thermophysics,* 27**,** 507-529.

CALIXTO, S. & PADILLA, G. P. 1996. Micromirrors and microlenses fabricated on polymer materials by means of infrared radiation. *Applied optics,* 35**,** 6126-6130.

CHEN, S., KANCHARLA, V. V. & LU, Y. 2003. Laser-based microscale patterning of biodegradable polymers for biomedical applications. *International Journal of Material & Product Technology,* 18**,** 457-468.

CHICHKOV, B., MOMMA, C., NOLTE, S., VON ALVENSLEBEN, F. & TÜNNERMANN, A. 1996. Femtosecond, picosecond and nanosecond laser ablation of solids. *Applied Physics A,* 63**,** 109-115.

CHIVEL, Y. & SMUROV, I. 2010. On-line temperature monitoring in selective laser sintering/melting. *Physics Procedia,* 5**,** 515-521.

CHU, C. C. 1990. *Polyesters and Polyamides*, Pergamon Press, New York.

CIURANA, J., ARIAS, G. & OZEL, T. 2009. Neural network modeling and particle swarm optimization (PSO) of process parameters in pulsed laser micromachining of hardened AISI H13 steel. *Materials and Manufacturing Processes,* 24**,** 358-368.

CRIALES, L., ARISOY, Y. M. & ÖZEL, T. 2015a. Sensitivity analysis study on the material properties and process parameters for selective laser melting of Inconel 625. *2015 ASME International Conference on Manufacturing Science and Engineering.* Charlotte, NC, USA.

CRIALES, L., ARISOY, Y. M. & ÖZEL, T. 2016. Sensitivity Analysis of Material and Process Parameters in Finite Element Modeling for Selective Laser Melting of Inconel 625. *International Journal of Advanced Manufacturing Technology*.

CRIALES, L. & ÖZEL, T. 2014. Prediction of Temperature Profile using a Finite Difference Method for Selective Laser Melting of Ti-6Al-4V Titanium Alloy. *42nd North American Manufacturing Research Conference.* Detroit, MI, USA.

CRIALES, L. E., OROZCO, P. F., MEDRANO, A., RODRÍGUEZ, C. A. & ÖZEL, T. 2015b. Effect of Fluence and Pulse Overlapping on Fabrication of Microchannels in PMMA/PDMS via UV Laser Micromachining: Modeling and Experimentation. *Materials and Manufacturing Processes*.

DAI, D. & GU, D. 2014. Thermal behavior and densification mechanism during selective laser melting of copper matrix composites: Simulation and experiments. *Materials & Design,* 55**,** 482-491.

DAY, D. & GU, M. 2005. Microchannel fabrication in PMMA based on localized heating by nanojoule high repetition rate femtosecond pulses. *Optics express,* 13**,** 5939-5946.

DEB, K. 2011. Multi-Objective Optimization Using Evolutionary Algorithms: An Introduction. Kanpur, India: Indian Institute of Technology Kanpur.

DEB, K., PRATAP, A., AGARWAL, S. & MEYARIVAN, T. 2002. A fast and elitist multiobjective genetic algorithm: NSGA-II. *IEEE Transactions on Evolutionary Computation,* 6**,** 182-197.

EAGAR, T. & TSAI, N. 1983. Temperature fields produced by traveling distributed heat sources. *Welding Journal,* 62**,** 346-355.

FISCHER, P., LOCHER, M., ROMANO, V., WEBER, H.-P., KOLOSSOV, S. & GLARDON, R. 2004. Temperature measurements during selective laser sintering of titanium powder. *International Journal of Machine Tools and Manufacture,* 44**,** 1293-1296.

GATES, B. D., XU, Q., LOVE, J. C., WOLFE, D. B. & WHITESIDES, G. M. 2004. Unconventional Nanofabrication. *Annual Review of Materials Research,* 34**,** 339-372.

GOLDAK, J., BIBBY, M. & CHAKRAVARTI, A. 1985. *A double ellipsoid finite element model for welding heat sources*, International Institute of Welding.

GÓMEZ, D., GOENAGA, I., LIZUAIN, I. & OZAITA, M. 2005. Femtosecond laser ablation for microfluidics. *Optical Engineering,* 44.

GONG, X., CHENG, B., PRICE, S. & CHOU, K. Powder-bed electron-beam-melting additive manufacturing: powder characterization, process simulation and metrology. 2013 ASME Early Career Technical Conference, ASME ECTC, 2013.

GORAL, V. N., HSIEH, Y.-C., PETZOLD, O. N., FARIS, R. A. & YUEN, P. K. 2010. Hot Embossing of Plastic Microfluidic Devices Using Poly(dimethylsiloxane) Molds. *14th International Conference on Miniaturized Systems for Chemistry and Life Sciences.* Groningen, The Netherlands.

GOWER, M. C. & RIZVI, N. H. Applications of laser ablation to microengineering. High-Power Laser Ablation, 2000. International Society for Optics and Photonics, 452-460.

GREFENSTETTE, J. J. 1986. Optimization of Control Parameters for Genetic Algorithms. *IEEE Transactions of Systems, Man, and Cybernetics,* 16**,** 122-128.

GU, D. & SHEN, Y. 2009. Balling phenomena in direct laser sintering of stainless steel powder: Metallurgical mechanisms and control methods. *Materials & Design,* 30**,** 2903-2910.

GUSAROV, A., LAOUI, T., FROYEN, L. & TITOV, V. 2003. Contact thermal conductivity of a powder bed in selective laser sintering. *International Journal of Heat and Mass Transfer,* 46**,** 1103-1109.

GUSAROV, A. & SMUROV, I. 2003. Near-surface laser–vapour coupling in nanosecond pulsed laser ablation. *Journal of Physics D: Applied Physics,* 36**,** 2962.

GUSAROV, A., YADROITSEV, I., BERTRAND, P. & SMUROV, I. 2007. Heat transfer modelling and stability analysis of selective laser melting. *Applied Surface Science,* 254**,** 975-979.

HE, T., WANG, C., URISU, T., NAGAHIRO, T., TERO, R. & XIA, R. 2010. The PDMS-based microfluidic channel fabricated by synchrotron radiation stimulated etching. *Optics Express,* 18**,** 9733-9738.

HOFMANN, O., NIEDERMANN, P. & MANZ, A. 2001. Modular approach to fabrication of three-dimensional microchannel systems in PDMS - application to sheath flow microchips. *Lab on a Chip,* 2001**,** 108-114.

HONG, T.-F., JU, W.-J., WU, M.-C., TAI, C.-H., TSAI, C.-H. & FU, L.-M. 2010. Rapid prototyping of PMMA microfluidic chips utilizing a CO2 laser. *Microfluidics and nanofluidics,* 9**,** 1125-1133.

HUANG, H. & GUO, Z. 2009. Ultra-short pulsed laser PDMS thin-layer separation and micro-fabrication. *Journal of Micromechanics and Microengineering,* 19**,** 055007.

HUSSEIN, A., HAO, L., YAN, C. & EVERSON, R. 2013. Finite element simulation of the temperature and stress fields in single layers built without-support in selective laser melting. *Materials & Design,* 52**,** 638-647.

JAHN, M., LUTTMANN, A., SCHMIDT, A. & PAUL, J. 2012. Finite element methods for problems with solid-liquid-solid phase transitions and free melt surface. *PAMM,* 12**,** 403-404.

JEONG, S., GREIF, R. & RUSSO, R. 1998. Numerical modeling of pulsed laser evaporation of aluminum targets. *Applied Surface Science,* 127**,** 177-183.

JIA, Q. & GU, D. 2014. Selective laser melting additive manufacturing of Inconel 718 superalloy parts: Densification, microstructure and properties. *Journal of Alloys and Compounds,* 585**,** 713-721.

JO, B.-H., VAN LERBERGHE, L. M., MOTSEGOOD, K. M. & BEEBE, D. J. 2000. Three-Dimensional Micro-Channel Fabrication in Polydimethylsiloxane (PDMS) Elastomer. *Journal of Microeletromechanical Systems,* 9**,** 76-81.

KARPAT, Y. & ÖZEL, T. 2007. Multi-objective optimization for turning processes using neural network modeling and dynamic-neighborhood particle swarm optimization. *The International Journal of Advanced Manufacturing Technology,* 35**,** 234-247.

KENNEDY, J. & EBERHART, R. C. 1995. Particle swarm optimization. *IEEE International Conference on Neural Networks.*

KI, H. & MAZUMDER, J. 2005. Numerical simulation of femtosecond laser interaction with silicon. *Journal of laser applications*, 17**,** 110-117.

KOLOSSOV, S., BOILLAT, E., GLARDON, R., FISCHER, P. & LOCHER, M. 2004. 3D FE simulation for temperature evolution in the selective laser sintering process. *International Journal of Machine Tools and Manufacture,* 44**,** 117-123.

KONAK, A., COIT, D. W. & SMITH, A. E. 2006. Multi-objective optimization using genetic algorithms: A tutorial. *Reliability Engineering and System Safety,* 91**,** 992-1007.

KRAUSS, H., ZEUGNER, T. & ZAEH, M. F. 2014. Layerwise Monitoring of the Selective Laser Melting Process by Thermography. *Physics Procedia,* 56**,** 64-71.

KRÜGER, J., MARTIN, S., MÄDEBACH, H., URECH, L., LIPPERT, T., WOKAUN, A. & KAUTEK, W. 2005. Femto-and nanosecond laser treatment of doped polymethylmethacrylate. *Applied surface science,* 247**,** 406-411.

KRUTH, J.-P., LEVY, G., KLOCKE, F. & CHILDS, T. 2007. Consolidation phenomena in laser and powder-bed based layered manufacturing. *CIRP Annals-Manufacturing Technology,* 56**,** 730-759.

LANE, B., MOYLAN, S., WHITENTON, E. & MA, L. 2015. Thermographic Measurements of the Commercial Laser Powder Bed Fusion Process at NIST. *Solid Freeform Fabrication Symposium.* Austin, TX.

LEVY, G. N. 2010. The role and future of the laser technology in the additive manufacturing environment. *Physics Procedia,* 5**,** 65-80.

MENDES, R., KENNEDY, J. & NEVES, J. 2004. The fully informed particle swarm: simpler, maybe better. *Evolutionary Computation, IEEE Transactions on,* 8**,** 204-210.

MERCELIS, P. & KRUTH, J.-P. 2006. Residual stresses in selective laser sintering and selective laser melting. *Rapid Prototyping Journal,* 12**,** 254-265.

MIOTELLO, A. & KELLY, R. 1995. Critical assessment of thermal models for laser sputtering at high fluences. *Applied Physics Letters,* 67**,** 3535-3537.

MITCHELL, M. 1996. *An Introduction to Genetic Algorithms*, The MIT Press.

MOMMA, C., NOLTE, S., CHICHKOV, B. N., ALVENSLEBEN, F. V. & TÜNNERMANN, A. 1997. Precise laser ablation with ultrashort pulses. *Applied surface science*, 109**,** 15-19.

MYERS, R. H., MONTGOMERY, D. C. & ANDERSON-COOK, C. M. 2009. *Response Surface Methodology: Process and Product Optimization Using Designed Experiments,* John Wiley & Sons.

PARK, H., ZHANG, X., GRIGOROPOULOS, C., POON, C. & TAM, A. 1996. Transient temperature during the vaporization of liquid on a pulsed laser-heated solid surface. *Journal of heat transfer,* 118**,** 702-708.

PATIL, R. B. & YADAVA, V. 2007. Finite element analysis of temperature distribution in single metallic powder layer during metal laser sintering. *International Journal of Machine Tools and Manufacture*, 47**,** 1069-1080.

PINKERTON, A. J. & LI, L. 2004. Modelling the geometry of a moving laser melt pool and deposition track via energy and mass balances. *Journal of Physics D: Applied Physics,* 37**,** 1885.

PUGMIRE, D. L., WADDELL, E. A., HAASCH, R., TARLOV, M. J. & LOCASCIO, L. E. 2002. Surface characterization of laser-ablated polymers used for microfluidics. *Analytical Chemistry,* 74**,** 871-878.

RAMANATHAN, D. & MOLIAN, P. A. 2002. Micro-and sub-micromachining of type IIa single crystal diamond using a Ti: Sapphire femtosecond laser. *Journal of manufacturing science and engineering,* 124**,** 389-396.

ROBERTS, I., WANG, C., ESTERLEIN, R., STANFORD, M. & MYNORS, D. 2009. A three-dimensional finite element analysis of the temperature field during laser melting of metal powders in additive layer manufacturing. *International Journal of Machine Tools and Manufacture,* 49**,** 916-923.

ROBERTS, M. A., ROSSIER, J. S., BERCIER, P. & GIRAULT, H. 1997. UV laser machined polymer substrates for the development of microdiagnostic systems. *Analytical chemistry,* 69**,** 2035-2042.

ROGERS, J. A. & NUZZO, R. G. 2005. Recent progress in soft lithography. *Materials today,* 8**,** 50-56.

ROSENTHAL, D. The theory of moving sources of heat and its application to metal treatments. 1946. ASME.

RUSSO, A. P., APOGA, D., DOWELL, N., SHAIN, W., TURNER, A. M. P., CRAIGHEAD, H. G., HOCH, H. C. & TURNER, J. N. 2002. Microfabricated Plastic Devices from Silicon Using Soft Intermediates. *Biomedical Microdevices,* 4**,** 277-283.

SANTOS, E., SHIOMI, M., OSAKADA, K. & LAOUI, T. 2006. Rapid manufacturing of metal components by laser forming. *International Journal of Machine Tools and Manufacture,* 46**,** 1459-1468.

SIMONELLI, M., TSE, Y. & TUCK, C. Microstructure of Ti-6Al-4V produced by selective laser melting. Journal of Physics: Conference Series, 2012. IOP Publishing, 012084.

SONG, B., DONG, S., ZHANG, B., LIAO, H. & CODDET, C. 2012. Effects of processing parameters on microstructure and mechanical property of selective laser melted Ti6Al4V. *Materials & Design,* 35**,** 120-125.

STIEGLITZ, T., BEUTEL, H., SCHUETTLER, M. & MEYER, J. U. 2000. Micromachined, Polyimide-Based Devices for Flexible Neural Interfaces. *Biomedical Microdevices,* 2**,** 283-294.

SUN, J., YANG, Y. & WANG, D. 2013. Mechanical properties of a Ti6Al4V porous structure produced by selective laser melting. *Materials & Design,* 49**,** 545-552.

SURIANO, R., KUZNETSOV, A., EATON, S. M., KIYAN, R., CERULLO, G., OSELLAME, R., CHICHKOV, B. N., LEVI, M. & TURRI, S. 2011. Femtosecond laser ablation of polymeric substrates for the fabrication of microfluidic channels. *Applied Surface Science,* 257**,** 6243-6250.

TANG, L. & LANDERS, R. G. 2010. Melt Pool Temperature Control for Laser Metal Deposition Processes—Part II: Layer-to-Layer Temperature Control. *Journal of Manufacturing Science and Engineering,* 132**,** 011011.

TEIXIDOR, D., OROZCO, F., THEPSONTHI, T., CIURANA, J., RODRÍGUEZ, C. A. & ÖZEL, T. 2013. Effect of process parameters in nanosecond pulsed laser micromachining of PMMA-based microchannels at near-infrared and ultraviolet wavelengths. *The International Journal of Advanced Manufacturing Technology,* 67**,** 1651-1664.

TEIXIDOR, D., THEPSONTHI, T., CIURANA, J. & ÖZEL, T. 2012. Nanosecond pulsed laser micromachining of PMMA-based microfluidic channels. *Journal of Manufacturing Processes,* 14**,** 435-442.

THIJS, L., VERHAEGHE, F., CRAEGHS, T., VAN HUMBEECK, J. & KRUTH, J.-P. 2010. A study of the microstructural evolution during selective laser melting of Ti–6Al–4V. *Acta Materialia,* 58**,** 3303-3312.

VAN ELSEN, M., BAELMANS, M., MERCELIS, P. & KRUTH, J.-P. 2007. Solutions for modelling moving heat sources in a semi-infinite medium and applications to laser material processing. *International Journal of heat and mass transfer,* 50**,** 4872-4882.

VANDENBROUCKE, B. & KRUTH, J.-P. 2007. Selective laser melting of biocompatible metals for rapid manufacturing of medical parts. *Rapid Prototyping Journal,* 13**,** 196-203.

VÁSQUEZ, F., RAMOS-GREZ, J. A. & WALCZAK, M. 2012. Multiphysics simulation of laser–material interaction during laser powder depositon. *The International Journal of Advanced Manufacturing Technology,* 59**,** 1037-1045.

VAZQUEZ, E., CIURANA, J., RODRIGUEZ, C. A., THEPSONTHI, T. & ÖZEL, T. 2011. Swarm intelligent selection and optimization of machining system parameters for microchannel fabrication in medical devices. *Materials and Manufacturing Processes,* 26**,** 403-414.

VERHAEGHE, F., CRAEGHS, T., HEULENS, J. & PANDELAERS, L. 2009. A pragmatic model for selective laser melting with evaporation. *Acta Materialia,* 57**,** 6006-6012.

VLACHOPOULOU, M.-E., KOKKORIS, G., CARDINAUD, C., GOGOLIDES, E. & TSEREPI, A. 2013. Plasma Etching of Poly(dimethylsiloxane): Roughness Formation, Mechanism, Control, and Application in the Fabrication of Microfluidic Structures. *Plasma Processes and Polymers,* 10**,** 29-40.

WADDELL, E. A., LOCASCIO, L. E. & KRAMER, G. W. 2002. UV laser micromachining of polymers for microfluidic applications. *Journal of the Association for Laboratory Automation,* 7**,** 78-82.

WANG, Z., GUAN, K., GAO, M., LI, X., CHEN, X. & ZENG, X. 2012. The microstructure and mechanical properties of deposited-IN718 by selective laser melting. *Journal of Alloys and Compounds,* 513**,** 518-523.

WOLYNSKI, A., HERRMANN, T., MUCHA, P., HALOUI, H. & L'HUILLIER, J. 2011. Laser ablation of CFRP using picosecond laser pulses at different wavelengths from UV to IR. *Physics procedia,* 12**,** 292-301.

WU, H., ODOM, T., CHIU, D. T. & WHITESIDES, G. M. 2002. Fabrication of Complex Three-Dimensional Microchannel Systems in PDMS. *Journal of the American Chemical Society,* 125**,** 554-559.

XIA, Y. & WHITESIDES, G. M. 1998. Soft Lithography. *Annual Review of Materials Science,* 28**,** 153-184.

YADROITSEV, I., GUSAROV, A., YADROITSAVA, I. & SMUROV, I. 2010. Single track formation in selective laser melting of metal powders. *Journal of Materials Processing Technology,* 210**,** 1624-1631.

YADROITSEV, I., KRAKHMALEV, P. & YADROITSAVA, I. 2014. Selective laser melting of Ti6Al4V alloy for biomedical applications: Temperature monitoring and microstructural evolution. *Journal of Alloys and Compounds,* 583**,** 404-409.

YADROITSEV, I., KRAKHMALEV, P., YADROITSAVA, I., JOHANSSON, S. & SMUROV, I. 2013. Energy input effect on morphology and microstructure of selective laser melting single track from metallic powder. *Journal of Materials Processing Technology,* 213**,** 606-613.

YIN, J., ZHU, H., KE, L., LEI, W., DAI, C. & ZUO, D. 2012. Simulation of temperature distribution in single metallic powder layer for laser micro-sintering. *Computational Materials Science,* 53**,** 333-339.

YUAN, D. & DAS, S. 2007. Experimental and theoretical analysis of direct-write laser micromachining of polymethyl methacrylate by CO2 laser ablation. *Journal of applied physics,* 101**,** 024901.

YUN, K.-S. & YOON, E. 2008. Fabrication of complex multilevel microchannels in PDMS by using three-dimensional photoresists masters. *Lab on a Chip,* 8**,** 245-250.

ZENG, K., PAL, D., PATIL, N. & STUCKER, B. A new dynamic mesh method applied to the simulation of selective laser melting. Proceedings of the Solid Freeform Fabrication Symposium, Austin, TX, Aug, 2013. 12-14.